Modelling and Control of Submerged-Arc Ferrosilicon Furnaces

Dr. ing. thesis

Aasgeir Mikael Valderhaug

Department of Engineering Cybernetics
The Norwegian Institute of Technology

1992

Report 92-81-W
Department of Engineering Cybernetics
The Norwegian Institute of Technology
N-7034 Trondheim, Norway

Preface

This thesis presents my work for the partial fulfillment of the requirements for the Doktor Ingeniør degree at The Norwegian Institute of Technology (NTH).

The work has been carried out between 1990-1992 at The Department of Engineering Cybernetics (ITK) at NTH in cooperation with Elkem Thamshavn, Norway and Elkem Research, Norway. I have been financially supported by Elkem a/s, Norway and The Royal Norwegian Council for Scientific and Industrial Research (NTNF) through projects PT 28.25481 and MT 27775.

I am grateful for receiving the opportunity of working on industrial problems within the frame of a doctoral degree. I acknowledge the cooperative spirit and helpfulness that I have met within Elkem, and I especially wish to thank Halvard Tveit at Elkem Thamshavn and Anders Schei and Svenn Anton Halvorsen at Elkem Research for their valuable support and cooperation.

I appreciate the cooperation with my supervisor Professor Jens G. Balchen, whose enthusiasm has been a great inspiration for me during this work. I further acknowledge the cooperation and discussions with Professor Bjarne A. Foss. I wish to thank my colleague Jan Åge Walseth, who I have been sharing office with for the last four years. Our daily discussions about solving the world's problems, in addition to professional subjects, have given me valuable inputs during these years. Furthermore, I wish to thank my colleagues and the rest of the staff at ITK for their cooperation and support. I also wish to thank Stewart Clark at NTH for his advice and corrections of the English in this thesis.

Finally, I want to express my eternal gratitude to my wife Merethe for her patience and encouragement.

Trondheim, November 30, 1992 Aasgeir Mikael Valderhaug

Summary

This thesis considers the modelling and control of submerged-arc ferrosilicon furnaces.

The occurrence of electric arcs plays an important role in a ferrosilicon furnace. As the arcs are the main source of electric power generation in the furnace, changes in the arcing conditions will affect the total process conditions significantly. In addition, using electric measurements the effects of electric arcing may indirectly give important information about inner process variables.

Based on these facts, the thesis gives a comprehensive review of arcing theory related to the arcs present in submerged-arc furnaces. Focus is placed on the properties of such arcs and their influence on the conditions in the cavities in a ferrosilicon furnace. Attention is also given the modelling aspects of electric arcs. Different model descriptions of DC arcs are reviewed, and three-dimensional analytic models and channel models are discussed. A further subject is dynamic models of AC arcs. Empirical dynamic models of AC arcs are briefly described, while dynamic AC arc models based on arc channel modelling, are considered in more detail. This part of the thesis concludes with the recommendation to use dynamic AC arc channel models to describe the arcing in submerged-arc ferrosilicon furnaces.

The electrical conditions in a ferrosilicon furnace are treated in detail regarding possible current paths, current transfer modes, charge resistivities, the electrical interaction effect, and the effects of arcing and furnace operations. Three distinct electrical model descriptions of the electrical conditions in the furnace with different application purposes are developed:

- A steady-state electrical model based on a comprehensive equivalent circuit and implemented with different electrical control strategies, is used in analyses of these control strategies by simulation studies.

  An optimization guideline regarding the control parameters in a conventional current controller is proposed based on these simulations.

- A simplified steady-state electrical model is developed for analytic analyses of the electrical interaction effect between the electrical phases, which is also analyzed by furnace experiments.

  A decoupling electrode current controller is proposed based on these analyses, and this is compared to the conventional current controller through simulation examples.

- A transient electrical model implemented with dynamic AC arc models, is used in simulation analyses of the effects of arcing on the electrical variables. This has also been analyzed by measurement data.

  Furthermore, this model is implemented in an estimator scheme for estimating inner process variables based on the electrical measurements.

The study of the electrical conditions in a ferrosilicon furnace has verified the importance of a satisfactory electrical control system. It can be further concluded that significant information about inner process variables is accessible by the use of a model-based estimator operating on electrical measurements.

The chemical reactions in the ferrosilicon process are treated and a stoichiometric model is described. Important terms related to the process are defined, and models of possible reaction patterns are discussed. The main focus has been on the metallurgical control of the process, where the important issues have been:

- The metallurgical control tasks and metallurgical optimization.
- A systematic discussion of the input variables, the inner state variables and the output variables of the process.
- Difficulties related to metallurgical control.

This discussion concludes with a recommendation about how the process variables should be used in the metallurgical control of the furnace.

Furthermore, a conventional carbon control strategy is described, and furnace step-response experiments have been carried out in order to improve this controller. The metallurgical furnace conditions are further analyzed by measurement data and simulation studies of a dynamic model of the silicon process, and qualitative models are proposed and related to furnace observations.

Two model-based measurement systems for estimating inner process variables in a ferrosilicon furnace, are presented. The metallurgical control of

a ferrosilicon furnace is considered, and two different metallurgical control strategies are discussed:

- A model-based control strategy based on the dynamic silicon model is presented. However, since the present status of available model descriptions of a complete ferrosilicon furnace is unsatisfactory, this argue against such a control strategy.

- A control strategy based on the use of the available measurements and local estimators of inner process variables is proposed. This strategy is actually an extension of the present carbon controller applied at several furnaces.

The conclusion is that the latter control strategy is recommended for metallurgical control. However, if the dynamic model of the silicon process is properly adapted, this model should be included in the control strategy.

Table of Contents

List of Figures

List of Tables

Nomenclature

General rules:

- Vectors and matrices are written in bold phase lower case and upper case letters such as $\underline{\boldsymbol{x}}$ and $\boldsymbol{X}$, respectively.
- Time varying electrical signals are written in lower case Latin letters, while upper case Latin denotes rms-values of electrical variables.
- Characteristic variables per length unit and estimated variables are represented as $\hat{x}$.
- The mean value of variables is represented as $\bar{x}$.

Abbreviations

AC	alternating current
AJD	anode jet dominated
CJD	cathode jet dominated
DC	direct current
LTE	local thermodynamic equilibrium
TE	thermodynamic equilibrium
rms	root mean square

Mathematics

∇ differential operator

- in Cartesian coordinates: $\nabla = \frac{\partial}{\partial x}\boldsymbol{i}_x + \frac{\partial}{\partial y}\boldsymbol{j}_y + \frac{\partial}{\partial z}\boldsymbol{k}_z$
- in cylindrical coordinates: $\nabla = \frac{\partial}{\partial r}\boldsymbol{i}_r + \frac{1}{r}\frac{\partial}{\partial \theta}\boldsymbol{j}_\theta + \frac{\partial}{\partial z}\boldsymbol{k}_z$

grad f	=	∇f :	gradient of a scalar
div $\underline{f}$	=	$\nabla \cdot \underline{f}$:	divergence of a vector
curl $\underline{f}$	=	$\nabla \times \underline{f}$:	curl of a vector

General notation

A	area
$\boldsymbol{A}$	system matrix
$\boldsymbol{B}$	magnetic field, system matrix
C	capacitance
C_q	power distribution constant
C_Q	optimal power distribution constant
C_w	Westly's constant
D	distance
$\boldsymbol{D}$	decoupler matrix, system matrix
E	electric field strength, activation energy
F	force
$\boldsymbol{F}$	interaction factor matrix
$\boldsymbol{F}_L$	Lorentz force
G	conductance
$\boldsymbol{G}$	control matrix
H	enthalpy
$\boldsymbol{H}$	system matrix
$\boldsymbol{H}_D$	decoupled system matrix
HF	high-pass filter
I	current (DC, rms)
J	optimization index
$J_\$$	profit function
L	self inductance
M	mutual inductance
N	particle density
P	power
$\boldsymbol{P}$	weight matrix
Pr	price
Q	heat flow
$\boldsymbol{Q}$	weight matrix
R	resistance, reaction rate, molar gas constant
S	smelting rate
T	temperature, transformer, time constant
$T1$	transformer phase
$T2$	transformer phase
$T3$	transformer phase
U	inner energy
V	voltage (DC, rms), volume
X	reactance
Z	impedance, partition function

General notation, cont'd

a	complex three-phase operator, model parameter, constant
b	model parameter, constant
$\underline{b}$	model vector
c	model parameter, constant
c_p	heat capacity at constant pressure
c_{SB}	Stefan-Boltzmann's constant
d	length, distance
e	electron elementary charge
f	electrical frequency, interaction factors
g	gravitational constant, constant
h	height, Planck's constant, input-output model
i	current (time-varying)
j	current density
k	Andreae's k-factor, discrete time variable, model gain, reaction rate constant
k_a	arc voltage characteristic
$\tilde{k}_a$	effective arc voltage characteristic
k_B	Boltzmann's constant
k_{arc}	arc power factor
l_R	absorption length
m	mass
$\dot{m}$	mass flow
n	number of segments
p	pressure, power density, thermal efficiency factor
q	heat flow
$\dot{q}$	power density emission
$\underline{q}$	derived state vector
r	radius, radial variable
s	partial pressure of SiO
t	time variable
u	control input variable
$\underline{u}$	control input vector
v	voltage (time-varying), velocity
w	noise variable, material flow
x	state variable, concentration, silicon yield
$\underline{x}$	state variable vector
y	measurement variable
$\underline{y}$	measurement vector
z	axial variable
$\underline{z}$	property state vector

General notation, cont'd

α	interaction model parameter, convective heat transfer coefficient
β	interaction model parameter, plasma flow convection coefficient
ϵ	emission coefficient
$\underline{\epsilon}$	model error vector
θ	angle, rotation variable
$\underline{\theta}$	parameter vector
κ	cell constant
λ	thermal conductivity
μ	viscosity
μ_0	magnetic permeability
ρ	mass density, electrical resistivity
σ	electrical conductivity
τ	time constant, time delay
$\boldsymbol{\tau}$	stress tensor
ϕ	working function, electrical phase angle
Δ	indicate variable deviation
$\Delta I_e{}^\star$	current dead-zone bound
$\Delta h^\star$	fixed electrode displacement
Δp	reaction pressure
$\Delta t^\star$	time-before-action period
Δt_m	arc mass time constant
Θ	cross section area
Φ	electric potential

Subscript notation

0	stationary conditions, working-point
o	electrical star-point
1	electrode, electrical phase
2	electrode, electrical phase
3	electrode, electrical phase
12	electrode-to-electrode
23	electrode-to-electrode
31	electrode-to-electrode
A	anode
Ae	electrode as anode
Am	metal bath as anode
At	anode region
AC	anode and cathode regions
C	cathode
Ce	electrode as cathode
Cm	metal bath as cathode
Ct	cathode region
D	distance
$\boldsymbol{D}$	electrical star-point
El	electrode
F	convection, plasma flow
$FixC$	fixed carbon content
HF	high frequency
I	ionization
L	conduction
Mwh	energy consumption
M	electrical neutral-point
R	radiation
$R1$	thin radiation
$R2$	thick radiation
T	transformer, turbulent
$T1$	transformer phase
$T2$	transformer phase
$T3$	transformer phase
V	vaporization
a	arc, arc states
arc	arcing
b	furnace bottom
c	charge

Subscript notation, cont'd

cav	cavity
e	electron, electrode
ec	electrode portion in cavity
el	electrode portion in charge, electrical states
eu	electrode portion above cavity
eff	effective
h	hearth
i	ion, electrical phases
k	resulting resistance
kin	kinetic
l	cavity resistance with short-circuited arc
m	metal bath, mass transfer, measured, mechanical
max	maximum
n	neutral particles
ohm	ohmic conduction
p	pressure
qa	ratio between cavity resistances
qc	ratio between cavity resistances with short-circuited arc
r	radial, ionization stage, reaction volume
ref	reference value
rms	rms values
s	solid
sc	phase resistance with short-circuited arc
sum	summation
th	thermal
vol	volume
w	cavity wall
z	axial
Δi	current alternation
Π	multiplicative terms
θ	angle, rotation

Superscript notation

0	electrical working-point
$\star$	arc power minimum

Chapter 1

Introduction

The production of ferrosilicon alloys in three-phase electric submerged-arc furnaces consumes large amounts of electric energy. The financial potential of optimal furnace operation is considerable, and strong efforts have been put into studying and analyzing the operation of this process. However, as a ferrosilicon furnace is a complex process consisting of various closely interacting sub-processes, such as metallurgical (chemical), thermal, electrical and mechanical processes, the control of such a furnace has turned out to be quite complicated. The main problems are the lack of direct measurements of the process variables in the heart of the furnace, and the limited knowledge of the complex interactions between the electrical, thermal and metallurgical conditions in the furnace.

Improved ferrosilicon furnace operations was the topic of a research program at Elkem Thamshavn, Norway in 1989. These activities led to a demand for academic research on a ferrosilicon furnace from the point of view of control engineering. This resulted in a research program on the modelling and control of submerged-arc ferrosilicon furnaces at the Department of Engineering Cybernetics at The Norwegian Institute of Technology between 1990-1992, which has resulted in this dr. ing. thesis.

The research program has been financially supported by Elkem a/s, Norway and The Royal Norwegian Council for Scientific and Industrial Research (NTNF), through the programs PT 28.25481: *Control of Ferrosilicon Furnace*, and MT 27775: *Elkem Ferroalloys - Control of Ferrosilicon Furnace*, and the work has been organized as an external activity in the internal Elkem project: *FeSi 8000*. The thesis does not deal with any restricted information from Elkem that has been made available during the work.

1.1 Outline of the thesis

This thesis can be divided into three parts:

1. **The electric arc.**

   The electric arc is an important factor in a ferrosilicon furnace, and therefore a comprehensive discussion of its features is carried out in Chapter 3.

2. **The electrical conditions.**

   The electrical conditions in the furnace are treated in Chapters 4, 5 and 6, together with important issues like modelling and analyzing, and electrical control strategies.

3. **The metallurgical conditions.**

   The metallurgical conditions in the furnace are the topics of Chapters 7, 8 and 9, where the metallurgical reactions are discussed with respect to the operation and control of the furnace.

Outline of the chapters

The different chapters in the thesis can be outlined as follows:

- Chapter 2 gives a brief introduction to submerged-arc ferrosilicon furnaces. An overview of a ferrosilicon plant is given and ferrosilicon furnace equipment is described. The process features are outlined and the operation and control of the furnace are briefly described.

- The electric arc is the topic of Chapter 3, and the physics and properties of electric arcs are described in detail. The chapter is mainly focused on arcing in electric furnaces.

  The different regions and the electrical characteristics of an electric arc are discussed and possible arc classifications based upon different arc features are outlined.

  The three arc regions; the arc column, the cathode region and the anode region, are described in detail. The different arc region properties such as electrical conductivity, flow phenomena and energy balances, are examined. Arcing in electric furnaces and particularly AC arcing in electric furnaces, is also discussed.

  The chapter also deals with the modelling aspects of electric arcs. Different model descriptions of DC arcs are reviewed, and both three-dimensional analytic models and channel models, are discussed. The

chapter also considers dynamic models of AC arcs. Empirical dynamic models of AC arcs such as the Cassie's model, are briefly described, and dynamic AC arc models based on arc channel modelling, are described in detail.

- The topic of Chapter 4 is the modelling of the electric environment in a ferrosilicon furnace.

  Electrical conduction in submerged-arc furnaces is treated in general where important issues are possible current paths, current transfer modes, and charge resistivities.

  Next, a survey of proposed models of electric furnaces is given. This ranges from simple empirical models to three-dimensional analytic models, and modelling based on equivalent circuit descriptions.

  The chapter develops two steady-state models and one transient model of the electrical conditions in a ferrosilicon furnace.

- Chapter 5 analyzes the furnace's electrical environment.

  The effect of arcing on the electrical conditions is discussed and analyzed by measurements and simulation studies.

  Then, the electrical interaction effect is modelled and analyzed by furnace experiments and simulation studies.

  The electrical aspects of furnace operation are discussed as a basis for discussions of electrical control strategies. The behavior of the electrical variable is investigated, and the effects of furnace operations on the electrical variables are discussed and demonstrated by furnace measurements.

- Chapter 6 discusses electrical strategies for a ferrosilicon furnace.

  A conventional electrical control system is described and analyzed.

  Next, a decoupling electrode current controller is proposed and compared to a conventional current controller by simulation examples.

  The chapter uses the simulation studies to propose an optimization guideline regarding the control parameters in a conventional current controller.

- Chapter 7 considers the ferrosilicon process.

  The first part of the chapter describes the chemical reactions in the ferrosilicon process and a stoichiometric model.

  Next, important terms related to the process are defined, and models of possible reaction patterns are discussed.

The next topic is the metallurgical control of the process. There is then a systematic discussion of the metallurgical control tasks, how they can be achieved by control actions, the different process input variables, the process state variables and the process output variables.

Finally, a dynamic model of the silicon process, which is used in further analyses of the process, is described.

- Chapter 8 analyzes the metallurgical process condition in the furnace in more detail.

  The effects of furnace operations on the process conditions are discussed, and their long-term variations are treated.

  Step-response experiments by altering the carbon content in the added charge, are described, and models used in the synthesis of conventional carbon controllers, are derived.

  The chapter discusses different furnace operation conditions such as over- and undercoked conditions, and qualitative models are proposed. Over- and undercoked operation cycles are simulated by using the dynamic silicon model, and the results are discussed and related to furnace operation.

  Finally, two model-based measurement systems for estimating inner process variables in a ferrosilicon furnace, are discussed.

- The metallurgical control of a ferrosilicon furnace is further treated in Chapter 9, and two different metallurgical control strategies are discussed:

  - A model-based control strategy based on the dynamic silicon model in Section 7.6.
  - A strategy using the available measurements in addition to local estimators of inner process variables, as presented in Section 8.4.

- Appendix A contains some derivations of electric arc models.

- Appendix B contains derivations of electrical models related to the analysis of the electrical interaction effects.

- Appendix C contains two papers that have been written in connection with the work:

  - Valderhaug and Sletfjerding (1992).
  - Valderhaug, Balchen and Halvorsen (1992).

1.2 Contribution of the thesis

1.2.1 Main contributions

The main contributions of the thesis are:

- A system theoretical discussion of the metallurgical control of the furnace and the proposed control strategies.
- The development of different electrical models and subsequent analyses of the electrical conditions and the electrical control.
- The development of an estimator scheme based on the transient electrical model including dynamic arc models.

1.2.2 Detailed contributions

The detailed contributions of the thesis can be outlined as follows:

- **Chapter 3.**
  - The general description of arcing phenomena occurring in electric arc furnaces, based on literature studies.
  - The proposed model of the anode and cathode regions in AC arcing, described in Section 3.7.4.
- **Chapter 4.**
  - The development of steady state and transient electrical models for submerged-arc ferrosilicon furnaces, described in Sections 4.3.2, 4.3.3 and 4.4.2.
- **Chapter 5.**
  - The development of a model of a current-controlled submerged-arc furnace, described in Section 5.2.1 and App. B, used in the analysis of the electrical interaction effect.
  - The derivation of Barker's interaction factors in App. B.3, based on the derived current-resistance model in App. B.1.
  - The analysis of the interaction effect by furnace experiments and simulation studies in Sections 5.2.3 and 5.2.4.

- **Chapter 6.**
  - The development of the non-interacting current controller, described in Section 6.3.
  - The simulation studies of the various current control strategies in Section 6.4.
  - The optimization guideline for the conventional current control algorithm, described in Section 6.4.2.
- **Chapter 7.**
  - The qualitative models of different reaction patterns in the ferrosilicon furnace, described in Section 7.4.
  - The system theoretic discussion of the metallurgical control of ferrosilicon furnaces in Section 7.5:
    * The discussion of the process state variables, described in Section 7.5.3.
    * The furnace optimization strategy, discussed in Section 7.5.4.
    * The classification of metallurgical control input variables, discussed in Section 7.5.5.
    * The discussion of the furnace output variables in Section 7.5.6.
    * The discussion about the difficulties related to the metallurgical control of a ferrosilicon furnace in Section 7.5.7.
- **Chapter 8.**
  - The carbon content step-response experiments and the subsequent derivation of input-output models used in the synthesis of the conventional carbon controllers, described in Section 8.1.3.
  - The discussions of the over- and undercoked furnace conditions in Section 8.2.
  - The development of an electrical model estimator scheme, described in Section 8.4.1.
- **Chapter 9.**
  - The model-based control strategy based on the dynamic simulation model, described in Section 9.1.
  - The metallurgical control strategy based on available measurements and estimators of inner process variables, described in Section 9.2.

1.3 Limitations of the thesis

The main objectives of the thesis are to improve the operation and control of ferrosilicon furnaces. The thesis only covers the conditions in the submerged-arc ferrosilicon furnace in a ferrosilicon plant. As this has necessitated a restriction in the extent of the research, this means that important issues that are not covered in the thesis, include:

- Handling of raw materials prior to the furnace.
- The system of energy and silica fume recovery from the waste gas of the furnace.
- The further processing of the tapped metal.
- The electrical conditions on the primary side of the furnace transformers are not discussed, and thus the transformer voltages are assumed to be stiff source voltages for the secondary circuits.
- The baking-process of the Søderberg electrodes are not treated, and this thesis does not discuss the slipping control strategies for the electrodes.

Chapter 2

A submerged-arc ferrosilicon furnace

This chapter gives a brief introduction to submerged-arc ferrosilicon furnaces. It is organized as follows: First, a ferrosilicon plant is described and particular attention is given to the submerged-arc furnace. Then the electrical equipment in the furnace and the furnace operations are covered. The chapter closes with a discussion of the furnace process geometry and metallurgical aspects.

2.1 A ferrosilicon plant

This section briefly describes the main parts of a ferrosilicon plant. The description is related to the Elkem Thamshavn 75% ferrosilicon plant at Orkanger, Norway, but will cover ferrosilicon plants in general, as well as other ferroalloy plants. The production at the Elkem Thamshavn plant is illustrated in Figure 2.1, which shows the main production lines and the plant constituents from the unloading of raw materials to the loading of packed ferrosilicon products. In general, such a plant can be divided into handling of raw materials, the furnace(s), energy recovery and cleaning of waste gas, and metal product processing.

1. **Handling of raw materials.**

   This part of the plant includes transport, storage, mixing and weighing of the raw materials which are consumed in the furnace. The various raw materials are unloaded and stored in large halls or outdoors. According to the demand the materials are moved by conveyers to different day bins, which roughly contain the daily consumption. Below the day bins there are weights where the raw materials are

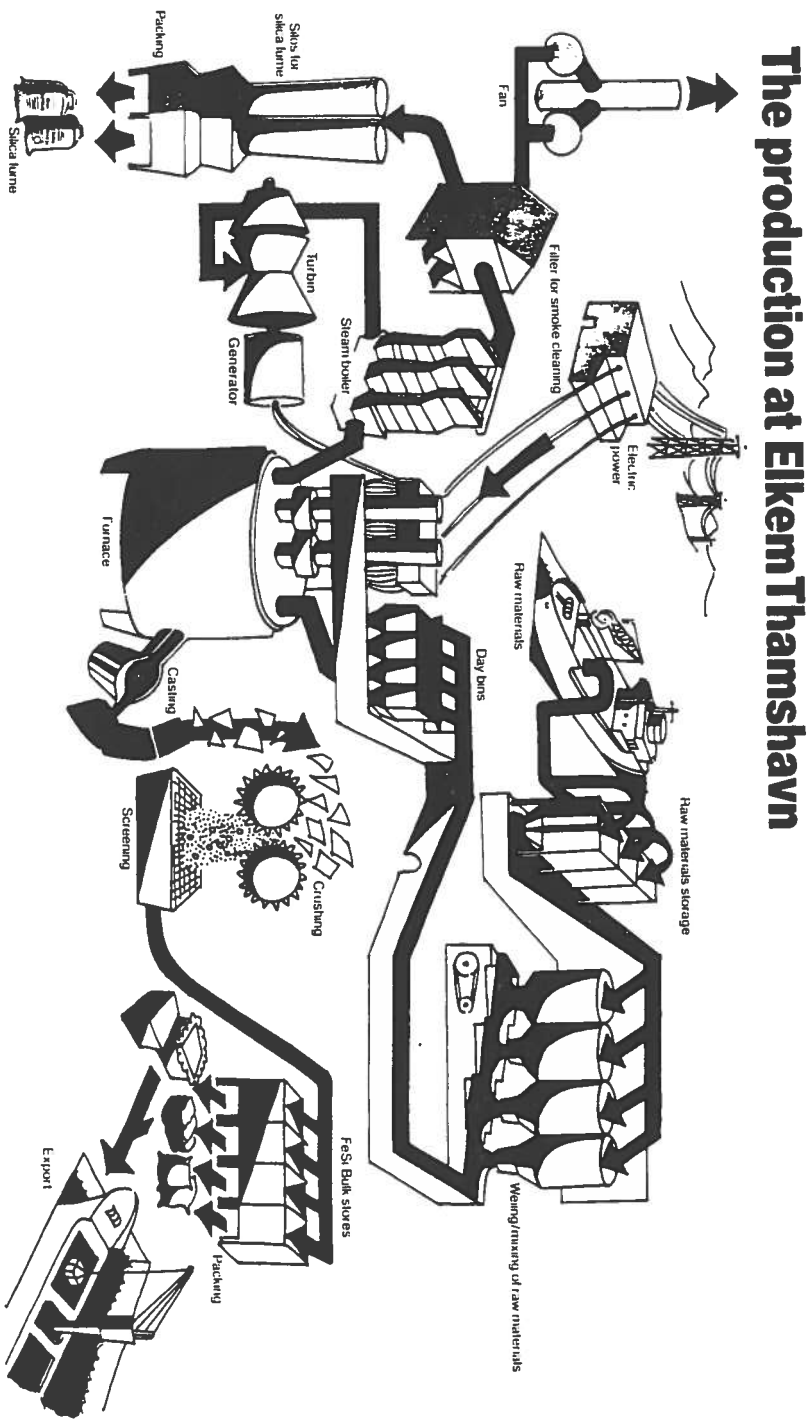

Figure 2.1: The Elkem Thamshavn ferrosilicon plant.

weighed. The raw materials are subsequently weighed and mixed according to prescribed specifications and moved to smaller furnace bins close to the furnace, and finally added at the top of the furnace through charging tubes.

2. **The furnace(s).**

   A ferrosilicon plant can in principle contain several furnaces. The raw materials are heated in the furnace(s) by large amounts of electric energy and molten metal (the ferrosilicon) is produced. The furnace at Elkem Thamshavn can operate at 65 MVA and has a daily production of up to 130 tonnes of 75% ferrosilicon, demanding an energy consumption of about 1000 MWh.

3. **Energy and silica fume recovery.**

   The waste gas from production leaves the furnace at very high temperatures and contains large amounts of silica fume ("microsilica"), which can damage the environment. Therefore, an energy recovery system is implemented, and significant amount of electric energy is produced by utilizing the heat in the waste gas. This energy recovery corresponds to a third of the total electric energy consumption in the furnace. Furthermore, the waste gas is cleaned by removing the microsilica through filtration. The original microsilica waste product has become a usable product with an increasing economic potential.

4. **Metal product processing.**

   The tapped ferrosilicon product is further processed by casting, crushing and screening, or granulating to meet the purchasers' specifications.

The topic of the thesis is the ferrosilicon furnace and related problems and the other constituents of the plant will not be further treated.

2.2 Description of a submerged-arc ferrosilicon furnace

This section briefly describes a ferrosilicon furnace. The description is related to the three-phase 65 MVA submerged-arc furnace at Elkem Thamshavn, producing 75% ferrosilicon. which has been the case study in this work, but the description will cover other submerged-arc furnaces as well.

A schematic diagram of a three-phase submerged-arc ferrosilicon furnace is shown in Fig. 2.2. Three electrodes are symmetrically arranged in the

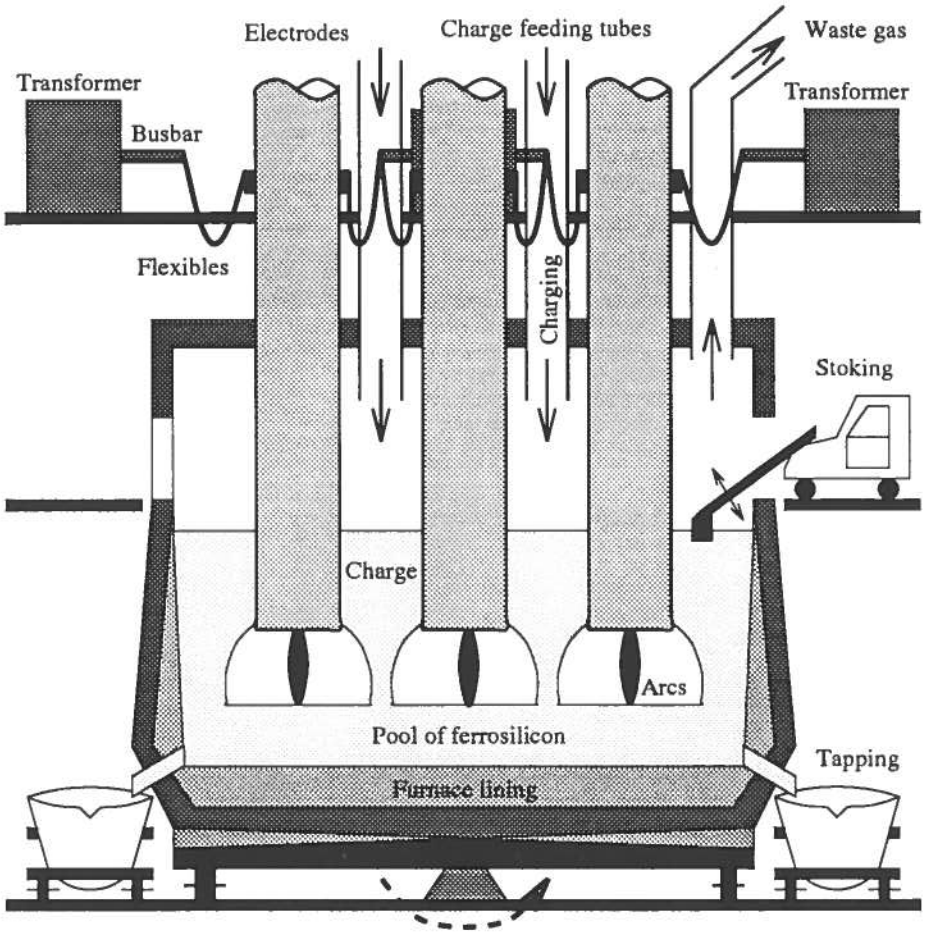

Figure 2.2: A three-phase submerged-arc ferrosilicon furnace.

circular furnace and submerged into a charge of raw materials consisting of a proportional mixture of the solid process reactants: quartz (SiO_2), coke and coal (C), and iron oxide (Fe_2O_2). The raw materials are added ("**charged**") at the top of the furnace through several charge feeding tubes. The charging tubes are situated around the furnace cross section area, as illustrated in Fig. 2.3, and designed in a special way in order to obtain an uniform distribution of the raw materials on the furnace surface and avoid particle segregation.

Cavities, in which the currents form electric arcs, appear as results of the extensive heat generation in the charge around the electrode tips. The process reactants are partly heated by the electric arcs and electrical conductance in the charge in parallel to the arcs, and the main part of the chemical pro-

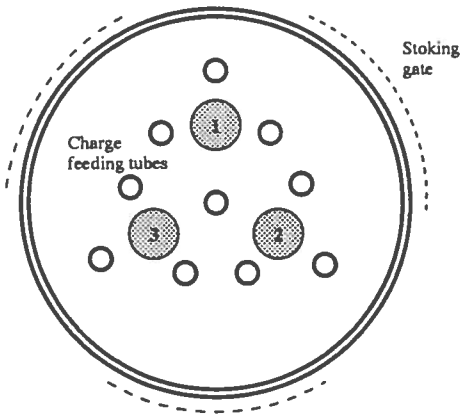

Figure 2.3: Electrodes and spatial distributon of charging tubes and stoking gates.

cesses occur at high temperatures in and near these cavities. The quartz and iron oxide are reduced, and ferrosilicon ("FeSi") is produced. The ferrosilicon forms pools in and below the cavities and is drained from tap-holes at the bottom of the furnace, as shown in Fig. 2.2. The gaseous products of the furnace silicon monoxide (SiO) and carbon monoxide (CO), are released and burn with air at the top of the furnace, forming silica fume (SiO_2) and carbon dioxide (CO_2). The **silicon yield** for a 75% FeSi furnace is about 90 %, which means that 10% of the added silicon leaves the furnace as silica fume, and the silica fume is subsequently recovered from the furnace waste gas.

The furnace shell and lining is designed in a special way to ensure a long operation life. The lining consists of a thick layer of a kind of carbon blocks that are suitable for the high temperatures in the furnace, while the furnace shell is made of steel. The carbon layer is conductive and ensures an electrical connection to the furnace hearth. Submerged-arc furnaces are today mainly closed-top furnaces in order to collect and control the high-temperature gas releases from the furnace. With such furnaces it is necessary to have special gates in the furnace walls to facilitate the stoking operation.

The furnace at Elkem Thamshavn has a diameter of 12.0 m and the furnace pot is 4.0 m deep. The furnace pot is placed on special wheels and rotates with a rotation velocity of about 200 hours per rotation, in order to break down any crusts in the charge. It is equipped with 10 charging tubes and three stoking gates are placed around the furnace wall as shown in Fig. 2.3.

2.3 The ferrosilicon process

Ferrosilicon alloys are produced with different iron contents. The most common alloys are FeSi 45, FeSi 75 and FeSi 90, where the figure indicates the percentage weight content of silicon. The overall reaction for FeSi 75 with 100% silicon yield, can be described by:

$$12\ SiO_2 + Fe_2O_3 + a\ C \rightarrow 2\text{“}FeSi_6\text{”} + b\ CO + c\ CO_2 \qquad (2.1)$$

where a, b and c depend on the reduction of the iron oxide. The ferrosilicon process is closely related to the **silicon process**. If the alloy has more than 60% silicon content, the process behaves similarly to the pure silicon process. The reduction of quartz is the limiting factor in the ferrosilicon process, and in qualitative terms the process will be easier to carry out the higher the iron content of the alloy (Schei and Larsen, 1982; Schei and Halvorsen 1991). Thus, the ferrosilicon process can be described by models of the pure silicon process, provided the model parameters are properly adjusted. The pure silicon process is treated in the further discussion.

The overall reaction in the silicon process can be stated as:

$$(1+x)\ SiO_2 + (2+x)\ C \rightarrow Si + x\ SiO + (2+x)\ CO \qquad (2.2)$$

where x denotes the **silicon loss**, silicon monoxide (SiO) leaving the furnace in proportion to added silica (quartz). The **silicon yield**, produced silicon in proportion to added silica (quartz), is given as $1/(1+x)$.

2.3.1 Process geometry and metallurgical aspects

The inner structure of ferrosilicon furnaces has been investigated among others by Otani et al. (1968) and Zherdev et al. (1968), who established the formation of cavities in the charge around the electrode tips and the occurrence of significant arcing between the electrode tips and the metal bath in these cavities. The various regions of the charge burden in ferrosilicon furnaces have been investigated by “dig-outs” of various furnaces, mostly experimental furnaces. The disadvantage with such dig-outs is that they have to be carried out in a “cold” furnace, and the original furnace environment may have changed considerably. Nevertheless, dig-out investigations have revealed significant information about the spatial distribution of the different charge materials and the nature and properties of the cavities in the heath of the furnace. Besides the dig-outs, the development of furnace observation and measurement equipment have made it possible to investigate the cavity conditions directly in experimental furnaces. The inner process geometry and some related metallurgical aspect of ferrosilicon

furnaces are briefly outlined in the following. This is based on Otani et al. (1968), Zherdev et al. (1968), Müller, Olsen and Tuset (1972), Schei and Larsen (1979, 1982) and Person (1985).

The cavities

In submerged-arc ferrosilicon furnaces cavities appear as a result of heavy heat generation in the charge around the electrode tips. The presence of such cavities in the charge of ferrosilicon furnaces was established by Zherdev et al. (1968), who used probes which were inserted into the charge. Otani et al. (1968) used visual peep pipes which were inserted towards the cavities in the charge of laboratory furnaces and small industrial furnaces. They established the occurrence of a cavity around the electrode tip by observations and film recordings and saw an electric arc burns between the electrode tip and a liquid metal bath in the cavities. At the metal bath surface lumped materials floated which continuously appeared in spite of a rapid consumption due to the arc heating. These experiments have been re-established by among others Schei at Elkem Research, who has carried out several experiments on 50 kW and 500 kW laboratory furnaces. The results of these experiments have so far not been non-restrictively published, but have been documented in film recordings (Schei and Larsen, 1979) and recently in video recordings. The cavities have the following typical features:

1. The arcs burn between the electrode and the liquid metal bath.

2. After tapping the furnace the cavity bottom consisting of solid materials, is observed, which disappears as the liquid metal is produced.

3. Just after stoking and charging of raw materials, tough materials, probably silica (quartz), sag down from the cavity roof and partly cover the liquid metal bath. This sagging soon decreases.

4. Next, a somewhat different sagging of tough materials with solid particles, occurs. These materials float at the liquid metal surface and are consumed continuously in the reactions.

5. As time goes by, the cavity size increases, mainly upwards, provided the furnace is operated at a correct stoichiometric balance. This is due to the continuous sagging of materials from the cavity roof.

   If the balance is not fulfilled, the result can be a build-up of SiC and the cavity bottom will grow upwards.

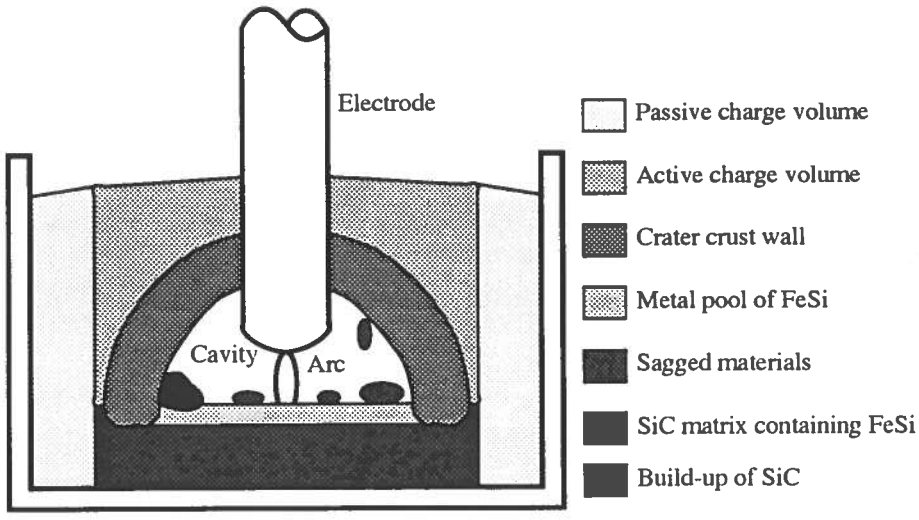

Figure 2.4: Simplified scheme of the inner structure of a ferrosilicon furnace.

The cavity formation in ferrosilicon furnaces has been found to depend on the silicon yield of the produced metal, with an increased size as the silicon content of the alloy rose (Person, 1985). The temperatures in the cavities, or in fact the temperatures at the cavity walls, are measured and found to be about 2000 ° C.

The charge burden

The distribution of the charge reactant materials in a ferrosilicon furnace is schematically illustrated in Fig. 2.4, for the case of a single electrode furnace. In the middle of the furnace a cavity is present surrounding the electrode tip. In the cavity an electric arc burns between the electrode tip and the liquid metal bath of FeSi. At the liquid metal surface sagged materials from the cavity roof are floating, and some build-up of SiC is indicated. In the bottom of the furnace below the cavity there is a solid SiC matrix containing liquid FeSi. The cavity wall and roof are crust-like and contain melting silica and condensed materials. Above the cavity crust the charge reactants are heated and chemical reactions occur, and this region can be regarded as the active charge volume. The active charge volume and the cavity are surrounded by a passive charge volume that hardly takes part in the chemical reactions.

The ferrosilicon process differs from other processes in the way that there is no (or little) continuous movement of the reactant materials caused by gravity effects, and hence it is the reaction zone (the cavity region) that

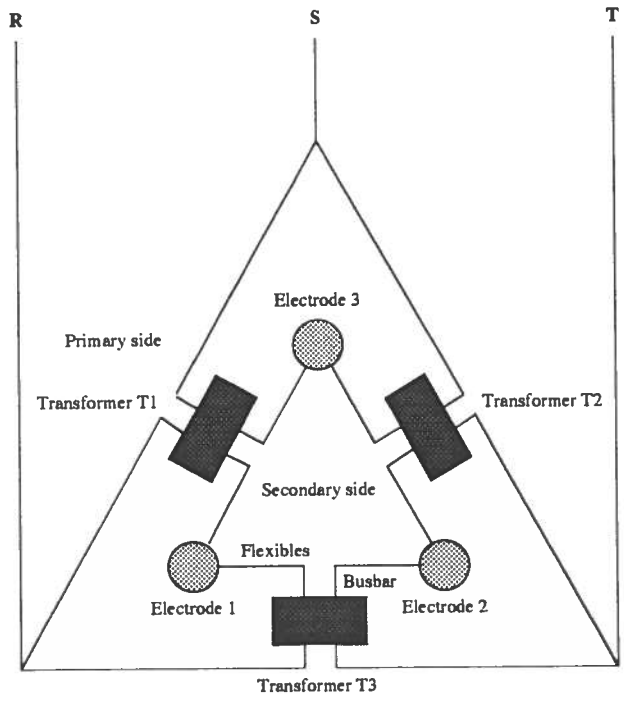

Figure 2.5: The furnace electrical connection, "The Knapsack-connection".

reaches the reactant materials and not vice versa (Müller, Olsen and Tuset, 1972). As a consequence of this it is necessary at regular time intervals to break down the crater crust and mix the charge burden, resulting in a discontinuous furnace operation cycle which will be further discussed in Section 2.5.1. The ferrosilicon process and the chemical reactions occurring in the charge and the cavities will be further discussed in Chapter 5.

2.4 The furnace's electrical environment

Electrical connection

The electric energy is supplied from high-voltage three-phase AC mains by three separate single-phase transformers in the so-called Knapsack-connection, as shown in Fig. 2.5. The three transformers are situated 120° apart around the furnace in order to provide electrical symmetry. The three secondary circuits are brought out separately by busbars from each of the transformer, and a delta-connection is made at the electrodes by using flexible conductors that allow vertical movements of the electrodes, as indicated in Fig. 2.2. To minimize reactance effects the busbars are arranged symmetrically right up to the flexibles close to the electrodes.

The Knapsack-connection methodology is discussed among others by Bretthauer and Farschtschi (1980), Stewart (1980), Stewart and Sommer (1981) and Horoszko (1982).

Furnace transformers

The furnace transformers are different from standard power system transformers and are forced to supply very high currents at low voltages on the secondary side. Typically, the electrical energy is transformed from primary line voltages of 22 kV to secondary line voltages of 250 V. The furnace resistivity is low, in the range of 1 mΩ, and therefore the secondary currents are very high, typically secondary transformer currents up to 100 kA and electrode (phase) currents of about 150 kA for a 60 MVA furnace. At such high currents the magnetic induction is considerable, and a symmetrical transformer connection, as described above, is necessary to obtain symmetrical reactances in the furnace and avoid large reactive losses.

Furthermore, special requirements have to be made regarding the design and operation of the furnace transformers, and also the busbars on the primary and secondary sides and the flexibles. It is required that the secondary voltages can be varied over a wide voltage range in order to control the power dissipation in the furnace by adjusting the applied electrode-electrode voltage. This requires that the transformers must allow on-load tap changing. The tap changing is carried out on the primary sides because of the high current regime at the secondary sides. The transformers allow for asymmetric tap changing, but this is usually avoided because of problems this leads to at the primary side. However, an asymmetric tap changing strategy will result in a tighter transformer voltage control, since the effective applied voltage steps then become smaller. The electrical furnace equipment on the transformer primary side and related problems, which have been discussed in detail by Stewart (1980) and Stewart and Sommer (1981), will not be further treated in this work. The transformers are treated in the following as ideal voltage suppliers that can be controlled by the transformer tap positions.

The transformer-furnace circuits form a delta-star equivalent circuit as shown in Fig. 2.6 (Bretthauer and Farschtschi, 1980). The electrodes conduct the current into the heart of the furnace, which corresponds to the electrical neutral point, and form an electrical star-circuit. In Fig. 2.6 the three transformer secondary voltages are represented by V_{T1}, V_{T2} and V_{T3}, respectively. The busbar impedances in the transformer circuits are denoted Z_{T1b}, Z_{T2b} and Z_{T3b}, the flexible impedances are denoted Z_{T1f},

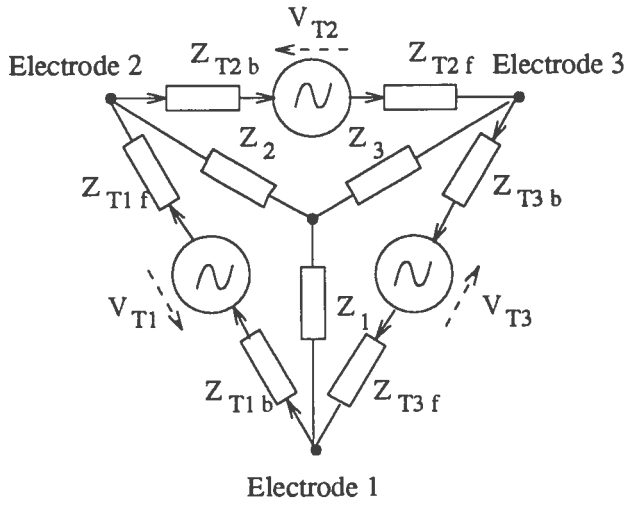

Figure 2.6: Equivalent circuit description of transformer-furnace circuits.

$Z_{T2\,f}$ and $Z_{T3\,f}$, and Z_1, Z_2 and Z_3 represent the phase impedances in the star circuit.

Current paths in the furnace

The currents are conducted through the electrodes into the heart of the furnace, where several current paths are available in principle. The main current paths in a ferrosilicon furnace are between the electrode tips and the metal pools in and beneath the cavities. The alternative current paths are conduction in the charge directly between the electrodes and directly between an electrode and the furnace wall. However, in normal furnace conditions these currents are small and negligible compared with the main currents from the electrode tip to the metal pools in the furnace bottom. The electrical secondary circuit in the furnace can therefore be assumed to be a delta-star circuit as shown in Fig. 2.6. It should be stressed that the currents in the charge are spatially distributed and that a lumped description is only a simplified model of the actual electrical circumstances. The main part of the electric energy in the furnace is dissipated in the cavities by electric arcs between the electrodes and the molten pool, or near the cavity walls by ohmic conductance in parallel with the arcs. The electrical conditions in the furnace are further treated in Chapters 4 and 5.

2.4.1 The electrodes

The electrodes in submerged-arc furnaces conduct the electrical energy from the power supply equipment to the hot furnace reactions and must have the capability of carrying high currents and resist the very high temperatures generated by the electric arcs. However, the furnace operation results in a significant electrode consumption. The electrodes used in ferrosilicon furnaces are mainly the so-called Søderberg electrodes, utilizing a continuous self-baking property, which means that the electrodes can be made in the same proportion as they are consumed.

Søderberg electrodes

The production of a Søderberg electrode starts by welding successive steel casings onto the top of the electrode structure and placing carbon paste cylinders into the casings. The paste consists of calcined anthracite (coal) particles with tar and pitch used as binding materials. Subsequently, the carbon paste cylinders melt and as the temperature increases, the baking of the electrode occur. A baked electrode is formed at the electrical contact clamping point, which is suitable for use in the furnace. The steel casings have an inner grid of steel fins with a double task, it strengthens the electrode structure while the electrode baking occurs, and furthermore, it leads the electric current from the electrical contact shoes into the center of the electrode. The necessary heat for baking the electrode is a result of the electrical conductance within the electrode. The steel casings melt in this region and a baked electrode column without any surrounding steel casing, is available for use in the furnace. The principle of a Søderberg electrode system is illustrated in Fig. 2.7 and is further treated by among others Innvær (1992).

The electrode system consists of the Søderberg electrode itself together with its supporting structure and a current connection system between the flexibles and the electrode. Figure 2.7 shows the common electrode system used in large ferrosilicon furnaces. The electrode column is surrounded by a suspension casing in the baking zone. The complete electrode system is supported from the furnace floor by hydraulic hoists connected to the electrode holder clamp system, and the electrode system can be moved vertically. The electrode column itself is held by two clamp rings that can be operated interactively with the slipping system to allow the electrode to slip. The electric current is led from the transformers by busbars and flexibles to an electrical connection equipment with electrical contact shoes clamped on the electrode, which makes it possible to maintain the electrical connection as the electrode slips.

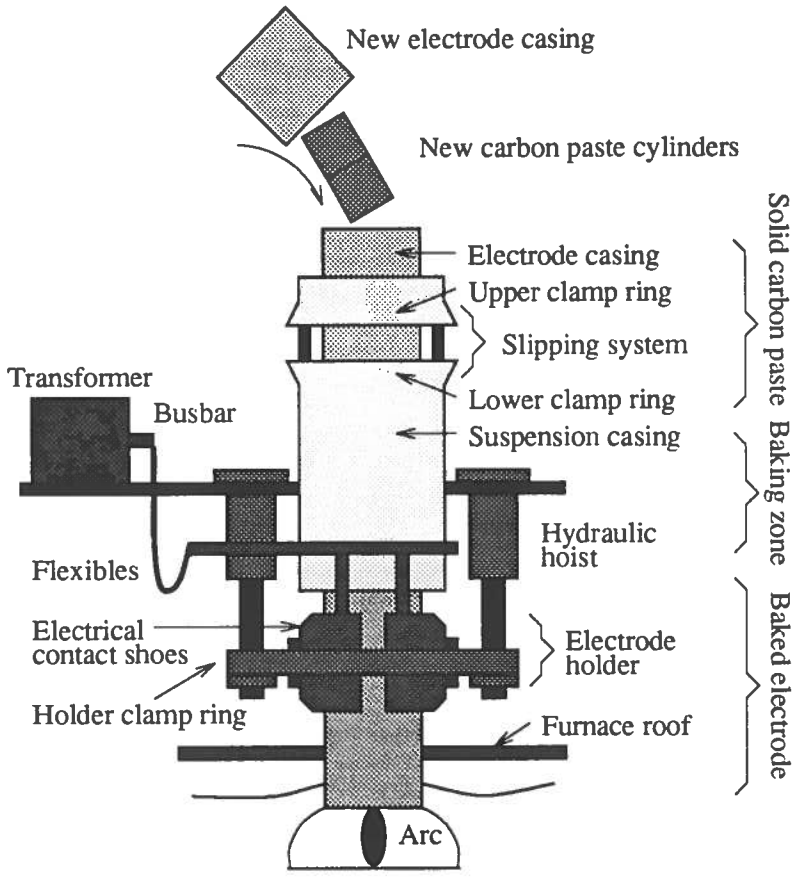

Figure 2.7: A Søderberg electrode system.

Electrode slipping

The furnace operation implies electrode erosion due to arcing effects and chemical reactions. Therefore, a periodic slipping of the electrode column is necessary in order to maintain the electrical conditions and compensate the electrode consumption. The slipping operation is executed by the slipping system and the electrode is slipped about 1-2 cm during each operation.

The maximum slipping rate will depend on the dimension of the electrode and the current passing through the electrode, which in fact corresponds to the rate of electrode baking. If the electrode is slipped too fast, the soft paste zone can be lowered until it reaches the electrical contact clamps in the electrode holding region without the necessary baking having occurred. Then the steel casing surrounding the soft carbon paste, probably will melt and the carbon paste will flow out of the casing and the electrode baking

process is destroyed. Such an electrode "**break**" is usually denoted as a "**soft break**", creating large difficulties in the furnace operation and reduced furnace power levels. Another kind of electrode breaks because too fast slipping can occur if the soft zone is lowered to the holding region. Then, the electrode may break because the electrode that is not completely baked, does not have the necessary strength to hold the electrode column.

Electrode breaks can also occur at the electrode tip or elsewhere in the baked electrode column, as the result of thermal and mechanical stresses, which often is a result of previously poor electrode baking. Breaks in the baked electrode column are usually denoted "**hard breaks**". If the electrode slipping rate is low, the baking zone may become too high up in the electrode column, leading to a situation where thermal and mechanical stresses occur in the baked electrode and subsequently, hard breaks may occur.

Electrode control

The electrode system can be moved vertically by the hydraulic hoist equipment which means that the electrode penetration in the furnace burden charge can be varied. This property is utilized in the electrical control of the furnace. By moving the electrode tip up or down, the electrical resistance between the transformer-electrode connection and the electrical star-point in the furnace is increased or decreased, respectively, and thereby the current is decreased or increased. The vertical displacements of the electrodes and the transformer tap positions are the available control inputs in the electrical control of a submerged-arc furnace. This will be further discussed in Chapter 6

2.4.2 Electrical measurements

The most important electrical measurements on a submerged-arc furnace are the electrode currents and the phase voltages between the electrical connections at the electrodes and the electrical star-point in the furnace bottom, which is usually denoted as "the electrode voltages" or "the electrode-hearth voltages". Measurements on the primary side are also to be made. All these measurements are necessary for controlling the power delivered between the three electrodes in the furnace. This is especially important for unbalanced furnace conditions and with furnaces with high reactances or low power factor. Measurements of other electrical states on the secondary side, such as power dissipation in each electrode, resistances and reactances, can be derived based on the measurements of the electrode currents and electrode voltages. The electrical measurements on submerged-arc furnaces

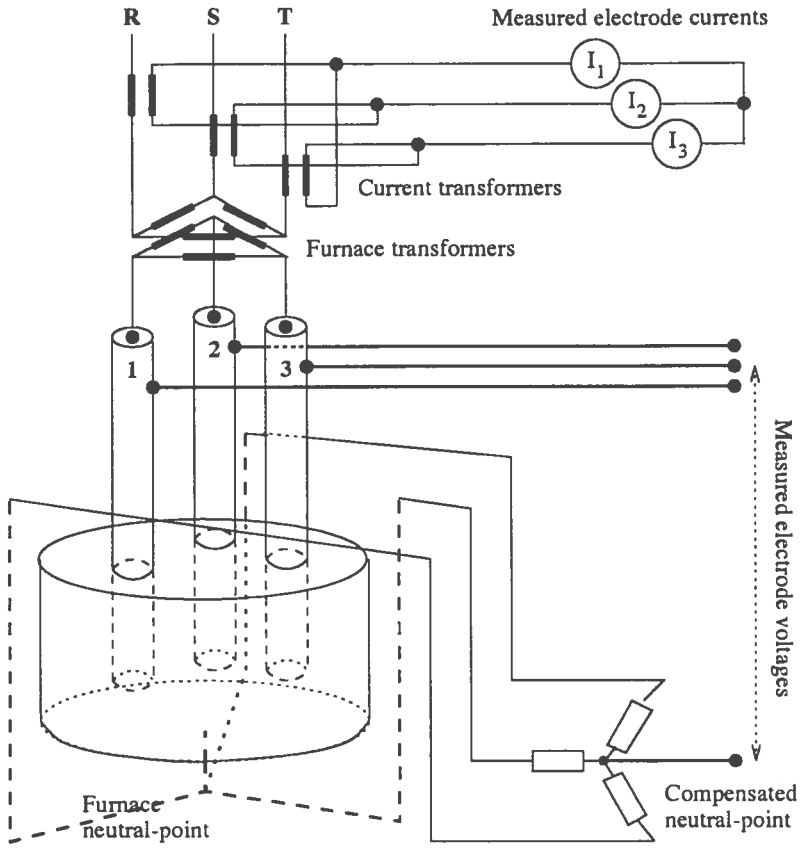

Figure 2.8: Principle of electrical measurements on a submerged-arc furnace.

are treated among others by Stewart (1980), Stewart and Barker (1980), Stewart and Sommer (1981) and Holmelid, Westly and Kvassheim (1984).

Electrode current measurement

Measurements of the electrode currents directly on the electrodes on the secondary side of the transformer are difficult because of the very high currents and the electrode dimensions. The most common way of obtaining readings of the electrode currents in submerged-arc furnaces is by measuring corresponding currents in a special measurement transformer circuit on the transformer primary side (Stewart, 1980; Stewart and Sommer, 1981).

The current measurement equipment as illustrated in Fig. 2.8, is based on an assumption of a balance of current-turns between the primary and secondary windings of the transformer. The method is generally accepted

as providing accurate measurements of the secondary currents. The transformer tap changing is compensated for in the measurement equipment by the use of an intermediate current transformer. The measurement circuit is arranged in a delta-star circuit corresponding to the furnace secondary circuit, and the secondary star currents in the measurement transformer are directly proportional to the electrode currents in the furnace. It can be shown that this will be so even at highly asymmetric furnace conditions, provided that the assumption of the transformers prevails.

Direct measurements of the electrode currents on the primary side are in principle possible and is described among others by Dmochowski (1981). However, the current measurement system based on primary currents has turned out to be a reliable and accurate method.

Electrode voltage measurement

In the vicinity of the furnace secondary circuit and especially the electrodes, there is an extremely high magnetic field regime due to the high secondary currents. This will result in induced voltages in any electrical circuit close to the furnace. The electrode voltages therefore cannot be measured by a simple voltage measurement between the electrodes and the furnace bottom, because the measured voltages will consist of both the correct electrode voltage values and the induced error voltages, which are proportional to the secondary currents. This problem is discussed among others by Bretthauer and Timm (1971), Bretthauer, Farschtschi and Timm (1975), Stewart (1980), Stewart and Sommer (1981) and Grigat and Timm (1990). The induction effects are given by the geometry of the furnace and the measurement equipment. In principle, the inductivities can be found and the induction effects can be compensated, and in open-arc furnaces this will be possible (Bretthauer and Timm, 1971; Bretthauer, Farschtschi and Timm 1975; Grigat and Timm, 1990). However, according to Stewart (1980) and Stewart and Sommer (1981), this method cannot be applied in submerged-arc furnaces because of a different furnace structure.

The electrode voltage measurement method used at the furnace at Elkem Thamshavn is the so-called Bøckman-method, which is illustrated in Fig. 2.8, and where the electrode voltages are measured in a way that almost removes measurements error due to induced inductive voltages. In the Bøckman method the furnace electrical star-point (neutral-point) is assumed to correspond to a rod inbedded in the center of the lining at the furnace bottom. Three separate leads are brought up from the neutral-point and up the side of the furnace shell in a symmetrical way adjacent to the electrodes. Then, in a region of low-magnetic fields at some distance

from the furnace, the three measurement leads are connected through equal resistors, making a "compensated" neutral-point. The electrode voltages are then measured as the voltages between the electrical connection at the electrodes and the new neutral-point. The geometry of the secondary side is fairly symmetrical due to the Knapsack connection, and if the furnace inductivities in the three electrode circuits are equal, the Bøckman method will compensate for the induction errors in the measured electrode voltages. The method reduces the measurement errors significantly and has turned out to be fairly reliable despite some errors, which are especially prevalent with asymmetric furnace conditions.

2.5 The operation and control of ferrosilicon furnaces

2.5.1 Furnace operations

The operation of a ferrosilicon furnace consists of the addition of raw materials, the maintenance of the furnace production, and the tapping of the molten metal product.

The stoking and charging operation cycle

The addition of raw materials and the management of the production in the furnace burden charge are usually organized in the following operation cycle:

- **Stoking** of the furnace charge burden.
- **Charging** of raw materials.

The stoking and charging operations are closely related. Prior to a charging of new raw materials, the upper part of the "old" furnace burden is stoked ("stirred") and the charge materials are mixed, possible gas channels in the charge are destroyed, and the cavities may to some extent be broken down and filled with charge materials. Then the furnace is charged by adding raw materials until the furnace is filled up to a given level of burden. After the charging, the added charge is softly stoked in order to mix the reactants properly and distribute the charge across the furnace surface and against the electrodes.

The stoking is carried out by the help of a special truck equipped with a stoking rod that can be moved both horizontally and vertically, as illustrated in Fig. 2.2. The stoking gates and the charging tubes can be

operated from the stoking truck. The stoking and charging operation is usually subsequently performed at one furnace sector at the time, accessible from one stoking gate, as indicated in Fig. 2.3, by stoking this region and charging through the related feeding tubes. The stoking and charging operation lasts for about ten minutes.

After stoking and charging, there is a period with no operations. As time passes the cavities increase, gas channels are formed in the charge, and the charge is heated. The reactivity of the charge decreases due to reduced contact between the gases and the reactants. Finally, the temperature of the gas leaving the furnace increases strongly, and the fraction of silica fume flow in it increases rapidly, and a new stoking is necessary. The length of this operation cycle is between half an hour and one hour. In the case of unsteady furnace conditions with the presence of large blows, separate stoking operations without any charging, can be necessary to break down the gas channels in the charge.

The separate addition of raw materials directly at the furnace surface can be used as inputs to the metallurgical control of the furnace in addition to the corrections in the ordinary charge mix. This charge supplement usually only contains quartz, and is placed directly against the electrodes by special charging trucks, in order to reestablish the local metallurgical balance.

Tapping

The tapping of the ferrosilicon product from the tapholes into tap-vessels, is also a discontinuous operation, and the content of produced metal in the furnace will fluctuate within the tapping periods. A more or less continuous tapping is favorable, because long periods without tapping can lead to too large amounts of metal in the furnace and corresponding unsteady furnace conditions. The tapping periods usually lasts between one and two hours, where the tapping accounts for about two-thirds of the time. Several tapholes are situated around the furnace pot, and the tapping operation is subsequently moved between the tapholes, corresponding to the furnace rotation. The tapholes are tightened by some kind of a plug consisting of clay, coke and metal particles, and are opened by the use of an electrical lance with an electric arc that melts the plugs, and the metal flows out and is collected in the vessels.

2.5.2 Process measurements

A submerged-arc ferrosilicon furnace has no direct measurements of the inner process conditions, and the measurements cover only the process vari-

ables that are available from the outer furnace:

- The amount of tapped metal, which indicates the production rate of ferrosilicon.
- The fraction of silica fume flow in the waste gas leaving the furnace.
- The temperature of the tapped metal.
- The temperature of the waste gas.
- The electrode holder positions.

These measurements hardly represent the inner process conditions satisfactorily, and main problems in the operation of such furnaces are due to the lack of direct measurements.

The electrical states, on the other hand, are well instrumented, but they will at best be indirect measures of the process conditions in the hearth of the furnace. The electrical measurements contain among others:

- The active line power delivered to the furnace.
- The electric power, active and reactive, dissipated per electrical phase.
- The electrode currents.
- The electrode-to-hearth voltages (the electrode voltages).
- The resistance and reactance for each electrical phase.

which are used in controlling the furnace electrical environment. The electrical measurements are also used to describe the inner process conditions indirectly by applying Fourier transformation and wave form analyses on the electrical signals. This is further described in Section 5.1.

2.5.3 Furnace control

The control tasks concerning ferrosilicon furnaces can be divided into:

1. Electrical control
2. Metallurgical control

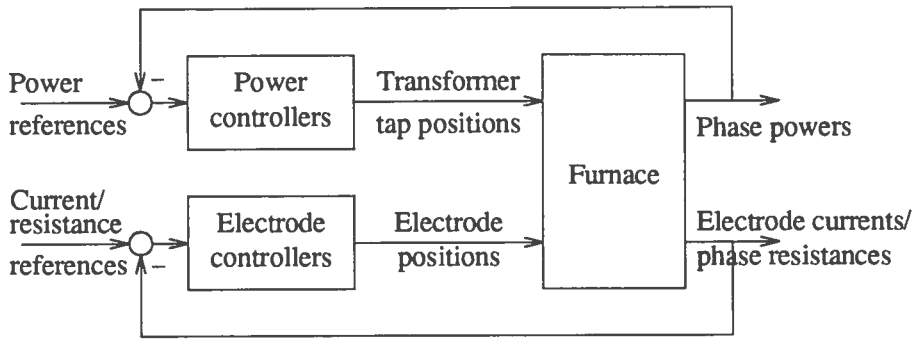

Figure 2.9: A conventional electrical control system for submerged-arc furnaces.

Electrical control

The electrical environment is a fundamental basis for the metallurgical reaction processes in a submerged-arc furnace, and a satisfactory electrical control is essential. The objects of the electrical control system are to control the electrical power dissipation in the furnace and its distribution between the three electrodes and between the different regions in the furnace. A conventional electrical control system for a submerged-arc furnace is usually hierarchic and consists of "high-level" power controllers and "low-level" electrode controllers. Depending on the choice of control variables, two different kinds of electrode controllers are used; electrode current controllers or or secondary phase resistance controllers, which are often just denoted resistance-controllers. The principle of a conventional electrical control system is illustrated in Fig. 2.9. The power controllers use the transformer tap positions as control input, while the electrode currents or phase resistances are controlled by the electrode displacements. A satisfactory electrical control of a ferrosilicon furnace is a critical factor in the work to achieve optimal furnace conditions. This is further treated in Chapter 6.

Metallurgical control

The ferrosilicon process consists of a complex environment of various chemical, thermal, electrical and mechanical sub-processes. The chemical reactions occurring in the cavities and charge depend on several factors related to both exterior conditions such as raw material properties, and interior conditions such as temperatures and material flow patterns. The major problems in controlling the furnace production are the complex interaction between these sub-processes, the still limited knowledge about the chemical

reaction patterns in the furnace, and considerable process disturbances and control input uncertainties. The task of controlling the chemical processes and reaction patterns in the furnace is usually termed metallurgical control. At present, this is mainly a manual operation and is the responsibility of the metallurgists based on process knowledge and observations. No reliable automatic control systems are available. This is particularly due to the lack of direct measurements of the process conditions in the hearth of the furnace which complicates the development of reliable metallurgical control systems.

In principle, potential approaches are feasible for use as control variable in the metallurgical control of a ferrosilicon furnace. The most important of these variables are:

- The composition of added charge. This will be denoted **carbon content**, referring to the stoichiometric relationship between carbon and quartz.
- The amount of charge added to the furnace during the stoking operation and its distribution across the furnace surface. This is denoted **feed control** and is usually determined by the operator.
- The choice of electrical working-point, usually utilized as the set-points of the electrical control system.

Other important factors are raw material properties and furnace operation procedures. This is further treated in Section 7.5 and Chapter 9.

Chapter 3

Electric arcs

The electric arc plays an important role in many different process operations. An electric arc can be regarded as an electrical conductance through a gaseous medium which has been ionized by an electric field. Electric arcs are used in a wide range of applications from arc welding to electric smelting furnaces. The electric arcs are the major source of the consumed electric energy in electric furnaces and provide the necessary high temperatures for the various metallurgical reactions.

The topics of this chapter are the nature and properties of electric arcs related to electric arc furnaces. First, arcing theory is briefly described. Next, the occurrence of arcing in electric furnaces is discussed and a survey of related investigations of arcing conditions in electric furnaces is given and major results are described. The last section of the chapter discusses the modelling aspects of electric arcs, and various static and dynamic models of electric arcs are treated.

3.1 The physics of electric arcs

This section considers the behavior and some basic properties of electric arcs. The literature on arcing theory is considerable. Good references in general arcing theory are Hoyaux (1968) and Pfender (1978), while Edels (1973) and Jones and Fang (1980) give a comprehensive survey on properties of high-power arcs.

The major part of this chapter deals with DC electric arcs. The basic features of arcing that occurs in DC arcs, are similar in AC arcs. However, the frequent change of polarity in AC arcs results in complex electrode phenomena, that obscures the effects which are significant for a basic understanding of arc behavior (Pfender, 1978). Thus, the discussion in this

chapter will mainly be concentrated on steady-state DC arcs, while the behavior of AC arcs is treated together with arcing in electric furnaces in Sect. 3.5. Furthermore, models of AC arcs are discussed for the last sections in this chapter.

3.1.1 Arc regions

An electric arc can be defined as an electrical discharge sustained by a current flowing in a gaseous medium between two electrodes (Jones and Fang, 1980). The presence of arcing is dependent on the strength of the applied electric field and various properties of the gaseous medium and the electrodes.

The transformation of electric energy to thermal energy in an electric arc is closely related to the potential drop along the arc axis. Therefore, the potential distribution along the arc provides insight into the energy dissipation and other properties of the arc. Figure 3.1 schematically shows the potential distribution of an electric arc. This distribution is nearly linear in the major part of the arc, corresponding to an almost constant field strength, while towards the electrodes the field strength increases rapidly. An electric arc can be divided into physically distinct regions with different properties based upon the potential distribution. It should be stressed that the thickness of the electrode regions is strongly exaggerated in this depiction. Referring to Fig. 3.1, an electric arc can be described by the following regions (Pfender, 1978; Jones and Fang, 1980):

- **The arc column (3)** consists of the inter-connecting plasma column between the electrode regions. This region constitutes the main part of the arc. The conditions in the arc column are almost homogeneous with axially constant temperature and field strength, which is relatively low. The influence of the electrodes on the plasma is no longer felt in the arc column.

- **The electrode regions** which contain **the cathode region (1+2)** and **the anode region (4+5)**. Each of these two electrode regions consist of:

  1. The part of the discharge which contains the electrode surface which is often denoted **the sheath**.
  2. The region of the net space charge immediately in front of the electrode surface which is denoted "the fall zone". In the two electrode regions we have **the cathode fall (1)** and **the anode fall (5)**, respectively.

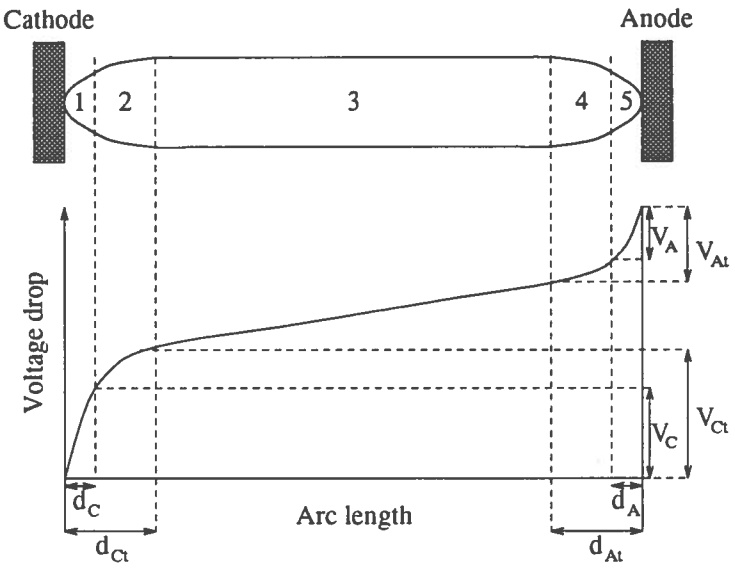

Figure 3.1: The potential distribution and different regions of an electric arc.

3. The transition or contraction zone towards the arc column. In the two regions we have **the cathode transition zone (2)** and **the anode transition zone (4)**, respectively.

The fall zones may be considered as electrical boundary layers accommodating the transition between metallic and gaseous plasma conduction. This is the "true" cathode and anode falls (V_C and V_A). The field strengths are considerable in these regions due to production and transport of space charges. The thickness of these zones (d_C and d_A) is in order of one free path length of an electron. With high-intensity arcs at atmospheric pressure this corresponds to a thickness in the range of 10^{-2} to 10^{-3} mm.

The transition zones may be interpreted as as thermal boundary layers in which there are strong axial gradients of plasma properties such as temperature, potential, particle densities, current density and radiation, in contrast to the homogeneous arc column. Towards the electrodes the arc contracts to limit the heat losses to the electrodes, which are colder than the arc column, and the temperature decreases, resulting in an increased field strength compared to the arc column. The potential drop of the transition regions ($(V_{Ct} - V_C)$ and $(V_{At} - V_A)$) is in the order of the true cathode and anode falls, but at the anode region it could even be considerably larger than the true anode fall. The thickness of the transition zones ($(d_{Ct} - d_C)$ and $(d_{At} - d_A)$) in a high-intensity arc at atmospheric pressure is in the

order of 0.1 to 10 mm, but this will be a function of pressure and the temperatures in the electrode regions.

The electrode regions of an electric arc are characterized by much higher electric field strength, temperature gradients and current densities than in the arc column. In addition, electromagnetic and fluid dynamic effects give rise to plasma jet flow phenomena. The complex interaction between electrical, magnetic, thermal and fluid dynamic, in addition to the electrode surface phenomena, have meant that the electrode regions of an electric arc are still poorly understood.

3.1.2 Electrical characteristics

Referring to Fig. 3.1, the overall voltage drop of an electric arc can be expressed as:

$$V_a = V_{Ct} + V_{At} + \int_{d_{Ct}}^{h_a - d_{At}} E_a \, dx \tag{3.1}$$

where E_a represents the field strength in the arc column, and V_{Ct} and V_{At} represent the cathode and anode voltages, respectively. Since the lengths of the cathode and anode regions d_{Ct} and d_{At} are negligible compared to the arc length h_a, the integration can be taken from $x = 0$ to $x = h_a$ without significant error. Assuming a constant electric field strength E_a along the arc length, the arc voltage becomes:

$$V_a = V_{Ct} + V_{At} + E_a h_a \tag{3.2}$$

According to Pfender (1978), the contribution of the last term dominates for long arcs, whereas for short arcs the current-voltage characteristics essentially reflect the current dependence of the cathode and anode voltages.

Electrical characteristics

One of the most common and also useful, representations of the overall arc behavior, is the current-voltage characteristic, or slightly modified the current-field strength characteristic, describing only the arc column. The current-voltage characteristic for a general free-burning electric arc is illustrated in Fig. 3.2. At low currents the arc current-voltage characteristic has a falling trend, as the current increases the trend becomes more horizontal, and at high currents the characteristic has a flat or even rising trend (Pfender, 1978). The falling trend of low-current arcs is a result of increasing arc conductance with increasing current, caused by an increase in electrical conductivity with temperature or an increase in arc diameter, provided the arc can freely expand. The flat or rising trend of high-intensity

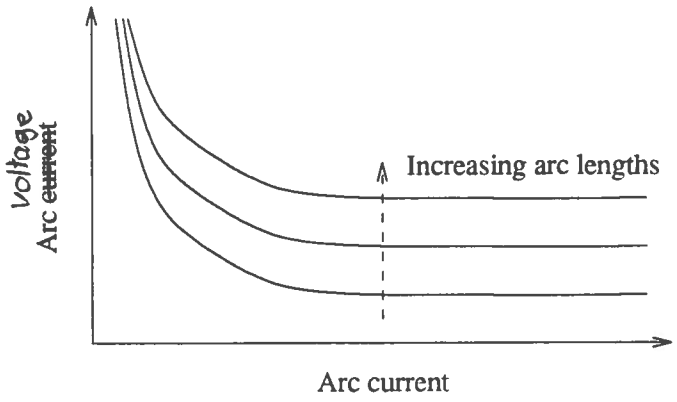

Figure 3.2: The current-voltage characteristic of a static arc.

high-current arcs can be explained by an overbalance by disproportionally high energy losses from the arc, which the arc responds to with an increase of the field strength. This is further discussed in Section 3.2.1. There is however no general prediction about the trend of the arc characteristics, because external conditions like magnetic and gas dynamic fields, may reverse the trend (Pfender, 1978). The dependence of arc voltage to variations in arc lengths h_a is schematically illustrated in Fig. 3.2.

Electrical stability

An arc with a falling or even flat characteristics requires specific precautions in the electric circuit. The falling characteristic of the arc means that the arc is an "unstable" electrical load, since the arc current increases with decreasing arc voltage. However, the arc circuit can be stabilized by inserting a proper resistive load in the circuit. This can be illustrated as in Fig. 3.3. The interception between the load line and the arc characteristics A and B, are the possible working-points of the circuit, but only A is a stable one. According to Pfender (1978), the following criterion states the stable working point:

$$\frac{dV_a}{dI_a} + R > 0 \Rightarrow R > \left|\frac{dV_a}{dI_a}\right| \tag{3.3}$$

A complete stabilization analysis involves consideration of inductances and capacitances in the circuit, and the following stabilization criterion can be derived (Pfender, 1978):

$$\frac{dV_a}{dI_a} + R > 0 \Rightarrow R > \left|\frac{dV_a}{dI_a}\right|$$

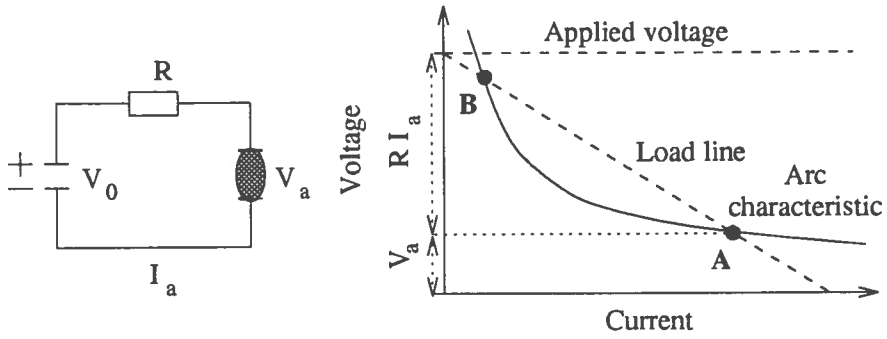

Figure 3.3: Electrical stability of an arc with falling characteristic.

$$\frac{1}{L}\frac{dV_a}{dI_a} + \frac{1}{RC} > 0 \;\Rightarrow\; R < \frac{L}{C\,|dV_a/dI_a|} \tag{3.4}$$

where L denotes serial inductances and C denotes conductance in parallel with the arc. These conditions give upper and lower limits for the arc circuit resistor, but the upper limit is not essential for high-current arcs (Pfender, 1978).

Hoyaux (1968) recommends that in situations with a flat or slightly rising characteristic, the same precautions as with a falling trend, should be taken, because the arc current will then be extremely sensitive to variations in voltage.

Empirical arc models

A large number of proposed static models are found in the literature which attempt to use experimental results to establish relations between the arc voltage V_a and the arc current I_a. This subject is treated among others by Browne (1955) and Billings (1975). The proposed models are in the general form:

$$V_a = f(I_a) \tag{3.5}$$

The first and according to Browne (1955), the best one, is the well-known relation developed by Ayrton in 1902:

$$V_a = a + b\,h_a + \frac{c + d\,h_a}{I_a} \tag{3.6}$$

where h_a is the arc length, and a, b, c and d are constants that must be determined experimentally. Later studies by Nottingham in the 1920s yielded a slightly modified expression, known as "**The Nottingham equation**":

$$V_a = a + b\,h_a + \frac{c + d\,h_a}{I_a^n} \tag{3.7}$$

where n is a parameter that is dependent on the properties of the anode material. The model corresponds to the low-current part of the general arc characteristic illustrated in Fig. 3.2, and the models in Eqs. 3.6 and 3.7 can only be applied to arcs with falling characteristics.

For high-current arcs the last terms in Eq. 3.7 are negligible, and the model becomes (Browne, 1955):

$$V_a = a + b\, h_a \tag{3.8}$$

Comparing Eq. 3.8 with Eq 3.2 we can see that parameter a corresponds to the sum of the cathode and anode voltages V_{Ct} and V_{At}, while b corresponds to the electrical field strength E_a:

$$a = V_{Ct} + V_{At}$$
$$b = E_a$$

This model is originally stated for static DC arcs, but Eq. 3.8 can also represent AC arcs, relating the rms voltage to the arc length and neglecting the non-linear behavior in the AC periods (Browne, 1955; Billing, 1975).

According to Pfender (1978), the value of such empirical model relations may be limited because it is difficult to attach physical significance to the various constants. However, these simple empirical relations may be useful when analyzing electrical circuits in the presence of arcing.

3.1.3 Classification of electric arcs

The nature and behavior of electric arcs will depend on the size of arc current and power dissipation in the arc, and external conditions in the arcing surroundings such as pressure, temperature, magnetic fields, and boundary conditions given by the geometry surrounding the arc column. Thus, a classification of electric arcs based on some of these circumstances is preferable. Jones and Fang (1980), Pfender (1978) and Edels (1973) give a good description of arc classification and their related properties.

Electric arc discharges are usually divided into (Chang and Szekely, 1982):

1. **High-pressure arcs**

2. **Low-pressure arcs**

Arcs burning at high-pressure are assumed to attain approximately thermodynamic equilibrium. The concept of thermodynamic equilibrium is

discussed below. High-pressure arcs are in this respect, arcs at pressures at or above the atmospheric pressure.

Electric arcs have different behavior and properties depending upon the size of the arc current and a classification based upon this is useful:

1. **Low-current arcs.** Arcs with currents up to 1 kA is usually denoted low-current arcs. A typical example of low-current arcs is arc welding.

2. **High-current arcs.** If the currents are between 1 kA to 10 kA, the arcs are denoted high-current arcs.

3. **Ultra high-current arcs.** Arc with currents above 10 kA are denoted ultra high-current arcs.

The two types of arcing that occur in electric furnaces are high-current and ultra high-current arcs. The published information on the properties of ultra high-current arcs is rather limited, but more frequent investigations of high-current arc are clearly relevant. According to Edels (1973), the properties of high and ultra high-current discharges differ only in the degree of complexity of the similar phenomena, and ultra high-current arcing can be understood by an extension of the concept for high-current arc conditions.

A similar classification based on the power dissipation in the arc can also be done, and correspondingly to the current classification, we get:

1. **Low-power arcs**

2. **High-power arcs**

3. **Ultra high-power arcs**

High-power arcing implies dissipation of sufficient power within the discharge to promote intensive and complex interaction between the arc and its surrounding, involving phenomena like intensive radiative energy transfer, gross electrode melting and strong self-magnetic field effects.

A classification depending upon the arc's boundary conditions can also be applied. This classification is related to the "stabilization" of an arc, referring to the mechanism which keeps the arc column in a given, stable position. Arcs can for instance be classified into the following (Pfender, 1978):

1. **Free-burning arcs.** If no external stabilizing mechanism is imposed we will have free-burning arcs. However, the arc has its own stabilizing mechanism due to free convection effects. The free convection

effects can easily be eliminated by additional flow fields, and free-burning arcs are usually dominated by convection effects induced by the arc itself and stabilized by these effects. Such arcs may therefore be denoted **self-stabilized arcs**. The convection effect is a result of gas and plasma flows induced by the interaction of the arc current with its own electromagnetic field in the transition zone at the cathode region where the arc is highly contracted (Hsu, Etemadi and Pfender, 1983).

This induced flow is usually denoted **the cathode jet** and is treated in Section 3.3.2 and App. A.1. The cathode region of a free-burning arc acts like an electromagnetic pump drawing gas from the surroundings and ejecting it towards the anode in form of a jet. As the cathode jet impinges on the anode, a stagnation layer is formed in the front of the anode, resulting in the well-known bell shape of free-burning high-intensity arcs (Hsu, Etemadi and Pfender, 1983), as shown in Fig. 3.4.

Self-stabilized arcs are frequently denoted free-burning arcs in spite of the self-stabilizing effect, referring to the free-burning operation mode. Free-burning arcs is used hereafter.

2. **Wall-stabilized arcs.** If the arc is confined within a constant cross-section tube it is called wall-stabilized. Such arcs provide an ideal form of a plasma column for fundamental property investigations on account for its axial uniformity, cylindrical symmetry and exclusion of the electrode influences (Jones and Fang, 1980).

3. **Arcs in axial gas flow.** If a coaxial gas flow is imposed to an arc in a free-burning arc mode we may get an axial convection-stabilized arc. The convective effect of the imposed flow field will compete with the self-magnetically induced convection to govern the behavior of the arc column. The properties of arcs in axial gas flow will depend heavily upon the imposed flow field.

Electric arcs can further be divided into axisymmetric arcs and arcs in transverse flow and magnetic fields. In the following discussion only axisymmetric arcs are treated.

The stability of arcs is closely related to intensity of the arc column, and electric arcs can be classified based on the observed intensity:

1. **Low-intensity arcs.** A low-intensity arc column is subject to irregular motions induced by free-convection effects. Low intensity arcs occur at atmospheric pressure with arc currents below 50 A.

In AC electric furnace operations with ultra-high current arcing, behavior similar to low-intensity arcs can be observed in the halfcycles when the electrode is anode.

2. **High-intensity arcs.** A high-intensity arc has a motionless and stiff arc column with a visually well defined boundary. A free-burning high-intensity arc is self-stabilized by the cathode jet.

The topic in this chapter is arcing in electric furnaces. As discussed earlier, arcs can be divided into several classes, but in the further discussion we will concentrate on the arcs occurring in electric furnaces, which are high-pressure, (ultra) high-current, high-power, self-stabilized arcs operated in the free-burning arc mode.

3.2 The arc column

The arc column can be considered as the body of an arc, while the cathode and anode regions may be considered as thin boundary layers between the electrodes and the arc column. In contrast to the regions immediately in front of the electrodes, the arc column represents a true plasma in which quasi-neutrality prevails.

The pressure in the arc column is uniform and equal to the pressure in the surrounding fluid, with the exception of ultra-high current arcs. In such arcs the interaction of the arc current with the self-magnetic field produce a pressure gradient in the radial direction, which is called "**the pinch effect**", so that the pressure becomes elevated in the axis of the column (Pfender, 1978).

The surrounding gas is heated by energy loss from the plasma column by re-absorption of radiation and convection, forming a non-luminous thermal layer, that surrounds the arc column along the length of the arc. The temperature in the thermal layer is reduced from the luminous arc core boundary to the environment. The layer temperature is insufficient to sustain significant ionization, so its electrical conductivity is negligible compared with that of the arc plasma column. The layer plays an important role in the energy transfer from the plasma column, especially for high and ultra high-current arcs, the thermal layers may be extensive and support considerable mass and enthalpy flows, and considerable energy transfer between conductive to convective loss mechanisms occurs in these layers. The thermal layer has about twice the diameter of the plasma column (Jones and

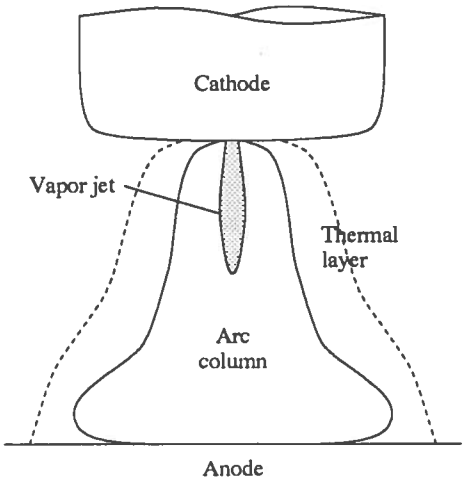

Figure 3.4: A free-burning arc column with its surrounding thermal layer in the presence of a vapor jet.

Fang, 1980).

The arc plasma may in turn be influenced by the cathode through the evaporation and subsequent transport of vaporized electrode materials, known as vapor jets. Figure 3.4 schematically shows a free-burning arc with its surrounding thermal layer and the presence of a vapor jet.

3.2.1 Arc plasma properties

The electric arc is a kind of a plasma phenomena. A plasma, originally defined as "**a luminous conducting gas**", can more formally be defined as an electrical quasi-neutral gas of charge particles and neutrals that show collective behavior. The term electrical quasi-neutral implies that no electrical fields are created by space charges in the plasma, and that the overall plasma is electrically neutral. The collective behavior of the plasma constituents is a result of particle collisions and electromagnetic forces. An external electric field is applied to an electric arc plasma, and the plasma will conduct current and the arc will be a part of an electric circuit. The main part of the electric energy is dissipated by Joule heating.

The thermodynamic state of the arc plasma

The thermodynamic state of an arc plasma is treated among others by Pfender (1978). Thermodynamic equilibrium (TE) prevails in a uniform, homogeneous plasma if kinetic and chemical equilibriums as well as con-

ceivable plasma properties, are unambiguous functions of the temperature. The temperature in turn, has to be the same for all plasma constituents and their possible reactions. An actual plasma will deviate from the ideal conditions of TE, and local thermodynamic equilibrium must be considered.

Local thermal equilibrium (LTE) exists in a steady-state, optically thin plasma when the following conditions are simultaneously fulfilled (Pfender, 1978):

1. The different species which form the plasma have a Maxwellian distribution.

2. Electric field effects are small enough, and the pressure and the temperature are sufficiently high, so that the electron temperature T_e and the temperature of the heavy species (ions and neutral gas) T_i are the same.

$$T_e = T_i \tag{3.9}$$

3. Collision are the dominating mechanism for excitation and ionization.

4. Spatial variations of the plasma properties are sufficiently small.

LTE implies that equilibrium considerations can be applied locally and may be considered as a special case of the more general concept of complete TE.

Thermal arcs can be defined as a discharge mode in which the thermodynamic state of the arc column approaches LTE.

According to Jones and Fang (1980), the plasma in a high-power high-pressure arc column has a sufficiently high electron density ensuring that the plasma is dominated by collisions, and the particle species attain a common temperature. Furthermore, according to Pfender (1978), LTE is favored by high pressure and temperature levels which bring the electron density close to its maximum in the arc. This is directly associated with the energy balance of the arc column. In general, high temperatures in the arc column will prevail if the energy dissipation per unit length in the arc column is sufficiently high, or if the energy losses are kept small. The minimum value of this energy dissipation required for LTE conditions is about 100 kW/m, and arcs satisfying this can be classified as high-intensity arcs. Thus, LTE is a valid assumption for high-pressure arcs, and the plasma in such arcs can be classified as thermal. The plasma column in high-pressure arcs can therefore be treated as a single fluid and

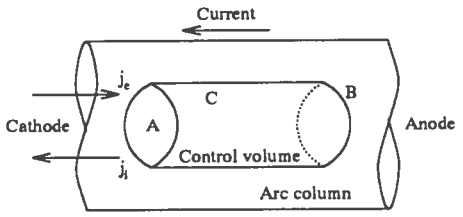

Figure 3.5: Control volume within arc column

its thermodynamics and transport properties can be uniquely described by temperature and pressure.

Investigations of a 10 kA free-burning DC arc in air established LTE for each plasma species and yielded plasma temperatures in the range 20000-30000 K. However, the present of any vapor cathode jet may complicate the column structure, since a vapor jet containing electrode materials, will usually have a temperature that is somewhat lower than the host plasma. The electrical conductivity of the vapor jet can be similar to that of the plasma column if the vapor temperature is significantly high ($\sim$ 15000 K), resulting in a radially uniform current distribution and negligible radial variations of the electric field strength in spite of the presence of a vapor jet (Jones and Fang, 1980).

At a given current the conditions in the column, such as temperature distribution and distribution of thermodynamics and transport properties, adjust themselves in such a way that the field strength required for driving the current becomes a minimum (Pfender, 1978). The relative small field strength prevailing in the arc column may also be interpreted as a consequence of the favorable energy balance, which, in turn, is to a large degree determined by the charge carrier balance.

Charge carrier balance

The current in an arc column is carried by electrons and positive ions. Under the influence of the applied electric field, the electrons are traveling towards the anode and the positive ions in the opposite direction. The ion contribution to the total current in the arc column is negligible due to the smaller mobility of ions compared to electrons.

The charge carrier balance of an arc column can be analyzed by considering a small control volume in a rotationally symmetric, fully developed arc column, as shown in Fig. 3.5 (Pfender, 1978). The applied electric field imposes a drift velocity on electrons j_e and ions j_i in the column, which

gives rise to a certain current flow. At steady-state the same number of electrons entering surface A per unit time must again leave surface B. The same argument holds for ions traveling in the opposite direction. There will however, be a continuous loss of charge carriers by ambipolar diffusion across the surface C, accompanied by a re-combination outside the control volume. Neutral particles diffuse in the opposite direction maintaining the mass balance within the control volume, and they must be ionized at the same rate as charge carriers are lost to maintain steady-state conditions. Enhanced cooling of the arc column fringes by for instance convection, not only increases the temperature gradient, but also the charged particle density gradient. This results in a corresponding increase in the diffusion losses of charged particles. These losses must be compensated by a correspondingly higher rate of ionization in the control volume, which can be achieved by a higher field strength.

In summary, the arc responds to increased cooling of its fringes by an increase of the field strength E_a and therefore, of the energy dissipation $E_a I_a$, per unit length of the arc column. This increased energy dissipation leads to higher temperatures in the core of the arc column. Thus, the net effect of cooling the arc fringes is an increase in the core temperature, provided that the arc current I_a is kept constant. The actual field strength is however, determined by the entire energy balance including heat conduction and convection and radiation (Pfender, 1978).

Plasma conductivity

The electric charge carriers in an arc plasma are mainly electrons and positive ions as the result of ionizations at different stages of plasma atoms. Other sources for ion charge carrier production may be the dissociation of plasma gas molecules and the ionization of impurities in the plasma atmosphere.

The dominating process responsible for ionization is due to electron impact. Charge carrier production must be accomplished by thermal ionization rather than field emission. The field strength in the arc column in a high-pressure arc is insufficient for an electron to accumulate enough kinetic energy over a mean free path to make an ionization collision. The charge carrier production in this situation must therefore be accomplished by thermal emission rather than field emission. However, electrons in the tail of the Maxwellian velocity distribution possess sufficient energy to make ionization collisions (Pfender, 1978).

The particle densities of neutrals, electrons and ions can be described by

the Saha equation, which may be considered as a mass action law (Hoyaux, 1968; Pfender, 1978):

$$\frac{N_{r+1} \cdot N_e}{N_r} = \left(\frac{2\, Z_{r+1}}{Z_r}\right) \frac{(2\,\pi\, m_e\, k_B)^{\frac{3}{2}}}{h^3}\, T_a^{\frac{3}{2}}\, \mathrm{e}^{e\, V_{r+1}/k_B\, T_a} \tag{3.10}$$

where N_{r+1} and N_r represent the particle densities of ions at the $(r+1)$ and (r) stages, N_e the electron density, Z_{r+1} and Z_r the partition functions of the ions at the $(r+1)$ and (r) stages, e the electron elementary charge, and V_{r+1} the potential required to produce an $(r+1)$ times ionized atom from an (r) ionized atom (the ionization potential). T_a is the plasma temperature, m_e electron mass, k_B the Boltzmann constant, and h the Planck constant. It should be stressed that a plasma is considered a "fully" ionized gas when the degree of ionization is about 0.01.

Assuming a monatomic plasma gas and disregarding higher ionized states, the Saha equation becomes (Hoyaux, 1968):

$$\frac{N_i \cdot N_e}{N_n} = \left(\frac{2\, Z_i}{Z_n}\right) \frac{(2\,\pi\, m_e\, k_B)^{\frac{3}{2}}}{h^3}\, T_a^{\frac{3}{2}}\, \mathrm{e}^{e\, V_i/k_B\, T_a} \tag{3.11}$$

where subscripts i, e, and n represent ions, electrons and neutral atoms, and V_i denotes the ionization potential. According to Hoyaux (1968), the electron and ion densities are statistically equal to each other and the proportion between the partition functions is approximately one, and it can be derived that the electron density is proportional to:

$$N_e \sim \sqrt{N_n}\, T_a^{\frac{3}{4}}\, \mathrm{e}^{e\, V_i/2\, k_B\, T_a} \tag{3.12}$$

From this expression Hoyaux (1968) deduces an expression of the electron current density j_e:

$$j_e = N_e\, e\, E_a \cdot \left(c_1\, \frac{\sqrt{T_a}}{N_n}\right) \tag{3.13}$$

where E_a is the electric field strength, and the last term represents the electron velocity, where c_1 is a constant. Eliminating N_n by introducing the pressure p_a

$$p_a \approx N_n\, k_B\, T_a \tag{3.14}$$

and assuming that the ion current is negligible, the following expression for the plasma conductivity σ_a can be derived:

$$\sigma_a \sim \frac{1}{\sqrt{p}}\, T_a^{\frac{3}{4}}\, \mathrm{e}^{e\, V_i/2\, k_B\, T_a} \tag{3.15}$$

The electrical conductivity of the arc plasma can therefore be given in the general form:

$$\sigma_a(T_a) = c_1 \, T_a^{c_2} \, \mathrm{e}^{-c_3/T} \tag{3.16}$$

In the case where the plasma contains impurities due to vaporization of the electrode materials for instance, expressions describing the plasma conductivity in the presence of impurities, can be derived similarly to Eq. 3.15. The presence plasma of plasma impurities may have a significant effect on the total conductivity as the vaporization potential of the electrode materials may be considerable smaller than the ionization potential of the plasma constituents.

The Saha equation states that ionization increases with rising plasma temperature. At given plasma conditions a specific temperature will correspond to a given current. If the current increases the temperature and the arc cross section will rise and more electrons and ions are produced, and this explains the falling current-voltage characteristic of the arc.

3.2.2 Energy balance and heat transfer

The heat transfer and energy balance of an electric arc column is treated among others by Hoyaux (1968), Lowke (1970), Edels (1973), Pfender (1978) and Jones and Fang (1980). The main heat transfer mechanism within a free-burning arc column, and between the arc column and the surroundings are:

1. **Thermal conduction.** The extent of thermal conduction or diffusion in an arc column depends strongly on the temperature distribution across the arc section. The conductive heat loss effects in a free-burning arc column are negligible when considering the overall energy balance. However, radial thermal conduction may be significant when considering local energy balances. A flat radial temperature distribution indicates that the thermal conduction losses may be significant in relatively restricted zones close to the conducting boundary of the arc column (Edels, 1973).

2. **Radiation.** Considerable radiation losses are apparent in the central region of the arc column, but a gain will be achieved in the outer regions and the thermal layer by absorption of radiative energy. The radiation from a plasma can be divided into (Hoyaux, 1968):

(a) **Optically thin radiation.** An arc plasma is termed optically thin for a certain radiation wavelength if the mean free path of a relevant photon in the arc plasma is much larger than a characteristic length, such as the arc column diameter. Therefore, an emitted photon anywhere by the arc plasma, will most probably be able to leave the arc column without being intercepted.

According to Hoyaux (1968), optically thin radiation in an arc column generally consists of:

i. Radiation from characteristic wavelengths emitted by low-density impurities or gases (bound-bound radiation).

ii. Radiation from re-combinations of ions with electrons (free-bound radiation).

iii. Bremsstrahlung, which is a radiation effect as a result of the interaction between free electrons and other charged particles (free-free transition).

Bound-bound radiation is a line radiation effect, while the others are continuous radiation effects. Continuous radiation is usually dominant in arc plasma, but line radiation may be significant depending on the extent of impurities and plasma properties. The properties of optically thin radiation are further treated by Hoyaux (1968) and Pfender (1978).

Optically thin radiation may be regarded as a volume effect of the local plasma temperature and of its pressure and chemical composition.

(b) **Optically thick radiation.** An arc plasma is termed optically thick for another radiation wavelength if the opposite prevails and the mean free path of the relevant photon is much shorter than the same characteristic length. Now, the emitted photon will most probably be intercepted and stored temporally in an atom or molecule in some form of potential energy. This radiation mode is a surface effect that is somewhat similar to black-body radiation.

The optically thick radiation mode in an arc plasma can be looked upon as a power density which is eventually carried to the plasma boundary by a diffusion phenomenon ("radiation trapping"), which involves radiation and subsequent re-conversion into heat and re-radiation from heat. Thus, according to Hoyaux (1968), optically thick radiation can be accounted for as an increment in conductive losses in the energy balance.

The radiation flux in a wall-stabilized arc column can formally be calculated theoretically for some well-known gas atmospheres (Jones and Fang, 1980). However, a corresponding calculation of the radiation from high and ultra high-current free-burning arcs is impractical because of the complex nature of the radiation present in such arcs. The arc plasma is optically thin to some ranges of radiation and optically thick to others, depending on the radiation waveforms. The absorbed power is thus sensitive to the total geometry and structure of the plasma, and a calculation of total emitted radiative flux is difficult. This is further complicated by the presence of vapor jets containing electrode materials. Investigations of radiative spectra show that LTE prevails in a 10 kA free-burning arc with plasma temperatures of 20 000-30 000 K, but the presence of a vapor jet with high concentrations of electrode materials at somewhat lower temperatures ($\sim$ 15 000 K), leads to increased radiative losses, consisting of continuum radiation and especially line radiation from vaporized electrode materials (Jones and Fang, 1980). According to Edels (1973), radiation accounts for approximately 20-30% of the total energy input in high-current free-burning arcs, and the extent of radiation varies axially across the arc column, from 10% near the cathode to 35% in the expanded column.

The radiative losses P_R can approximately be described by (Jones and Fang, 1980):

$$P_R = 4\pi\, \epsilon\,(T_a, r_a) \tag{3.17}$$

where ϵ is the net emission coefficient as a function of local temperature T_a and radius r_a. The emission coefficient can be expressed in terms of spectral intensities and absorption coefficients which can be found experimentally (Lowke, 1970).

An alternative description of the heat flow due to radiation is given by Ahlers (1988) and Pfeifer, Fett and Bebber (1989). The emitted radiation is expressed in terms of the radiative absorption length l_R, representing the mean free path of a relevant plasma photon. The emitted radiation power density depends exponentially on the arc column radius and the absorption length:

$$P_R = \dot{q}_R\, 2\pi h_a\, l_R \left[\frac{r_a}{l_R} - 1 + \mathrm{e}^{-r_a/l_r}\right] \tag{3.18}$$

where the homogeneous radiative power density $\dot{q}_R(T_a, p_a)$ depends on the arc temperature, pressure and plasma composition. This is further discussed by Jones and Fang (1980).

The radiation will generally consist of both optically thin and optically thick radiation:

$$P_R = P_{R1} + P_{R2} \tag{3.19}$$

In the case of optically thin radiation the absorption length is significantly larger than the arc column radius: $r_a \ll l_R$, and the radiative heat flow in Eq. 3.18 can be simplified to:

$$P_{R1} = \left(\pi {r_a}^2 h_a\right) \dot{q}_R \tag{3.20}$$

and can be considered as radiation from the plasma volume with homogeneous radiation power density.

In the case of optically thick radiation, the arc radius dominates the absorption length: $r_a \gg l_R$, and Eq. 3.18 becomes:

$$P_{R2} = (2\pi r_a h_a)\, l_A\, \dot{q}_R \tag{3.21}$$

and optically thick radiation can be looked upon as radiation from the arc column surface with thickness of the absorption length with homogeneous radiation power density. The case of optically thick radiation is further discussed when regarding the energy balance.

3. **Convection** The dominant convective losses in a free-burning arc column are the axially directed gas streams and vapor jets. These losses may be envisaged as mainly occurring in the outer regions and transporting away the energy gained in these regions from both conduction and radiation, energy originally gained by Joule heating in the central core of the arc column.

According to Edels (1973), the local radial heat transfer distribution can in principle be described as shown in Fig. 3.6, which illustrates the energy balance integrated over an arc cross section. Radial thermal conduction and re-absorbed radiation do not constitute a net loss mechanism, but merely serve to redistribute the power, mainly radially (Jones and Fang, 1980). At high-current arcs the radial re-distribution of energy is dominated by radiation at the arc axis and turbulent exchange processes (as opposed to conventional thermal conduction) at the electrical boundary of the arc column.

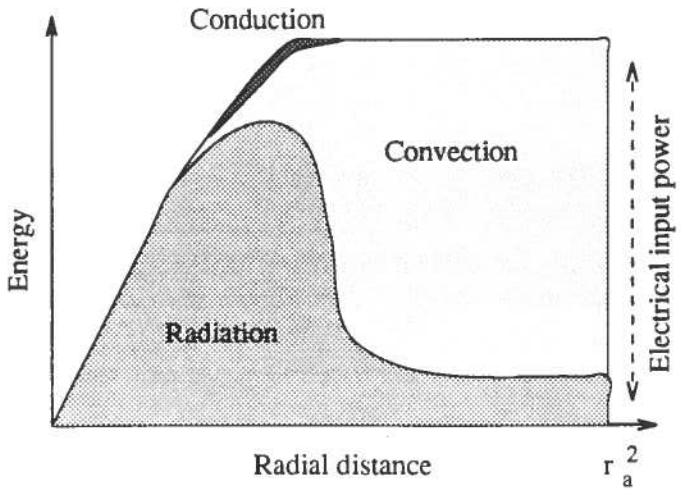

Figure 3.6: Principal energy balance integrated over the cross section of a free-burning arc column.

Energy balance

According to Edels (1973), a plasma energy balance for ultra high-current arcs should account for Joule heating input and energy transport particularly by convection and radiation. In addition, the possible effects of local plasma vaporization and plasma-electrode phenomena should be considered. The free-burning arc analysis is complicated by strong axial gradients, an unresolved two stream velocity effect close to the electrode, the variable gas-metal vapor compositions and the influence of generated pressure gradients on material and radiative transport coefficients. Furthermore, the plasma and electrode energy balances are difficult to decouple due to the strong interaction, and in a dynamic arc mode the gross melting time constants are present.

Major energy transport occurs near the cathode where the field strength is high enough to give the energy required to heat up both the incoming gas and the vapor jet to plasma temperatures. The gas gains further energy in flowing towards the anode. At the anode much of this energy is transferred to the anode surface, while the remaining energy is transported completely out of the arc volume and into the environment (Edels, 1973).

According to Pfender (1978), the following simplified steady-state energy balance can be applied to a rotationally symmetric arc column (r, z, θ), if

the convective flow effects are neglected:

$$\frac{1}{r}\frac{\partial d}{\partial r}\left(r\,\lambda_a\,\frac{\partial T}{\partial r}\right)+\sigma_a\,E_z^2-P_R=0 \tag{3.22}$$

where the first term describes thermal conduction, the next the Joule heat input and the last radiation, and r denotes the arc radial distance, λ_a the thermal conductivity, σ_a the electrical conductivity, E_z the axial electric field strength, and P_R the optically thin radiative heat losses per unit time and unit volume. Equation 3.22 is known as the Elenbaas-Heller equation.

Optically thick radiation may be considered as a conductive heat transfer effect (Hoyaux, 1968), and the energy balance for both optically thin and thick radiation, becomes:

$$\frac{1}{r}\frac{\partial d}{\partial r}\left(r\,(\lambda_a+\lambda_R)\,\frac{\partial T}{\partial r}\right)+\sigma_a\,E_z^2-P_{R1}=0 \tag{3.23}$$

where P_{R1} denotes losses per unit time and unit volume due to optically thin radiation, and λ_R denotes the thermal conductivity corresponding to optically thick radiation.

In the case of a free-burning arc column with a steady, incompressible, axially symmetric flow field without swirl effect components, and with optically thin radiation, the energy balance becomes (Pfender, 1978):

$$\rho_a\left(v_z\frac{\partial H_a}{\partial z}+v_r\frac{\partial H_a}{\partial r}\right)=\frac{1}{r}\frac{\partial d}{\partial r}\left(r\,\lambda_a\,\frac{\partial T_a}{\partial r}\right)+\sigma_a\,E_z^2-P_R \tag{3.24}$$

where the terms on the left-hand side describe axially and radially convection, ρ_a is the mass density, v_z the axial flow velocity component, v_r the radial velocity component, and H_a the enthalpy. Furthermore, optically thin radiation is assumed, and viscous dissipation and self-magnetic flow effects are neglected. The current conservation can be described by:

$$I_a=2\pi\,E_z\int_0^{r_a}\sigma_z r\,dr \tag{3.25}$$

According to Jones and Fang (1980), radial flow and heat conduction effects can be neglected in an overall energy balance, and the following simplified overall energy conservation equation may be considered for the arc column:

$$E_a I_a=\frac{\partial}{\partial z}\left(\int_0^{r_a}\rho_a\,v_z\,H_a\,2\pi r\,dr+P_R\right) \tag{3.26}$$

Following its radial re-distribution, the energy is removed by axial convection, which accounts for 50-70 % of the local energy input midway along

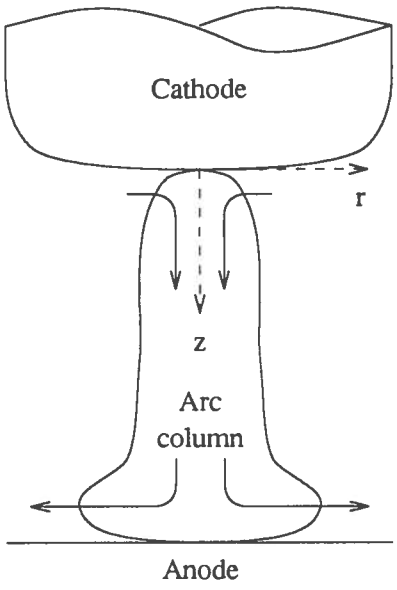

Figure 3.7: Free-burning DC arc.

a free-burning arc. The effects of self-magnetically induced convection, electrode vapor jets and turbulent convection are inherent in the energy conservation equation through their influence of the density ρ_a, the axial velocity v_z and enthalpy H_a. The energy balance of an arc column is further treated when considering analytic models of DC arcs in Section 3.6.

3.2.3 Arc column characteristics

A free-burning arc is schematically illustrated in Fig. 3.7. The arc column characteristics, such as flow fields, the arc geometry and the spatial distributions of current density and temperature, are described among others by Edels (1973) and Pfender (1978), Szekely and McKelliget (1981) and McKelliget and Szekely (1983).

Flow field

In the cathode region, gas enters from the arc surroundings, induced by the electromagnetic pumping force. The induced flow enters the arc core from its fringes and flows towards the anode. As it approaches the anode, it is forced to turn around and flow outward in radial direction. This flow phenomena is similar to gas jet flow and can be described by jet theory.

Transient flow is a common assumption in jet theory (Szekely and Themelis, 1971). This leads to an exponential radial distribution of the jet's axial flow

component:

$$v_z(r,z) = v_{max}(z) \cdot e^{-k\,r} \;,\quad 0 < r < r_a \tag{3.27}$$

where k is a constant. The arc axial velocity has its maximum v_{max} at the arc axis at the vicinity of the cathode:

$$v_{max} = v_z(r = 0, z \approx 0) \tag{3.28}$$

and $v_{max}(z)$ denotes the axial velocity at the arc axis:

$$v_{max}(z) = v_z(r = 0, z) \tag{3.29}$$

The axial velocity distribution in the jet can be described by:

$$v_z(r = 0, z) = c\, v_{max}\, \frac{r_C}{z} \tag{3.30}$$

where c is a constant, and r_C is the radius of the jet root, which in arcing corresponds to the cathode spot radius.

However, according to Sanders et al. (1982), laminar flow is also a common assumption in arc modelling. Assuming circular laminar flow, the axial velocity component will have the following radially distribution near the cathode:

$$v_z(r, z = 0) = v_{max} \cdot \left(1 - \left(\frac{r}{r_a}\right)^2\right) \;,\quad 0 < r < r_a \tag{3.31}$$

where r_a is the arc radius. According to Szekely and Themelis (1971), the averaged laminar flow can be derived as :

$$\bar{v}_z = \frac{v_{vol}}{\pi {r_a}^2} = \frac{1}{\pi {r_a}^2} \int_0^{r_a} v_z(r)\, 2\pi r\, dr = \frac{1}{2}\, v_{max} \tag{3.32}$$

An alternative radial flow distribution to Eq. 3.31 is given by Szekely and McKelliget (1981):

$$v_z(r, z = 0) = v_{max} \cdot \left(1 - \left(\frac{r}{r_a}\right)^{\frac{3}{2}}\right)^2 \;,\quad 0 < r < r_a \tag{3.33}$$

In the cathode region the axial velocity decreases rapidly towards the arc column, while it is almost constant along the axis within the arc column. The cathode flow phenomena and expressions for the maximal flow v_{max}, are further discussed in Section 3.3.2.

The radial velocity component is negligible in the arc column (McKelliget and Szekely, 1983). In front of the anode, the axial velocity drops sharply and results in a stagnation layer.

Arc geometry

The arc is strongly contracted towards the cathode in the cathode region. The arc column spreads slightly towards the anode, and the radius in the arc column can be described by (McKelliget and Szekely, 1983):

$$r_a = r_C \sqrt{1 + \frac{z}{r_C}} \tag{3.34}$$

where r_C is the cathode spot radius. The bell-form is formed near the anode as a result of the stagnation flow field.

Current density distribution

The current density is very high in the cathode region near the cathode tip, but decreases rapidly towards the arc column. The axial current density can be described by a parabolic radial distribution (McKelliget and Szekely, 1983):

$$j_z(r, z = 0) = j_C \cdot \left(1 - \left(\frac{r}{r_a}\right)^2\right) \ , \ 0 < r < r_a \tag{3.35}$$

where j_C is the current density at the cathode spot. Hsu, Etemadi and Pfender (1983) assumed an exponential distribution of the axially current density in a plane around the cathode surface:

$$j_z(r, z = 0) = j_C \cdot \mathrm{e}^{-b\,r} \ , \ 0 < r < r_a \tag{3.36}$$

where b is a constant. The cathode current density is usually assumed to be homogeneous:

$$j_C = \frac{I_a}{2\pi r_C} \tag{3.37}$$

and the constant b in Eq. 3.36 can be determined from:

$$I_a = 2\pi \int_0^{r_C} j_z(r)\, r\, dr \tag{3.38}$$

The electrical conductivity is almost constant along the centerline of the arc column and the current density can be assumed to be constant. Assuming that the radial component of the current is negligible in the arc column, the arc current I_a can be written:

$$I_a = 2\pi E_z \int_0^{r_a} \sigma_a\, r\, dr \tag{3.39}$$

where E_z is the axial field strength. Towards the anode the current density does not show the characteristic bell shape of the arc and that can be drawn by isotherms from temperature measurements.

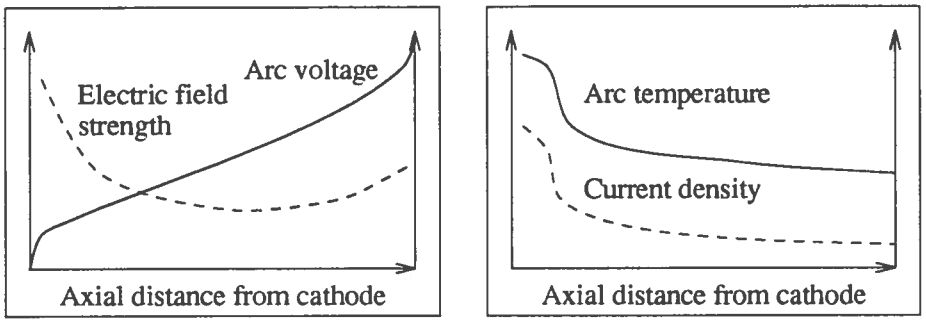

Figure 3.8: Axial distribution of arc characteristics.

Temperature distribution

The temperature shows a rapid increase in front of the cathode due to Joule heating. The temperature radial distribution can be expressed by (McKelliget and Szekely, 1983):

$$T(r, z = 0) = T_{max} \cdot \left(1 - \left(\frac{r}{r_a}\right)^2\right) \ , \ 0 < r < r_a \qquad (3.40)$$

where T_{max} is the temperature at the arc core in the vicinity of the cathode. The temperature will drop as the arc spreads, and thereby, the current density decreases. The temperature is almost constant along the arc column axis.

The axial distributions of the arc characteristics axial velocity, electric field strength, axial current density and temperature are illustrated in Fig. 3.8. This outline is based on Edels (1973) and shows that assumptions about uniform conditions along the arc axis seem reasonable.

The radial distributions of the arc axial current density and temperature in a cross section of the arc column, together with the axial velocity distribution, are schematically shown in Fig. 3.9, which is based on Bowman (1972) and Edels (1973).

3.3 The cathode region

The cathode region and especially the flow phenomena occurring in this region of an arc, play an important role for the condition in the arc column as well as in the anode region. Thus, the physics of the cathode region have been the subject of a large number of studies. McKelliget and Szekely

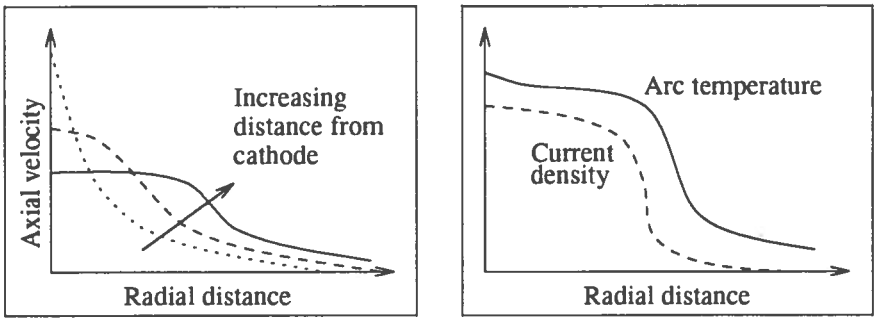

Figure 3.9: Radial distribution of arc characteristics.

(1983) give a survey of presented related literature and present a mathematical model of the cathode region of a high-intensity carbon arc. Other important references are Mentel (1977), Pfender (1978), Jones and Fang (1980).

3.3.1 Current transfer mechanism

The current transfer mechanism between the cathode electrode and the plasma column depends in a complicated manner upon material properties and operating conditions (Jones and Fang, 1980). This region of an arc is commonly denoted **"the arc root"**.

The various forms which arc roots can take on different cathode electrodes, can be roughly classified according to Ecker's contraction theory (Mentel, 1977). Both an electron current and an ion current must flow immediately before the cathode. In the cathode region the ion current is much larger than the ion current present in the arc column, which is predominated by the electron current and can be described by:

$$I_i = I_e \sqrt{\frac{m_e}{m_i}} \tag{3.41}$$

where I_i and I_e are the ion and electron currents in the arc column, and m_i and m_i are the ion and electron masses. The ion current is generated thermionically in the cathode region, and the current density is proportional to the ion density N_i and the thermal velocity v_{th} of positive ions at the cathode:

$$j_i \propto \frac{1}{4}\, e\, N_i(T_C)\, v_{th} \tag{3.42}$$

where e is the elementary electron charge and T_C is the temperature in the cathode region. The ion current density increases with temperature,

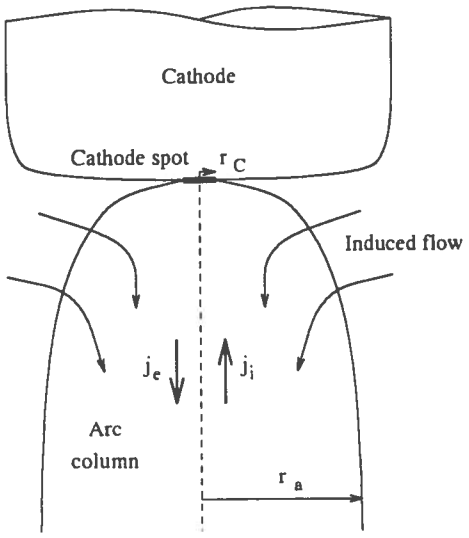

Figure 3.10: Cathode region of free-burning arc.

especially within the ionization region or the cathode fall zone. The larger the total current density:

$$j = j_e + j_i \tag{3.43}$$

the higher the plasma temperature at the cathode. Therefore, the ion current density increases as the arc root contracts, and initially the same is true for the ion current:

$$I_i = j_i \, \Theta_a \tag{3.44}$$

where Θ_a is the arc cross-section area. As the constriction becomes more pronounced, the decrease of the area Θ_a predominates over the increase in the ion current density, so that the total ion current diminishes again. According to Pfender (1978), a certain fraction of the current flow in the cathode region is due to ions which impinge on the cathode surface giving off their charge. At the same time the ions release kinetic and potential energy, heating the cathode surface to temperature levels that are sufficient for thermionic emission. Thus, the total ion current is responsible for the temperature of the cathode, and its density is responsible for the increased electric field strength near the cathode surface. The cathode region of a free-burning arc is illustrated in Fig. 3.10.

The arc is usually self-sustaining, and it must take care of its own electron supply at the cathode. In general, the electron emission of the cathode is a superposition of two different emission phenomena:

1. **Thermionic emission**

2. **Field emission**

The cathode emission can be calculated as a function of the ion current and the contraction of the arc root. The current attachment at the cathode can generally be divided into three different current transfer modes (Mentel, 1977; Pfender, 1978):

1. **Very little contraction.** The current flowing in the cathode region predominantly comprises a thermionically generated electron current. The energy supplied to the cathode is sufficient to produce thermal electron emission, but not to vaporize the cathode material. The current attachment is **diffuse** without any evidence of single or multiple cathode spots.

2. When the arc root is **highly contracted**, the current is predominantly carried by field-emitted electrons. The total ion current is low, but the ion current density and the field strength at the cathode surface are large. This type of current transfer is observed at "cold electrodes". The arc burns on field-enhancing projections and on impurities having reduced work functions. The current attachment is in the form of one or several distinct spots. If an increase in temperature destroys the emission-enhancing conditions, the arc root moves to new emission sites, but strong vaporization does not occur. This mode can be clearly distinguished from the diffuse attachment mode, with a much severe constriction and with current densities in the spots in the range 10^6-10^8 A/cm^2. The cathode attachment can be clearly observed as one or several bright spots on the cathode surface, and the spots are usually moving randomly with high velocities over the cathode surface. This mode can be denoted as **true spot attachment**.

3. If the contraction lies between the two extremes above, the ion current contributes significantly to the total current in the cathode region. The cathode is strongly heated by the ion current, and pronounced vaporization of the cathode electrode material can be expected. The current attachment is somewhat between the diffuse mode and the true spot mode, and this mode is frequently referred to in the literature as **spot attachment**. The arc current can be considerably constricted in front of the cathode, so that the actual current transition zone appears as a "spot", with current densities in the range 10^3-10^4 A/cm^2, which is at least one magnitude higher than the cur-

rent density in the arc column. The cathode attachment is stationary or slowly moving.

The diffuse attachment and the spot attachment mode are restricted to cathode materials with very high boiling points, for instance carbon and refractory metals, denoted "thermionic cathodes". In this mode, the governing mechanism for the liberation of electrons from the cathode is thermionic emission, which is characterized by relatively stationary cathode spots (Pfender, 1978). Furthermore, the current densities in the cathode spots are largely independent of the arc current. This implies that the cathode spot radius r_C can be described by (McKelliget and Szekely, 1983):

$$r_C = \sqrt{I_a / \pi j_C} \tag{3.45}$$

where I_a is the total arc current and j_C is the current density at the cathode.

The thermionic emission is generally a function of the cathode surface temperature T_C and a characteristic property of the cathode material, known as the work function ϕ_C. The thermionic emission can be described by the Richardson-Dushman (R-D) equation, which relates the cathode temperature to the cathode current density (Hsu, Etemadi and Pfender, 1983; McKelliget and Szekely, 1983):

$$j_C = A\, T_C^2 \cdot \mathrm{e}^{-(e\,\phi_C / k_B T_C)} \tag{3.46}$$

where A is a constant, e is the elementary electron charge and k_B is the Boltzmann constant. The cathode white-hot spot appears as a hemisphere and it can be assumed that this part, which seems to be molten, uniformly emits a constant current density. The thermionic emission is highly dependent on the temperature, and emission beyond the cathode spot can be neglected (Hsu, Etemadi and Pfender, 1983).

The cathode electron emission mechanism in the true spot mode is entirely different from the diffuse attachment mode. This mode occurs at "cold" electrodes ("nonthermionic cathodes"), and the cathode surface temperature is insufficiently high to promote thermionic emission of electrons. The governing mechanism of electron emission is therefore field emission (Pfender, 1978). The two different electron emission mechanisms can be summarized in Table 3.1 (Pfender, 1978).

The arc sustaining current mainly flows through the plasma, and therefore the current transfer to the cathode predominantly occurs via the surrounding host plasma, rather than through the vapor jets. The current transfer mechanism of cathodes with high erosion is probably identical to that of the low erosion operation mode (Jones and Fang, 1980).

Table 3.1: Properties of thermionic and nontherionic cathodes.

Cathode mode	Surface temperature	Current density	Cathode attachment	Emission mode
Thermionic (hot)	> 3500 K	10^3-10^4 A/cm^2	fixed or slowly moving	thermionic
Nonthermionic (cold)	< 3500 K	10^6-10^8 A/cm^2	rapidly moving	field

3.3.2 Cathode flow phenomena

Cathode flow phenomena have been observed both in arcs with thermionic and with nonthermionic electrodes, and especially at higher current levels. According to Pfender (1978), these cathode flows may be attributed by four different sources:

1. Electromagnetically induced gas and plasma flow.
2. Vaporization of cathode material and/or surface impurities.
3. Explosive release of cathode material.
4. Chemical reactions on the cathode surface producing gases.

Gas flows entering through a conducting plasma, transport enthalpy. As the gas enters the plasma and flows against the temperature gradient, the gas is heated and enthalpy is transported and yielded to downstream plasma volumes. The expansion of the column downstream reduces the field strength and temperature in the flow direction.

The electromagnetic induced flow effect

High energy arcs are generally dominated by high velocity plasma flows consisting of magnetically pumped gas, directed away from the cathode electrode, and sometimes from the anode electrode, too. This is a result of the Lorentz force field produced by the interaction of the spatially non-uniform high current density and its associated magnetic field, and can be explained by the variation of the magnetic pinch force produced by the sharp contraction of the arc column near the electrodes. This creates an axially directed gas and plasma flow in and around the arc column, and this

flow effect is often denoted as "**a plasma jet**". The strong electromagnetic force and the high rate of Joule heat dissipation are responsible for the characteristics features of high energy arcs with gas velocities above 1000 m/s and plasma temperatures above 20 000 K (McKelliget and Szekely, 1983).

The electromagnetic pumping effect for a stationary free-burning arc is treated among others by Pfender (1978), Jones and Fang (1980), Sanders et al. (1982) and Ahlers (1988). The source for the induced flow is the electromagnetic Lorentz force $\boldsymbol{F}_L$, due to the interaction between the arc current and its self-magnetic field:

$$\boldsymbol{F}_L = \boldsymbol{j} \times \boldsymbol{B} \tag{3.47}$$

where $\boldsymbol{j}$ is the current density and $\boldsymbol{B}$ is the self-magnetic field vector.

According to Jones and Fang (1980), the plasma acceleration due to self-magnetic effects arises in two different ways:

1. An **axial** Lorentz force $\boldsymbol{F}_{L\,z}$ may be produced by the interaction of the azimuthal self-magnetic field $\boldsymbol{B}_\theta$ with the radial component of the current density j_r. This force component is usually large in the cathode region due to the constriction of the arc column.

2. A **radial** Lorentz force $\boldsymbol{F}_{L\,r}$ may be produced by the interaction of the axial component of the current density j_z and the azimuthal magnetic field $\boldsymbol{B}_\theta$.

The induced flow phenomena in the cathode region can be described by the momentum and continuity equations for a high-intensity arc column (Pfender, 1978; Sanders et al., 1982; Ahlers, 1988). The derivation of the flow description will be significantly simplified if homogeneous conditions are assumed in the arc regions. This is the technique used when a channel model is applied to describe the arc column.

Appendix A.1 outlines the derivation of Ahlers (1988), who based his derivation on power balances of the different arc regions in the vicinity of the cathode and with a further assumption of a uniform current distribution across the arc column (Eq. 3.45), and deduced descriptions of the axial plasma flow and its mass flow. The radial distribution of the axial plasma flow $v_z(r)$ is derived in Eq. A.21, and can be expressed as:

$$v_z(r) = \sqrt{\frac{\mu_0}{2\,\rho_a}}\, r_C\, j_C \sqrt{1 - \left(\frac{r_C}{r_a}\right)^2} \sqrt{1 - \left(\frac{r}{r_a}\right)^2} \tag{3.48}$$

where μ_0 is the magnetic permeability of vacuum. The velocity has its maximum v_{max} at the arc axis:

$$v_{max} = v_z(r=0) = \sqrt{\frac{\mu_0}{2\,\rho_a}}\, r_C\, j_C \sqrt{1-\left(\frac{r_C}{r_a}\right)^2} \tag{3.49}$$

and thus the velocity distribution can be expressed as:

$$v_z(r) = v_{max} \sqrt{1-\left(\frac{r}{r_a}\right)^2} \tag{3.50}$$

The axial pressure increase is derived as:

$$\Delta p(r) = \frac{\mu_0}{4}\, {j_z}^2\, {r_a}^2 \left(1-\left(\frac{r}{r_a}\right)^2\right) \tag{3.51}$$

According to McKelliget and Szekely (1983), an alternative expression of the maximum velocity can be derived by using a parabolic current distribution:

$$v_{max} = \sqrt{\frac{5}{6}\,\frac{\mu_0}{\rho_a}}\, r_C j_C \sqrt{1-\left(\frac{r_C}{r_a}\right)^2} \tag{3.52}$$

An alternative expression of the pressure increase in Eq. 3.51 can be derived by inserting Eq. 3.45 (Sanders et al., 1982):

$$\Delta p(r) = \frac{\mu_0}{4\pi}\, I_a\, j_z \left(1-\left(\frac{r}{r_a}\right)^2\right) \tag{3.53}$$

The pressure increase has its maximum at the arc axis:

$$\Delta p_{max} = \Delta p(r=0) = \frac{\mu_0}{4\pi}\, I_a\, j_z \tag{3.54}$$

This shows that the pressure gradient in the arc axis is proportional to the product of the arc current and current density. An alternative expression of the maximum plasma velocity can be derived (Sanders et al., 1982). As soon there is a constriction of the arc channel in the cathode region the current density as well as the self-magnetic field will increase. According to Eq. 3.53, the overpressure at the arc axis will increase too, and an axial pressure gradient will be generated towards the cathode. Radial expansions of the plasma arc column with distance away from the cathode therefore produce a negative pressure gradient along the arc axis. The pressure

gradient gives rise to an axial flow v towards the anode which maintain the vapor and plasma flow through the arc column:

$$\Delta p = \frac{1}{2}\,\rho_a\, v_z^2 \tag{3.55}$$

Combining Eqs. 3.53, 3.54 and 3.55, an expression of the maximal axial velocity is derived:

$$v_{max} = \sqrt{\frac{\mu_0}{2\pi\,\rho_a}(I_a\, j_z)} \tag{3.56}$$

An expression of the plasma mass flow can be found by integrating Eq. A.13 in App. A.1 (Ahlers, 1988):

$$\begin{aligned}\dot{m} &= \int_0^{r_a} 2\pi\,\rho_a\, v_z(r) r\, dr \\ &= \frac{2}{3}\,\rho_a\,\pi\, {r_a}^2\, v_{max} \qquad (3.57)\\ &= \frac{1}{3}\sqrt{2\,\mu_0\,\rho_a\,\pi\, j_C}\,\sqrt{I_a}\,{r_a}^2\sqrt{1-\left(\frac{r_C}{r_a}\right)^2} \qquad (3.58)\end{aligned}$$

An alternative expression of the mass flow can be found using the average flow velocity and assuming laminar flow (Pfeifer, Fett and Bebber, 1989):

$$\dot{m} = \rho_a\,\pi\, r_a^2\,\bar{v}_z = \frac{1}{2}\,\rho_a\,\pi\, r_a^2\, v_{max} \tag{3.59}$$

Inserting the alternative expressions of the maximum axial velocity in Eqs. A.22 and 3.52, yields:

$$\dot{m}_a = \frac{1}{2}\,{r_a}^2\sqrt{k\,\frac{\mu_0}{\rho_a}\,\pi\, j_C}\,\rho_a\,\sqrt{i_a} \tag{3.60}$$

where k can be 1/2 or 5/6 depending on the choice of model description.

According to Sanders et al. (1982), another expression of the mass flow rate can be derived by assuming a uniform distribution over the arc cross section:

$$\dot{m} = \rho_a\,\pi\, r_a^2\, v_{max} \tag{3.61}$$

Inserting Eqs. A.2 and 3.56 yields:

$$\dot{m} = \sqrt{\frac{\mu_0}{2\pi}\,\bar{\rho}\,\pi r_a^2}\cdot I_a \tag{3.62}$$

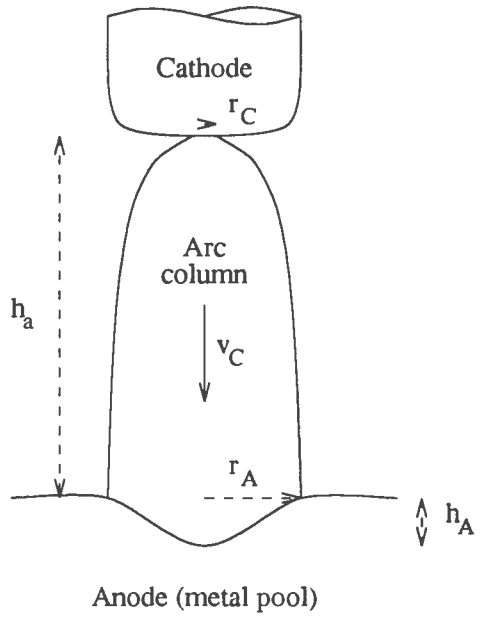

Figure 3.11: Cathode jet imping on the anode metal pool.

According to Sanders et al. (1982), the expression under the square root as a first approximation can be considered to be constant due to the opposite trends of the current dependencies of $\bar{\rho}$ and πr_a^2. The mass flow rate of the cathode jet can therefore be approximated to be proportional to the arc current:

$$\dot{m} \sim I_a \tag{3.63}$$

The total arc thrust can be expressed by (McKelliget and Szekely, 1983):

$$F_a = \frac{\mu_0}{4\,\pi} I_a{}^2 \ln \frac{r_a}{r_C} \tag{3.64}$$

The cathode jet will impinge on the anode surface. In an electric furnace when the electrode is cathode, the anode often consists of a liquid pool of metal, and the jet will create a penetration in the liquid pool as shown in Fig. 3.11. The depth of penetration can be expressed as (Szekely and Themelis, 1971):

$$h_A = \frac{1}{2\,g} \frac{\rho_a}{\rho_A} v_z(h_a)^2 \tag{3.65}$$

where h_A is the depth of the anode penetration, g is the acceleration of free fall, ρ_A is the mass density of the anode metal liquid, and the velocity at

the arc axis at the anode $v_z(h_a)$ can be expressed by Eq. 3.30:

$$v_z(z = h_a) = c\, v_{max}\, \frac{r_c}{h_a} \tag{3.66}$$

if transient jet flow is assumed.

The cathode jet may enhance the stiffness of the cathode region, and have a stabilizing effect on free-burning arcs. Substantial axial flow velocities may be generated at high current values. At ultra high currents the plasma flow velocities tend towards the sonic value corresponding to the plasma temperatures.

Vaporization in the cathode region and vapor jets

The presence of vaporization will have a strong influence on the arc behavior. The effect of vaporization in the cathode region of high-current arcs is investigated by Mentel (1977). He claims that evaporation will generally occur in high-current arcs. The vapor can be identified in observations principally by its brightness compared with that of the arc column. It originates from the arc root at the cathode and escapes the electrode in form of a directed jet.

The vaporization depends on the mechanism of current transfer from the arc column to the cathode electrode. According to Mentel (1977), various forms of vaporization can exist, depending upon electrode parameters and form of the arc root.

Mentel (1977) investigated the evaporation mechanism on a graphite electrode. If the electrode is cooled, little or no evaporation occurs even at high arc currents. On the other hand, if the electrode is only weakly cooled, the electrode erosion increases in an erratic manner as the current rises. Initially small carbon particles become detached from the edge of the electrode and accelerated to the axis. This leads to the formation of a cone shaped tip and broadening of the arc root. As the current is further increased, a large cathode spot develops accompanied by pronounced erosion. This generates a broad jet which envelopes the electrode tip. However, the arcs root with an axially symmetric vapor jet is not very stable, and even small disturbances of the rotational symmetry can cause separation of the arc column and the vapor jet. A slightly different mode is also observed with very little vapor emission from the surface, and instead sudden eruptions of vapor occur from within the interior of the electrode. Also vaporization was observed outside of the current transfer region. The occurrence of different vapor jets is illustrated in Fig. 3.12.

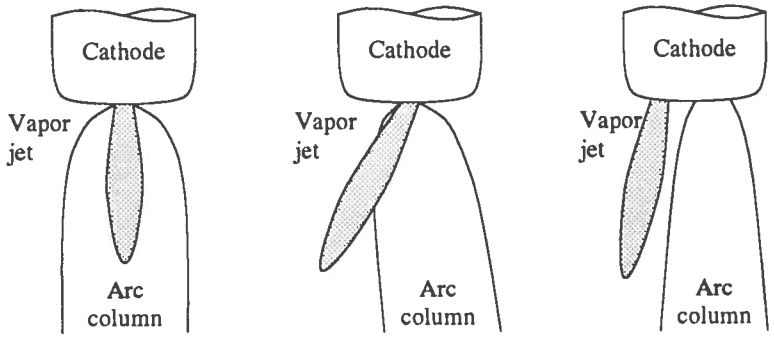

Figure 3.12: Three different occurrences of vapor jets. From left to right: An axially symmetric vapor jet, then separation of the vapor jet and the arc column, and the presence of a vapor jet outside the arc column.

Mentel (1977) concludes that the electrode evaporation and vapor eruptions are not directly correlated with the current transfer to the electrode, but are only a consequence of the heating of the electrode material and vaporization from the electrode surface and from within the bulk of the material. The current transfer itself only takes places in regions with reduced vaporization. At the cathode a reduction of vaporization inside the current transfer region can be caused by an ion current directed to the cathode. The vapor from outside the current transfer region is apparently cold immediately in front of the electrode and thus is a poor electrical conductor. The differing form of the arc roots that are observed, are not governed by basically different current transfer mechanism, but by the various forms which the vaporization process can take.

A high erosion mode of evaporation is also accompanied by the formation of vapor jets as the result of the considerable power dissipation at the electrodes. This effect depends on the energy balance at the electrodes and hence on the energy densities, electrode geometry and materials and discharge duration, and has been found to be proportional to the arc current.

As a result of vaporization, explosive release of cathode materials and electrode impurities, and gas producing chemical reactions, cathode jets originate at the cathode surface. Such jets will contain cathode material, electrode impurities in vapor form or gases stemming from chemical reactions on the cathode surface. Such reactions are common in electric furnace operations. Metal vapor and cathode material impurities have a lower ionization potential than permanent gases, and these materials will have strong influ-

ence on the plasma properties, including the transport coefficients of the plasma in the cathode regions.

The identity of a cathode vapor jet is present within the high-current arc column at a substantial distance from the cathode. The interaction between the gas flow and vapor jets is important. According to Edels (1973), it has been shown that there are separate streams for appreciable distances before fully mixing.

The vapor jets have been detected within the luminous streaming plasma. Such observations are possible because the gas flow and the vapor jets usually have distinct radiation properties. As a result of this it has been possible to find evidence for time constants for melting and evaporation after arc initiation. Shortly after initiation, radiation from the gas species are dominant, but after some time radiation from the vapor particles increase rapidly and become dominant. This radiative time lag is assumed to be clearly observable in AC arcs, and can be applied when analyzing the alternating operating regimes in AC arcing. According to Edels (1973), the typical evaporation time constant is in the range 1-3 ms in high-current arcs.

Arc instability

Arc instability may be produced by the deformation of the arc column itself by its interaction with imposed axial flow or by motion of the arc root along the cathode.

Electrode-induced instability may occur if there is strong evaporation of the electrode. Asymmetric self-magnetic field effects close to the cathode surface may produce mobile arc roots which induce unstable column behavior. These will be due to lower electrical conductivity or relatively cool vapor jets emitted from the cathode. The resulting Lorentz force drives the current carrying arc root away from the source of the vapor jet.

3.3.3 Energy balance for the cathode region

According to Mentel (1977), the energy is supplied to the cathode principally by an ionic current comprising the ionized cathodic material, and thus heat transfer from the arc column to the cathode electrode due to radiation, convection and conduction can be neglected. The main heat loss mechanisms that have a cooling effect of the cathode, are thermionic emission of electrons, vaporization of cathode materials and radiation. In addition,

heat losses due to convection and conduction may be present, but are negligible. The presence of any field emission of electrons will not remove energy from the cathode. The electrons which are emitted thermionically from the cathode are accelerated by the field in the cathode fall zone away from the cathode. In the same way ions that enter the anode fall zone or are generated in this zone, are accelerated towards the cathode.

With the assumptions stated above the total energy balance for the cathode region per unit area and unit time, can be written (Mentel, 1977; Pfender, 1978):

$$j_e \phi_C + j\,(V_R + V_V) = j_i \left[V_C + (V_I - \phi_C) + \frac{5}{2}\frac{k_B}{e}(T_i - T_C) \right] \qquad (3.67)$$

where j_e and j_i denote the electron and ion current density, $j = j_e + j_i$ is the total current density, ϕ_C is the cathode work function, V_R and V_V are the potential drops due to vaporization and radiation, V_C is the potential drop in the cathode fall zone, V_I is the ionization potential of the working fluid, k_B is the Boltzmann constant, e is the elementary electron charge, T_i is the temperature of ions entering the cathode fall zone, and T_C is the temperature of the cathode surface. According to Mentel (1977), graphite cathodes have a working function of 4.36 eV, an ionization energy of 11.23 eV, and an vaporization enthalpy of 30 kJ/g.

The first term on the left-hand side represents the energy releases from the cathode due to thermionic electron emission, and the second terms represent the releases due to vaporization and radiation from the cathode. On the right-hand side the first term represents the energy gained from the cathode fall. The second term represents the release of ionization energy which is reduced by the potential energy of the electron from the cathode, which neutralizes the ion. Finally, the third term represents enthalpy due to temperature differences between an incoming ion and the cathode surface.

The energy balance in Eq. 3.67 yields the following ratio between the ion current density and the total current density (Pfender, 1978):

$$\frac{j_i}{j} = \frac{\phi_C + V_R + V_V}{V_C + V_I + \frac{5}{2}\frac{k_B}{e}(T_i - T_C)} \qquad (3.68)$$

According to Pfender (1978), this expression yields ion current densities at the cathode in the range from 15 to 50 % of the total current density. The ion current density increases towards the cathode. This is consistent with the formation of a net positive space charge which determines the cathode fall zone. This space charge gives rise to an electric field which enhances

electron emission in the thermionically emitting cathode, provided the field is sufficiently strong.

The cathode fall for an arc with a thermionically emitting cathode is typically 10 V for high-intensity arcs, but with some minor variation with current. For low-intensity arcs on the other hand, the cathode fall can be substantially higher, approaching values close to the ionization potential of the working fluid.

3.3.4 Properties of carbon cathodes

Carbon electrodes are commonly used in electric furnaces. The properties of carbon cathode electrodes can be summarized as follows:

1. Thermionic emission rather than a field type emission mechanism.

   However, the electrode emission mechanism does not only depend on the cathode properties like materials, temperatures and geometry, but also on the properties of the arc column, such as gas composition and pressure, and the discharge current.

2. Current carrying spots occur at the cathode surface. A high current density, for carbon electrodes with ultra high-currents arcs ($\sim 10^5$ A/cm^2), but this is a relatively low cathode current density compared to other electrode materials.

3. The cathode voltage fall in the range $\sim 10 - 30$ V.

4. A high erosion mode with substantial cathode evaporation is accompanied by the formation of vapor jets. The evaporation effect is significant in the energy balance at the surface of the carbon cathode (Jones and Fang, 1980).

   The carbon vapor jets may be considerably cooler (4000 K) than the host arc plasma (12000 K), and as a result of that the electrical conductivity of the vapor jet may be significantly less than that of the host plasma (Jones and Fang, 1980).

3.4 The anode region

There are a number of similarities and common features between the cathode and anode regions in an electric arc. In contrast to the cathode region, the anode region plays a more passive role. This fact is also reflected in a comparable small number of investigations and available data. However,

Sander et al. (1982) studied the anode regions of high-intensity arcs, and Pfender (1978) gives a survey of earlier investigations.

The anode region of a high-pressure high-intensity arc can be divided into the following zones (Sanders et al., 1982):

1. A flow effected zone, which is common denoted as the transition or contraction zone. This zone has a thickness in the order of 10 mm, and lies between the arc column and the anode fall zone.

2. A diffusion or anode boundary layer, which is commonly denoted as the true anode fall zone. The thickness of this zone is in the order of 0.1 mm.

3. A sheath at the bottom of the anode layer overlaying the anode surface. The thickness of the sheath is in order of 10^{-5} mm.

3.4.1 Current transfer mechanism

The principal task of the anode region is to provide an electrical connection between the high temperature plasma of an arc and the "low" temperature anode. This embraces several effects imposed by the conservation equations (Pfender, 1978) :

1. **Energy conservation:** The field strength and current density will adjust themselves so that the total net energy losses suffered by a volume element are compensated for by Joule heating in the same volume element. Because of the steep gradients in front of and normal to the anode surface, losses in axial direction may be substantially larger than those in the radial direction.

2. **Charge carrier conservations:** The conservation of charge carriers in the anode region demands ion production. However, the ion current only accounts for a small fraction ($\approx 1\%$) of the total current, and the current between the anode surface and the arc column is essentially carried by electrons, assuming that the anode does not emit ions. At the anode surface the current is exclusively carried by electrons that give rise to a net negative space charge. This space charge tapers off with increasing distance normal to the anode due to the ion production, until the unpertubed state is reached in the plasma column. The potential drop in the anode fall zone is a consequence of the net space charge adjacent to the anode surface.

According to Pfender (1978), the task of the anode region can be summarized as follows:

1. Production of ions to maintain the ion flux passing through any cross section towards the cathode. Since the ion mobility is very small compared to the electron mobility, the required ion production is rather small.

2. The directed velocity of the ions due to the high field strength in the anode fall, has to be transformed into random motion as the plasma column is approached, in order to match the boundary conditions at the interface between the plasma column and the anode fall regions.

3. The opposite is true for the electrons which receive a large directed velocity as they approached the anode. In this way, the anode fall provides the necessary electron collection.

In charge carrier generation, the anode fall zone may occur by two basically different ionization mechanisms:

1. **Field ionization:** This phenomena plays an important role in low-intensity arcs where anode falls have been observed in the order of the ionization potential of the working fluid.

2. **Thermal ionization:** For high-intensity arcs the anode falls are considerable smaller. For such arcs thermal ionization is the governing ionization mechanism. Electrons in the high energy tail of the Maxwellian distribution are responsible for the ionization.

Two different ways of attaching the arc at the anode are possible (Pfender, 1978):

1. **Diffusive attachment**

2. Severely **constricted (spot) attachment**

According to Pfender (1978), it is not clear under which conditions constrictions will occur. However, chemical reactions at the anode surface seem to favor a constricted anode root that, at the same time, may travel more or less randomly, over the anode surface with large velocities. Anode evaporation is another mechanism that will lead to spot formation.

Additional structures in terms of the anode root can be shown in both anode attachment modes. Bright legs or channels may develop under certain conditions immediately in front of the anode, forming anode spots. These legs, superimposed to a more or less diffuse plasma are observed, both in a quasi-steady mode and in more rapidly moving modes, where the anode root is wandering freely around the periphery of the anode arc attachment

area. Such phenomena are also observed at higher current levels (Sanders et al., 1982).

In short high-current arcs the diffusive anode attachment is directly associated with the cathode jet, resulting in the well-known "bell-shape" of a free-burning arc. The intense cathode jet impinging on the anode surface pushes hot plasma against the anode, eliminating the need for ionization in the anode fall zone (Pfender, 1978). If the distance between the electrodes is increased, the influence of the cathode jet will decrease, and this encourages the formation of bright legs and the arc will form one or several spots on the anode surface. Furthermore, impurities in the anode material will also contribute to the formation of legs.

The anode attachment is governed by the thermal conditions at and adjacent to the anode surface. Any effect which has a favorable influence of the energy balance in the anode region, in the sense that internal heat generation by the arc may be decreased, seems to favor a diffuse arc attachment. The cathode jet may be able to provide a continuous flow of hot plasma into the anode region and reducing the necessity of heat generation by the arc itself. A reduction of the anode fall with increased arc current, and thereby an increased cathode jet, is therefore expected.

A non-evaporation mode of operation is possible with diffuse current collection. Under such a condition the anode voltage and therefore the energy input is low and the possibility for evaporation is reduced, and the anode will act as a simple current collector.

3.4.2 Anode flow phenomena

Different flow regimes are possible at the anode. The anode region and the anode root depend upon the flow induced by the arc. The bell shape of an arc, with its axis normal to a plane anode surface, reflects the effect of the cathode jet impinging on the anode. If the cathode-anode distance is increased sufficiently, the cathode jet is no longer felt in the vicinity of the anode. As a consequence the arc becomes unstable, and at the same time, one or several anode spots are formed and the creation of a magnetically pumped plasma stream ("**the anode jet**") and an anode vapor jet is possible (Sanders et al., 1982).

The behavior of the anode region can be divided into two distinct operation modes based on the existing flow phenomena:

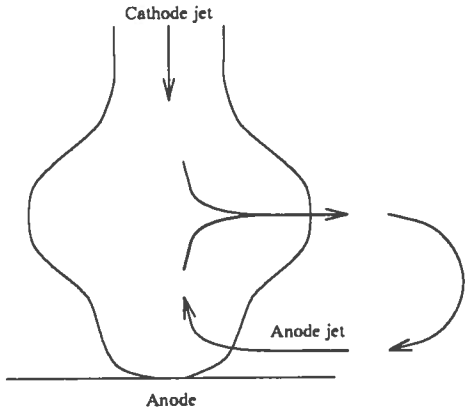

Figure 3.13: Flow field in an anode jet dominated (AJD) arc.

1. A **cathode jet dominated (CJD)** mode is present when the cathode flow is responsible for the conditions in the anode region. The bell shape of free-burning arcs is a typical example.

2. An **anode jet dominated (AJD)** mode is present when the plasma flow in the anode region is a result of phenomena in the anode region.

The AJD mode may occur if the cathode flow against the anode is reduced considerable either by increased cathode-anode distance, by reducing the arc current, or by reducing the current density at the cathode. If the effect of the cathode jet in the neighborhood of the anode is diminished, the arc loses its stability, and at the same time, one or several anode spots appear on the anode surface. Furthermore, if a constricted arc root appears at the anode, an electromagnetic pumping effect will occur, similar to that at the cathode region. The induced gas in the anode region is heated and accelerated towards the cathode (Sanders et al., 1982; Maske, 1985).

Sanders et al. (1982) studied the flow phenomena in the anode region of a high-intensity argon arc experimentally as well as by simulation studies of analytic models, and the simulation results and experiments analysis yield comparable results. The flow fields in the anode region for the CJD and AJD modes are schematically shown in Figs. 3.13 and 3.14, respectively. In the AJD mode the flow fields reveals a circulation due to the self-induced flow close to the anode. This circulation, impinging with the flow arriving from the cathode, forces the axial flow out in radial direction. Towards the anode the arc column is constricted, resulting in an increase in the Joule heating. At the outflow region the arc expands, resulting in lower temperatures. In the CJD mode a somewhat different flow field is present,

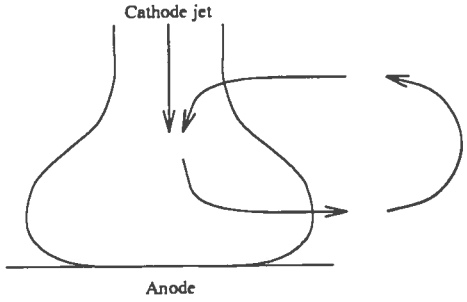

Figure 3.14: Flow field in a cathode jet dominated (CJD) arc.

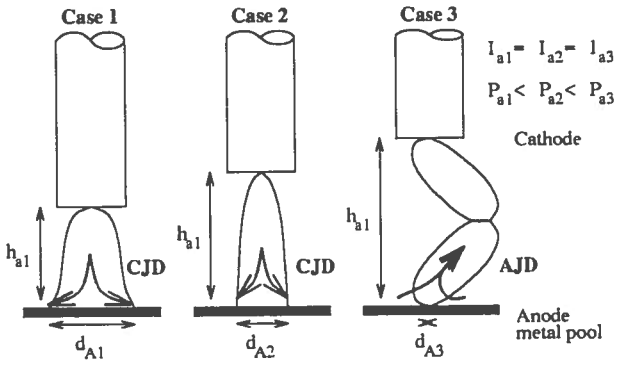

Figure 3.15: Anode flow field transformation from CJD to AJD regime, based on Maske (1985).

and the induced flow in the anode region is reversed compared to the AJD mode.

The anode flow fields are also investigated by Maske (1985), who carried out experiments on a low-power experimental transferred-arc plasma furnace. Figure 3.15 schematically shows the change in the arc flow from a CJD flow regime to an AJD flow regime. Such a regime transformation can be obtained by the maintenance of the arc current with an increase in the arc length or more correctly the electrode displacement, in order to increase the electrical power input. The change in the anode flow regime will also have significant influence on the heat transfer to the anode surface.

Anode jets

The presence of the jet creation mechanisms in the anode region will depend on the anode geometry and material properties. The flow components of an anode jet are similar to that of a cathode jet:

1. Electromagnetically induced plasma jets.
2. Evaporation of anode materials.
3. Chemical reactions from the anode surface.

Electromagnetically induced anode jets may develop if the arc column contracts in the anode region. This will correspond to the induced flow phenomena in the cathode region.

The anode jet production is often a result of vaporization at the anode. The vaporization and hence the anode jet production can be avoided if the anode surface is sufficiently large and with short arc duration periods. If the anode surface is large enough to collect the full current from the cathode, little or no anode vaporization develops. With increased current values the anode temperature may reach the evaporation point, and vapor jets develop. The same may happen if the anode surface is reduced. If the evaporation mode is reached, the anode voltage drop will increase, and the vaporization condition accelerates.

The presence of anode jets and particularly vapor jets, will have a significant effect on the space charge distribution in the anode region, and thereby, on the anode fall. According to Edels (1973), the energy used in evaporation account for effectively all the energy input at the anode and a major fraction of the energy input at the cathode.

With ultra high-current arcs and small electrode areas both vapor jets and gas pumping anode and cathode jets can be created and resulting in two contracting directed jets and unstable arcing conditions .

3.4.3 Energy balance for the anode region

Energy balances for the anode region of free-burning arcs are treated among others by Pfender (1978) Ushio, Szekely and Chang (1981), Sanders et al. (1982) and Maske (1985). The major heat transfer mechanisms to the anode surface are:

1. Convective heat flux due to the plasma flow impinging on the anode surface.
2. Radiative heat transfer from the arc column to the anode.
3. Anode fall and electron condensation on the anode surface.
4. Thompson effect due to temperature differences between incoming electrons and the anode surface.

The energy conveyed to the anode is employed for:

1. Anode heating and possible metallurgical reactions.
2. Anode vaporization.
3. Radiation from the anode to the surrounding.

The local anode energy balance per unit area and unit time can be expressed as:

$$q_F{}^{\text{in}} + q_R{}^{\text{in}} + j_e \left[V_A + \phi_A + \frac{5}{2}\frac{k_B}{e}(T_e - T_A) \right] = q_A{}^{\text{in}} + q_R{}^{\text{out}} + q_V \quad (3.69)$$

where $q_F{}^{\text{in}}$ represents local heat flux by convection and any conduction, as a result of the plasma flow, and $q_R{}^{\text{in}}$ represents radiative heat input. j_e denotes the electron current density at the anode surface, V_A the anode fall, and ϕ_A the working function of the anode material, k_B is the Boltzmann constant, e the elementary electron charge, T_e is the electron temperature entering the anode fall zone, and T_A is the temperature at the anode surface. $q_A{}^{\text{in}}$ represents the energy input to the anode available for for instance metallurgical reactions, $q_R{}^{\text{out}}$ represents radiation from the anode to the surroundings, and q_V represents energy losses due to vaporization at the anode surface.

The first term in the current-dependent expression in Eq. 3.69 represents the energy release at the anode surface due to increased electron potential as a result of the anode fall, the second term represents energy release due to condensation of electrons at the anode surface, and the third term represents the release of enthalpy due to temperature differences between incoming electrons and the anode surface, which is denoted the Thomson effect.

The spatial distribution between the different sources for heat input at the anode surface, convection, energy release due to the anode fall and electron condensation, and Thomson effect, is illustrated in Fig. 3.16. According to Ushio, Szekely and Chang (1981), the anode heat transfer mechanisms have the following mutual distribution:

1. 30-40% of the total high-current arc energy input is released at the anode by convection.
2. The energy input due to anode fall and electron condensation represents about 10% of the total arc energy input.

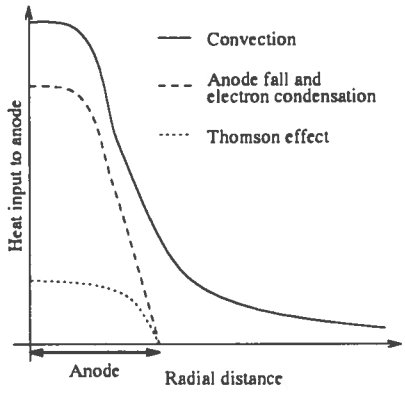

Figure 3.16: Local heat input distribution at the anode surface.

3. Heating due to the Thompson effect is below 5% of the total arc energy input.

4. Radiative energy input to the anode surface from arc column represents about 10% of the total arc energy input.

This result indicates that the total heat input to the anode surface is about 70% of the total arc energy input, and that about 30% of the arc energy input is carried away from the anode due to the convection effect of the flow field.

According to Maske (1985), the relative contribution between the various anode heat transfer mechanisms depend on the presence of the anode flow regime. In a CJD regime convection accounted for about 50% of the anode heat input, while electron condensation accounted for 12 %. In a AJD regime no cathode jet impinges on the anode surface, and the convection contribution is therefore negligible, and thus the electron condensation accounted for 83% of the total energy conveyed to the anode.

3.5 Arcing in electric arc furnaces

Arcing in AC electric furnaces has been a topic for a large number of studies. Most of these studies have focused on electric arc operations in open-arc furnaces. This was the topic for an extensive study by Bowman and colleagues at British Steel around 1970, resulting in some of the main references in this area (Bowman, Jordan and Fitzgerald, 1969; Jordan, Bowman and Wakelam, 1970; Bowman, 1972). Other important references are Billings (1975), Okamura et al. (1972), Edels (1973) and Veillette and Simard (1985). The number of studies on AC arcing in submerged-arc furnaces is considerable

less. Some of the main references are Otani et al. (1968) and Zherdev et al. (1968) in the 60s, and investigations at the National Institute for Metallurgy in South Africa in the 70s, among others Channon, Urquhart and Howat (1974), Urquhart, Jochens and Howat (1974) and Stewart (1980). In the recent years DC arc application in plasma-arc furnaces has been the topic for an increasing number of studies (Chang and Szekely, 1982; Ahlers and Timm, 1987a, 1987b; Ahlers, 1988).

3.5.1 AC arcs in electric furnaces

In an electric furnace the arc burns between an electrode, usually a carbon or graphite electrode, and a more or less molten metal pool surface. The polarity of the arc changes as a result of the AC operation mode, and therefore the arc burns alternating from the electrode towards the metal pool, and from the metal pool towards the electrode. This leads to different arcing conditions compared to DC arcs.

An AC arc experiences continuing transient regimes, and no stationary conditions are reached. Furthermore, the arc's anode and cathode regimes alternate between the electrode and the metal pool. Therefore, the anode and cathode properties depart, depending on the electric polarity, leading to alternating arcing conditions and the occurrence of hysteresis effects, and there will be a marked difference in appearance between the periods of opposite polarity.

The most common electric arc furnaces are the so-called three-phase **open-arc furnaces** used in steel production, as illustrated in Fig. 3.17. Three arcs burn between the electrodes and the more or less molten metal, providing the necessary energy for melting and the subsequent refining of metal scrap. In open-arc furnaces the arcs can be observed and measured directly, and detailed studies of the arcs and the arcing conditions can be carried out.

The arcing conditions in open-arc furnaces will be changed as result of the furnace operation cycle (Bowman, Jordan and Fitzgerald, 1969):

1. During the melt-down phase the electrodes bore down through the metal scrap. In this period the arc surroundings are "cold" and the arc lengths vary. The arcs are observed as noisy and unstable, and the current and voltage waveforms are heavily distorted.

2. In the refining phase the metal has been melted, and the arcs burn between the electrodes and the molten bath. The arc lengths are almost constant, the surroundings are "warm" and subsequently "hot",

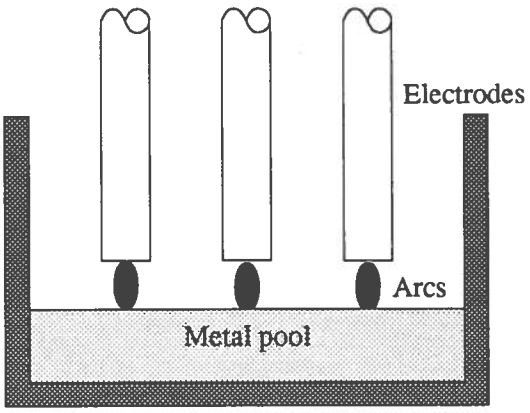

Figure 3.17: Schematic diagram of arcing in an open-arc furnace

and the gases in the region between the electrodes and the bath become more ionized as the temperature increases. The arcs are now observed as stable and the current and voltage waveforms are less distorted.

At the top, Fig. 3.18 shows typical voltage waveforms at "cold", "warm" and "hot" conditions, together with current waveforms at "hot" conditions, for the electrical half-period when the electrode is cathode (Bowman, Jordan and Fitzgerald, 1969). The current-voltage characteristics for an arc at "warm" and "hot" conditions are shown at the bottom of the figure (Okamura et al., 1972). In the following discussion, the "warm" and "hot" conditions are considered.

The distortion of the electrical waveforms due to the presence of electric arcs is further treated in Section 5.1.

The arcs in electric furnaces are high-current or even ultra high-current free-burning arcs. The ultra high-current arc is similar in many ways to the high-current arc, thus the axial gradients, stream energies and the electrode erosion factors are considerable greater. Ultra high-current AC arcs in electric furnace operation show a complex picture of large, grossly turbulent high temperature plasma volumes with large interacting gas flows and vapor jets, and the plasma form differs greatly with electrode polarity (Edels, 1973).

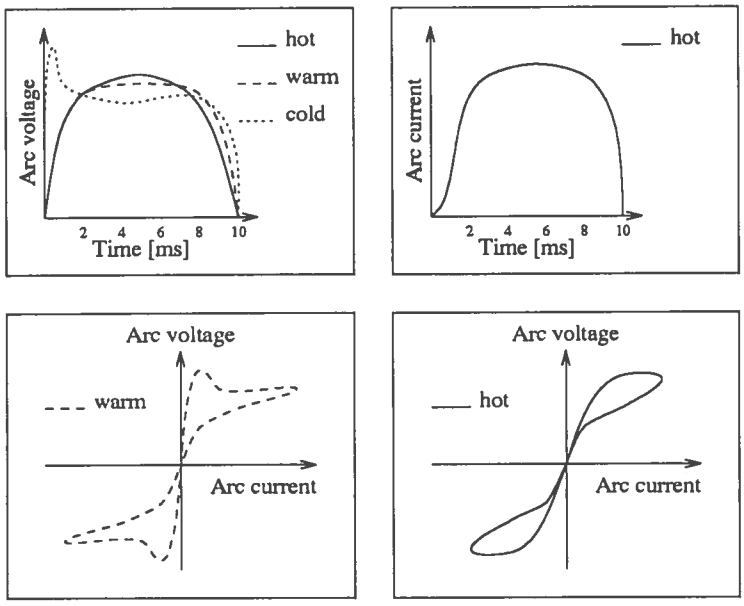

Figure 3.18: Schematic diagrams of current and voltage waveforms in arcing at various conditions, based on Bowman, Jordan and Fitzgerald (1969) and Okamura et al. (1972).

The AC arcing in electric furnaces is based on the electrical polarity, and can be divided into the following regimes:

1. **The electrode as cathode.** ("Negative polarity mode")

   (a) **The arc column:**
   When the electrode is the cathode, the arc column is comparable to a free-burning self-stabilized DC, and it is dominated by a strong plasma jet directed from the electrode towards the metal pool anode, except for the first milliseconds of the half-period, when the arc has a contorted filamentary shape (Jordan, Bowman and Wakelam, 1970; Bowman, 1972; Veillette and Simard, 1985). Furthermore, the arc tends to wander round the cathode electrode with velocities up to 100 m/s. The rigidity is maintained by the plasma jet, and thus, the direction of the plasma jet varies with time.

   According to Veillette and Simard (1985), the negative polarity arcing regime can be described as follows: The arc ignition takes place at the lowest point of the electrode tip. As the current rises, the arc diameter increases, and the arc starts to move at

the electrode surface, and the induced plasma jet develops in the cathode region. As the current decreases, the arc intensity and the arc diameter decreases. As the current reaches zero, the arc is extinguished, leaving a glowing electrode surface and a wisp of luminous gas.

A large content of metal vapor and electrode materials could be present in the arc column. According to Veillette and Simard (1985) most of the metal present in the arc column will be ionized, and most of the electrons required for current conduction can be supplied by the metallic species. According to Edels (1973) the arc plasma in ultra high-current arcs contains electrode particles and vapor, and it has strongly varying axial properties. The conduction radius is large, up to 30 cm, the current density is low 1000 A/cm^2, the field strength is low, up to 10 V/cm, and the temperature is high, more than 10 000 K.

According to Edels (1973), the major net energy losses are:

i. Convection due to the plasma flow: 50 – 70%.
ii. Radiation: 20 – 40 %.
iii. Thermal convection: < 10 %.

(b) **The cathode regime:**

The cathode spot has a constant movement around the electrode surface (Jordan, Bowman and Wakelam, 1970). Relatively stable cathode spots are present, and strong, self-induced plasma jets are directed from the electrode towards the anode surface, with velocities higher than 1000 m/s (Edels, 1973).

The high energy dissipation at the electrode produces significant electrode erosion and particle production, resulting in strong axially directed vapor streams from the electrode, with velocities as high as 10 000 m/s (Edels, 1973). The vaporization can also be observed as glowing vapor close to the cathode when the arc extinguishes (Veillette and Simard, 1985).

(c) **The anode regime:**

Arcing with the electrode as the cathode, usually results in a cathode-flow dominated anode region. The arc attempts to punch holes in the liquid metal, but the arc mobility tends to spread its thrust over a larger anode area. Furthermore, the arc

thrust results in the splashing of liquid metal and creates strong stirring in the metal pool (Bowman, 1972).

2. **The electrode as anode.** ("Positive polarity mode")

   (a) **The arc column:**

   When the metal pool is the cathode and the electrode is the anode, complex arcing conditions occur, and these arcing regimes are difficult to investigate. According to Jordan, Bowman and Wakelam (1970) and Bowman (1972), the arc contains a core which is usually contorted and highly mobile, with sideway velocities up to 600 m/s. This effect can be explained by magnetic instability.

   The power balance is different from the negative polarity mode. The high-velocity sideway movements result in significant convection losses.

   Furthermore, the arc column is considerably broader near the electrode compared to the negative polarity mode compared to the negative polarity mode. This leads to a decreased direct heat transfer to the metal and an increased heating of the electrode, something that can be observed by an increased electrode wear for arcs with an positive electrode (Bowman, 1972).

   According to Veillette and Simard (1985), the arc could also be dominated by a strong plasma flow from the anode electrode towards the cathode.

   (b) **The cathode regime:**

   According to McKelliget and Szekely (1983), strong, but unstable vapor jets may develop from the liquid metal cathode directed towards the electrode. Furthermore, the cathode spots are unstable and highly mobile.

   (c) **The anode regime:**

   The anode spot at the electrode is considerably larger than the cathode spot at the electrode in the opposite arcing regime (Jordan, Bowman and Wakelam, 1970). Furthermore, weak jets may develop from the anode electrode, but they will not be strong enough to stabilize the arc column and will results in complex arc forms by the interaction with possible cathode jets.

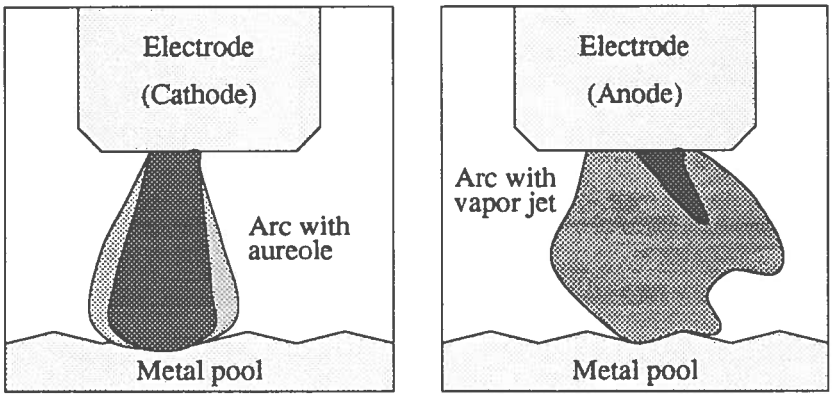

Figure 3.19: Schematic drawing of AC arcs in alternating regimes, based on Bowman, Jordan and Fitzgerald (1969). To the left arcing when the electrode is the cathode, and to the right arcing when the electrode is the anode.

The two distinct AC arcing regimes are illustrated in Fig. 3.19, which is based on Bowman, Jordan and Fitzgerald (1969). The negative polarity regime to the left shows a stable arc column comparable to DC arcing, surrounded by a thermal layer ("the aureole"). The positive polarity regime to the right shows an unstable, turbulent arc plasma volume with an anode vapor jet, developing from the electrode.

Arcing in submerged-arc furnaces

In submerged-arc furnaces the electrodes are submerged into the furnace burden to conduct the electric energy into the hearth of the furnace. The presence of arcing in submerged-arc furnaces will depend on what kind of production occurs in the furnace. In slag-free operations like the production of ferrosilicon and silicon, arcing is indubitable as the current and voltage waveforms are fairly distorted. In slag processes like the production of ferrochromium and ferromanganese on the other hand, the electric conduction is highly dominated by ohmic conduction and the presence of arcs is insignificant (Stewart, 1980). In the slag processes coke beds are present below the electrodes, with the result that ohmic conductance is favorable compared to arcing.

The occurrence of electric arcs in submerged-arc ferrosilicon and silicon furnaces was established by the studies by Otani et al. (1968) and Zherdev et al. (1968) on both laboratory and production furnaces. They observed the formation of large cavities around the electrode tips and the presence of a well-defined electric arc between the electrode and the metal pool in the

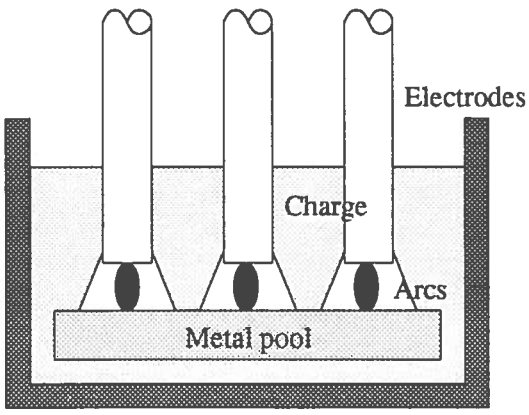

Figure 3.20: Schematic diagram of arcing in a submerged-arc furnace

cavities, and the term **submerged-arc** alludes to the presence of arcing in the cavities. The distortion of the electrical waveforms was considerably smaller than in open-arc furnaces, and decreased with higher cavity temperatures (Otani et al., 1968). The electric conduction in the charge burden of ferrosilicon furnaces was established by Zherdev et al. (1968), who found an increasing charge current density towards the electrodes and towards the cavities, and the charge current density decreased with increasing silicon content. Further studies on arcing in such furnaces, evaluated by Müller (1969) and Müller, Olsen and Tuset (1972), confirmed these results.

In a submerged-arc ferrosilicon furnace the electrodes are submerged into the furnace burden and cavities are formed around the electrode tips as a result of heavy heat generation. In these cavities the electric currents form arcs between the electrodes and the molten pools in the cavities and/or the cavity walls, as shown in Fig. 3.20. In addition to the arc conductance, parallel currents are present in the charge around the cavities. Since the arcs occur in the cavities, they cannot be observed directly in a production furnace, and only indirect measurements are available because of the current paths in the furnace. The arcing conditions in the cavities can be compared with the "hot" conditions in an open-arc furnace. The cavity atmosphere is ionized and stable arcs are expected. The current and voltage waveforms are less distorted than in "hot" open-arc furnace conditions. This could be a result of more ionization in the cavities as a result of higher temperatures and different gas compositions, but the ohmic conductance in parallel to the arcs will also reduce the distortion effect.

The electrical conditions and the presence of arcing in submerged-arc furnaces in which slag are formed, have been investigated among others by

Channon, Urquhart and Howat (1974), Urquhart, Jochens and Howat (1974) and Stewart (1980). They found that the appearance of cavities around the electrode tip and the presence of arcing between the electrode the coke bed, depend on the applied electrode voltage, the current density and charge temperature. At low voltages only ohmic conductance was present, but as the voltage increases, arcing could occur above a critical voltage. Such furnaces are usually operated below this critical voltage, and therefore the electrical conductance is mainly ohmic, but some arcing will occur, especially during the tapping of the furnaces. The presence of arcing is not desirable in furnaces designed for resistive heating and should be avoided because it results in reduced power generation at a given voltage and creates power imbalance in the furnace. Anyway, it can be concluded that the term **submerged-arc furnaces** misrepresents the conditions in furnaces with slag processes, since the main electric conductance is pure ohmic.

3.6 Model descriptions of DC electric arcs

3.6.1 Analytic model of DC arc columns

A large number of analytic models of free-burning DC arc columns have been presented in recent years, among others by Edels (1973), Pfender (1978), Jones and Fang (1980), Szekely and McKelliget (1981), Ushio, Szekely and Chang (1982), Sanders et al. (1982), McKelliget and Szekely (1983), Hsu, Etemadi and Pfender (1983) and Ahlers (1988). Appendix A.2 outlines the principle of these arc model descriptions, which generally consist of the following equations:

1. Equations describing equilibrium thermodynamics.

2. Conservation equations for mass, motion and energy of the plasma fluid (Szekely and Themelis (1970), modified to to include effects of the Lorentz force, radiation transport and Joule power input.

3. Maxwell's equations.

4. The generalized Ohm's law for partly ionized gases.

5. The radiation energy transport equations.

The various models are based on slightly different assumptions. Appendix A.2 describes a model which is based mainly on the work of Ushio, Szekely and Chang (1982), Sanders et al. (1982), McKelliget and Szekely (1983) and Hsu, Etemadi and Pfender (1983).

Reported simulation studies

Ushio, Szekely and Chang (1980) and Szekely and McKelliget (1981) investigated heat and fluid flow phenomena in high-current DC arc column, while McKelliget and Szekely (1983) focused on the cathode region of a high-intensity carbon arc. The models were similar to the model in Eqs A.24-A.42 in App. A.2, and they found that the simulation results were in good agreement with published measurements of Bowman, Jordan and Fitzgerald (1969), Jordan, Bowman and Wakelam (1969) and Bowman (1972).

Hsu, Etemadi and Pfender (1983) compared the results of model simulation with studies of high-intensity free-burning low-current argon arc, and the model shows good agreement with the experimental data.

The conditions in the anode region of a free-burning DC arc have been the subject to investigations by Pfender (1978) and Sanders et al. (1982). They developed a model restricted to the flow-affected zone of the anode region and compared the results of the model simulations with experiments. This region, as any other part of the arcs, is governed by the similar conservation equations as the model described in Eqs A.24-A.42 in App. A.2. Any attempt to solve these equations for the anode region, faced three major problems (Pfender, 1978):

1. The conventional conservation equations only apply as long as the continuum approach is valid. In the anode sheath this is not longer valid.

2. The necessary assumption of LTE conditions is not valid for the whole anode region.

3. The specification of realistic boundary conditions is difficult.

The model simulations yield results in accordance with the experiments, which has previously been discussed when focusing the anode flow phenomena in Section 3.4.2.

3.6.2 Channel models for DC arcs

An exact calculation of the electric arc properties is in principle possible using the model given in Eqs. A.24-A.42 in App. A.2, consisting of coupled partial differential equations, and with proper boundary conditions. However, according to Ahlers and Timm (1987b) and Ahlers (1988), the solution of this model equations is complicated by various physical effects and their influence on the model parameters and the boundary conditions:

1. The model parameters depend on the temperature in an extreme nonlinear manner, and in addition, correct values for these parameters can hardly be found for models describing arcs in electric furnaces.

2. Optical thick radiation must be considered since the radiative absorption within the arc column is not negligible. Furthermore, the radiative emission and absorption depend on the radiative wave lengths as well as the plasma temperature. This implies that several differential equations are necessary to describe the radiation effects properly.

3. The electrode regions have significant influence on the plasma conditions in the arc column. Vaporization of the electrode materials and the presence of vapor jets within the arc column affect the temperature and electrical conductivity, but such effects have not been considered in the model. Furthermore, the anode and cathode voltage drops must be taken into consideration in addition to the model of the arc column.

4. Proper boundary conditions of the model equations can hardly be found for practical cases such as arcing in electric furnaces. The reported applications of such models are either pure simulation studies or modelling of well-known experimental arc furnaces, focusing mainly of different region of an electric arc (Pfender, 1978; Ushio, Szekely and Chang, 1980; Sanders et al., 1982; McKelliget and Szekely, 1983; Hsu, Etemadi and Pfender, 1983).

Thus, such models seem impractical for the description of arcing in industrial electric furnaces.

A simplification to the model in App. A.2, is the introduction of so-called **channel models**. Channel models for DC arcs have been developed among others by Latham (1980), Sakulin (1981a, 1982a, 1982c), Ahlers and Timm (1987a, 1987b) and Ahlers (1988). Channel modelling makes use of a more global consideration of the arc and simplifies the description of important physical effects. Arc channel models are based upon the assumption of an ionized gas channel symmetrical around the arc axis. Various assumptions can be made about the conditions within the arc channel. In the most simple case homogeneous conditions are assumed, but others such as parabolic distribution models can also be applied (Hoyaux, 1968). In the following homogeneous conditions are assumed within the arc channel.

The main problem involved with channel modelling, is the choice of the arc channel radius, because the channel model equations do not prevail any expression for it. This problem can be solved by introducing the Steenbeck's

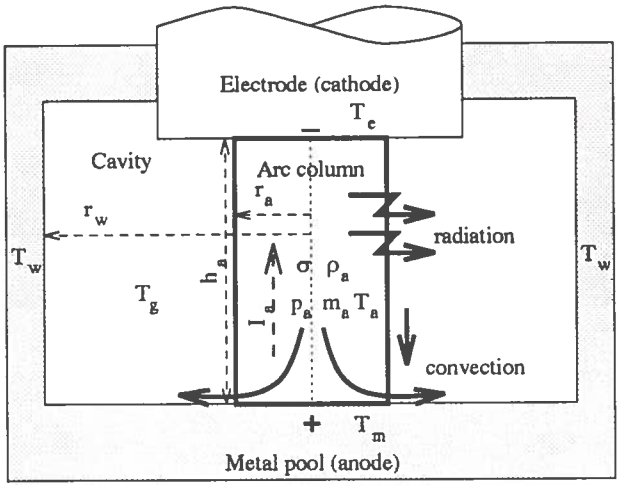

Figure 3.21: Channel model of a DC arc.

minimum principle or the principle of minimum arc power, which states that the arc resistance "adjusts itself" by altering the arc radius and temperature to minimize the power dissipation in the arc (Hoyaux, 1968).

The principle of arc channel modelling is illustrated in Fig. 3.21 for the case of a high-current arc in an electric furnace. The arc column is considered to be an electrically conducting cylindrical channel with radius r_a and height h_a, with an imaginary wall that can be moved radially. The arc channel is surrounded by an "outer wall", which can represent the furnace wall in an open-arc furnace or the cavity wall in a submerged-arc furnace. Homogeneous conditions are assumed within the channel, and the arc temperature T_a, the electrical conductivity σ_a, the pressure p_a and the mass density ρ_a, are constant. Furthermore, no electrical conduction occurs outside the arc channel. However considerable energy transport is present in the region between the arc channel and the outer wall. The temperature at the outer wall is denoted T_w, while $T_e = T_C$ represents the temperature at the cathode surface, and $T_m = T_A$ represents the temperature at the anode surface. From an electrical point of view, the arc is treated as an electric circuit element with the voltage drop:

$$V_a = V_A + V_C + R_a I_a \tag{3.70}$$

where V_A and V_C represent the anode and cathode voltage drops, respectively, I_a is the arc current, and R_a is the corresponding electrical resistance of the arc column. In the channel model description the arc resistance is

represented by:

$$R_a = \frac{h_a}{\pi \, {r_a}^2 \, \sigma_a(T_a)} \tag{3.71}$$

where the electrical conductivity of the arc plasma σ_a is given by:

$$\sigma_a(T_a) = c_1 \, {T_a}^{c_2} \, \mathrm{e}^{-c_3/T_a} \tag{3.72}$$

which is the expression derived in Eq. 3.16 and where the constants c_1, c_2 and c_3 depend on the arc plasma composition.

An arc channel model consists in principle of the same mass and energy conservation equations, thermodynamic state equations and Joule's law, as the partial differential equation model in Section 3.6.1, but the equations become significantly simplified as a result of the channel assumptions. The energy conservation equation expressed as a power balance, plays the most important role in arc channel modelling, together with the arc power minimization to determine the arc radius and the arc temperature.

Power balance

For a static DC arc, the power balance is satisfied:

$$P_{in} = P_{out} \tag{3.73}$$

which means that the supplied electrical power to the arc P_{in}, is transformed into heat and emitted to the surroundings P_{out}.

The electrical power input to the arc is:

$$P_{in} = R_a {I_a}^2 + (V_A + V_C) \, I_a \tag{3.74}$$

where the arc resistance is given in Eq. 3.71, and V_A and V_C represent the anode and cathode voltages, respectively. These voltages are modeled as constants depending on the material properties of the electrode and the metal pool. Compared to the energy balances for the cathode and anode regions in Eqs. 3.67 and 3.69, the anode working function term is included into the anode voltage term in Eq. 3.74, and the ionization potential term is included in the cathode voltage term in Eq. 3.74.

The main power abduction mechanisms from an electric arc:

- Radiation
- Convection

- Conduction

have previously been discussed in Section 3.2.2. These heat transfer mechanisms depend on the kind of the present arc and the arcing conditions. Sakulin (1982a) discussed the power abductions mechanisms from an arc column and focused especially on how these effects can be modeled and included in a channel model descriptions. According to Ahlers (1988), conventional convective heat transfer to the surroundings, as well as conduction effects, are negligible when considering high-intensity high-current arcs, and the power output from the arc channel is mainly governed by radiation and convection as a result of the plasma jet flow, besides heat transfer to the anode and cathode. Thus, the power abduction can be stated as:

$$P_{out} = P_R + P_F + P_{AC} \tag{3.75}$$

where P_R represents radiative emission and P_F convective heat losses due to the jet flow, and P_{AC} heat transfer to the anode and cathode.

1. **Radiation.** A part of the emitted radiation will be re-absorbed within the arc column and the radiation consists of both optically thin and optically thick radiation. According to Ahlers and Timm (1987b) and Ahlers (1988), the heat flow due to radiation can be expressed as:

$$P_R = \dot{q}_R \, 2\pi h_a \, l_R \left[\frac{r_a}{l_R} - 1 + \mathrm{e}^{-r_a/l_r} \right] \tag{3.76}$$

where the radiative power density $\dot{q}_{rad}(T_a, p_a)$ depends on the arc temperature, pressure and plasma composition, and where the radiative absorption length is represented by l_R.

2. **Convection.** The convective energy flow is mainly a result of the mass jet flow from the cathode to the anode in the arc column. This mass flow $\dot{m}_a$ can be expressed by Eq. 3.58, or alternatively Eq. 3.60. It can usually be assumed that the arc temperature is considerable higher than the cavity gas temperature: $T_a \gg T_g$. Therefore, the heat convection from the arc can be expressed as:

$$\begin{aligned} P_F &= c_p \, \dot{m}_a \, (T_a - T_g) \\ &= \frac{1}{3} \, c_p \, \sqrt{2 \, \mu_0 \, \rho_a \, \pi \, j_C} \, \sqrt{I_a} \, {r_a}^2 \sqrt{1 - \left(\frac{r_C}{r_a} \right)^2} \, (T_a - T_g) \end{aligned} \tag{3.77}$$

where the plasma enthalpy is expressed as:

$$\mathrm{d}H_a = m_a \, c_p \, \mathrm{d}T_a \tag{3.78}$$

3. **Anode and cathode heat transfer.** The heat transfer mechanisms due to the anode voltage drop and the anode working function, and the cathode voltage drop and the plasma ionization potential, are taken into account in the power input expression in Eq. 3.74. The remaining heat transfer effects in the anode and cathode regions are results of the Thompson effect as described in Eqs. 3.67 and 3.69. This can be described as a current-dependent convective heat transfer effect (Ahlers and Timm, 1987b; Ahlers, 1988):

$$\begin{aligned} P_{AC} &= \pi r_a^2 \frac{5}{2}\frac{k_B}{e} I_a \{(T_a - T_A) + (T_a - T_C)\} \\ &= \pi r_a^2 \alpha_A(I_a)(T_a - T_A) + \pi r_a^2 \alpha_C(I_a)(T_a - T_C) \end{aligned} \quad (3.79)$$

where $\alpha_A(I_a)$ and $\alpha_C(I_a)$ represent the current-dependent convective heat transfer coefficients to the anode and cathode, respectively.

Arc power minimization

The electrical power input given in Eq. 3.74, is dependent on the arc radius and temperature through their influence on the resistance and electrical conductivity, and hence:

$$P_{in} = f_1(r_a, T_a) \quad (3.80)$$

The total power output given in Eq. 3.75, will depend on the arc radius and temperature and can generally be expressed as:

$$P_{out} = f_2(r_a, T_a) \quad (3.81)$$

The arc resistance is expressed in terms of the arc radius and temperature by using Eqs. 3.71 and 3.72. The power balance in Eq. 3.73 makes it possible to derive a functional dependence between the arc radius and the temperature:

$$T_a = f_3(r_a) \quad \text{or} \quad r_a = f_4(T_a) \quad (3.82)$$

and thus the arc voltage in Eq. 3.70 can be expressed in terms of the arc radius or temperature.

The arc power minimization in accordance with Steenbeck's minimum principle, which is treated in detail by Sakulin (1981, 1982a), can be outlined as follows:

The power input and output is minimized with respect to the arc channel radius and temperature:

$$\min_{T_a, r_a} P_a \Rightarrow \begin{cases} \partial P_{in}/\partial T_a + \partial P_{in}/\partial r_a = 0 \\ \partial P_{out}/\partial T_a + \partial P_{out}/\partial r_a = 0 \end{cases}$$

$$\Rightarrow T_a^*(r_a^*) \tag{3.83}$$

where the arc temperature is chosen as the independent variable, and where $T_a^*(r_a^*)$ characterizes the arc power minimum. The minimization can be evaluated by an analytic or geometric solution procedure (Sakulin, 1982a).

DC arc channel simulation model

The DC arc channel model described above, makes it possible to calculate current-voltage characteristics for DC arcs and analyzes the effects of variation in various arcing conditions, such as arc length and conductivity. Ahlers and Timm (1987a, 1987b) and Ahlers (1988) analyzed the arcing conditions in an open-arc DC furnace by experimental investigations and developed channel model descriptions for different furnace operation stages.

3.7 Dynamic models of AC arcs

Dynamic arc characteristics

The dynamic characteristics of electric arcs are treated among others by Browne (1955) and Norden (1980). The AC arc operation mode can be analyzed by studying changes in the arc current in the static operation mode. At slow arc current changes the arc voltage drop will follow the static voltage-current characteristic, which is previously discussed in Section 3.1.2. With more rapid changes of the arc current, hysteresis effects become more evident, and the transient arc voltage will depart from the static characteristic by an amount dependent on the rate of the current change and the arc nature and properties. The difference between the dynamic characteristic:

$$v_a = f(i_a)$$

and the static characteristic:

$$V_a = f(I_a)$$

is a result of dynamic thermal effects of the arc plasma. A change in the arc current, at otherwise constant arcing conditions, results with time, in changes in the arc temperature and thus the electrical conductivity of the arc. According to Browne (1955). there is a critical frequency of the current alternation, for which the dynamic arc fails to follow the static characteristics. However. the common frequencies of AC furnace operations, 50 or 60 Hz, are far below the critical frequency of high-current arcs. Such arcs will follow the corresponding static characteristic rather closely,

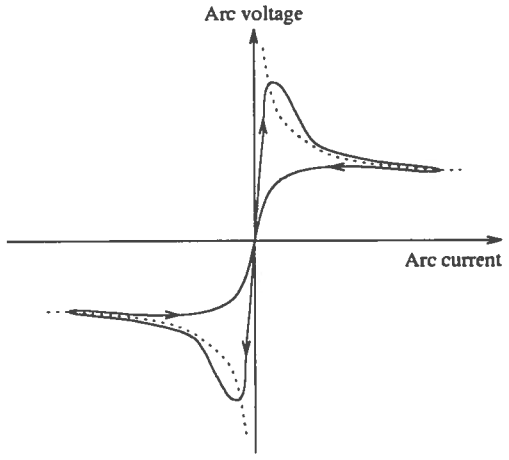

Figure 3.22: Dynamic current-voltage characteristic of an electric arc and the corresponding static characteristic.

except in the vicinity of current zero, where the voltage reversal occurs. Figure 3.22 shows the principal dynamic current-voltage characteristic in a low-frequency arc, together with the corresponding static characteristics for the two half-periods. Except for a short period after zero current, the dynamic arc voltage is larger than the static characteristic at increasing current and lower than the static characteristic at decreasing current:

$$\begin{aligned} v_a < V_a \quad &\text{for} \quad \frac{di_a}{dt} < 0 \\ v_a > V_a \quad &\text{for} \quad \frac{di_a}{dt} > 0 \end{aligned} \tag{3.84}$$

Considering the half-period when the arc voltage and current are positive, the dynamic characteristics can be explained as follows:

The relative slow increase in arc current after zero passing is due to the fact that the "old" ionization of the arc plasma from the previous period has disappeared, and thereby the electrical conductivity is low. Therefore, a "new" ionization of the arc column is necessary, which in time, is obtained by Joule heating. This leads to a "delayed" dynamic characteristic and there is a "deficiency" of ionization compared to the static case, resulting in a higher dynamic arc voltage until current maximum is achieved. When the current decreases towards zero, the opposite prevails, and there is an "excess" of ionization compared to the static case, and the dynamic arc voltage is therefore lower than in the static case.

Electric arc furnaces operate as very high arc currents, and the correspond-

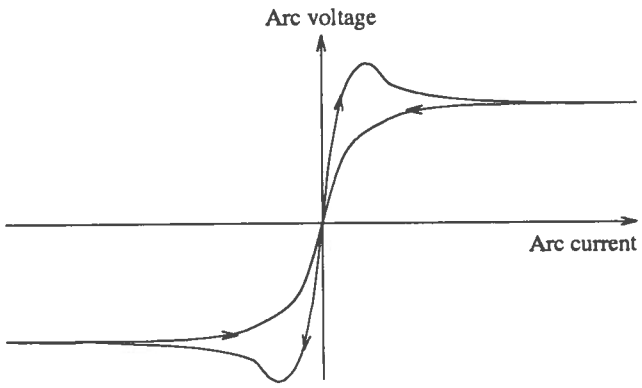

Figure 3.23: Dynamic current-voltage characteristic of arcing in electric furnaces.

ing static current-voltage characteristics are almost flat, as discussed in Section 3.1.2. Therefore, the dynamic characteristic in Fig. 3.22 hardly represents current-voltage characteristics that are expected for arcing occurring in electric furnaces. A more typical dynamic arc characteristic for electric arcs is shown in Fig. 3.23, which is based on measurements reported by Norden (1980). It should however be stressed that this would be an ideal dynamic characteristic of an arc in an electric furnace, since the arcing conditions are usually heavily disturbed.

3.7.1 Empirical dynamic models for AC arcs

Dynamic model descriptions of electric arcs have been developed based on the fact that the dynamic arc characteristic tries to follow the corresponding static arc characteristic. Such models can be denoted as **phenomenological models** or **empirical models**, since they attempt to describe the observed electrical arcing phenomena. Such models contrast to **physical models**, based on "first principles", that describe the physical processes involved in the arc to some extent.

Empirical arc models are treated among others by Browne (1955) and Norden (1980). The models describe the electric arc as an electrical circuit element, characterized by the arc voltage v_a, the arc current i_a, and the arc resistance per length unit $\hat{R}_a$ or equivalently, the arc conductance per length unit $\hat{G}_a = 1/\hat{R}_a$. The two most common empirical models are **Cassie's model** and **Mayr's model**, both originally derived around 1940, but several other model proposals and combinations of models exist. This is further treated by Norden (1980). Cassie's model is suitable to describe high-current AC arcs and can be applied to the simulation of arcing in

an electric furnace, while Mayr's model is best suitable for descriptions of low-current AC arcs or investigations of arc conditions near current zero-passing.

Cassie's model for AC arcs

Cassie's model describes the electric arc as a circuit element by using the electrical conductance per length unit $\hat{G}_a$. The derivation of Cassie's model as well as Mayr's model, is based on an assumption that the change with time in the inner energy per length unit of the arc $\hat{U}_a(t)$, is equal to the difference between the electrical power input per length unit $\hat{P}_{in}(t)$, and the power dissipation per length unit in the arc column $\hat{P}_{out}(t)$:

$$\frac{d\hat{U}_a(t)}{dt} = \hat{P}_{in}(t) - \hat{P}_{out}(t) \tag{3.85}$$

Cassie's model is further based on the assumptions of a convection-dominated arc as a result of the axial plasma flow, and that the arc cross section is proportional to the arc current at constant temperature. The electrical power input to the arc column per length unit is given as:

$$\hat{P}_{in}(t) = E_a(t) i_a(t) \tag{3.86}$$

where E_a is the electrical field strength equivalent to the voltage drop per length unit. This yields:

$$\frac{d\hat{U}_a(t)}{dt} = E_a(t) i_a(t) - \hat{P}_{out}(t) \tag{3.87}$$

It is further assumed that the characteristic arc conductance is proportional to the inner energy content of the arc:

$$\hat{G}_a(t) = g_0 \, \hat{U}_a(t) \tag{3.88}$$

where g_0 is a constant, and that the power dissipation per length unit in the arc can be described by:

$$\hat{P}_{out}(t) = E_0 \, i_a(t) = E_0{}^2 \, \hat{G}_a(t) \tag{3.89}$$

where E_0 is a constant that can be looked upon as the electric field strength in a corresponding static arc. By inserting Eqs. 3.88 and 3.89 into Eq. 3.87, the Cassie's model equation is obtained:

$$\frac{1}{\hat{G}_a(t)} \frac{d\hat{G}_a(t)}{dt} = \frac{1}{\tau_a} \left[\left(\frac{E_a(t)}{E_0} \right)^2 - 1 \right] \tag{3.90}$$

where τ_a represents a time constant characterizing the arc dynamics:

$$\tau_a = \frac{1}{g_0 \, E_0{}^2} \tag{3.91}$$

This time constant expression can be derived from the proportion between the energy excess and the power dissipation per length unit of the arc length:

$$\tau_a = \frac{\text{energy excess}}{\text{power dissipation}} = \frac{\hat{G}_a / g_0}{E_0{}^2 \, \hat{G}_a} = \frac{1}{g_0 \, E_0{}^2} \tag{3.92}$$

An equivalent expression to Eq. 3.90 can be derived by inserting the characteristic arc resistance $\hat{R}_a$:

$$\frac{d\hat{R}_a(t)}{dt} = \frac{1}{\tau_a} \left[1 - \left(\frac{E_a(t)}{E_0} \right)^2 \right] R_a(t) \tag{3.93}$$

and the total arc column resistance becomes:

$$R_a(t) = h_a \, \hat{R}_a(t) \tag{3.94}$$

The steady-state version of Cassie's model in Eq. 3.90 or Eq. 3.93 yields:

$$\begin{aligned} E_a &= E_0 \\ V_a &= h_a \, E_a = h_a \, E_0 \end{aligned} \tag{3.95}$$

where V_a is the total arc voltage and h_a is the arc length. By comparing this expression with the Nottingham equation in Eq. 3.7, we see that Cassie's model in the stationary case corresponds to the Nottingham equation for high-current arc columns, which is given in Eq. 3.8. It should be stressed that Cassie's model only describes the arc column electrical characteristics, and that the voltage drop in the anode and cathode regions are not taken into consideration in the model. Therefore, it is necessary to extend Cassie's model with a description of the anode and cathode regions in order to get a complete description of the arc.

The advantage of Cassie's model is its simplicity. It consists of only two equations Eqs. 3.93 and 3.94, and it uses only three model parameters, the time constant τ_a, the static electric field strength E_0, and the arc length h_a, which can rather easily be adjusted so that the model produces the desired dynamic characteristic. Furthermore, Cassie's model is suitable to describe the dynamics effects of high-current arc circuits, such as electric furnaces, and it can easily be implemented in a transient simulation model of an electrical circuit. Norden (1980) analyzed the electrical conditions in an open-arc furnace by using a slightly modified version of Cassie's model and identified the model parameters from furnace measurement data.

3.7.2 Channel models for AC arcs

Dynamic models of AC electric arcs based on modified versions of the DC arc channel model descriptions, have been developed by Sakulin (1980, 1981b, 1982b, 1982c) and Pfeifer, Fett and Bebber (1989). The dynamic channel models are based on assumptions similar to the DC arc channel models presented in Section 3.6.2 and App. A.2.

The AC electric arc is considered to be an electrically conducting cylindrical channel with homogeneous conditions. The arc voltage is thereby given as:

$$v_a(t) = v_A(t) + v_C(t) + R_a(t) i_a(t) \tag{3.96}$$

and the arc resistance and conductivity are given by:

$$R_a(t) = \frac{h_a(t)}{\pi\, r_a(t)^2\, \sigma_a(T_a(t))} \tag{3.97}$$

$$\sigma_a(T_a(t)) = c_1\, T_a(t)^{c_2}\, \mathrm{e}^{-c_3/T_a(t)} \tag{3.98}$$

Since the arc channel model only takes the arc column into account, the anode and cathode voltages have to be considered separately. A simple model of the anode and cathode voltages is to consider them as constants within the electric half-periods:

$$v_A(t) = \begin{cases} v_{Ae}, & i_a(t) > 0 \\ v_{Am}, & i_a(t) < 0 \end{cases} \quad v_C(t) = \begin{cases} v_{Cm}, & i_a(t) > 0 \\ v_{Ce}, & i_a(t) < 0 \end{cases} \tag{3.99}$$

where v_{Ae}, v_{Am}, v_{Cm} and v_{Ce} represent the different anode and cathode voltages in the two half-periods. These voltages are dependent on the material properties of the electrode and the metal pool.

The instant power equilibrium of the AC arc channel:

$$P_{in}(t) = P_{out}(t) \tag{3.100}$$

in contrast to DC arcing equilibrium in Eq. 3.73, will not be fulfilled at every moment, but the energy balance will be satisfied for the electrical period T:

$$\int_t^{t+T} P_{in}(\tau)\, d\tau = \int_\tau^{\tau+T} P_{out}(\tau)\, d\tau \tag{3.101}$$

and the changes in the inner energy U_a or enthalpy H_a stored in the arc channel, must be considered in the instant power balance.

Sakulin's AC arc channel model (Sakulin, 1981b, 1982b, 1982c)

Sakulin takes his starting-point in the following instant power balance:

$$\frac{dU_a(t)}{dt} = P_{in}(t) - P_{out}(t) - p_a \frac{dV_a}{dt} + P_m(t) \tag{3.102}$$

where p_a is the arc channel pressure, V_a is the arc volume, and P_m represents power transfer due to arc mass variations. The power balance in Eq. 3.102 can alternatively be expressed in terms of the arc enthalpy H_a:

$$\frac{dH_a(t)}{dt} = P_{in}(t) - P_{out}(t) + P_m(t) \tag{3.103}$$

The electrical power input is equivalent to the corresponding term in Eq. 3.74 in the DC arc channel model:

$$P_{in}(t) = R_a(t) i_a(t)^2 + [v_A(t) + v_C(t)]\ i_a(t) \tag{3.104}$$

The power output expression will be equivalent to the corresponding terms in the DC channel model given in Eqs. 3.75 to 3.79. Depending on how the power abduction phenomena are modeled, the AC channel model describes different arcing conditions, as discussed in Sakulin (1982a). Sakulin (1981b, 1982b, 1982c) neglected the effects of the electromagnetic induced plasma flow and stated the following heat transfer description:

$$P_{out}(t) = P_R(t) + P_L(t) + P_F(t) \tag{3.105}$$

where P_R denotes radiative, P_L conductive and P_F convective heat transfer.

1. **Radiation.** The radiation is treated as optically thick, and possible gray radiation, with the possibility of reflection from the outer wall:

$$P_R = 2\pi r_a(t) h_a(t) \frac{\epsilon_a\, c_{SB}}{1 + r_a(t)/r_w\, \epsilon_a\, (1/\epsilon_w - 1)} \tag{3.106}$$

$$\cdot \left[T_a(t)^4 - T_w(t)^4\right] \tag{3.107}$$

where c_{SB} is Stefan-Boltzmann's constant, and ϵ_a and ϵ_w are the emissitivity of the arc channel and the outer wall, respectively, and T_w is the outer wall temperature. Furthermore, line radiation could be considered (Sakulin, 1982c).

2. **Conduction.** Heat conduction is considered through the cylindrical lateral area and also through top and bottom plates to the anode and cathode:

$$\begin{aligned} P_L(t) = & \frac{2\pi h_a(t)}{\ln(r_w/r_a(t))}\,\lambda_w \cdot [T_a(t) - T_w(t)] \\ & +2\pi r_a(t)\,\lambda_A \cdot [T_a(t) - T_A(t)] \\ & +2\pi r_a(t)\,\lambda_C \cdot [T_a(t) - T_C(t)] \end{aligned} \tag{3.108}$$

where λ_w, λ_A and λ_C are the thermal conductivity of the thermal layer surrounding the arc channel, the anode and the cathode, respectively; and T_A and T_C are the anode and cathode temperatures, respectively.

3. **Convection.** The heat convection from the arc channel is described by two terms:

$$P_F(t) = P_{F\,1} + P_{F\,2} \tag{3.109}$$

The first term represents convection between the arc channel wall and its surroundings:

$$P_{F\,1}(t) = 2\pi r_a(t) h_a(t)\,\alpha_a \cdot [T_a(t) - T_g(t)] \tag{3.110}$$

where α_a is the convective heat transfer coefficient.

The convection effect due to the plasma flow, is described by an arc current-dependent term:

$$P_{F\,2}(t) = \beta_a\, i_a(t)^2 \cdot [T_a(t) - T_g(t)] \tag{3.111}$$

where β_a represents the plasma flow convection coefficient.

It is further assumed that the thermodynamic state variations are quasi-stationary and isobaric, that the specific heat capacity c_p is constant, and that the thermodynamic state equation can be used:

$$p_a(t)\,V_a(t) = m_a(t)\,R\,T_a(t) \tag{3.112}$$

where R is the molar mass constant. The arc channel radius is thus related to temperature by:

$$r_a(t) = \sqrt{\frac{m_a(t)\,R\,T_a(t)}{p_a\,\pi\,h_a(t)}} \tag{3.113}$$

and the arc channel enthalpy can be expressed in terms of the arc temperature:

$$dH_a(t) = c_p\, d\left(m_a(t)\, T_a(t)\right) \tag{3.114}$$

The power balance in Eq. 3.103 can therefore be written as:

$$\frac{dT_a(t)}{dt} = \frac{1}{c_p\, m_a(t)} \left[P_{in}(t) - P_{out}(t) + P_m(t)\right] \tag{3.115}$$

The heat transfer due to arc mass variation is described as:

$$P_m(t) = \begin{cases} c_p \frac{dm_a(t)}{dt}\, T_g(t) & \text{for } \frac{dm_a(t)}{dt} > 0 \\ c_p \frac{dm_a(t)}{dt}\, T_a(t) & \text{for } \frac{dm_a(t)}{dt} < 0 \end{cases} \tag{3.116}$$

where T_g is the surrounding gas temperature. An alternative representation is given by:

$$P_m(t) = c_p \frac{dm_a(t)}{dt} \cdot \frac{1}{2} \left[T_a(t) + T_g(t)\right] \tag{3.117}$$

which describes turbulent mass transfer through the channel wall (Sakulin, 1982b).

According to Sakulin (1982c), the dynamic arc tries to fulfill the principle of minimal arc power at every moment. The power equilibrium cannot be reached, and thus the mass variation in the arc within the electrical periods will follow the principle of minimum arc power. Sakulin (1981b, 1982b, 1982c) therefore proposed an imaginary arc mass controller to describe the arc mass variations:

$$\frac{dm_a(t)}{dt} = k_m \cdot \left[T_a(t) - T_a^*(t)\right] \tag{3.118}$$

where k_m is the "controller gain", and T_a^* represents the temperature corresponding to the arc power minimization characteristic in Eq. 3.83. This mass modelling strategy involves arc power minimizations at every time-step in the simulation of the model.

Sakulin's simplified arc channel model (Sakulin, 1980)

The AC arc channel model will be significantly simplified if a constant arc mass is assumed (Sakulin, 1980). The arc mass could for instance be chosen to be equal to the corresponding arc power minimum calculated at the rms values of the applied arc current and voltage. The thermodynamic state equation then becomes:

$$p_a(t)\, dV_a(t) = m_a(t)\, R\, dT_a(t) \tag{3.119}$$

By combining this with the power balance in Eq. 3.115, the following expression of the channel radius is obtained:

$$\frac{dr_a(t)}{dt} = \frac{1}{2\pi\, r_a(t)\, h_a(t)\, c_p/R\, p_a}\,[P_{in}(t) - P_{out}(t) + P_m(t)] \quad (3.120)$$

and the temperature is found from the thermodynamic state equation in Eq. 3.119:

$$T_a(t) = \frac{\pi r_a(t)^2 h_a(t)\, p_a(t)}{m_a\, R} \quad (3.121)$$

or alternatively:

$$T_a(t) = T_a{}^* \frac{V_a(t)}{V_a{}^*} = T_a{}^* \frac{r_a(t)^2 \pi\, h_a(t)}{r_a{}^{*2} \pi\, h_a{}^*} \quad (3.122)$$

where $V_a{}^*$, $T_a{}^*$ and $r_a{}^*$ correspond to characteristic arcing conditions, for instance the arc power minimum at rms-values of applied arc current and voltage.

Pfeifer's AC arc channel model (Pfeifer, Fett and Bebber, 1989)

A slightly modified version of Sakulin's channel model is proposed by Pfeifer, Fett and Bebber (1989). The model is based on an instant power balance equivalent to Eq. 3.103:

$$\frac{dH_a(t)}{dt} = \frac{dU_a(t)}{dt}\, m_a(t) + U_a(t)\, \frac{dm_a(t)}{dt}$$

$$\frac{dH_a(t)}{dt} = P_{in}(t) - P_R(t) - P_F(t) \quad (3.123)$$

$$= P_{in}(t) - P_R(t) + H_{in}(t)\,[\dot{m}_a(t)]_{in} - H_{out}(t)[\dot{m}_a(t)]_{out} \quad (3.124)$$

where H_{in} and H_{out} are the enthalpy contents in the gas flowing in and out of the arc channel, and $[\dot{m}_a]_{in}$ and $[\dot{m}_a]_{out}$ represent the mass in- and outflow.

By inserting the relationship between the enthalpy and temperature in Eq. 3.114 into Eq. 3.123, the following temperature description is obtained:

$$\frac{T_a(t)}{dt} = \frac{1}{c_p\, m_a(t)}\,[P_{in}(t) - P_R(t) + [H(t)\,\dot{m}_a(t)]_{in} - [H(t)\,\dot{m}_a(t)]_{out}] \quad (3.125)$$

where the two last terms represent the convective heat flow P_F. The input power expression P_{in} is similar to Eq. 3.104, while Pfeifer, Fett and Bebber (1989) use the radiative power transfer description proposed by Ahlers (1988) in Eq. 3.76:

$$P_R(t) = \dot{q}_R(t)\, 2\pi h_a(t)\, l_R \left[\frac{r_a(t)}{l_R} - 1 + \mathrm{e}^{-r_a(t)/l_r}\right] \tag{3.126}$$

The convective heat transfer is expressed similarly to Eq. 3.77 in the DC channel model. It is assumed that the arc channel temperature is significantly higher than the surrounding gas temperature, and thus the effect of the enthalpy content in the instreaming gas can be neglected. This yields:

$$P_F(t) \approx (H(t)\, \dot{m}_a(t))_{out} \tag{3.127}$$

The plasma mass flow rate is expressed as:

$$\dot{m}_a(t) = \rho_a\, \pi\, r_a(t)^2 \bar{v}_a(t) \tag{3.128}$$

where a constant mass density ρ_a is assumed, and where $\bar{v}_a$ is the averaged flow velocity, which is given by:

$$\frac{d\bar{v}_a(t)}{dt} = \frac{1}{m_a(t)} \left[F_L(t) - \rho_a\, \pi\, r_a(t)^2 \bar{v}_a(t)^2\right] \tag{3.129}$$

where F_L represents the pinch force necessary to accelerate the entering mass flow:

$$F_L(t) = \dot{m}_a(t)\, \bar{v}_a(t) = \frac{1}{2}\, \rho_a\, \pi\, r_a(t)^2\, v_{max}(t)^2 \tag{3.130}$$

and v_{max} can be found from Eq. A.22 or Eq. 3.52. The mass variation in the arc channel is described similarly to Eq. 3.118:

$$\frac{dm_a(t)}{dt} = \frac{1}{\Delta t_m} \left[m_a{}^*(t) - m_a(t)\right] \tag{3.131}$$

where Δt_m represents the arc mass time constant, and $m_a{}^*$ represents arc the mass corresponding to the stationary mass at the arc power minimum given by Eq. 3.83. The arc mass is related to the arc dimensions by:

$$m_a(t) = \rho_a(t)\, \pi r_a(t)^2 h_a(t) \tag{3.132}$$

3.7.3 A dynamic simulation model of AC arc columns

A dynamic simulation model of AC arcs has been developed based on Sakulin simplified model (Sakulin, 1980) and Pfeifer's model (Pfeifer, Fett and Bebber, 1989). The model has been derived by a further assumption of a constant mass in the arc channel in Pfeifer's model, similarly to Sakulin's simplified model. The arc mass m_a, and the arc radius r_a, are assumed to correspond to the arc power minimum calculated at the rms values of the applied arc current and voltage.

The arc temperature is described by combining Eqs. 3.125 and 3.127, and the instant energy balance can be expressed by:

$$\frac{\mathrm{d}T_a}{\mathrm{d}t} = \frac{1}{m_a\, c_p}\left[P_{in}(t) - P_R(t) - P_F(t)\right] \tag{3.133}$$

and where the power input P_{in} is given by Eq. 3.104, and the radiation terms are given by Eq. 3.126.

The convective effect due to the plasma flow is given by Eq. 3.127:

$$\begin{aligned} P_F(t) &\approx \left(H(t)\,\dot{m}_a(t)\right)_{out} \\ &= c_p\,\dot{m}_a(t)\,\left[T_a(t) - T_g(t)\right] \end{aligned} \tag{3.134}$$

The plasma mass flow rate is expressed similarly to Eq. 3.128:

$$\dot{m}_a(t) = \rho_a\,\pi\,{r_a}^2\bar{v}_a(t) \tag{3.135}$$

This can be expressed as previously derived in Eq. 3.60:

$$\dot{m}_a(t) = \frac{1}{2}\,{r_a}^2\sqrt{\frac{5}{6}\,\frac{\mu_0}{\rho}\,\pi\, j_C\,\rho_a\,\sqrt{|i_a(t)|}} \tag{3.136}$$

This leads to an expression of the plasma flow convection effect $P_F(t)$ that is dependent on the arc current $i_a(t)$. This expression in Eq. 3.136 is somewhat similar to Sakulin's current dependent term in Eq. 3.111.

This arc model together with Sakulin simplified model, have been implemented in simulation models, describing the transient electrical conditions in a submerged arc ferrosilicon furnace. This is further described in Section 4.4. The simulation models have been applied in analyzing the effects of arcing on the furnace electrical environment, as discussed in Section 5.1, and they have been implemented in an estimator scheme for estimating the inner process conditions in a ferrosilicon furnace, as discussed in Section 8.4.1.

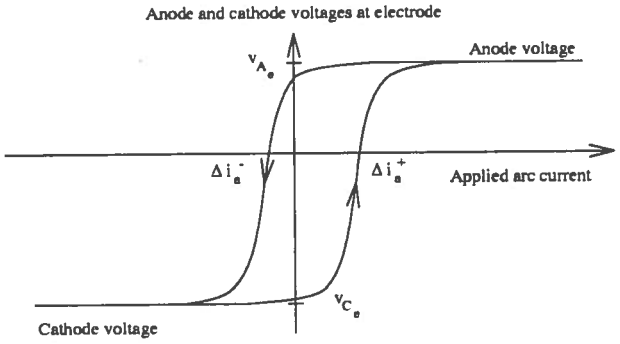

Figure 3.24: Illustration of the alternation between the anode and cathode voltages at the electrode.

3.7.4 Model of anode and cathode regions in AC arcing

The AC arc channel models only describes the arc column, and thus the anode and cathode regimes must be considered separately. The description of the anode and cathode regimes should account for the anode and cathode voltages, which can be applied to yield a total arc voltage description, as described in Eq. 3.96:

$$v_a(t) = v_A(t) + v_C(t) + R_a(t)i_a(t) \tag{3.137}$$

A simple model of the anode and cathode voltages is to consider them as constants within the electric half-periods:

$$v_A(t) = \begin{cases} v_{Ae}, & i_a(t) > 0 \\ v_{Am}, & i_a(t) < 0 \end{cases} \quad v_C(t) = \begin{cases} v_{Cm}, & i_a(t) > 0 \\ v_{Ce}, & i_a(t) < 0 \end{cases} \tag{3.138}$$

where v_{Ae}, v_{Am}, v_{Cm} and v_{Ce} represent the different anode and cathode voltages in the two half-periods. These voltages are dependent on the material properties of the electrode and the metal pool.

In AC arcing a hysteresis effect is present in the alternation of the anode and cathode regimes. The anode and cathode voltages are delayed compared to the applied current and voltage, and a capacitive effect may occur in the vicinity of applied current zero. When the applied current reaches zero, the anode and cathode voltages are still present and will subsequently diminish until the new voltages are built up. This effect is illustrated in Fig. 3.24, showing the anode and cathode voltages at the electrode. According to Edels (1973), the time constants connected with the anode and cathode

voltages are in the range of 1 ms.

The following simple model describes the alternation between the anode and cathode voltages at the electrode and the metal pool:

$$v_e(t) = \frac{v_{Ae} + v_{Ce}}{2} + \frac{v_{Ae} - v_{Ce}}{2} \cdot \tanh\left(\tau_e \cdot [i_a(t) - \Delta i_{ae}(t)]\right) \quad (3.139)$$
$$v_m(t) = \frac{v_{Am} + v_{Cm}}{2} + \frac{v_{Am} - v_{Cm}}{2} \cdot \tanh\left(\tau_m \cdot [i_a(t) - \Delta i_{am}(t)]\right)$$

where v_{Ae} and v_{Ce} represent the alternating anode and cathode voltages at the electrode, and v_{Am} and v_{Cm} represent in the same way the alternating anode and cathode voltages at the metal pool. The connected time constants are denoted τ_e and τ_m, respectively. The current deviations Δi_{ae} and Δi_{am} represent the current values for which the voltages alternate, which can similarly be described by:

$$\Delta i_a(t) = \frac{\Delta i_a{}^+ + \Delta i_a{}^-}{2} + \frac{\Delta i_a{}^+ - \Delta i_a{}^-}{2} \cdot \tanh\left(\tau_{\Delta i} \cdot \frac{di_a(t)}{dt}\right) \quad (3.140)$$

where $\Delta i_a{}^+$ and $\Delta i_a{}^-$ represent the the current values for which the voltage alternate, as shown in Fig. 3.24. The time constant $\tau_{\Delta i}$ is chosen to ensure a smooth transition between these current values.

The total anode and cathode voltages v_{AC} are then given as:

$$v_{AC}(t) = v_A(t) + v_C(t) = v_e(t) + v_m(t) \quad (3.141)$$

This model of the anode and cathode voltages is implemented in the arc channel simulation models, which gives a complete description of AC electric arcs.

3.8 Concluding remarks

A brief description of arc physics has been given in this chapter. The different regions of an electric arc have been described and various phenomena and connected properties have been treated in order to give a basis for physical modelling. The discussions have focused on arcing in electric furnaces and the phenomena, that occur as a result of arcing, have been described.

Various mathematical models of electric arcs have been described. Analytic models as well as arc channel models, are described for DC arcs, giving a basis for AC arc modelling. Finally, dynamic models for AC arcs are

described. Both empirical models and dynamic channel models for the AC arc column are discussed and a simple model of the anode and cathode voltages in AC arcing is proposed.

The dynamic channel models for AC arcs are further implemented in simulation models describing the transient electrical conditions in ferrosilicon furnaces.

Chapter 4

Modelling the electrical system

The topic of this chapter is modelling of the electric environment of a ferrosilicon furnace. First, electrical conduction in submerged-arc furnaces is treated in general. Important issues are possible current paths, current transfer modes, and charge resistivities. Next, a survey of proposed models of electric furnaces is given, from simple empirical models to three-dimensional analytic models. Then, modelling based on equivalent circuit descriptions is considered. Finally, two steady-state models and one transient model of the electrical conditions in a ferrosilicon furnace are proposed.

4.1 Electrical conduction in submerged-arc furnaces

In a three-phase submerged-arc ferrosilicon furnace the three electrodes are submerged into the charge burden, and the currents flow from the transformer delta circuit through the electrodes, and into the charge, as previously discussed in Sections 2.2 and 2.4. The electrical circuit in the furnace can usually be looked upon as a delta-star circuit, where the metal bath in the furnace bottom acts like the electrical star-point. The main current paths are assumed to go from the electrode tips through the electric arcs in the cavities, to the metal bath in and below these cavities. In addition, some conduction is present in by-pass to the arcs, from the electrode tips through the cavity wall regions, towards the metal bath. However, the current could also flow directly between the electrodes, or even between the electrodes and the furnace shell, without passing through the metal bath in the bottom of the furnace. The various conduction paths in such a furnace

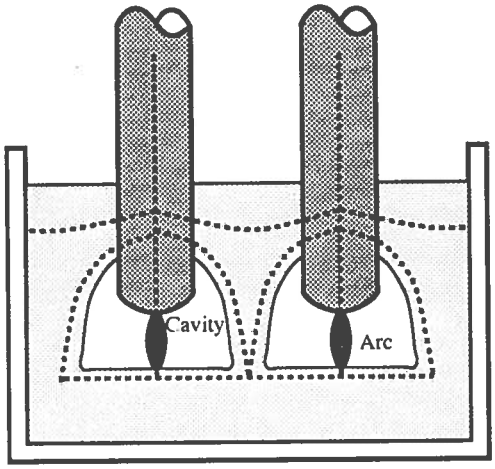

Figure 4.1: Electrical conduction paths in the charge burden of a submerged-arc ferrosilicon furnace.

are illustrated in Fig. 4.1.

If there is significant conduction in the upper part of the charge, directly between the electrodes or towards the furnace shell, less dissipation of electric energy will occur in the hearth of the furnace, compared to a situation with mainly electrode-to-bath conduction. This can lead to a situation where there is a lack of the required energy for the chemical reactions in that region, and undesirable reaction may occur as a result of the heat generation in the upper part of the charge. Significant electrode-to-electrode conduction will make the electrical control system less effective, as this control system uses the electrode movements as control inputs, because this kind of conduction is less sensitive to vertical electrode movements compared to electrode-bath conduction.

The current paths in the furnace burden are the result of the overall electrical resistance of the furnace burden, which is given by the resistivities in the various charge regions, as well as by geometrical conditions, such as electrode spacing, the depth of which the electrodes are submerged in the charge, the cavity dimensions, and the distance between the electrode tip and the metal bath. Assuming that the charge can be looked upon as a homogeneous conducting medium with resistivity ρ, the charge resistance can be expressed as (Downing and Urban, 1966; Urquhart, Jochens and Howat, 1974):

$$R = \rho \cdot \kappa \tag{4.1}$$

where "the cell constant" κ is given by the geometrical configuration. Based on this description, Downing and Urban (1966) have developed a electrical model of both electrode-to-bath conduction and electrode-to-electrode conduction. This is further described in the next section.

The portion of the direct electrode-to-electrode conduction depends on the resistivity of the charge between the electrodes, seen in association with the effective resistance in the region below the electrodes. Relatively large resistivity in the upper part of the charge is desirable in order to obtain a favorable electrical power distribution in the furnace. The current paths and hence the electrical power distribution, are crucial factors in the operation of submerged-arc furnaces, and considerable efforts have been made in investigations of charge conductivity and in attempts to control the current distribution in the charge burden. According to Urquhart, Jochens and Howat (1974) the maximum production in a submerged-arc furnace will be a direct function of the electrical resistance of the charge burden.

As a result of this a large number of studies have focused on electrical conduction phenomena in the charge of submerged-arc furnaces, among others Downing and Urban (1966), Urquhart, Jochens and Howat (1974), Channon, Urquhart and Howat (1974), Rennie (1975a, 1975b, 1984) and Urquhart (1978). These investigations have mainly concentrated on analyses of the charge burden resistivity and its dependency on variations in temperature, material compositions and particle sizes, as well as analyses of the resistivity of the charge burden components. Others have focused on possible current transfer modes and current paths in the charge.

4.1.1 Current transfer modes in the charge burden

Urquhart, Jochens and Howat (1974) and Channon, Urquhart and Howat (1974) investigated the electrical conductivity and the current transfer mode in the charge burden in submerged-arc furnaces. In general, they found that two current transfer mechanisms were possible:

1. Ohmic conduction at low voltages.

2. Arcing between the burden particles at high voltages.

and that there is "a critical voltage", this being the voltage at which the ohmic conduction starts to break down.

At low voltages the current passes from particle to particle via a relatively large contact resistance between the particles, and the resistance of the charge is the sum of many inter-particulate contact resistances in series and

in parallel. A decrease in the particle sizing in the charge mix will lead to a higher resistivity because of an increase in the amount of inter-particulate contacts. According to Urquhart, Jochens and Howat (1974) the major reason for the decrease in charge resistivity with increasing temperature is believed to be effects of temperature on the semi-conducting properties of the various burden components. Increased charge temperature also leads to expansion and increase in the contact pressure between the charge particles, and results in a decreased resistivity because of the increased contact area.

According to Urquhart, Jochens and Howat (1974), who analyzed charging consisting of different mixes of coal char, chromite and quartz, arcing was only found to occur when coal char was present. Furthermore, an increase in the charge particles made arcing easier as the critical voltage became smaller. Arcing was observed both between two char particles and between a char particle and a chromite or quartz particle. The occurrence of arcing can be explained in the following way:

1. Consider two particles, for instance carbon and quartz particles, in the charge burden, and that electric conduction occurs between the two particles. If the electrical power dissipation at the contact point between the particles is sufficiently high to overcome heat losses, the reaction temperature for carbon and quartz can be reached at the contact point, and the chemical reaction can occur, producing liquid silicon and carbon monoxide.

2. This reaction will result in a gap formation between the particles. If this gap is sufficiently small, the occurrence of arcing is possible, provided that the applied voltage is large enough to ignite the arc. The arc will produce more heat and further reactions will occur between the particles until the distance between the particles is too large for the applied voltage to sustain arcing, and the arc extinguishes.

Thus, once the critical voltage of ohmic conductance has been exceeded, the contact-resistance paths are rapidly broken down, resulting in sporadic conduction at an apparently high resistance. According to Urquhart, Jochens and Howat (1974) this can explain the low conduction in the upper part of the charge of a submerged-arc furnace.

4.1.2 Charge resistivity

The resistivity of the charge burden in submerged-arc furnaces depends on several complex circumstances, for instance the charge mix composition,

the particle sizes of the charge materials, and the temperature distribution, as well as the material distribution of the charge burden.

Downing and Urban (1966) conducted a comprehensive investigation of the charge resistivity in submerged-arc furnaces. They concentrated on analyzing the specific resistivity of the charge materials and attempted to relate the specific charge resistance with electric furnace conditions and the performance of industrial furnaces. They found that the coke resistivity decreased with increasing particle size, that the slag resistivity increased with increasing content of reactants, and that the slag and coke resistivities were comparable at operating temperatures.

Urquhart, Jochens and Howat (1974) analyzed the resistivity of the charge burden and the charge components quartz, chromite and coal char, for temperatures up to about 1500°C. They confirmed the general trend of decreasing charge resistivity with increasing temperature. They found that quartz initially behaved like an insulator, but that the resistivity started to decrease with temperatures above 700°C, and the coal char had a very low resistivity, which was only slightly affected by temperature. However, the coal char resistivity increased temporarily at the temperatures where the volatiles they contain, are driven off. The total burden mix had a falling resistivity with increasing temperature, but was found to be affected by chemical reactions when the current reaction temperature was reached. The burden resistivity was also found to be decreasing with time at high temperatures, something that Urquhart, Jochens and Howat (1974) explained as a result of increased contact area between the charge particles.

Rennie (1975b) analyzed the electrical conductivity of charges corresponding to the production of 75% ferrosilicon for temperatures up to 1700° and verified the results of Urquhart, Jochens and Howat (1974). He found that quartz was virtually a non-conductor over the whole temperature range, and that the conduction in the charge only could occur via a combination of series and parallel carbon paths. The conductivity of the coal and char changed very little over the temperature range once the volatiles had been driven off. The conductivity of the total charge burden had an increasing trend, and effects due to chemical reactions were noticed. At a temperature about 1450°C, a sudden increase in the conductivity occurred, which was explained to be due to the softening of silica, and better surface contact between the particles could explain the the increased conductivity. Rennie (1975b) further analyzed the effects of different coal and char materials on the electrical conductivity and the chemical reactivity of the charge.

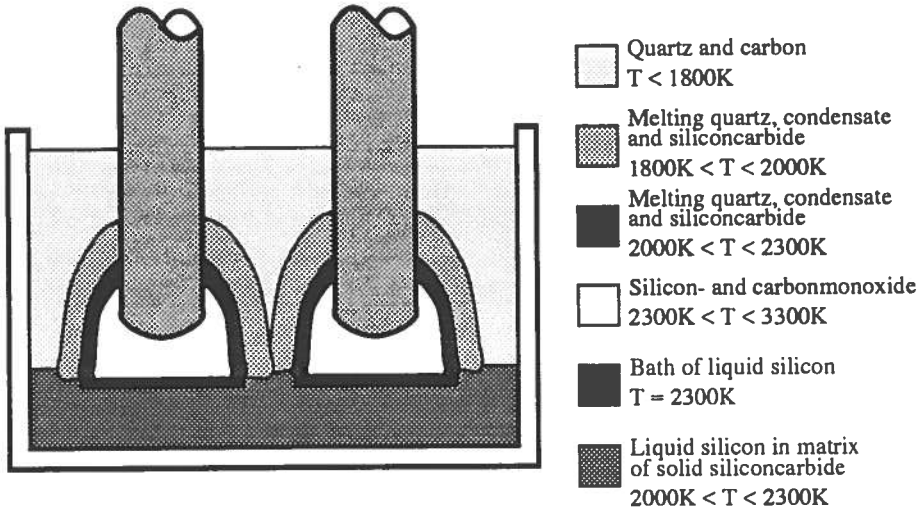

Figure 4.2: Temperature and material distribution in the charge burden of a submerged-arc silicon furnace.

4.1.3 Conduction in the charge burden of a silicon furnace

Schäfer (1984) investigated the electrical conduction paths in the charge of a submerged-arc silicon furnace. Figure 4.2 shows the idealized distributions of temperature and material components in the charge burden of a silicon furnace (Müller, Olsen and Tuset (1972); Rennie, 1975b; Schäfer, 1984). The upper part of burden consists of mainly unreacted charge materials, at temperatures up to 1800 K. Below this region towards the cavities, the temperature increases to about 2000 K, and the charge contains melting or softening silica (quartz), silicon carbide and "condensate" as result of the condensation of silicon monoxide flowing up from the cavities. The condensate consists of liquid silicon within a matrix of silica. The cavity walls consist of melting quartz, silicon carbide and condensate at temperatures at 2000-2300 K. The cavities contain silicon- and carbon monoxide at temperatures up to 3000 K. Baths of liquid silicon can be found at temperatures of about 2000-2300 K at the bottom of these cavities. Below the cavities there is a region of silicon carbide, containing liquid silicon. The burden of a ferrosilicon furnace will mainly correspond to this description.

According to Schäfer (1984), the charge material components have the following resistivities in the temperature region between 1500-2300 K:

Quartz. The resistivity of quartz decreases with temperature:

$T < 1800$ K	$\rho > 10^4$ Ωcm
1800 K $< T <$ 2000 K	10^2 Ω m $< \rho < 10^4$ Ωcm

Carbon materials. The resistivities of the various carbon materials decrease slightly with temperature in this region. The resistivities of some coal materials at such temperatures are:

$T < 1800$ K	$\rho > 1 - 2$ Ωcm

Silicon carbide. The resistivity of silicon carbide depends on the structure of the material. At current temperatures the resistivity is:

$T \approx 2000$ K	$\rho \approx 0.01 - 0.1$ Ωcm

Silicon. The liquid silicon can at such temperatures be looked upon as a metallic conductor with a resistivity given as:

$T \approx 2000$ K	$\rho \approx 10^{-4}$ Ωcm

Schäfer (1984) has derived the resistivity of the different sections in the furnace burden based on the assumed temperature and material distribution shown in Fig. 4.2, and the resistivities of the charge components in order to find the probable current paths in the furnace.

The quartz and the carbon materials in the upper part of the furnace have a lower temperature and a higher resistivity than the silicon carbide, condensate and the silicon around the cavities. Thus, the electrical resistance between the electrodes above the cavities will be relatively high, and the most probable current paths are from the electrodes towards the metal baths in the cavities, either by electric arcs, or by conductance through the high-conductive cavity walls or the layer around these walls.

According to Stewart (1980) and Schäfer (1984), the electrode-to-electrode currents in submerged-arc ferrosilicon furnaces amount to about 1% of the total electrode currents and thus they can to some extent be neglected in the analyses of the electrical conditions.

4.2 A survey of proposed models of electric furnaces

The application of submerged-arc electric furnaces to produce different alloys by the smelting of difficult reducible oxides has reached a high degree of development, and simultaneously the knowledge about the design and operation of such furnaces has increased, here the knowledge about the electrical environment in the furnaces plays an important role. According to Downing (1977) there are three different stages of the incorporation of this knowledge into a theory by developing models of the electrical circumstances in submerged-arc furnaces:

1. Empirical models of electrical, thermal and metallurgical conditions.
2. Analytical models of electrical conditions based on models of the charge conductivity.
3. Three-dimensional mathematical models describing more or less the electrical, magnetic and thermal conditions, heat and mass flows and chemical reactions in the furnace based on fundamental physical laws and conservation equations. A large number of such models have been proposed during the recent decades, which are different in complexity and describe slightly different furnace operations.
4. Models based on electrical equivalent circuits of the furnace with lumped resistances and reactances, describing either the steady-state or the transient electrical conditions in the furnace. Such models are much simpler than the three-dimensional models above, but still yield much information about electrical environment in the various regions of the furnace.

A survey of some proposals for models in the different groups is given below.

4.2.1 Empirical models of the electrical circumstances in submerged-arc furnaces

Empirical models of the electrical circumstances in submerged-arc furnaces have been developed based on furnace experience and data correlations for a large number of years. This is further described among others by Westly (1974, 1976) and Stewart (1980).

Andreae's formula

As early as in the 1920s and 30s Andreae proposed the following relationship between the furnace resistance (the phase resistance) and the electrode

dimension at optimal furnace conditions:

$$R \cdot \pi \cdot d_e = \pi \cdot \frac{V_e}{I_e} \cdot d_e = k \tag{4.2}$$

where R is the furnace resistance, d_e is the electrode diameter, V_e is the electrode voltage, I_e is the electrode current, and where "**Andreae's k-factor**" k, was assumed to be a constant for a specified charge compositions, independent of the furnace dimensions.

It can be shown that Andreae's k-factor is related to the resistivity in the charge. If the current is assumed to flow through a homogeneous reaction zone below the electrode, with the same diameter as the electrode, and with the height h, the resistance in this charge zone becomes:

$$R = \rho \cdot \frac{h}{\pi {d_e}^2/4} \tag{4.3}$$

where ρ is the charge resistivity. This leads to the following relation between the k-factor and ρ:

$$k = \frac{4h}{d_e} \cdot \rho \tag{4.4}$$

If it is assumed that the proportion between the furnace dimensions h/d_e, remains constant, this explains why the k-factor is a constant for specified charge compositions in different furnaces. This was the first attempt to relate the electrical conditions to metallurgical conditions in submerged-arc operations, and Andreae's formula in Eq. 4.2, was fundamental in the design and operation of such furnaces for several decades.

Kelly's model

Andreae's k-factor varies with the charge materials and with the specific load of the electrodes. In the 1950s Kelly proposed a modified version of Andreae's formula and found that the k-factor was proportional to the electrode power density p_e, and that the electrode current density j_e, was proportional to the inverse square root of the electrode diameter:

$$\begin{aligned} k &\propto p_e \\ j_e &\propto 1/\sqrt{d_e} \end{aligned} \tag{4.5}$$

where

$$p_e = \frac{RI_e^2}{\pi {d_e}^2/4} \tag{4.6}$$

denotes the electrical power density of the electrode, and

$$j_e = \frac{I_e}{\pi {d_e}^2/4} \tag{4.7}$$

denotes the electrode current density. A combination of the expressions in Eq. 4.5, yields:

$$k \propto R \cdot d_e \tag{4.8}$$

which shows that Kelly's observations are consistent with Andreae's formula.

Person's model

The sizes of submerged-arc furnaces increased considerably in the 1960s and 70s. It turned out that Andreae's formula failed to describe such furnaces. In 1971 Persson suggested that instead of the straight line relationship between the k-factor and the power density in Eq. 4.5 proposed by Kelly, a hyperbolic relationship should be applied, and that the k-factor was inversely proportional to the power density. The power density can be expressed as:

$$p_e = \frac{{V_{e,I}}^2}{R} \cdot \frac{1}{\pi {d_e}^2/4} \tag{4.9}$$

where $V_{e,I}$ is the electrode voltage component in phase with the electrode current. Rearranging and inserting Andreae's formula in Eq. 4.2, yields:

$$V_{e,I} = k \cdot p_e \cdot \frac{d_e}{4} \tag{4.10}$$

or, equivalently:

$$\frac{V_{e,I}}{\sqrt{d_e}} = \sqrt{\frac{k \cdot p_e}{4}} \tag{4.11}$$

Persson showed that the parameter $V_{e,I}/\sqrt{d_e}$ was a constant for a particular type of process, and stated that Andreae's formula should be slightly modified to:

$$k = \pi \cdot \frac{V_{e,I}}{I_e} \cdot d_e \tag{4.12}$$

when considering furnaces with low power factors.

Westly's model

Another version of Andreae's formula was proposed by Westly (1974, 1976). Based on furnace observations and data analyses, Westly found the following relationship between the k-factor and the electrode current density:

$$k^2 \propto \frac{1}{j_e} \tag{4.13}$$

Combined with Andreae's formula in Eq. 4.2, this yields:

$$R \propto \frac{1}{4\pi} \cdot \frac{1}{P^{1/3}} \tag{4.14}$$

This can also be expressed in terms of the electrode current:

$$I_e \propto 4\pi \cdot P^{2/3} \tag{4.15}$$

Westly found that this expression described optimal furnace conditions at different power levels as well as distinct furnaces of different sizes. The so-called Westly's formula is found by rearranging Eq. 4.15:

$$I_e = C_w \cdot P^{2/3} \tag{4.16}$$

where C_w is "**Westly's factor**", which is commonly used in ferrosilicon furnace operation.

Figure 4.3, which is based on Westly (1974), shows the relationship between furnace resistance, electrode currents and furnace loads and illustrates the differences between the furnace electrical operational lines based on the models of Andreae, Kelly, Persson and Westly. According to Westly his model seems to describe optimal conditions in ferrosilicon and silicon furnaces better than the other models.

4.2.2 Models based on analytic charge resistivity descriptions

The simple empirical models of Andreae and others have been the starting point in the development of improved models of the conductivity in submerged-arc furnaces (Downing and Urban, 1966). Andreae's formula given in Eq. 4.2, can be written as:

$$R = \frac{k}{\pi d_e} \tag{4.17}$$

This expression of the furnace resistance can be rewritten as:

$$R = \rho \cdot \kappa \tag{4.18}$$

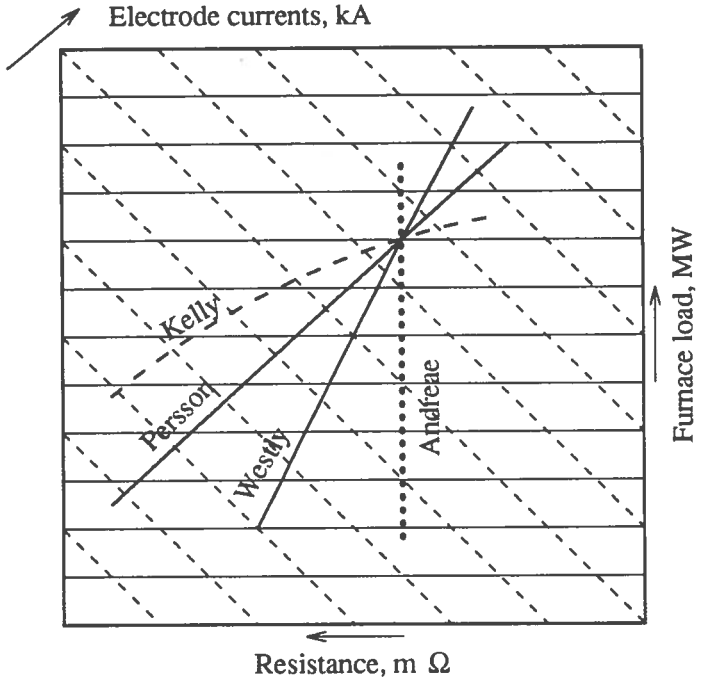

Figure 4.3: Furnace electrical operational lines, based on Westly (1974).

which is the same as Eq. 4.1, and where ρ is the charge resistivity and κ is "the cell constant", which is given by the conducting geometries.

According to Downing and Urban (1966) several cell constant expressions have been proposed in order to represent the conduction paths in a submerged-arc furnace, but all of them assumed negligible electrode-to-electrode conduction. Downing and Urban (1966) derived an expression of the resistance between two electrodes submerged into a conductive charge, as shown in Fig. 4.4. The derivation was based on relations between capacitance and conductance for a conductive medium, and the conductance were calculated based on capacitance formulas. The conductance between the two electrodes G, was found to be:

$$G = \frac{\pi}{\rho}\left[\frac{h_c}{\ln\left(\frac{D_e}{2\,r_e} + \sqrt{\left[\frac{D_e}{2\,r_e}\right]^2 - 1}\right)} + r_e\left(1 + \left[\frac{r_e}{D_e}\right] + \left[\frac{r_e}{D_e}\right]^2 + \ldots\right)\right] \quad (4.19)$$

where r_e is the electrode radius, D_e is the distance between the electrode centers, and h_c is the electrode immersion in the charge, as illustrated in

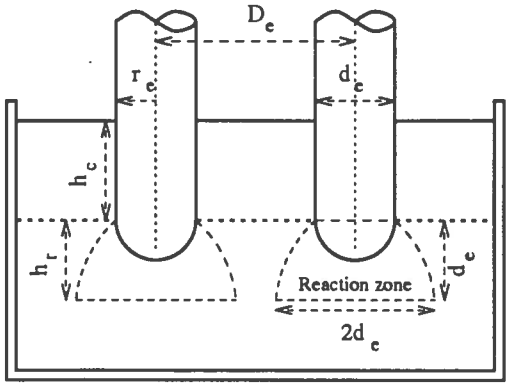

Figure 4.4: Schematic illustration of the burden of a submerged-arc furnace.

Fig. 4.4. The resistance between the electrodes is given as:

$$G = \frac{1}{R} \tag{4.20}$$

The derivation of the conductance in Eq. 4.19 is in fact based on an assumption of an infinitely extended conduction medium around the electrode pair in Fig. 4.4. However, according to Persson (1979), this assumption will be satisfied if the distance between the electrodes and the metal bath is more than one third of the electrode diameter.

Downing (1977) and Downing and Leavitt (1979) separated the conductance expression in Eq. 4.19 into expressions of the electrode-to-electrode and electrode-to-hearth conductances:

$$G = G_i + G_{ij} \tag{4.21}$$

where subscript i denotes electrode-to-hearth conduction, and subscript ij denotes conduction direct between the electrodes. These conductances can also contain different resistivities ρ_i and ρ_{ij}, in order to describe different conduction regimes:

$$G_i = \frac{\pi\, r_e}{\rho_i}\left(1 + \left[\frac{r_e}{D_e}\right] + \left[\frac{r_e}{D_e}\right]^2 + \ldots\right) \tag{4.22}$$

$$G_{ij} = \frac{\pi\, h_c}{\rho_{ij}\, \ln\left(\frac{D_e}{2\,r_e} + \sqrt{\left[\frac{D_e}{2\,r_e}\right]^2 - 1}\right)} \tag{4.23}$$

The overall resistance between the electrodes can then be found as:

$$R = \frac{1}{G_i + G_{ij}} \tag{4.24}$$

The current distribution in the furnace is governed by the resistivity of the charge regions, which depend strongly on temperature. Therefore, Downing (1977) further extended the model by including temperature dependent resistivities $\rho_i(T)$ and $\rho_{ij}(T)$ in Eqs. 4.22 and 4.23.

According to Downing and Leavitt (1979), the two-electrode resistance model can be applied to three-phase furnaces with three electrodes by imagining that a three-electrode furnace consists of three, identical two-electrode pairs, and that the total furnace power is equally divided among the three electrodes. If the furnace is represented by a star-circuit with equal electrode-to-hearth resistances R_e, the calculated electrode-to-electrode resistance R in Eq. 4.24, can be expressed as:

$$R_e = \frac{1}{2} R = \frac{3 V_e}{P} = \frac{V_e}{I_e} \tag{4.25}$$

if a unity power factor is assumed. In Eq. 4.25, P is the total furnace power, V_e is the secondary electrode voltage, and I_e is the electrode current. The resistivities of the two conduction regions can be found from electrical measurements, using Eq. 4.25 in combination with and Eqs 4.22, 4.23 and 4.24. In this way valuable information about the distribution of electrical power dissipation in the charge burden can be achieved.

The cell constant descriptions given in Eqs. 4.19, 4.22 and 4.23, have been successfully applied when analyzing industrial furnaces (Downing, 1977; Downing and Leavitt, 1979; Persson, 1979). It can further be shown that the resistance model in Eq. 4.24 is related to Andreae's formula in Eq. 4.2 in the following way:

$$k = \frac{2}{3} \rho_i \tag{4.26}$$

if the conduction between the electrodes is neglected. This explains the success of the Andreae's formula. At optimal furnace conditions the current flows from the electrode to the hearth and the inter-electrode currents are negligible (Downing and Leavitt, 1979).

According to Rennie (1984), most of the current in a submerged-arc furnace and hence most of the power generation, is contained within a region extending from the electrode tip to the metal bath. Experiments on industrial furnaces by moving the electrodes and monitoring the change in

resistance, have confirmed that more than 90% of the current flows in this way. As a result of this Rennie (1984) and Bean and Rennie (1985) have developed an alternative cell constant model based on a parabolic reaction zone below the electrodes, as illustrated in Fig. 4.4. The reaction zone is divided into several horizontal segments, and the model consists of the cell constants κ_i for these segments:

$$\kappa_i = \frac{4}{3\ \pi\ d_e} \ln\left(\frac{h + \Delta h + d_e/3}{h + d_e/3}\right) \tag{4.27}$$

where subscript i denotes the segment number, d_e is the electrode diameter, h is the distance from the segment to the electrode, and Δh is the segment thickness. The resistance of such a segment is:

$$R_i = \rho_i\ \kappa_i \tag{4.28}$$

where ρ_i is the resistivity of this segment. If the metal bath is a distance h_r below the electrode, the electrode-bath resistance will be given as:

$$R = \sum_{i=1}^{h_r/\Delta h} \rho_i\ \kappa_i \tag{4.29}$$

Assuming a constant resistivity ρ in the reaction zone, the resistance is given as:

$$R = \frac{4\ \rho}{3\ \pi\ d_e} \ln\left(\frac{h_r + d_e/3}{d_e/3}\right) \tag{4.30}$$

According to Rennie (1984), this methodology has been successfully applied to analyses of the electrical power dissipation in the reaction zone of submerged-arc furnaces.

The models of simple electrical conduction in the burden of electric furnaces have limitations. They are based strictly on resistive considerations, and hence they will fail to describe the thermal conditions in the furnaces, because important factors such as thermal conduction, chemical reactions and magnetic effects, are not described.

4.2.3 Three-dimensional distributed models of electric furnaces

A large number of three-dimensional models describing the stationary electrical environments in submerged-arc furnaces have been developed in the 1970s and 80s. The various mathematical models focus mainly on the electrical, magnetic and thermal circumstances in the furnace burden, but some

of them contain descriptions of the heat and mass flows and the chemical reaction patterns. The models are generally based on fundamental physical laws and conservations equations. Some of these models developed for submerged-arc furnaces, are listed below:

- **Downing's model** was developed in the second half of the 1970s and describes the spatial distribution of the electrical and thermal conditions and the mass flow patterns, in addition to a simplified description of the chemical reactions in a three-phase submerged-arc furnace. The model includes the effects of variations in electrode spacing, electrode radii, electrode tip positions and applied electrode voltages. The required model input parameters include the electrical and thermal conductivities of the charge as functions of temperature, and chemical reactions rate descriptions. In addition, the required boundary conditions must be stated. The model calculates the temperature field and the distribution of energy dissipation density and voltage in the charge. The model is described by Downing (1977) and Downing and Leavitt (1979, 1980).

- **Heiss' model** describes the electrical and thermal circumstances in electric smelting furnaces. The model contains a current density distribution model given by the Maxwell equations of electromagnetic fields, together with a model of the energy density distribution and heat flow. The model calculates the spatial distribution of current density and the electrical power density dissipation, and the effective resistance in the furnace charge. The model is further described by Heiss (1978, 1979, 1981, 1982).

- **Bowman's model** describes the current and magnetic field distributions in the metal bath in an open-arc steelmaking furnace. The model is found by using the Maxwell equations and is described by Bowman (1979).

- **Ekrann and Sira's model** describes the electrical environment in a three-phase submerged-arc furnace with symmetric geometry. The model is based on solving the Maxwell equations for electromagnetic fields. The model is further described by Ekrann and Sira (1982)

- **Szekely and McKelliget's model** describes the heat transfer and fluid flows in the metal bath in an open-arc steelmaking furnace. The model is developed from the Maxwell equations, the Navier-Stoke equations and thermal energy balances, and is combined with a DC arc plasma model describing the temperatures, velocities and heat

fluxes in the arc column (Szekely and McKelliget, 1981). The model is described by Szekely and McKelliget (1984).

- **Budde et al.'s model** is a result of a comprehensive study on modelling and analyses of submerged-arc furnaces producing calciumcarbid, and consists of distributive models of both electromagnetic and chemical reaction for the different sections of the furnace. The model is further described by Budde, Strauß and Schmidt (1976, 1978), Budde, Strauß and Schreier (1978), Budde et al. (1979, 1980, 1988), Budde, Schreier and Schöter (1989a, 1989b). The work has also resulted in a dissertion by Wintzer (1988).

- **Juuso's model** describes a three-phase submerged-arc furnace producing high-carbon ferrochromium. The model describes and calculates the spatial distribution of current density and temperature, heat and material flow and energy consumption in the chemical reactions in such a furnace. The model consists of analytic models describing the current conduction, the material flows and the chemical reactions, while the heat flow is governed by a partial differential equation. The model is described by Juuso (1980, 1989a, 1989b, 1990)

The electrical environment in a submerged electrode smelting furnace is comprehensively treated by Stanek (1977), in a textbook on electric melting of glass. Stanek describes the concept of three-dimensional modelling of the electrical and magnetic circumstances in a smelting furnace burden, and according to Budde et al. the methodology can be applied on submerged-arc furnaces in general. The main research efforts in several of the models listed above, had been made on just the modelling of the electrical environment in the furnace. Thus, at the same time this was available in Stanek's textbook and the modelling efforts would had benefit from it. This illustrates the importance of a good literature review.

Three-dimensional models of the electrical environments in submerged-arc furnaces are especially useful in improving the knowledge about the furnace conditions and especially in detailed analyses, such as the distribution of the current paths in the charge burden. The models are complex and usually of comprehensively sized, and suffer from requiring large computational times and the lack of knowledge in the choice of model input parameters. As a result of this such models are less suitable for overall analyses and on-line simulation studies of the electrical conditions in such furnaces.

4.2.4 Electrical models based on equivalent circuit descriptions

In general, analyses of electrical circuits using equivalent circuit descriptions are frequent, and models are developed based on these equivalent circuits. When considering the electrical environment in electric furnaces, the same methodology can be applied. The equivalent circuits then describe the assumed current paths in the furnace by lumped resistive and inductive circuit elements. These elements can in their turn be estimated by consideration of the resistivity and geometrical conditions in the current regions, similar to the development of the cell constants as discussed previously.

A large number of such models have been reported in literature. Some of the models describe the steady-state electrical conditions in open-arc or submerged-arc furnaces, while others describe the corresponding transient conditions in such furnaces.

Open-arc furnaces

The majority of equivalent circuit based models in the literature describe the electrical conditions in open-arc furnaces. The electrical secondary side of an open-arc furnace corresponds to an almost pure delta-star circuit, which makes such models especially suitable. A large number of the models also describe the primary side electrical conditions. The models are mainly steady-state descriptions, but also some transient model applications are reported.

Steady-state models have been used among others by Billings (1975, 1981), Billings, Boland and Nicholson (1979) and Schwartz (1988) in analyses of the electrical conditions in electric furnaces and in the development of electric control systems. Further analyses of the electrical conditions have been carried out by Kurbiel (1982), Kalic, Bogdanovic and Bulajic (1980, 1982) and Köhle (1985, 1988, 1989), using equivalent circuits in the development of steady-state, as well as transient, models. Sakulin (1982c, 1985) used transient models in the investigation of arcing in electric furnaces.

Submerged-arc furnaces

Stewart (1980) and Schäfer (1984) have both developed steady-state models, as well as transient models, of submerged-arc furnaces based on equivalent circuit descriptions. Furthermore, Barker (1980, 1981) and Stewart and Sommer (1981) have used such models in analyses of the electrical environment in submerged-arc furnaces.

4.3 Developing steady-state electrical models

In this section an electrical equivalent circuit for a ferrosilicon furnace is described. Next, a steady-state model of the electrical conditions is derived based on this equivalent circuit. Finally, a simplified equivalent circuit is proposed and the connected steady-state model is derived.

4.3.1 Equivalent circuit descriptions of submerged-arc furnaces

When analyzing the electrical circuit of a submerged-arc furnace it is usual to represent the various sections of the circuit as lumped impedances, which together make up an equivalent circuit of the furnace. A simple equivalent circuit of a three-phase submerged-arc furnace has earlier been shown in Fig. 2.6. This circuit describes the electrical conditions in the furnace from point of view of the primary side of the transformer, and the electrical circuit in the furnace is assumed to be a pure delta-star circuit. When analyzing the electrical conditions in the furnace more closely, a more detailed equivalent circuit, viewed from the secondary side, should be considered. Figure 4.5 shows an electrical equivalent circuit that is suitable for such analyses.

The electrical energy is supplied from three-phase AC mains by three transformers connected to the electrodes in the Knapsack-connection. This was previously discussed in Section 2.4 and shown in Fig. 2.5. In Fig. 4.5 the applied voltages are represented by V_{T1}, V_{T2} and V_{T3}, respectively.

The currents I_{e1}, I_{e2} and I_{e3}, are conducted through the electrodes into the heart of the furnace. The main current paths in the furnace are between the electrode tips and the metal pools in and beneath the cavities. However, electrical conduction may occur in the charge directly between the electrodes, and thus the electrical circuit in the furnace burden is in fact a combined delta-star circuit. The electrode-to-electrode currents I_{12}, I_{23} and I_{31} are usually negligible compared to the currents between the electrodes and the metal bath, accounting for 1% according to Stewart (1980) and Schäfer (1984), but may become significant given sluggy furnace conditions. The remaining electrode currents I_{el1}, I_{el2} and I_{el3}, flow towards the cavities.

The main part of the electric energy in the furnace is dissipated in the cavities by electric arcs, burning between the electrodes and the molten pool, or near the cavity walls by ohmic conductance in parallel with the arcs. The arc currents are represented by I_{a1}, I_{a2} and I_{a3}, while the bypass

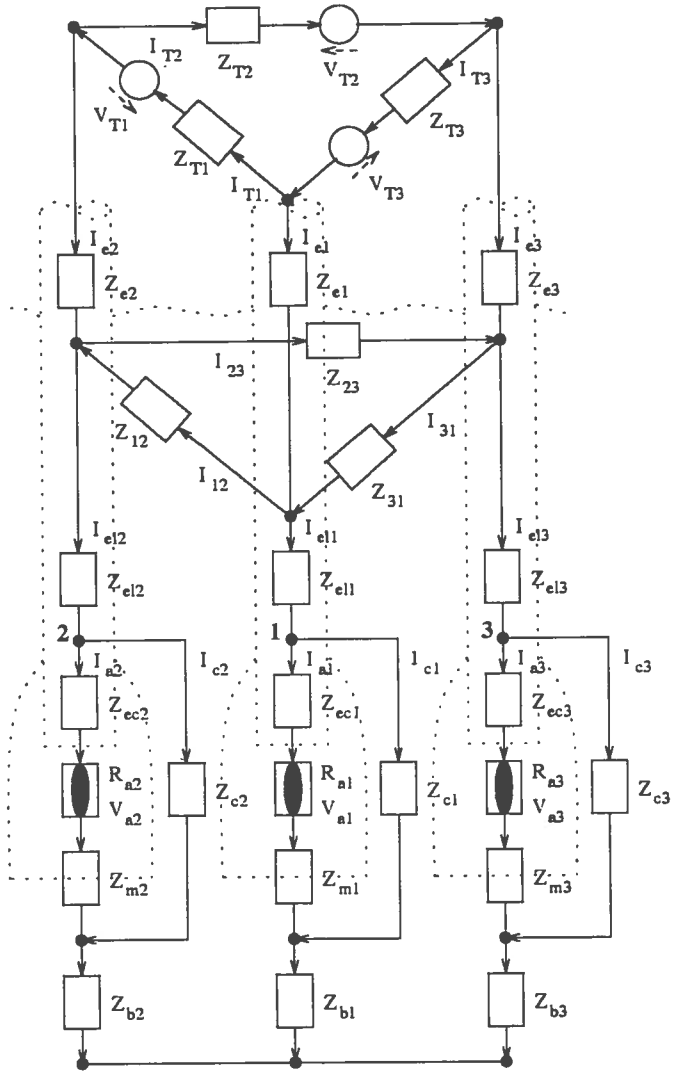

Figure 4.5: Equivalent circuit of a three-phase submerged-arc furnace. The electrodes and cavity geometry are indicated.

currents are denoted I_{c1}, I_{c2} and I_{c3}. The arcs are also represented by the voltages V_{a1}, V_{a2} and V_{a3}, and the resistances R_{a1}, R_{a2} and R_{a3}.

The notation used in the equivalent circuit is further summarized below:

- Voltages are represented by V and currents by I. Uppercase letters denote phasors, and thus, the variables are complex quantities. Furthermore, bold phase letters denote vectors and matrices.

- The impedances are represented by $Z = R + j \cdot \omega L$, where R denotes the resistance and L denotes the inductance.
- The following subscript notation is used:

T1, T2, T3	transformers, transformer circuit elements
1, 2, 3	electrode or phase numbers
12, 23, 31	direct conduction between electrodes
e	electrodes, parts above charge
el	electrodes, parts in charge
ec	electrodes, parts in cavities
a	electric arcs
c	charge around cavities
m	metal baths
b	charge bottom in furnace

4.3.2 A steady-state model description

A model description of the steady-state electrical conditions in the furnace is developed based on the equivalent circuit in Fig. 4.5.

The transformer circuit

The secondary transformer voltages V_{T1}, V_{T2} and V_{T3} are assumed to be symmetrical in the phase sequence T1-T2-T3:

$$V_{T1} = |V_T| \cdot [1 + j \cdot 0]$$
$$V_{T2} = |V_T| \cdot \left[-1/2 - j \cdot \sqrt{3}/2\right] \quad (4.31)$$
$$V_{T3} = |V_T| \cdot \left[-1/2 + j \cdot \sqrt{3}/2\right] \quad (4.32)$$

where $|V_T|$ is the common voltage magnitude. This yields:

$$V_{T1} + V_{T2} + V_{T3} = 0 \quad (4.33)$$

The transformer circuit is described by the voltage balance around the circuit:

$$Z_{T1}I_{T1} + V_{T1} + Z_{T2}I_{T2} + V_{T2} + Z_{T3}I_{T3} + V_{T3} = 0 \quad (4.34)$$

Combined with the transformer voltage expression, this yields:

$$Z_{T1}I_{T1} + Z_{T2}I_{T2} + Z_{T3}I_{T3} = 0 \quad (4.35)$$

Kirchhoff's law applied to the nodes between the transformer circuit and the electrodes, yields:

$$\begin{aligned} I_{T1} &= I_{T3} - I_{e1} \\ I_{T2} &= I_{T1} - I_{e2} \\ I_{T3} &= I_{T2} - I_{e3} \end{aligned} \tag{4.36}$$

A combination between Eqs. 4.35 and 4.36 gives the following expressions for the transformer currents in terms of the electrode currents:

$$\begin{aligned} (Z_{T1} + Z_{T2} + Z_{T3})\, I_{T1} + Z_{T3} I_{e1} - Z_{T2} I_{e2} &= 0 \\ (Z_{T1} + Z_{T2} + Z_{T3})\, I_{T2} + Z_{T1} I_{e2} - Z_{T3} I_{e3} &= 0 \\ (Z_{T1} + Z_{T2} + Z_{T3})\, I_{T3} + Z_{T2} I_{e3} - Z_{T1} I_{e1} &= 0 \end{aligned} \tag{4.37}$$

The electrode-electrode currents

The voltage balance around the electrode-electrode circuit is:

$$Z_{12} I_{12} + Z_{23} I_{23} + Z_{31} I_{31} = 0 \tag{4.38}$$

and Kirchhoff's law applied on the electrode-electrode circuit nodes, yields:

$$\begin{aligned} I_{el1} &= I_{31} + I_{e1} - I_{12} \\ I_{el2} &= I_{12} + I_{e2} - I_{23} \\ I_{el3} &= I_{23} + I_{e3} - I_{31} \end{aligned} \tag{4.39}$$

which describes the relations between the electrode currents in and above the charge.

A combination between Eq. 4.38 and 4.39 gives expressions for the electrode-electrode currents:

$$\begin{aligned} (Z_{12} + Z_{23} + Z_{31})\, I_{12} - Z_{31} I_{e1} + Z_{23} I_{e2} + Z_{31} I_{el1} - Z_{23} I_{el2} &= 0 \\ (Z_{12} + Z_{23} + Z_{31})\, I_{23} - Z_{12} I_{e2} + Z_{31} I_{e3} + Z_{12} I_{el2} - Z_{31} I_{el3} &= 0 \\ (Z_{12} + Z_{23} + Z_{31})\, I_{31} - Z_{23} I_{e3} + Z_{12} I_{e1} + Z_{23} I_{el3} - Z_{12} I_{el1} &= 0 \end{aligned} \tag{4.40}$$

The cavity circuits

The arc voltages are assumed to be described by the simplified version of the Nottingham equation as described in Eq. 3.8 in Section 3.1.2:

$$V_{ai} = V_{ACi} + E_{ai} h_{ai} \tag{4.41}$$

where V_{ACi} is the sum of the anode and cathode voltages of the current arc, E_{ai} is the arc voltage gradient, and h_{ai} is the arc length.

In the model the arc model parameters are assumed to be given by external conditions. It will be further assumed that a movement of one electrode Δh_i, will lead to a corresponding change in the arc length Δh_{ai}:

$$.\Delta h_i = \Delta h_{ai} \tag{4.42}$$

Kirchhoff's law applied at the nodes between the arc circuit and the charge by-pass circuit, yields:

$$I_{eli} = I_{ai} + I_{ci} \tag{4.43}$$

where i denotes phases 1,2 or 3. A voltage balance around the cavity circuits, gives:

$$Z_{ci}I_{ci} - (Z_{eci} + Z_{mi})\,I_{ai} = V_{ai} \tag{4.44}$$

Combined with Eq. 4.43, this gives expressions for the arc currents in terms of the lower electrode currents and the arc voltages:

$$\begin{aligned} Z_{c1}I_{el1} - (Z_{c1} + Z_{ec1} + Z_{m1})\,I_{a1} &= V_{a1} \\ Z_{c2}I_{el2} - (Z_{c2} + Z_{ec2} + Z_{m2})\,I_{a2} &= V_{a2} \\ Z_{c3}I_{el3} - (Z_{c3} + Z_{ec3} + Z_{m3})\,I_{a3} &= V_{a3} \end{aligned} \tag{4.45}$$

The electrode currents

Voltage balances around the closed electrical circuits between transformer T1 and electrodes 1 and 2, and transformer T2 and electrodes 2 and 3, yield:

$$\begin{aligned} -Z_{T1}I_{T1} + Z_{e1}I_{e1} + (Z_{el1} + Z_{c1} + Z_{b1})\,I_{el1} - Z_{c1}I_{a1} \\ -Z_{e2}I_{e2} - (Z_{el2} + Z_{c2} + Z_{b2})\,I_{el2} + Z_{c2}I_{a2} = V_{T1} \\ -Z_{T2}I_{T2} + Z_{e2}I_{e2} + (Z_{el2} + Z_{c2} + Z_{b2})\,I_{el2} - Z_{c2}I_{a2} \\ -Z_{e3}I_{e3} - (Zel3 + Z_{c3} + Z_{b3})\,I_{el3} + Z_{c3}I_{a3} = V_{T2} \end{aligned} \tag{4.46}$$

Kirchhoff's law applied at the furnace star-point gives the relation between the lower electrode currents:

$$I_{el1} + I_{el2} + I_{el3} = 0 \tag{4.47}$$

Equations 4.46 and 4.47 express the lower electrode currents in terms of the transformer, electrode and arc currents.

The steady-state model

A complete model of the steady-state electrical conditions is obtained by the 15 equations given in Eqs. 4.37, 4.39, 4.40, 4.45, and 4.46 and 4.47. The model equations are:

$$
\begin{aligned}
(Z_{T1}+Z_{T2}+Z_{T3})\,I_{T1}+Z_{T3}I_{e1}-Z_{T2}I_{e2} &= 0\\
(Z_{T1}+Z_{T2}+Z_{T3})\,I_{T2}+Z_{T1}I_{e2}-Z_{T3}I_{e3} &= 0\\
(Z_{T1}+Z_{T2}+Z_{T3})\,I_{T3}+Z_{T2}I_{e3}-Z_{T1}I_{e1} &= 0\\
-I_{e1}+I_{12}-I_{31}+I_{el1} &= 0\\
-I_{e2}+I_{23}-I_{12}+I_{el2} &= 0\\
-I_{e3}+I_{31}-I_{23}+I_{el3} &= 0\\
(Z_{12}+Z_{23}+Z_{31})\,I_{12}-Z_{31}I_{e1}+Z_{23}I_{e2}+Z_{31}I_{el1}-Z_{23}I_{el2} &= 0\\
(Z_{12}+Z_{23}+Z_{31})\,I_{23}-Z_{12}I_{e2}+Z_{31}I_{e3}+Z_{12}I_{el2}-Z_{31}I_{el3} &= 0\\
(Z_{12}+Z_{23}+Z_{31})\,I_{31}-Z_{23}I_{e3}+Z_{12}I_{e1}+Z_{23}I_{el3}-Z_{12}I_{el1} &= 0\\
Z_{c1}I_{el1}-(Z_{c1}+Z_{ec1}+Z_{m1})\,I_{a1} &= V_{a1}\\
Z_{c2}I_{el2}-(Z_{c2}+Z_{ec2}+Z_{m2})\,I_{a2} &= V_{a2}\\
Z_{c3}I_{el3}-(Z_{c3}+Z_{ec3}+Z_{m3})\,I_{a3} &= V_{a3}\\
-Z_{T1}I_{T1}+Z_{e1}I_{e1}+(Z_{el1}+Z_{c1}+Z_{b1})\,I_{el1}-Z_{c1}I_{a1} & \\
-Z_{e2}I_{e2}-(Z_{el2}+Z_{c2}+Z_{b2})\,I_{el2}+Z_{c2}I_{a2} &= V_{T1}\\
-Z_{T2}I_{T2}+Z_{e2}I_{e2}+(Z_{el2}+Z_{c2}+Z_{b2})\,I_{el2}-Z_{c2}I_{a2} & \\
-Z_{e3}I_{e3}-(Z_{el3}+Z_{c3}+Z_{b3})\,I_{el3}+Z_{c3}I_{a3} &= V_{T2}\\
I_{el1}+I_{el2}+I_{el3} &= 0
\end{aligned}
\tag{4.48}
$$

This set of equations can be expressed as:

$$\boldsymbol{A}\,\underline{\boldsymbol{x}} = \underline{\boldsymbol{b}} \tag{4.49}$$

where vector $\underline{\boldsymbol{x}}$ represents the unknown currents, and vector $\underline{\boldsymbol{b}}$ represents the source voltages in the circuit:

$$\underline{\boldsymbol{x}}^T = \left[\, I_{T1}\ I_{T2}\ I_{T3}\ I_{e1}\ I_{e2}\ I_{e3}\ I_{12}\ I_{23}\ I_{31}\ I_{a1}\ I_{a2}\ I_{a3}\ I_{el1}\ I_{el2}\ I_{el3} \,\right] \tag{4.50}$$

$$\underline{\boldsymbol{b}}^T = \left[\, 0\ 0\ 0\ 0\ 0\ 0\ 0\ 0\ 0\ V_{a1}\ V_{a2}\ V_{a3}\ V_{T1}\ V_{T2}\ 0 \,\right] \tag{4.51}$$

And where matrix $\boldsymbol{A}$ is given by the left-hand sides of the equation set given in Eq. 4.48 and in the equation sequence given above.

Simulation model of the electrical conditions

A simulation model implemented in Matlab, has been developed based on this model. The model continuously simulates the electrical conditions in the furnace by solving the equation set in Eq. 4.49 for each simulation sample. The simulation model has been further extended with an electrical

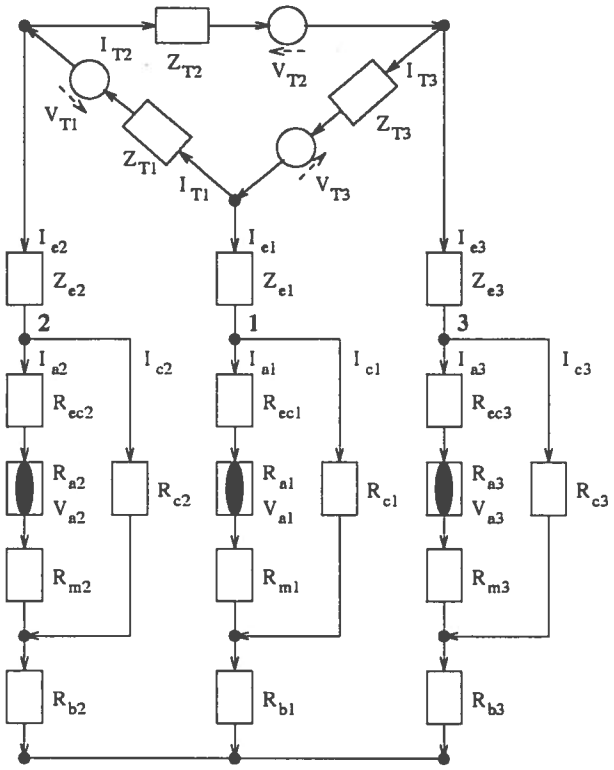

Figure 4.6: Simplified equivalent circuit of a three-phase submerged-arc furnace.

control system corresponding to the control system of the furnace. The model has been used for analyzing the electrical conditions and the electrical control system and for the developing improved control strategies. This will be further described in Chapter 6.

4.3.3 A simplified current model

A simplified steady-state model description of the electrode currents which is suitable for analytic analyses of the electrical circumstances in the furnace, is derived based on the further assumptions:

1. The electrical conditions in the furnace is described by the simplified equivalent circuit in Fig. 4.6.

   The direct electrode-electrode currents are now assumed to be negligible, and the inductances in each phase are lumped together in a common electrode inductance.

2. The transformer voltages V_{T1}, V_{T2} and V_{T3} are symmetrical in the phase sequence T1-T2-T3, and expressed in terms of the complex three-phase operator a.:

$$\begin{aligned} V_{T1} &= |V_T| \cdot [1 + j \cdot 0] \\ V_{T2} &= |V_T| \cdot \left[-1/2 - j \cdot \sqrt{3}/2\right] = V_{T1} \cdot a^2 \\ V_{T3} &= |V_T| \cdot \left[-1/2 + j \cdot \sqrt{3}/2\right] = V_{T1} \cdot a \end{aligned} \tag{4.52}$$

$$a = \left[-1/2 + j \cdot \sqrt{3}/2\right] \tag{4.53}$$

3. The impedances in the transformers, busbars and flexibles Z_{T1}, Z_{T2} and Z_{T3} are identical in all three phases:

$$Z_{T1} = Z_{T2} = Z_{T3} = Z_T \tag{4.54}$$

where Z_T is the common impedance.

4. The electrical reactances in each phase has been lumped into variable electrode reactances X_{ei}.

5. A movement of one electrode Δh_i, will lead to a corresponding change in the arc length Δh_{ai}:

$$\Delta h_i = \Delta h_{ai} \tag{4.55}$$

This assumptions will be applied when a model of a current-controlled submerged-arc furnace is derived based on this model.

Similar steady-state current models have been derived from equivalent circuit descriptions of steel furnaces by among others Nicholson and Roebuck (1972), Billings (1975, 1981) and Schwartz (1988). The current paths in submerged-arc furnaces are different from those in steel furnaces, and some modifications are necessary in these models to describe submerged-arc furnaces, but the derivation of the model mainly follows the derivation of the models of Nicholson and Roebuck (1972) and Billings (1975, 1981).

The transformer circuit

The derivation of a description of the transformer circuit is similar to the development of the steady-state model in Section 4.3.2. The transformer currents and voltages are described by Eqs. 4.35, 4.36 and 4.37. Inserting the assumption of equal transformer impedances in Eq. 4.54, the following

relations between the transformer currents and the electrode currents are derived:

$$\begin{aligned} I_{T1} &= 1/3\,[I_{e2} - I_{e1}] \\ I_{T2} &= 1/3\,[I_{e3} - I_{e2}] \\ I_{T3} &= 1/3\,[I_{e1} - I_{e3}] = -\,[I_{T1} + I_{T2}] \end{aligned} \tag{4.56}$$

The furnace circuits

Voltage balances applied on the closed electrical circuits between transformer T1 and electrodes 1 and 2, and transformer T2 and electrodes 2 and 3, give:

$$\begin{aligned} V_{T1} = {} & -Z_T I_{T1} + [Z_{e1} + R_{b1}]I_{e1} + [R_{ec1} + R_{m1}]I_{a1} + V_{a1} \\ & -([Z_{e2} + R_{b2}]I_2 + [R_{ec2} + R_{m2}]I_{a2} + V_{a2}) \\ V_{T2} = {} & -Z_T I_{T2} + [Z_{e2} + R_{b2}]I_{e2} + [R_{ec2} + R_{m2}]I_{a2} + V_{a2} \\ & -([Z_{e3} + R_{b3}]I_{e3} + [R_{ec3} + R_{m3}]I_{a3} + V_{a3}) \end{aligned} \tag{4.57}$$

where $Z_{ei} = R_{ei} + X_{ei}$ represent the impedances of the electrode portions in and above the charge, R_{eci} are the resistances of the electrode portions within the cavities, R_{mi} are the resistances in the liquid metal bath in the cavities, R_{bi} are the resistances in the furnace bottom, I_{ai} are the arc currents, and V_{ai} are the arc voltages.

Kirchhoff's law applied at the furnace star-point, gives the relation between the electrode currents:

$$I_{e1} + I_{e2} + I_{e3} = 0 \tag{4.58}$$

The simplified steady-state current model

According to Schwartz and Timm (1989) it is not possible to get an analytic expression of the electrode currents I_{ei} in terms of the arc voltages V_{ai}. However, this will be possible if the arcs are represented by nonlinear arc "resistances" R_{ai}, and thus the arc voltages are described by (Billings, 1981):

$$V_{ai} = R_{ai} I_{ai} \tag{4.59}$$

The relation between the electrode and arc currents given in Eq.4.45, now becomes:

$$I_{ai} = \frac{R_{ci}}{R_{eci} + R_{ai} + R_{mi} + R_{ci}} I_{ei} \tag{4.60}$$

Inserting the expressions of the arc voltages in Eq. 4.59 and the current relationship in Eq. 4.60 into the voltage balances in Eq. 4.57, eliminating the transformer currents by using Eq. 4.56, and rearranging the equations, gives:

$$\begin{aligned} V_{T1} &= Z_1 I_{e1} - Z_2 I_{e2} \\ V_{T2} &= Z_2 I_{e2} - Z_3 I_{e3} \end{aligned} \tag{4.61}$$

where the phase impedances Z_i are given by:

$$Z_i = R_i + j \cdot X_i \tag{4.62}$$

and the phase resistances R_i and reactances X_i are given by:

$$R_i = 1/3\, R_T + R_{ei} + R_{bi} + R_{ki} \tag{4.63}$$

$$X_i = 1/3\, X_T + X_{ei} \tag{4.64}$$

$$R_{ki} = \frac{R_{ci}(R_{eci} + R_{ai} + R_{mi})}{R_{ci} + R_{eci} + R_{ai} + R_{mi}} \tag{4.65}$$

R_{ki} can be looked upon as the resulting resistances for the parallel circuits in the cavities in the presence of arching.

A combination between the voltage balances in Eq. 4.61 with the currents balance in Eq. 4.58, gives a model of the electrode currents I_{ei}, expressed in terms of the phase impedances Z_i, the transformer voltage magnitude V_{T1}, and the three-phase operator a. The model equations are:

$$\begin{aligned} I_{e1} &= \frac{[-aZ_2 + Z_3]}{Z_1Z_2 + Z_2Z_3 + Z_3Z_1} V_{T1} \\ I_{e2} &= \frac{[a^2Z_1 - Z_3]}{Z_1Z_2 + Z_2Z_3 + Z_3Z_1} V_{T1} \\ I_{e3} &= \frac{[-a^2Z_1 + aZ_2]}{Z_1Z_2 + Z_2Z_3 + Z_3Z_1} V_{T1} \end{aligned} \tag{4.66}$$

The steady-state current model in Eq. 4.66 is suitable for analytic analyses of the electrical environment in the furnace. This model is applied in Section 5.2 for analyzing the interaction effect between the electrical phases in a submerged-arc furnace. An analytic model of a current-controlled submerged-arc furnace is derived based on this current model, and the electrical control system is analyzed and an improved current controller is proposed.

4.3.4 Identification of resistance and inductance elements

The various resistances and reactances in the models developed in Sections 4.3.2 and 4.3.3 and which are illustrated by the equivalent circuits in Figs. 4.5 and 4.6, are generally unknown quantities. However, estimates of the resistances and reactances based on the available electrical measurements and physical considerations may yield good results.

The transformer elements

The resistances and reactances in the transformer circuits, the busbars and flexibles, are in principle known and can found from direct measurements or geometric calculations.

The electrode column

The electrode resistances can be calculated to some degree of accuracy. The resistivity for a Søderberg electrode column is known for the temperatures found in the electrode, and the temperature distribution along the electrode column is established. Thus, the total resistance can be calculated if the electrode length is known. This is generally not fulfilled, but fairly accurate estimates of the electrode length can be obtained, using the measurements of the electrode positions and the electric power delivered through the electrode.

The electrode reactances, or more precisely the self and mutual inductances in and between the electrodes, can be calculated based on geometric considerations.

The charge burden elements

The resistances of the circuit elements corresponding to the different burden regions, can be estimated as previously discussed in Section 4.1.3 (Schäfer, 1984). These estimates will depend on the assumptions about the charge composition in the regions, the temperature distribution and the sizes of "active" current-conduction volumes.

The reactances of the charge burden elements can hardly be calculated, and estimates of them must mainly be made on assumptions. This speaks for the use of the simple equivalent circuit in Fig. 4.6 with a lumped reactance in each phase, instead of using the equivalent circuit in Fig. 4.5 with distributed reactive elements.

The electric arcs can be described as circuit elements by the use of the Nottingham equation in Eq. 4.41 for instance. The model parameters in

the arc description must be estimated based on the knowledge of the arcing conditions in the cavities and the cavity geometry.

Electrical measurements

The available electrical measurements for the identification of the various resistance and reactances are the electrode currents I_{ei} and the electrode-to-hearth voltages V_{ei}. Furthermore, the phase resistance R_i and X_i are deduced based on these measurements. The phase resistances and reactances can be expressed in terms of the resistances and reactances of the circuit elements, depending on the choice of complexity of the equivalent circuit.

The modelling of the electrical environment in submerged-arc furnaces turns out to be a weighing of how detailed the model description should be, against the identifiability of the resistances and reactances in the model.

4.4 A dynamic model of transient electrical conditions

A dynamic model of the transient electrical states is derived based on the equivalence circuit in Fig. 4.7. In contrast to the previous electrical models, which describe the steady-state electrical conditions, this model describes the actual transient time responses of the electrical states. The model derivation is based on the following assumptions:

1. The electrical conditions in the furnace can be described by the equivalent circuit in Fig. 4.7, which corresponds to the equivalent circuit Fig. 4.6 that was used in the derivation of the simplified steady-state model. The direct conduction between the electrodes through the charge is neglected.

2. The model notation principles are the same as before. The lower-case letters v and i denote time-varying voltages and currents. The functional dependence of the electrical states on the time variable t is usually omitted.

3. The transformer voltages v_{T1}, v_{T2} and v_{T3} are symmetrical in the phase sequence T1-T2-T3:

$$\begin{aligned} v_{T1}(t) &= V_T \cdot \sin(2\pi f t) \\ v_{T2}(t) &= V_T \cdot \sin(2\pi f t - 2\pi/3) \\ v_{T3}(t) &= V_T \cdot \sin(2\pi f t - 4\pi/3) \end{aligned} \tag{4.67}$$

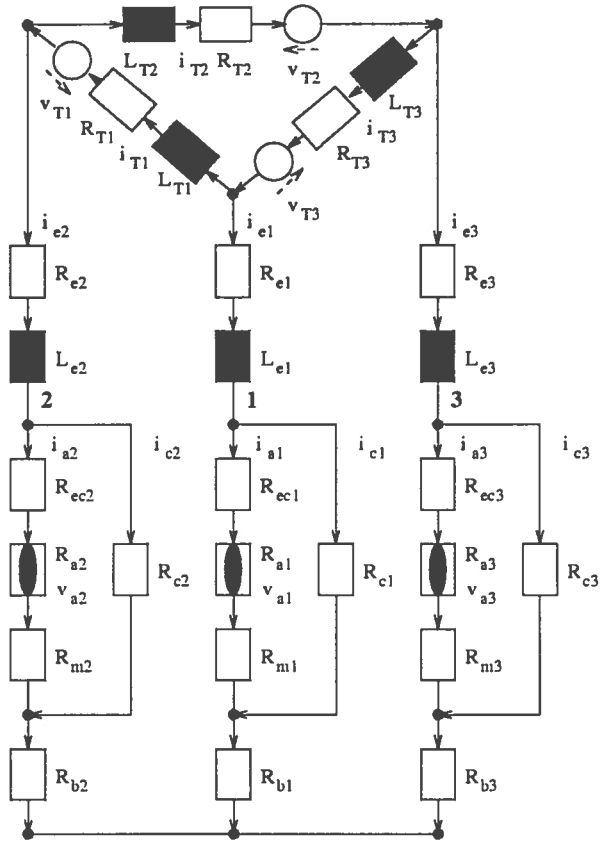

Figure 4.7: Simplified equivalent circuit of a three-phase submerged-arc furnace.

where V_T is the common voltage magnitude, f is the electrical frequency (50 Hz), and t is the time variable.

4. The inductances in the transformers, busbars and flexibles L_{T1}, L_{T2} and L_{T3} are identical in all three phases:

$$L_{T1} = L_{T2} = L_{T3} = L_T \tag{4.68}$$

where L_T is the common inductance.

5. The electrical inductivities in each phase have been lumped into variable electrode inductances L_{ei}. The assumption of lumped inductances requires further explanation and is discussed below.

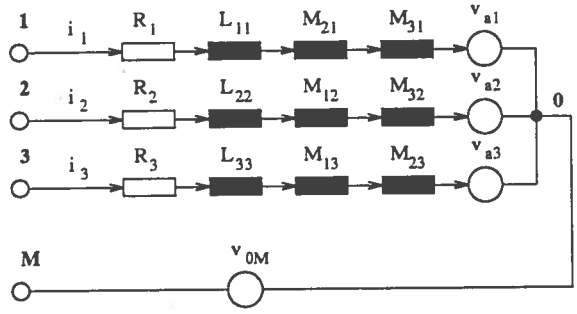

Figure 4.8: Simplified equivalent circuit of electric furnace illustrating self and mutual inductances.

4.4.1 Electrical induction effects in electric furnaces

The following analysis of the self and mutual inductivities in electric furnaces is based on the work of Kalic, Bogdanovic and Bulajic (1980, 1982). This subject is further treated among others by Köhle (1985, 1989).

The inductivities in each of the electrodes of a submerged-arc furnace consist of both self and mutual inductivity effects. Figure 4.8 shows a simplified equivalence circuit of the secondary electrical circuit of an electric furnace.

The electrical phases are represented by subscripts $i = 1, 2, 3$, the phase resistances are denoted R_i, the self inductances in each phase are denoted L_{ii}, the phase currents are denoted i_i, and the arc voltages are represented by v_{ai}. The mutual inductances in phase 1 are represented by M_{21} and M_{31}, in phase 2 by M_{12} and M_{32}, and in phase 3 by M_{13} and M_{23}. The circuit is assumed to be supplied from a symmetric three-phase voltage system:

$$\begin{aligned} v_{12} &= v_{1M} - v_{2M} \\ v_{23} &= v_{2M} - v_{3M} \\ v_{31} &= v_{3M} - v_{1M} \end{aligned} \tag{4.69}$$

In the figure, nodes **1**, **2** and **3** represent the electrical connection to the electrodes. The neutral point of the power supply is denoted M, while the electrical star-point in the furnace is denoted **o**. It is generally assumed that the mutual inductivities have equal effects in both directions, and thus:

$$\begin{aligned} M_{12} &= M_{21} \\ M_{23} &= M_{32} \\ M_{31} &= M_{13} \end{aligned} \tag{4.70}$$

According to Fig. 4.8, the line voltages v_{12} and v_{23} are given as:

$$\begin{aligned} v_{12} &= R_1 i_1 + L_{11}\frac{di_1}{dt} + M_{12}\frac{di_2}{dt} + M_{31}\frac{di_3}{dt} + v_{a1} \\ &\quad -R_2 i_2 - L_{22}\frac{di_2}{dt} - M_{23}\frac{di_3}{dt} - M_{12}\frac{di_1}{dt} - v_{a2} \\ v_{23} &= R_2 i_2 + L_{22}\frac{di_2}{dt} + M_{23}\frac{di_3}{dt} + M_{12}\frac{di_1}{dt} + v_{a2} \\ &\quad -R_3 i_3 - L_{33}\frac{di_3}{dt} - M_{31}\frac{di_1}{dt} - M_{23}\frac{di_2}{dt} - v_{a3} \end{aligned} \tag{4.71}$$

Current conservation at the furnace star-point yields:

$$\begin{aligned} i_1 + i_2 + i_3 &= 0 \\ \frac{di_1}{dt} + \frac{di_2}{dt} + \frac{di_3}{dt} &= 0 \end{aligned} \tag{4.72}$$

The "electrode-to-neutral" voltages v_{1M}, v_{2M} and v_{3M} can be derived as:

$$\begin{aligned} v_{1M} &= R_1 i_1 + L_{11}\frac{di_1}{dt} + M_{12}\frac{di_2}{dt} + M_{31}\frac{di_3}{dt} + v_{a1} + v_{0M} \\ v_{2M} &= R_2 i_2 + L_{22}\frac{di_2}{dt} + M_{23}\frac{di_3}{dt} + M_{12}\frac{di_1}{dt} + v_{a2} + v_{0M} \\ v_{3M} &= R_3 i_3 + L_{33}\frac{di_3}{dt} + M_{31}\frac{di_1}{dt} + M_{23}\frac{di_2}{dt} + v_{a3} + v_{0M} \end{aligned} \tag{4.73}$$

This set of equations is coupled in the sense that all three currents affect each of the three electrode-to-neutral voltages. These voltages can equivalently be expressed by:

$$\begin{aligned} v_{1M} &= v_{10} + v_{0M} \\ v_{2M} &= v_{20} + v_{0M} \\ v_{3M} &= v_{30} + v_{0M} \end{aligned} \tag{4.74}$$

where the three phase voltages are represented by v_{10}, v_{20} and v_{30}, respectively. The potential difference between the electrical star-point in the furnace **o** and the electrical neutral point M is represented by v_{0M}.

An alternative and "decoupled" model of the line voltages can be derived by subtracting the electrode-to-neutral voltages in Eq. 4.73 from each other, and inserting the current relations in Eq. 4.72. This yields:

$$\begin{aligned} v_{12} &= R_1 i_1 + L_1\frac{di_1}{dt} + v_{a1} - \left(R_2 i_2 + L_2\frac{di_2}{dt} + v_{a2}\right) \\ v_{23} &= R_2 i_2 + L_2\frac{di_2}{dt} + v_{a2} - \left(R_3 i_3 - L_3\frac{di_3}{dt} + v_{a3}\right) \\ v_{31} &= R_3 i_3 + L_3\frac{di_3}{dt} + v_{a3} - \left(R_1 i_1 + L_1\frac{di_1}{dt} + v_{a1}\right) \end{aligned} \tag{4.75}$$

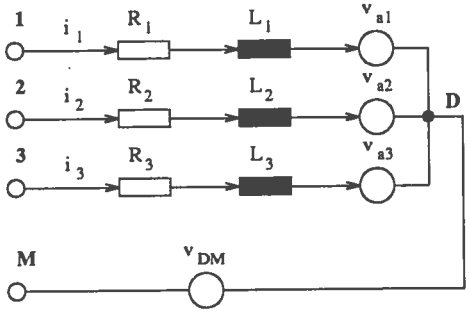

Figure 4.9: Equivalent circuit of decoupled electrical model.

where the "new" phase self inductances are given as:

$$\begin{aligned} L_1 &= L_{11} - M_{12} + M_{23} - M_{31} \\ L_2 &= L_{22} - M_{23} + M_{31} - M_{12} \\ L_3 &= L_{33} - M_{31} + M_{12} - M_{23} \end{aligned} \tag{4.76}$$

Figure 4.9 shows the equivalence circuit corresponding to the decoupled model in Eq. 4.75. In the figure $\boldsymbol{D}$ represents the electrical star-point in the circuit. The physical meaning of these three self inductances is discussed by Köhle (1985, 1989).

The electrode-to-neutral voltages can now be expressed as:

$$\begin{aligned} v_{1M} &= R_1 i_1 + L_1 \frac{di_1}{dt} + v_{a1} + v_{DM} \\ v_{2M} &= R_2 i_2 + L_2 \frac{di_2}{dt} + v_{a2} + v_{DM} \\ v_{3M} &= R_3 i_3 + L_3 \frac{di_3}{dt} + v_{a3} + v_{DM} \end{aligned} \tag{4.77}$$

In general there is a potential difference between the original star-point **o** in Fig. 4.8 and the "decoupled" star-point $\boldsymbol{D}$ in Fig. 4.9. Equivalently to Eq. 4.74, the electrode-to-neutral voltages can be expressed as:

$$\begin{aligned} v_{1M} &= v_{10} + v_{0M} = v_{1D} + v_{DM} \\ v_{2M} &= v_{20} + v_{0M} = v_{2D} + v_{DM} \\ v_{3M} &= v_{30} + v_{0M} = v_{3D} + v_{DM} \end{aligned} \tag{4.78}$$

where the three "decoupled" phase voltages are represented by v_{1D}, v_{2D} and v_{3D}, respectively. The potential difference between the star-point in the decoupled electrical circuit $\boldsymbol{D}$ and the electrical neutral point $\boldsymbol{M}$ is

represented by v_{DM}, and the potential difference between the electrical star-points Δv_0 is given as:

$$\Delta v_0 = v_{DM} - v_{OM} \tag{4.79}$$

An expression of this potential difference can be found by inserting Eqs. 4.73 and 4.77 into Eq. 4.79:

$$\Delta v_0 = (M_{12} - M_{23}) \frac{di_1}{dt} + (M_{12} - M_{31}) \frac{di_2}{dt} \tag{4.80}$$

It follows from Eq. 4.80 that the potential difference between the star-points vanishes if the three-phase circuit in Fig. 4.8 is perfectly symmetrical:

$$M_{12} = M_{23} = M_{31} \tag{4.81}$$

Expressions of the "coupled" phase voltages in terms of the decoupled phase voltages and the star-point potential difference, are found by rearranging Eq. 4.78:

$$\begin{aligned} v_{10} &= v_{1D} + \Delta v_0 \\ v_{20} &= v_{2D} + \Delta v_0 \\ v_{30} &= v_{3D} + \Delta v_0 \end{aligned} \tag{4.82}$$

The electrical conditions in a submerged-arc furnace correspond to the equivalence circuit shown in Fig. 4.8. The decoupled version in Fig. 4.9 will only be correct in the case of purely symmetric electrical conditions in the furnace. However, due to its simplicity the decoupled model description is useful for analyses and simulation studies of the electrical environments in a submerged-arc furnace, but the following should be stressed when applying the decoupled model:

1. The measurements of the electrode-to-hearth voltages in a submerged-arc furnace correspond to the phase voltages v_{10}, v_{20} and v_{30} in the "coupled" model.

   If the decoupled model is used to describe the electrical conditions in the furnace, the decoupled phase voltages v_{1D}, v_{2D} and v_{3D} must be corrected in accordance with Eq. 4.82 in order to correspond to the measured electrode voltages on the furnace.

2. The phase currents in the two model descriptions on the other hand, are similar and correspond to the electrode currents in the furnace.

4.4.2 The transient electrical model

The derivation of a dynamic model of the transient electrical states mainly follows the previous derivations of the steady-state models in Sections 4.3.2 and 4.3.3.

The transformer circuit

The transformer circuit is described by the voltage balance, corresponding to Eq. 4.35, and the equations describing the current conservation between the transformer circuit and the electrodes, corresponding to Eq. 4.36:

$$R_{T1}i_{T1} + L_{T1}\frac{di_{T1}}{dt} + R_{T2}i_{T2} + L_{T2}\frac{di_{T2}}{dt} + R_{T3}i_{T3} + L_{T3}\frac{di_{T3}}{dt} = 0 \quad (4.83)$$

$$\begin{aligned} i_{T1} &= i_{T3} - i_{e1} \\ i_{T2} &= i_{T1} - i_{e2} \\ i_{T3} &= i_{T2} - i_{e3} \end{aligned} \quad (4.84)$$

A combination between Eqs. 4.83 and 4.84, yields:

$$\begin{aligned} \frac{di_{T1}}{dt} &= \frac{1}{L_{T1}+L_{T2}+L_{T3}}\{-[R_{T1}+R_{T2}+R_{T3}]i_{T1} \\ &\quad -L_{T3}\frac{di_{e1}}{dt} - R_{T3}i_{e1} + L_{T2}\frac{di_{e2}}{dt} + R_{T2}i_{e2}\Big\}, \\ \frac{di_{T2}}{dt} &= \frac{1}{L_{T1}+L_{T2}+L_{T3}}\{-[R_{T1}+R_{T2}+R_{T3}]i_{T2} \\ &\quad -L_{T1}\frac{di_{e2}}{dt} - R_{T1}i_{e2} + L_{T3}\frac{di_{e3}}{dt} + R_{T3}i_{e3}\Big\} \\ \frac{di_{T3}}{dt} &= \frac{1}{L_{T1}+L_{T2}+L_{T3}}\{-[R_{T1}+R_{T2}+R_{T3}]i_{T3} \\ &\quad -L_{T2}\frac{di_{e3}}{dt} - R_{T2}i_{e3} + L_{T1}\frac{di_{e1}}{dt} + R_{T1}i_{e1}\Big\} \end{aligned} \quad (4.85)$$

A further assumptions about equal resistances and inductances in the transformer circuit:

$$\begin{aligned} R_T &= R_{T1} = R_{T2} = R_{T3} \\ L_T &= L_{T1} = L_{T2} = L_{T3} \end{aligned} \quad (4.86)$$

leads to the simplified expressions:

$$\frac{di_{T1}}{dt} = \frac{1}{3L_T}\left\{-3R_T i_{T1} + L_{T3}\left[\frac{di_{e2}}{dt} - \frac{di_{e1}}{dt}\right] + R_{T3}[i_{e2} - i_{e1}]\right\}$$

$$\frac{di_{T2}}{dt} = \frac{1}{3L_T}\left\{-3R_T i_{T2} + L_{T1}\left[\frac{di_{e3}}{dt} - \frac{di_{e2}}{dt}\right] + R_{T1}\left[i_{e3} - i_{e2}\right]\right\} \quad (4.87)$$
$$\frac{di_{T3}}{dt} = \frac{1}{3L_T}\left\{-3R_T i_{T3} + L_{T2}\left[\frac{di_{e1}}{dt} - \frac{di_{e3}}{dt}\right] + R_{T2}\left[i_{e1} - i_{e3}\right]\right\}$$

The electric arcs

The electric arcs in the cavities are in the model assumed to be described by a dynamic model of AC arc, corresponding to the models described in Section 3.7.3. Thus, the arc voltages v_{ai} will then be given as:

$$v_{a1} = v_{ACi} + R_{ai} i_{ai} \quad (4.88)$$

where v_{ACi} denotes the sum of the simultaneous anode and cathode voltages, i_{ai} is the arc current, and R_{ai} represents the time-varying arc resistance found from the dynamic AC arc model.

The arc currents can be expressed equivalently to Eq. 4.60:

$$i_{ai} = \frac{R_{ci}}{R_{eci} + R_{ai} + R_{mi} + R_{ci}}\left[i_{ei} - v_{ACi}\right] \quad (4.89)$$

The furnace circuits

The voltage balances of the closed electrical circuits between transformer T1 and electrodes 1 and 2, and transformer T2 and electrodes 2 and 3, are:

$$\begin{aligned} v_{T1} = {} & -L_{T1}\frac{di_{T1}}{dt} - R_{T1} i_{T1} + L_{e1}\frac{di_{e1}}{dt} + \left[R_{e1} + R_{b1}\right] i_{e1} + \left[R_{ec1} + R_{m1}\right] i_{a1} \\ & + v_{a1} - L_{e2}\frac{di_{e2}}{dt} - \left[R_{e2} + R_{b2}\right] i_{e2} - \left[R_{ec2} + R_{m2}\right] i_{a2} - v_{a2} \quad (4.90) \\ v_{T2} = {} & -L_{T2}\frac{di_{T2}}{dt} - R_{T2} i_{T2} + L_{e2}\frac{di_{e2}}{dt} + \left[R_{e2} + R_{b2}\right] i_{e2} + \left[R_{ec2} + R_{m2}\right] i_{a2} \\ & + v_{a2} - L_{e3}\frac{di_{e3}}{dt} - \left[R_{e3} + R_{b3}\right] i_{e3} - \left[R_{ec3} + R_{m3}\right] i_{a3} - v_{a3} \end{aligned}$$

where the lumped electrode inductances are given by Eq. 4.76.

The voltage balances are simplified by eliminating the transformer currents by assuming equal transformer conditions as given in Eq. 4.86 and inserting the transformer currents given by Eq. 4.87, and further simplified by eliminating the arc currents by inserting Eq. 4.89. This yields:

$$\begin{aligned} v_{T1} &= L_1\frac{di_{e1}}{dt} + R_1 i_{e1} + \tilde{v}_{AC1} - L_2\frac{di_{e2}}{dt} + R_2 i_{e2} + \tilde{v}_{AC2} \\ v_{T2} &= L_2\frac{di_{e2}}{dt} + R_2 i_{e2} + \tilde{v}_{AC2} - L_3\frac{di_{e3}}{dt} + R_3 i_{e3} + \tilde{v}_{AC3} \quad (4.91) \end{aligned}$$

where L_i represent the effective phase inductances and R_i represent the "effective" phase resistances, that are included the effect of the transformer inductances and reactances, while $\tilde{v}_{ACi}$ are expressions given by the anode and cathode voltages in each phase:

$$\begin{aligned} L_i &= L_{ei} + \frac{L_T}{3} \\ R_i &= \left\{ R_{ei} + \frac{[R_{eci} + R_{ai} + R_{mi}]\, R_{ci}}{R_{eci} + R_{ai} + R_{mi} + R_{ci}} + R_{bi} \right\} + \frac{R_T}{3} \\ \tilde{v}_{ACi} &= \frac{R_{ci}}{R_{eci} + R_{ai} + R_{mi} + R_{ci}} v_{ACi} \end{aligned} \tag{4.92}$$

Kirchhoff's law applied at the furnace star-point, gives the electrode current balance:

$$\begin{aligned} i_{e1} + i_{e2} + i_{e3} &= 0 \\ \frac{di_{e1}}{dt} + \frac{di_{e2}}{dt} + \frac{di_{e3}}{dt} &= 0 \end{aligned} \tag{4.93}$$

A combination between the voltage balance in Eq. 4.91 and the current balance in Eq. 4.93, gives the following current model:

$$\begin{aligned} \frac{di_{e1}}{dt} &= \frac{1}{L_1L_2 + L_2L_3 + L_3L_1} \{ (L_2 + L_3)\, v_{T1} + L_2 v_{T2} - [(L_2 + L_3)\, R_1 \\ &\quad + L_2R_3]\, i_{e1} + [L_3R_2 - L_2R_3]\, i_{e2} \\ &\quad - (L_2 + L_3)\, \tilde{v}_{AC1} + L_3\tilde{v}_{AC2} + L_2\tilde{v}_{AC3} \} \\ \frac{di_{e2}}{dt} &= \frac{1}{L_1L_2 + L_2L_3 + L_3L_1} \{ -L_3 v_{T1} + L_1 v_{T2} + [L_3R_1 - L_1R_3]\, i_{e1} \\ &\quad - [(L_1 + L_3)R_2 + L_1R_3]\, i_{e2} \\ &\quad + L_3\tilde{v}_{AC1} - (L_1 + L_3)\, \tilde{v}_{AC2} + L_1\tilde{v}_{AC3} \} \\ \frac{di_{e3}}{dt} &= -\left(\frac{di_{e1}}{dt} + \frac{di_{e2}}{dt} \right) \end{aligned} \tag{4.94}$$

Measurement variables

The main electrical measurements on a submerged-arc furnace are the electrode currents and electrode-to-hearth voltages (electrode voltages) as previously discussed in Section 2.4.2.

The state variables given by Eq. 4.94 correspond to the measurements of the electrode currents on a furnace. When considering the electrode voltages on the other hand, the electrical induction effects discussed in Section 4.4.1,

must be taken into account. The electrode voltages are found from Eqs. 4.90 and 4.91, and must therefore be corrected corresponding to Eq. 4.82. This yields:

$$\begin{aligned} v_{e1} &= [R_1 - R_T/3]\, i_{e1} + [L_{11} - M_{31}] \frac{di_{e1}}{dt} + [M_{12} - M_{31}] \frac{di_{e2}}{dt} + \tilde{v}_{AC1} \\ v_{e2} &= [R_2 - R_T/3]\, i_{e2} + [L_{22} - M_{12}] \frac{di_{e2}}{dt} + [M_{23} - M_{12}] \frac{di_{e3}}{dt} + \tilde{v}_{AC2} \\ v_{e3} &= [R_3 - R_T/3]\, i_{e3} + [L_{33} - M_{23}] \frac{di_{e3}}{dt} + [M_{31} - M_{23}] \frac{di_{e1}}{dt} + \tilde{v}_{AC3} \end{aligned} \quad (4.95)$$

The dynamic transient electrical model

In the dynamic model, the transient electrical conditions consist of the electrical model given in Eq. 4.94, the dynamic arc model and the electrical measurements described by Eq. 4.95. The model can be stated in the general form:

$$\begin{aligned} \dot{\underline{x}}_{el} &= \underline{f}_{el}(\underline{x}_{el}, \underline{x}_a, \underline{\theta}_{el}, \underline{u}) \\ \dot{\underline{x}}_a &= \underline{f}_a(\underline{x}_{el}, \underline{x}_a, \underline{\theta}_a) \\ \underline{y} &= \underline{g}(\underline{x}_{el}, \underline{x}_a, \underline{\theta}_{el}) \end{aligned} \quad (4.96)$$

where $\underline{x}_{el}$ represents the electrical state vector and contains the electrode currents, $\underline{x}_a$ represents the arc state vector, $\underline{u}$ is the model input vector and contains the transformer voltages, and $\underline{y}$ represents the model measurements vector and contains the electrode currents and the electrode voltages. Furthermore, $\underline{\theta}_{el}$ and $\underline{\theta}_a$ represent parameters in the electrical model and the arc models, respectively.

The state vectors are given as:

$$\underline{x}_{el} = \begin{bmatrix} i_{e1} \\ i_{e2} \\ i_{e3} \end{bmatrix} \qquad \underline{y} = \begin{bmatrix} i_{e1} \\ i_{e2} \\ i_{e3} \\ u_{e1} \\ u_{e2} \\ u_{e3} \end{bmatrix} \qquad \underline{u} = \begin{bmatrix} v_{T1} \\ v_{T2} \end{bmatrix} \quad (4.97)$$

The contents of the arc state vector contents will depend on which arc model description that are used. In the case of Sakulin's simplified model (Sakulin, 1980), described in Section 3.7.2, the state vector contains the arc radii r_{ai}. If the arc model proposed in Section 3.7.3 is used, the state vector contains the arc temperatures T_{ai}.

Simulation model

A simulation model has been developed based on the model in Eq. 4.96. The electrical model has been implemented with both the proposed AC arc model in Section 3.7.3, as well as Sakulin's simplified arc model (Sakulin, 1980), described in Section3.7.2.

The complete model of the transient electrical conditions has been implemented in Matlab, and the model has been used for analyzing the electrical behavior and especially the effects of arcing on the electrical states, which is described in Section 5.1. Furthermore, the model has been applied in an estimator scheme for estimating unknown process conditions in the hearth of a submerged-arc furnace. This is further discussed in Section 8.4.1 and in Valderhaug and Balchen (1993).

4.5 Concluding remarks

In this chapter the focus has been on modelling the electrical system of a ferrosilicon furnace. First, the conduction in the burden of such a furnace is treated. Next, a survey of proposed model descriptions of electric furnaces is given. Finally, three different model descriptions for the electrical conditions in a ferrosilicon furnace, are developed:

- A steady-state model description based on the equivalent circuit in Fig. 4.5, is derived. This is described in Section 4.3.2. This model is applied in simulation studies of the electrical conditions in a ferrosilicon furnace and analyses of electrical control strategies.

- A simplified steady-state model based on the simplified equivalent circuit in Fig. 4.6, is developed in Section 4.3.3. This model is used in analyzing the interaction effect between the electrical phases in a ferrosilicon furnace.

- A dynamic model of the transient electrical condition is derived based on the equivalent circuit in Fig. 4.7. This is described in Section 4.4.2. This model is used in analyses of the furnace's electrical environment and is applied in an estimator of inner process conditions.

Chapter 5

Analyzing the electrical system

In this chapter the furnace's electrical environment is analyzed. First, the effect of arcing on the electrical conditions is discussed and analyzed by measurements and simulation studies. Next, the electrical interaction effect is modeled and analyzed by furnace experiments and simulation studies. Then, the electrical aspects of furnace operation are discussed as a basis for the discussions of electrical control strategies. Finally, the behavior of the electrical variable is investigated, and the effects of furnace operations on the electrical variables are discussed and demonstrated by furnace measurements.

5.1 The effect of arcing on the electrical conditions

The presence of arcing in the cavities of a ferrosilicon furnace has a noticeable effect on the furnace's electrical environment. An electric arc corresponds to a nonlinear electric circuit element, and the presence of arcing in an electric circuit will cause distortion of the currents and voltages in the circuit. The distortion of the electrical variables will be manifested by the appearance of harmonics to the original sinusoidal signals.

Figure 5.1 shows typical waveforms for the measured electrode currents and electrode voltages on the furnace at Elkem Thamshavn. The current and voltage signals are only distorted in a minor way, and especially the currents have almost pure sinusoidal waveforms. The electrical distortion is better illustrated by drawing Lissajous figures of the measurement. This is shown in Fig. 5.2.

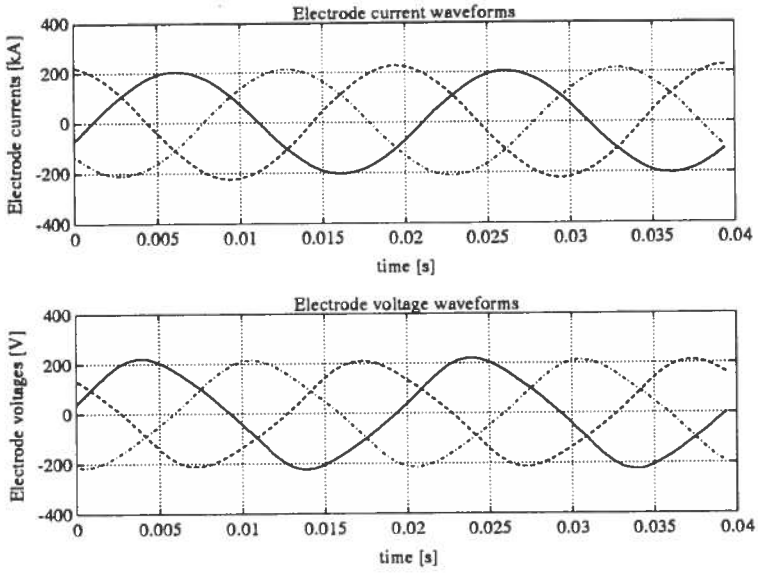

Figure 5.1: Typical current and voltage waveforms on a ferrosilicon furnace.

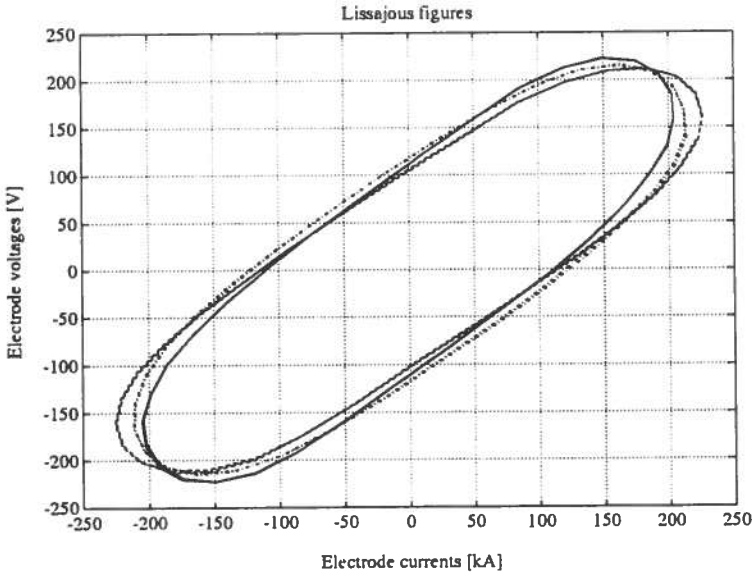

Figure 5.2: Lissajous figures of the current and voltage signals.

The effects of arcing on the electrical measurements on submerged-arc furnaces are significantly less than the effects noticed on open-arc furnaces. The reason for this is partly that the arcs are present in the cavities in the furnace charge, and that there will be charge conduction in parallel to the arcs, in contrast to the situation in an open-arc furnace. Therefore, the distortion of the measured variables are reduced. Another reason may be that the cavities prevail in an atmosphere with higher conductivity than an open-arc furnace. This will yield a more linear characteristic of the arc voltage itself, and thereby also give reduced distortion of the measured signals.

5.1.1 Describing the extent of arcing in electric furnaces

The extent of arcing and its effects on the electrical environments can be described and examined in various ways. The common way of analyzing the distortion effect on the electrical signals is harmonic analysis, and this methodology is commonly used to indicate the extent of arcing in submerged-arc furnaces.

The contents of harmonics in the electrical variables

The contents of harmonics in the electrode voltages and electrode currents can be found by applying high-pass filters on the electrical measurement signals. This is described among others by Skreien (1974), Stewart (1980) and Rennie (1983).

According to Stewart (1980) there is considerable interaction between the electrical phases regarding the contents of harmonics in both the electrode currents and electrode voltages. This interaction effect is smaller for the harmonic contents in the electrode voltages compared to the electrode currents. Furthermore, the portion of higher harmonics is larger in the electrode voltages. This has led to the use of the filtered electrode voltages as descriptions of the extent of arcing in the furnace. The filtered electrode voltages are commonly denoted "**the arc voltages**" (Rennie, 1983). However, this notation is not used in this thesis, because it is a somewhat artificial denotation.

The harmonic filter used at the furnace at Elkem Thamshavn is a sixth-order Tchebycheff high-pass filter with 0.2 dB ripple in the pass-band and a cut-off frequency of 130 Hz. This results in a rejection of the 50 Hz harmonic by 64.6 dB and a maximum rejection of frequencies above 130 Hz by 0.2 dB. Rennie (1983) describes the use of a fifth-order Butterworth

high-pass filter with a cut-off frequency of 150 Hz to filter the electrode voltages.

Fourier analysis

The power spectrum density can also be investigated in detail by the use of Fourier analysis at the furnace at Elkem Thamshavn . The furnace is equipped with a high-frequency data collector, and the measured electrode voltage and electrode current variables are sampled with time-intervals of $6.25 \cdot 10^{-5}$ s and collected in batches of 2048 at a total length 1.28 s. Fourier analysis is subsequently carried out on these data-batches and the power spectra are found. These sampling and analyzing operations continue and the power spectrum densities can be presented with time-intervals of less than one minute.

Figure 5.3 shows the typical power spectrum densities for the electrode currents and electrode voltages at the furnace at Elkem Thamshavn, while Fig. 5.4 gives a more detailed view of the higher harmonics.

The content of higher harmonics in the electrode currents is generally less than in the electrode voltages. The higher harmonics in the electrode currents are mainly the third (150 Hz) and the fifth (250 Hz) odd-harmonics, but also even-harmonics like the second (100 Hz), fourth (200 Hz) and the sixth (300 Hz), are present. The electrode voltages show a different distribution. The main odd-harmonic is the third, while the fifth harmonic is considerable smaller, and the main even-harmonic is the fourth, while the second harmonic is negligible.

A detailed analysis of the harmonic distribution in a submerged-arc furnace is complicated by the complex interactions between the arcing in the different electrical phases and between the changes in the electrical conditions and how they are manifested in the harmonic distribution. However, some main relations can be outlined:

1. The presence of even-harmonics in the measured electrode currents and electrode voltages is caused by a non-symmetric arc characteristic due to the different anode and cathode properties during the alternating cycles.

   Variations in the arc lengths, for instance due to the arc jet impinging in the metal bath during the half-cycle when the electrode is cathode, will cause formation of even-harmonics.

2. If a simple electrical star-circuit is assumed in the furnace burden, the presence of harmonics will meet some constraints. In the case of an

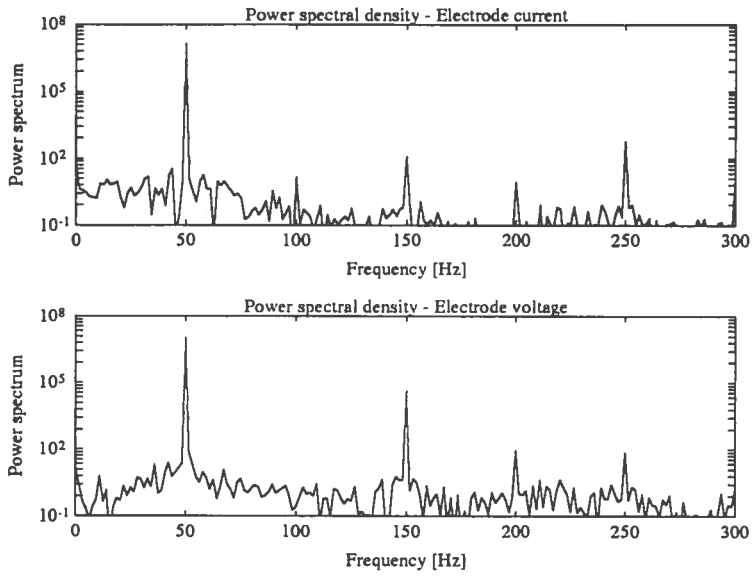

Figure 5.3: Power spectrum density of the measured current and voltage signals.

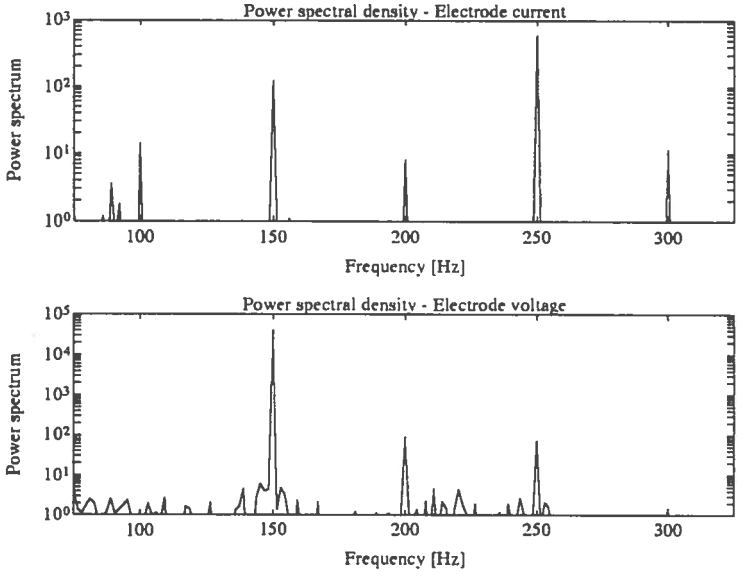

Figure 5.4: Detail view of the power spectrum density of the measured current and voltage signals.

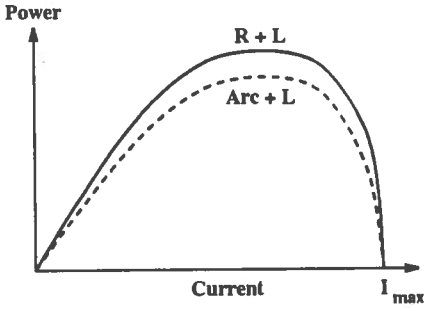

Figure 5.5: Principal power-current relations for resistor and arc heating.

electrical symmetric furnace, it can for instance be derived that the electrode currents will not contain any zero harmonic or any "thirds" harmonics (no 3rd, 6th, 9th ...).

However, a real furnace is asymmetric, and no constraints can be stated for the harmonic distribution in neither the electrode currents nor the electrode voltages.

Fourier analysis of electrical measurement data from electric furnaces and its application as a diagnostic tool are further treated among others by Ochs, Hartman and Witkowski (1986) and Rennie (1983). Rennie (1983) compared the filtered electrode voltage ("the arc voltage") with the harmonic distribution found from Fourier analysis, and concluded with stating that "the arc voltage" gives a satisfactory description of the contents of harmonics in the electrode voltage.

The arc power factor

The effects of arcing on the total power dissipation in a submerged-arc furnace are discussed among others by Barker (1980). He found that the power dissipated in a circuit consisting of an electric arc and an inductance, is less than in a circuit with a resistance and an inductance. This is illustrated in Fig. 5.5, where I_{max} is the maximum obtainable current with only the inductive element in the circuit: $I_{max} = V_e/X$, where V_e is the applied voltage and the circuit reactance is given by $X = \omega L$.

Barker (1980) proposed the following expression to describe the power dissipation in a single-phase electric circuit with arcing:

$$P = k_{arc} X I_{rms} \cdot \sqrt{{I_{max}}^2 - {I_{rms}}^2} \tag{5.1}$$

where k_{arc} is denoted the **arc power factor**, and I_{rms} is the current rms-magnitude. For a pure resistance-inductance circuit, $k_{arc} = 1.0$.

This single-phase expression can be applied to each of the phases in a balanced three-phase circuit, and the parameters k_{arc} and I_{max} can be found from furnace experiments.

The expression in Eq. 5.1 can alternatively be rearranged to:

$$P = k_{arc} \cdot I_{rms} \cdot \sqrt{V_e{}^2 - X^2 {I_{rms}}^2} \tag{5.2}$$

According to De Waal et al. (1992) calculations carried out on three-phase submerged-arc furnaces indicate that typical values of the arc power factors are:

$$k_{arc} \approx 0.95 \tag{5.3}$$

Barker (1980) have shown that if a pure sign-function model for the arc voltage:

$$v_a(t) = V_a \cdot \text{sign}\,(i(t)) \tag{5.4}$$

is applied on a symmetric three-phase furnace circuit, this will result in an arc power factor of $k_{arc} = 0.91$. Thus, the observed arc power factors indicate that the electric arcs occurring in submerged-arc furnaces have waveforms in between a square-wave and a sinusoid.

Alternative arc factor expressions based on principles similar to Barker's arc power factor have been proposed by Keyser (1987) and Person (1989).

5.1.2 Model simulation

The effects of arcing on the electrical conditions are investigated by simulation studies of the dynamic electrical model that was presented in Section 4.4.2. The electric arcs are described by the simplified version of Sakulin's model (Sakulin, 1980), which is described in Section 3.7.2, extended by the anode and cathode voltage model proposed in Section 3.7.4.

The simulation results, which are presented in the following, describe symmetric electrical condition in the furnace. The model parameters are adjusted manually to achieve model outputs corresponding to the furnace measurement data in Fig. 5.1. The electrical model parameters used during the simulations are given in Table 5.1, while the arc model parameters are given in Table 5.2.

Table 5.1: The parameters of the dynamic electrical model during simulations.

Transformer voltage	V_T	[V]	$\sqrt{2} \cdot 265.0$		
Transformer resistances	R_T	[mΩ]	0.03		
Transformer reactances	L_T	[μH]	0.96		
Electrode resistances	R_{ei}	[mΩ]	0.12	0.12	0.12
Electrode reactances	X_{ei}	[μH]	2.32	2.32	2.32
Metal bath resistances	R_{mi}	[mΩ]	0.12	0.12	0.12
Charge resistances	R_{ci}	[mΩ]	2.00	2.00	2.00
Bottom resistances	R_{bi}	[mΩ]	0.20	0.20	0.20

Table 5.2: The parameters of the dynamic arc models during simulations.

Arc lengths	h_{ai}	[m]	0.08
Anode and cathode voltages	V_{ACi}	[V]	5.0
Cavity radii	r_{wi}	[m]	0.80
Cavity gas temperatures	T_{gi}	[K]	2250.0
Cavity wall temperatures	T_{wi}	[K]	2250.0
Cavity bottom temperatures	T_{bi}	[K]	2250.0
Electrode tip temperatures	T_{ei}	[K]	2250.0
Cavity gas pressures	p_{ai}	[Pa]	$1.01325 \cdot 10^5$
Arc channel emissitivities	ϵ_{ai}		0.15
Cavity wall emissitivities	ϵ_{wi}		0.95
Thermal cond., thermal layer	λ_{wi}	[W/m^{2}K]	800.0
Thermal cond., cavity bottom	λ_{bi}	[W/m^{2}K]	800.0
Thermal cond., electrode tip	λ_{ei}	[W/m^{2}K]	800.0
Plasma jet convection coeffisients	β_{ai}	[W/A^{2}K]	$8.0 \cdot 10^{-8}$
Cavity gas specific heat capacity	c_p	[kJ/kg K]	200.0
Conductivity constants	c_{1i}		1200.0
Conductivity constants	c_{2i}		0.75
Conductivity constants	c_{3i}		30000.0

Figure 5.6 shows the simulated electrode currents and electrode voltages, while the corresponding Lissajous figure is shown in Fig. 5.7. By comparison with the furnace measurement data it can be seen that the model describes the furnace conditions in a qualitatively correct way. However, there is no exact correspondence, and the simulated Lissajous figure is for instance broader than the measured figures, which can be explained by too large phase reactance during the simulation.

Figure 5.8 shows the relations between the electrode, arc and charge currents, as well as the relation between the electrode and arc voltage in phase 1, during the simulation. The major portion of the electrode current goes through the electric arc, while the by-pass charge current is almost negligible. It can also be seen that the arc current is only minor distorted and is thereby comparable to the electrode current waveform. The arc voltage is considerable less than the electrode-to-hearth voltage, but significantly distorted. This means that there are considerable voltage drops along the electrode column and in the furnace charge bottom below the cavities.

Figure 5.9 gives a better view of the arc current and voltage waveforms. The arc voltages are heavily distorted, while the arc currents are almost sinusoidal signals.

Figure 5.10 shows the Lissajous figure of the arc current and voltage. This is commonly denoted the arc current-voltage characteristic. The nonlinear nature of the arc is clearly illustrated by the arc characteristic. The twist of the curve around the origin is a result of the model of the anode and cathode voltages, which is previously described in Section 3.7.4.

Figure 5.11 gives a closer view of the relation between the total arc voltage and the anode and cathode voltages in the model, and it also shows the applied anode and cathode voltage characteristic.

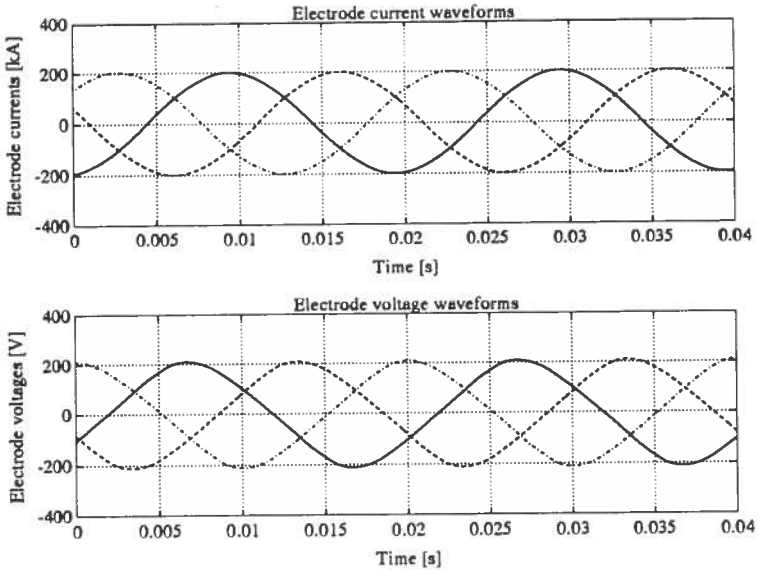

Figure 5.6: Simulated electrode current and electrode voltage waveforms.

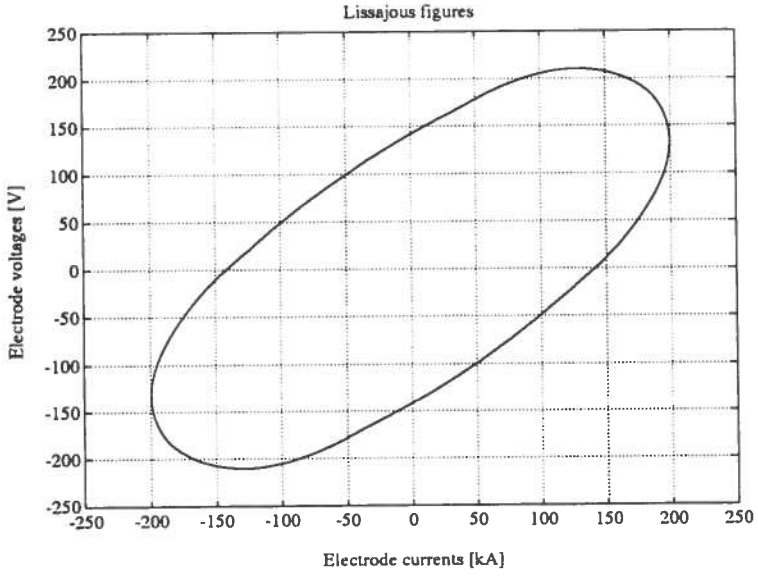

Figure 5.7: Simulated Lissajous figures for electrode voltages and currents.

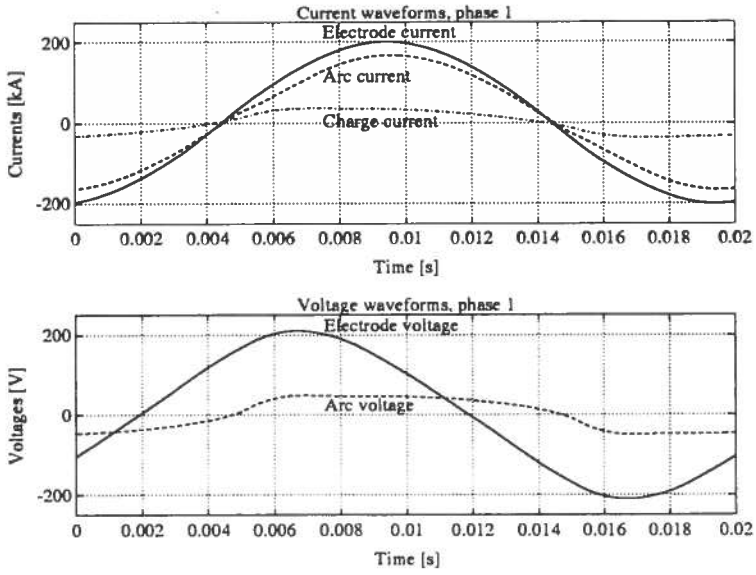

Figure 5.8: Simulated electrode, arc and charge currents and electrode and arc voltages.

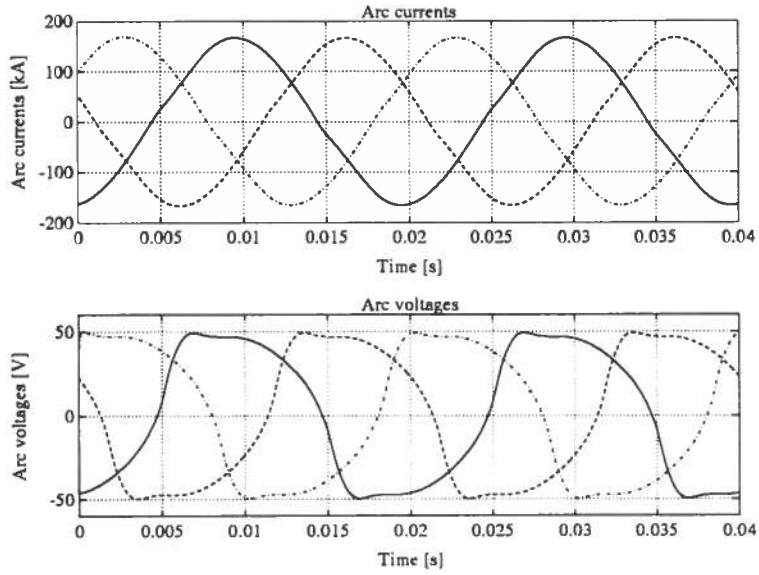

Figure 5.9: Simulated arc currents and voltages.

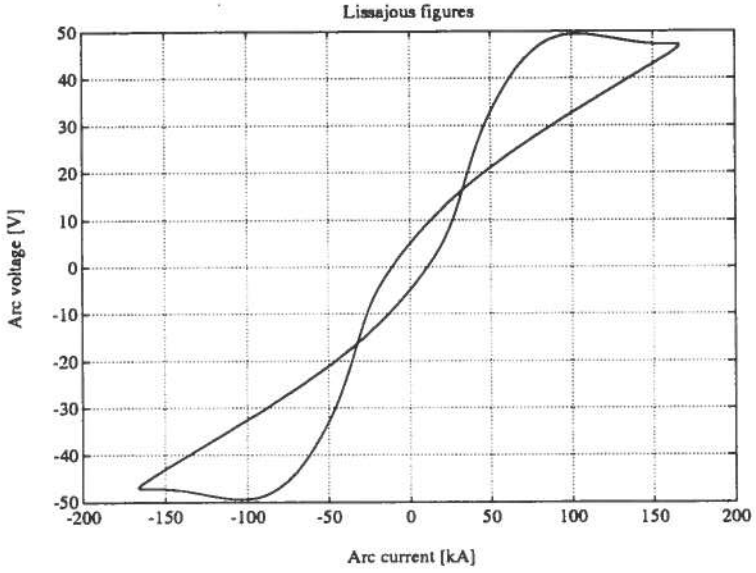

Figure 5.10: Simulated arc current and voltage characteristic.

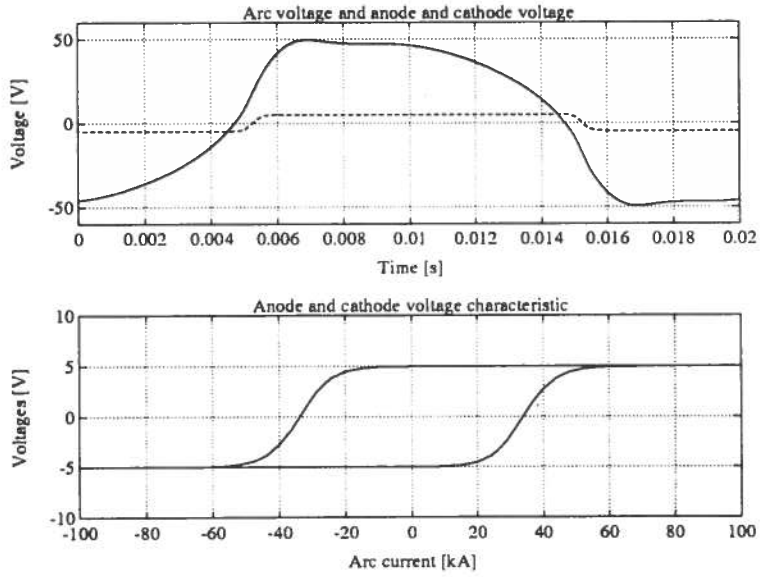

Figure 5.11: Simulated anode and cathode voltage characteristic.

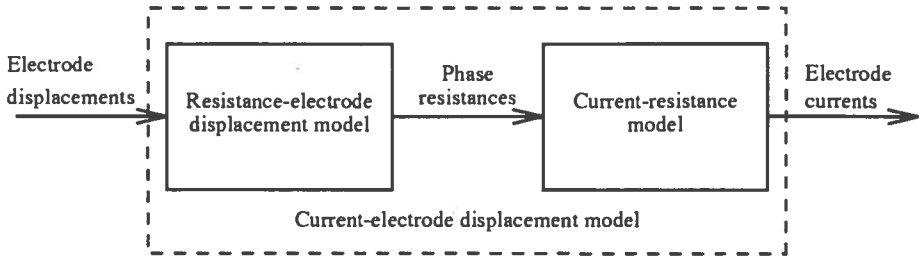

Figure 5.12: Illustration of the model of the current-controlled furnace.

5.2 The interaction effect between the electrical phases

5.2.1 A model of a current-controlled submerged-arc furnace

A model of how electrode displacements affect the electrode currents is developed based on the current model derived in Section 4.3.3 and which is stated in Eq. 4.66 (Valderhaug and Sletfjerding, 1992). The model can be written on the form:

$$\begin{pmatrix} \Delta i_{e1} \\ \Delta i_{e2} \\ \Delta i_{e3} \end{pmatrix} = \boldsymbol{H} \cdot \begin{pmatrix} \Delta h_{a1} \\ \Delta h_{a2} \\ \Delta h_{a3} \end{pmatrix} \tag{5.5}$$

where Δi_{ei} represent the current deviations as results from the electrode displacements Δh_{ai}. Matrix $\boldsymbol{H}$ is on the form:

$$\boldsymbol{H} = \begin{pmatrix} h_{11} & h_{12} & h_{13} \\ h_{21} & h_{22} & h_{23} \\ h_{31} & h_{32} & h_{33} \end{pmatrix} \tag{5.6}$$

The matrix elements h_{ij} describe the effect of electrode movements on the electrode currents. Matrix $\boldsymbol{H}$ depends on the resistances, the reactances and the arc characteristics in the furnace. The model in Eq. 5.5 is derived by combining two sub-models:

1. **A current-resistance model** which describes how phase resistance variations affect the electrode currents.

2. **A resistance-electrode displacement model** which describes how the phase resistance depends on the electrode movements.

This is illustrated in Fig. 5.12.

The common way of controlling the electrical environment is to control the electrode currents by using electrode displacements as control inputs. Hence, matrix $\boldsymbol{H}$ can be looked upon as the linearized, steady-state transfer matrix between the input and the output of the current-controlled electrical system in a submerged-arc furnace. Thus, the off-diagonal elements in $\boldsymbol{H}$ describe the interaction effect between the electrical phases.

The current-resistance model

A linearized model of how variations in the phase resistances Δr_i, affect the electrode currents is developed in Appendix B.1. The model is found to be:

$$\begin{aligned}
\Delta i_{e1} &= \frac{|V_T|^2}{{Z^0_{sum}}^2}\left\{\frac{\alpha_{11}}{|I^0_{e1}|}\Delta r_1 + \frac{\alpha_{12}}{|I^0_{e1}|}\Delta r_2 + \frac{\alpha_{13}}{|I^0_{e1}|}\Delta r_3\right\} \\
\Delta i_{e2} &= \frac{|V_T|^2}{{Z^0_{sum}}^2}\left\{\frac{\alpha_{21}}{|I^0_{e2}|}\Delta r_1 + \frac{\alpha_{22}}{|I^0_{e2}|}\Delta r_2 + \frac{\alpha_{23}}{|I^0_{e2}|}\Delta r_3\right\} \\
\Delta i_{e3} &= \frac{|V_T|^2}{{Z^0_{sum}}^2}\left\{\frac{\alpha_{31}}{|I^0_{e3}|}\Delta r_1 + \frac{\alpha_{32}}{|I^0_{e3}|}\Delta r_2 + \frac{\alpha_{33}}{|I^0_{e3}|}\Delta r_3\right\}
\end{aligned} \tag{5.7}$$

where the matrix elements α_{ij} are defined in Eq. B.6 and Z^0_{sum} is defined in Eq. B.2, and where superscript ^{0} denotes the electrical working-point. These model parameters are all expressions in terms of the phase impedances, which are measurable, and a numerical expression of the current-resistance model can easily be computed. The model in Eq. 5.7 can equivalently be expressed as:

$$\begin{pmatrix} \Delta i_{e1} \\ \Delta i_{e2} \\ \Delta i_{e3} \end{pmatrix} = \frac{|V_T|^2}{{Z^0_{sum}}^2} \begin{pmatrix} \frac{\alpha_{11}}{|I^0_{e1}|} & \frac{\alpha_{12}}{|I^0_{e1}|} & \frac{\alpha_{13}}{|I^0_{e1}|} \\ \frac{\alpha_{21}}{|I^0_{e2}|} & \frac{\alpha_{22}}{|I^0_{e2}|} & \frac{\alpha_{23}}{|I^0_{e2}|} \\ \frac{\alpha_{31}}{|I^0_{e3}|} & \frac{\alpha_{32}}{|I^0_{e3}|} & \frac{\alpha_{33}}{|I^0_{e3}|} \end{pmatrix} \begin{pmatrix} \Delta r_1 \\ \Delta r_2 \\ \Delta r_3 \end{pmatrix} \tag{5.8}$$

The resistance-electrode displacement model

A linearized model of how changes in the phase resistances Δr_i are related to electrode displacements Δh_{ai}, is developed in Appendix B.2. The model is assumed to be diagonal, which means that electrode movements in one phase only affect the resistance in the same phase. The model expression, which can be found in Eq. B.33, can be written as:

$$\begin{pmatrix} \Delta r_1 \\ \Delta r_2 \\ \Delta r_3 \end{pmatrix} = \begin{pmatrix} \beta_1 & 0 & 0 \\ 0 & \beta_2 & 0 \\ 0 & 0 & \beta_3 \end{pmatrix} \begin{pmatrix} \Delta h_{a1} \\ \Delta h_{a2} \\ \Delta h_{a3} \end{pmatrix} \tag{5.9}$$

This model depends on the partly unknown current paths in the furnace burden. The model parameters β_i, which are defined in Eq. B.33, are expressions in terms of the arc characteristics and the various resistances in the hearth of the furnace. These quantities can hardly be measured, and numerical values will more or less be based on assumptions. As a result of this, only an approximate model can be computed from Eq. 5.9. However, this model is useful in simulation studies of the electrical conditions in the furnace, and a more accurate numerical model can be achieved from furnace experiments.

The current-electrode displacement model

A complete model describing the changes in electrode currents Δi_{ei}, as a result of electrode displacements Δh_{ai}, is obtained by inserting the resistance model in Eq. 5.9 into the current-resistance model in Eq. 5.7. The model is found to be:

$$\begin{pmatrix} \Delta i_{e1} \\ \Delta i_{e2} \\ \Delta i_{e3} \end{pmatrix} = \frac{|V_T|^2}{Z_{sum}^{0\,2}} \begin{pmatrix} \frac{\alpha_{11}\beta_1}{|I_{e1}^0|} & \frac{\alpha_{12}\beta_2}{|I_{e1}^0|} & \frac{\alpha_{13}\beta_3}{|I_{e1}^0|} \\ \frac{\alpha_{21}\beta_1}{|I_{e2}^0|} & \frac{\alpha_{22}\beta_2}{|I_{e2}^0|} & \frac{\alpha_{23}\beta_3}{|I_{e2}^0|} \\ \frac{\alpha_{31}\beta_1}{|I_{e3}^0|} & \frac{\alpha_{32}\beta_2}{|I_{e3}^0|} & \frac{\alpha_{33}\beta_3}{|I_{e3}^0|} \end{pmatrix} \begin{pmatrix} \Delta h_{a1} \\ \Delta h_{a2} \\ \Delta h_{a3} \end{pmatrix} \tag{5.10}$$

or shortly written in the vector form of Eq. 5.5:

$$\underline{\boldsymbol{\Delta i_e}} = \boldsymbol{H} \cdot \underline{\boldsymbol{\Delta h_a}} \tag{5.11}$$

where vector $\underline{\boldsymbol{\Delta i_e}}$ contains the changes in the electrode currents and $\underline{\boldsymbol{\Delta h_a}}$ contains the electrode displacements. The model of how the electrode displacements affect the electrode currents, given in Eqs. 5.10 and 5.11, is illustrated in Fig. 5.12.

This model can be considered as a linearized input-output description at steady-state electrical conditions, of a current-controlled submerged-arc furnace, and where the off-diagonal elements in $\boldsymbol{H}$ describe the interaction effect between the electrical phases.

5.2.2 Barker's interaction factors

Barker (1981) analyzed the electrical interaction effect in electric furnaces and defined the so-called **interaction factors** for submerged-arc furnaces. In the analyses Barker (1981) used an electrical model, corresponding to the current model derived in Section 4.3.3 and illustrated in Fig. 4.6, simplified by assumptions of equal resistances and reactances in each of the phases

and stiff electrode-to-electrode voltages:

$$R_i = R\ ,\quad X_i = X\ ,\quad Z_T = 0\ ,\quad Z_m = R + j \cdot X \tag{5.12}$$

Barker (1981) derived a model that gives a dimensionless description of how variations in the phase resistances Δr_i result in electrode current deviations Δi_{ei}:

$$\begin{pmatrix} \frac{\Delta i_{e1}}{|I_{e1}|} \\ \frac{\Delta i_{e2}}{|I_{e2}|} \\ \frac{\Delta i_{e3}}{|I_{e3}|} \end{pmatrix} = \begin{pmatrix} f_{11} & f_{12} & f_{13} \\ f_{21} & f_{22} & f_{23} \\ f_{31} & f_{32} & f_{33} \end{pmatrix} \begin{pmatrix} \frac{\Delta r_1}{|Z_m|} \\ \frac{\Delta r_2}{|Z_m|} \\ \frac{\Delta r_3}{|Z_m|} \end{pmatrix} \tag{5.13}$$

where the model matrix elements f_{ij} are the so-called interaction factors. The model is symmetric because of the equal resistance and reactance assumption, and the interaction factors f_{ij} can be derived as:

$$\begin{aligned} f_{11} = f_{22} = f_{33} &= -\frac{2}{3} \cdot \frac{R}{|Z_m|} \\ f_{21} = f_{32} = f_{13} &= \frac{1}{3} \cdot \frac{-0.5R + 0.866X}{|Z_m|} \\ f_{31} = f_{23} = f_{12} &= \frac{1}{3} \cdot \frac{-0.5R - 0.866X}{|Z_m|} \end{aligned} \tag{5.14}$$

The nature of the electrical interaction effect depends on the phase sequence of the applied transformer voltages. The interaction model in Eq. 5.13 is valid for the "forward" phase sequence T1-T2-T3, in accordance with Eq. 4.52. If the "backward" phase sequence is applied, the corresponding interaction model will contain a matrix which is the transposed version of the interaction matrix in Eq. 5.13.

Barker's interaction factors described by Eqs. 5.13 and 5.14, are closely related to the current-resistance model derived in Eq. 5.7. Appendix B.3 shows how Barker's interaction factors can be derived from the current-resistance model, and that the interaction factor description is a special case of this model.

Barker's interaction factors give a simple description of the interaction effects between the electrical phases in a submerged-arc furnace. Compared to the more complex model in Eq. 5.10, which almost exclusively can be applied to simulation studies, Barker's interaction model in Eqs. 5.13 and 5.14, is especially suitable for more simple analyses of the electrical interaction and its dependency of the electrical conditions. This is among others

due to the dimensionless nature of the model, which makes the analyses independent of the electrical working-point of the furnace.

The interaction factors in Eq. 5.14 can alternatively be expressed in terms of the furnace power factor $\cos\phi$ (Barker et al., 1992):

$$\cos\phi = \frac{R}{|Z_m|} \tag{5.15}$$

where R and Z_m are the phase resistance and impedance, respectively. This gives the following expressions:

$$\begin{aligned} f_{11} = f_{22} = f_{33} &= -\frac{2}{3} \cdot \cos^2\phi \\ f_{21} = f_{32} = f_{13} &= \frac{1}{3} \cdot \left(-0.5\cos^2\phi + 0.866\sin\phi\cos\phi\right) \\ f_{31} = f_{23} = f_{12} &= \frac{1}{3} \cdot \left(-0.5\cos^2\phi - 0.866\sin\phi\cos\phi\right) \end{aligned} \tag{5.16}$$

In this connection it should be stressed that these interaction factor expressions only will be correct if the assumption of stiff electrode-to-electrode voltages in Eq. 5.12 can be applied. Usually this is not the case, and the impedances in the transformer circuit must be considered in the analysis. The phase resistances and reactances can for instance be adjusted in accordance with Eq. 4.62 in order to find the "effective" phase resistances and reactance, which in turn can be applied in Eqs. 5.14 and 5.15, in order to obtain a correct interaction description by Eq. 5.16.

The interaction effects depend on the furnace electrical power factor, in accordance with Eq. 5.16. This is illustrated in Fig. 5.13, which shows the interaction factors f_{11}, f_{12} and f_{13}, describing the effects of perturbations in the phase resistance R_1 on the the currents in the three electrodes, as functions of the furnace power factor $\cos\phi$.

Figure 5.13 shows that the interaction effect increases rapidly with decreasing power factor. At power factors below 0.5, the movement of one electrode will actually cause a greater change to the current in another electrode than to its own current. Naturally, this is of great importance to the electrical current control system. According to Barker and colleagues (1992) the interaction effects is seldom observed at current-controlled furnaces with power factors greater than 0.9. At furnaces with power factor at 0.8 the interaction problem is noticeable, and at 0.7 it is significant and impairs the furnace operation. At furnaces with power factors at 0.6 it is a major problem and contributes to major production losses.

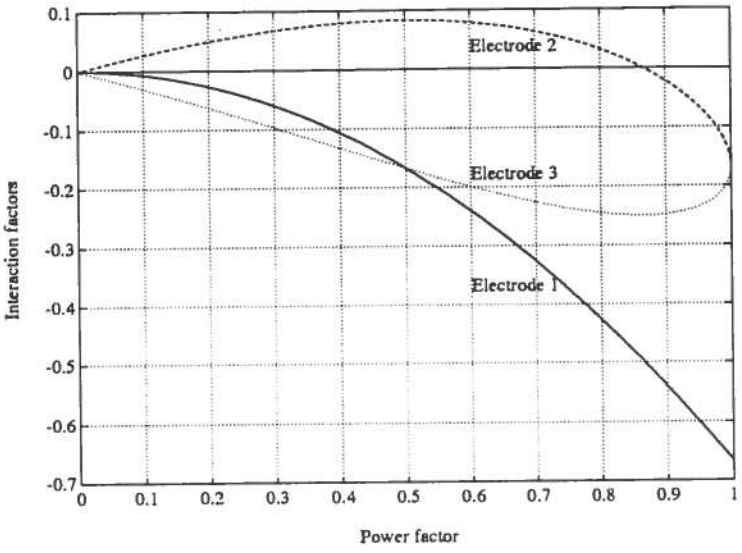

Figure 5.13: Barker's interaction factors for perturbations in phase resistance R_1, f_{11}, f_{12} and f_{13}, as functions of the furnace power factor $\cos\phi$.

5.2.3 Furnace experiments

The electrical interaction effect in a submerged-arc ferrosilicon furnace is analyzed by furnace experiments and simulation studies. The experiments have been carried out on the furnace at Elkem Thamshavn, producing 75% ferrosilicon.

The electrical interaction effect of the furnace was analyzed by moving one electrode at a time, while the others are held fixed, and examining the corresponding changes in the measurements of the electrode currents and the phase resistances. The furnace electrical working-point at the start of the experiment is summarized in Table 5.3. However, the electrical conditions changed somewhat during the experiment.

Several experiments were carried out in both directions for all electrodes by step-response analysis. Figures 5.14, 5.15, 5.16 and 5.17 show typical results of these experiments:

- Figure 5.14 shows how a lowering of electrode 1 affects the electrode currents and the phase resistances.
- Figure 5.15 shows the effects of lowering of electrode 2.
- Figure 5.16 shows the effects of lowering of electrode 3.

Table 5.3: The electrical working-point at the start of the experiment.

Electrode currents	I_{ei} [kA]	134.0	136.5	130.8
Electrode voltages	V_{ei} [V]	143.5	140.0	136.0
Phase resistance	R_i [mΩ]	0.83	0.74	0.76
Phase reactance	X_i [mΩ]	0.68	0.71	0.71
Phase power factor	$\cos\phi$	0.77	0.72	0.73

- Figure 5.17 show the effects of raising electrode 3.

Figures 5.14 to 5.17 show that there is a considerable variation in the electrical states due to disturbance effects. This is particularly due to occasional variations in the charge resistivity and the arcing conditions, and hence the current distribution in the furnace burden. Furthermore, the responses may also be suppressed by underlying trends of the electrical variables.

Despite the presence of disturbances, the effects of the applied electrode displacements on the electrode currents and resistances are significant. However, it is necessary to use some kind of filtering technique on the measured signals before numerical models, such as the resistance-electrode displacement model in Eq. 5.9 and the current-electrode displacement model in 5.10, can be computed based on the experiments. It should be further stressed that a considerable uncertainty will be connected with these model calculations.

The effects of electrode movements vary to some extent from one experiment to another, but displacements in the same direction yield corresponding results. Generally, the electrical conditions seemed to be more sensitive to downward displacements then upward, something that is a contradiction to the model assumption of accordance between electrode movements and changes in arc lengths. The experimental results are summarized in Table 5.4.

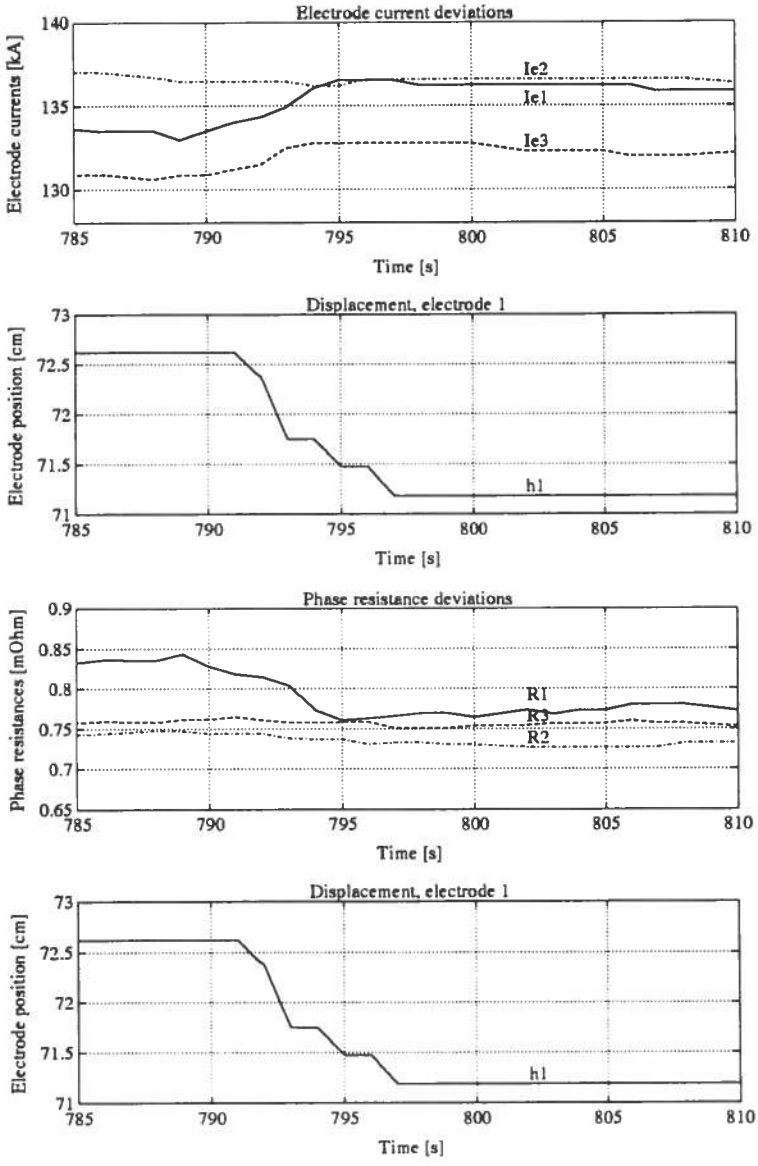

Figure 5.14: Electrode displacement experiment, electrode 1 lowered.

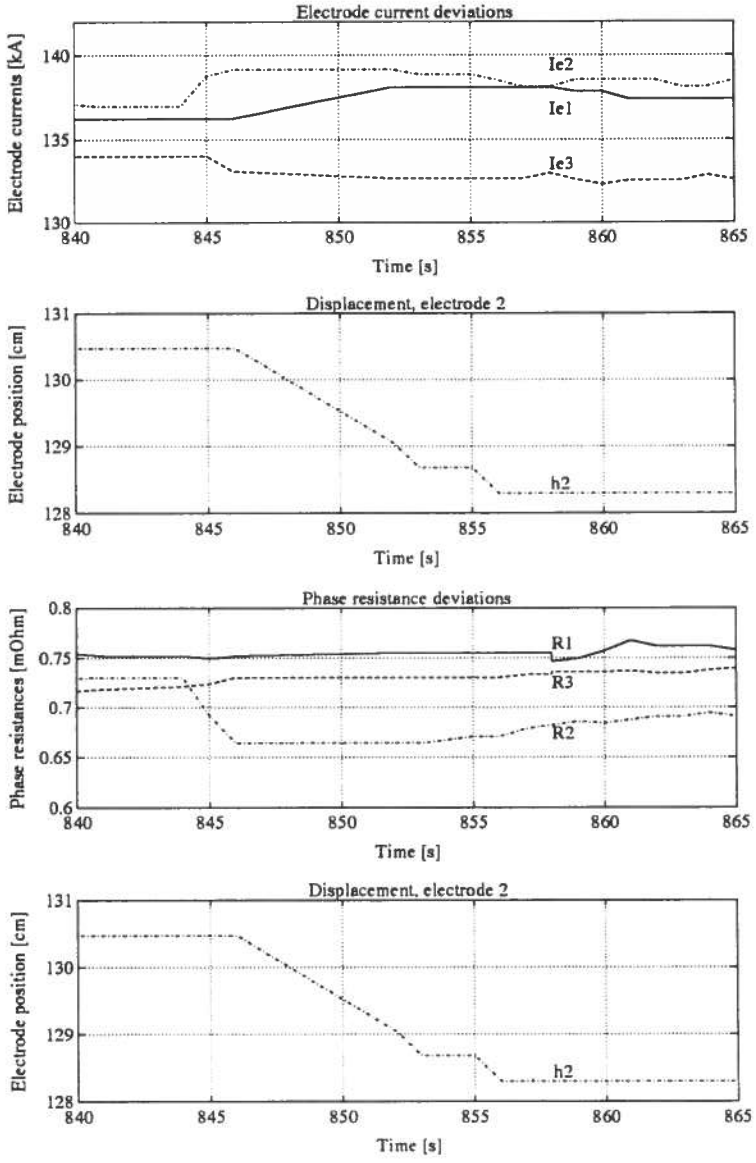

Figure 5.15: Electrode displacement experiment, electrode 2 lowered.

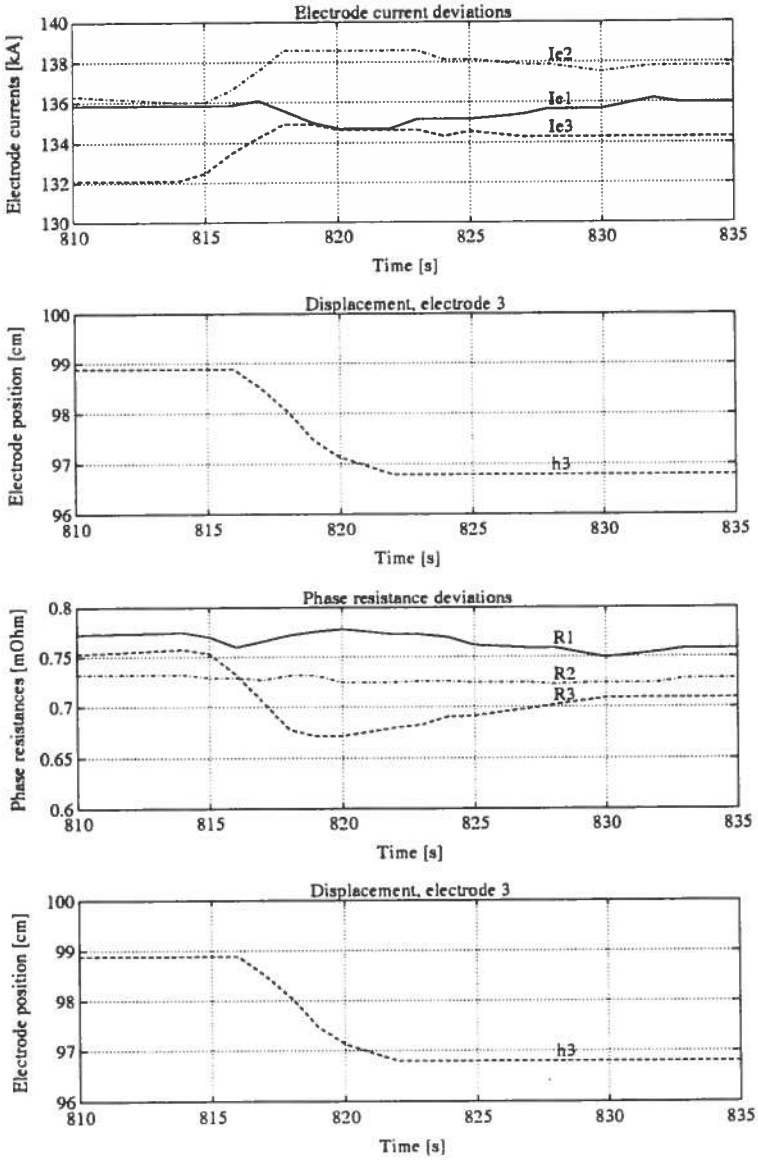

Figure 5.16: Electrode displacement experiment, electrode 3 lowered.

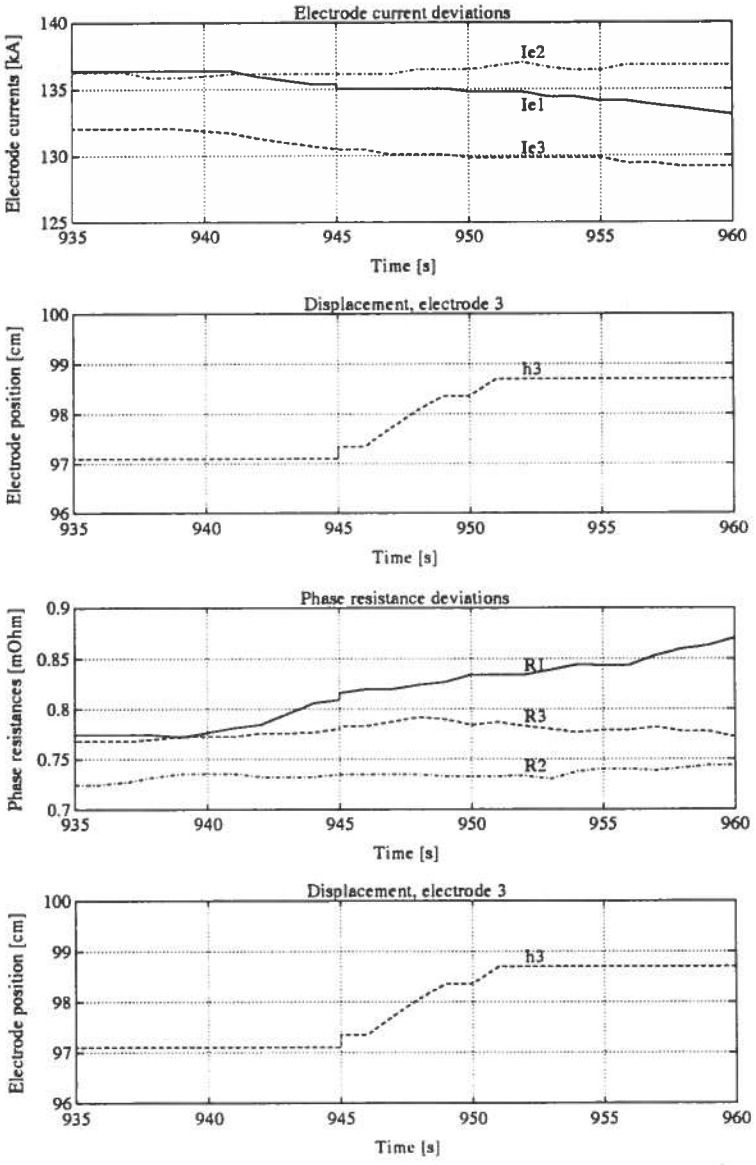

Figure 5.17: Electrode displacement experiment, electrode 3 raised.

Table 5.4: Results of the interaction experiments.

Displacements		Δi_{e1}	Δi_{e2}	Δi_{e3}	Δr_1	Δr_2	Δr_3
El. 1	+0.7 cm	−1.1	+0.3	−0.4	+0.01	−0.01	+0.01
El. 1	−1.4 cm	+2.6	−0.1	+1.8	−0.07	−0.01	−0.01
El. 2	+1.6 cm	+0.2	−0.3	−0.2	+0.00	+0.00	−0.01
El. 2	−2.2 cm	+1.8	+1.9	−1.3	+0.02	−0.07	+0.01
El. 3	+1.6 cm	−1.8	+0.1	−2.1	+0.07	+0.00	+0.02
El. 3	−2.1 cm	−0.3	+2.5	+2.2	+0.01	−0.00	−0.08

Model calculations

The resistance- and current-electrode displacement models derived in Eqs. 5.9 and 5.10, are calculated based on the experiment results. However, in the model calculations only the downwards experiments are used.

The resistance-electrode displacement model, corresponding to Eq. 5.9, is found as:

$$\begin{pmatrix} \Delta r_1 \\ \Delta r_2 \\ \Delta r_3 \end{pmatrix} = \begin{pmatrix} 0.050 & -0.009 & -0.005 \\ 0.007 & 0.032 & 0.001 \\ 0.007 & -0.005 & 0.038 \end{pmatrix} \begin{pmatrix} \Delta h_{a1} \\ \Delta h_{a2} \\ \Delta h_{a3} \end{pmatrix} \tag{5.17}$$

where the model is expressed in terms of [mΩ/cm].

Likewise, the input-output model of the current-controlled system, corresponding to the current-electrode displacement model in Eq. 5.10, is calculated as:

$$\begin{pmatrix} \Delta i_{e1} \\ \Delta i_{e2} \\ \Delta i_{e3} \end{pmatrix} = \begin{pmatrix} -1.90 & -0.82 & 0.14 \\ 0.07 & -0.86 & -1.19 \\ -1.29 & 0.59 & -1.05 \end{pmatrix} \begin{pmatrix} \Delta h_{a1} \\ \Delta h_{a2} \\ \Delta h_{a3} \end{pmatrix} \tag{5.18}$$

where the model is expressed in terms of [kA/cm].

Some electrical asymmetry was present while the experiments were carried out, something that can explain the asymmetric current model. Furthermore, the derived numerical models are connected with significant parameter uncertainty because of the difficulties in deciding the responses. However, the structure of the models will be less uncertain.

Table 5.5: The electrical working-point during simulations.

Electrode currents	I_{ei} [kA]	136.3	136.6	134.0
Electrode voltages	V_{ei} [V]	142.9	142.5	141.8
Phase resistance	R_i [mΩ]	0.77	0.75	0.77
Phase reactance	X_i [mΩ]	0.71	0.73	0.73
Phase power factor	$\cos\phi$	0.68	0.70	0.69

5.2.4 Simulation studies

The electrical interaction effect in the furnace is simulated by using the electrical steady-state model derived in Section 4.3.2, corresponding to the equivalent circuit in Fig. 4.5, and extended by a conventional electrical control system.

When analyzing the interaction effect by simulation studies, model parameters that were comparable to the furnace experiments, were used. Tables 5.5 and 5.6 outline the electrical working point and the electrical model parameters during the simulations.

The current-resistance model, derived in Eq. 5.8, is calculated to be:

$$\begin{pmatrix} \Delta i_{e1} \\ \Delta i_{e2} \\ \Delta i_{e3} \end{pmatrix} = \begin{pmatrix} -0.65 & -0.40 & 0.11 \\ 0.11 & -0.55 & -0.39 \\ -0.39 & 0.13 & -0.54 \end{pmatrix} \begin{pmatrix} \Delta r_1 \\ \Delta r_2 \\ \Delta r_3 \end{pmatrix} \tag{5.19}$$

where the model is expressed in terms of [kA/mΩ].

The resistance-electrode displacement model, derived in Eq. 5.9, is calculated as:

$$\begin{pmatrix} \Delta r_1 \\ \Delta r_2 \\ \Delta r_3 \end{pmatrix} = \begin{pmatrix} 0.042 & 0 & 0 \\ 0 & 0.034 & 0 \\ 0 & 0 & 0.033 \end{pmatrix} \begin{pmatrix} \Delta h_{a1} \\ \Delta h_{a2} \\ \Delta h_{a3} \end{pmatrix} \tag{5.20}$$

where the model is expressed in terms of [mΩ/cm]. This model is based on uncertain assumptions about the resistances in the heart of the furnace. However, a comparison between the model based on simulations in Eq. 5.20 and the numerical model in Eq. 5.17, which is based on the experiments, yields good accordance between the models.

The calculation of the current-electrode displacement model, derived in

Table 5.6: The electrical model parameters during simulations.

Transformer voltages	V_{Ti}	[V]	265.0	265.0	265.0
Transformer resistances	R_{Ti}	[mΩ]	0.03	0.03	0.03
Transformer reactances	X_{Ti}	[mΩ]	0.30	0.30	0.30
Electrode resistances (upper part)	R_{ei}	[mΩ]	0.10	0.10	0.10
Electrode reactances	X_{ei}	[mΩ]	0.71	0.73	0.73
Electrode resistances (part in cavities)	R_{eci}	[mΩ]	0.02	0.02	0.02
Metal bath resistances	R_{mi}	[mΩ]	0.11	0.10	0.12
Charge resistances	R_{ci}	[mΩ]	2.00	0.40	0.40
Electrode-to-electrode resistances	R_{ij}		∞	∞	∞
Bottom resistances	R_{bi}	[mΩ]	0.36	0.41	0.43
Arc voltage gradients	E_{ai}	[V/cm]	5.0	3.0	3.0
Arc lengths	h_{ai}	[cm]	5.5	8.5	8.0
Anode and cathode voltages	V_{ACi}	[V]	10.0	10.0	10.0

Eq. 5.10, by the use of the simulation model, gives the following result:

$$\begin{pmatrix} \Delta i_{e1} \\ \Delta i_{e2} \\ \Delta i_{e3} \end{pmatrix} = \begin{pmatrix} -2.33 & -1.33 & 0.38 \\ 0.46 & -1.84 & -1.28 \\ -1.63 & 0.42 & -1.80 \end{pmatrix} \begin{pmatrix} \Delta h_{a1} \\ \Delta h_{a2} \\ \Delta h_{a3} \end{pmatrix} \tag{5.21}$$

where the model is expressed in terms of [kA/cm]. This model matrix can also be found by multiplying Eq. 5.19 with Eq. 5.20.

A comparison between the simulated model in Eq. 5.21 and the numerical model in Eq. 5.18, which is found by experiments, shows some disagreements. The matrix elements differ significantly, with differences in the range of 50%. It turns out that the simulated current-resistance model in Eq. 5.19 may have too high gains compared to the furnace experiments. However, the models in Eqs. 5.21 and 5.18 have a similar structure. and an improved accordance between the models is achievable if the model parameters are more properly adjusted.

Barker's interaction factors give a dimensionless description of the interaction effect, which to some extent is similar to the current-resistance matrix

in Eq. 5.19. This is further discussed in App. B.3. The following interaction factor matrix $\boldsymbol{F}$ is calculated in the simulation model based on "effective" phase resistances and reactances:

$$\boldsymbol{F} = \begin{pmatrix} -0.46 & -0.32 & 0.09 \\ 0.10 & -0.45 & -0.33 \\ -0.32 & 0.10 & -0.46 \end{pmatrix} \tag{5.22}$$

This confirms that Barker's interaction factors give comparable results to the current-resistance matrix in Eq. 5.19 in spite of its simplicity. Anyway, this confirms that the interaction effect is considerable in a submerged-arc ferrosilicon furnace.

5.3 Electrical aspects of furnace operations

In this section some electrical aspects of the operation of a ferrosilicon furnace are treated. First, the power distribution in the furnace burden is discussed. Then, electrical operation characteristics related to the choice of electrical control strategy are discussed. Finally, the behavior of the electrical conditions is investigated by furnace measurement data, and the effects of furnace operations are illustrated.

5.3.1 The electrical power distribution in submerged-arc furnaces

The electrical power input level is a critical furnace operation parameter, and the furnace's process conditions are affected not only by the power level, but also by how the electrical power dissipation is distributed in the furnace. The electrical power distribution in submerged-arc furnaces is discussed by Westly (1974, 1975) and Holmelid, Westly and Kvassheim (1984).

Figure 5.18 shows a simplified model of a single-phase submerged-arc furnace, which is useful to illustrate the principle of power distribution. In Fig. 5.18 the furnace is assumed to consist of:

1. A charge zone with the resistance R_c.
2. A reaction zone with the resistance R_r.

In a three-phase furnace the single-phase charge conduction will mainly correspond to the electrode-to-electrode conduction in the charge, and to some extent the charge conduction in parallel to the cavities.

In the charge zone the electrical power generation P_c, will contribute to the heating and melting of the raw materials, while the energy required for the

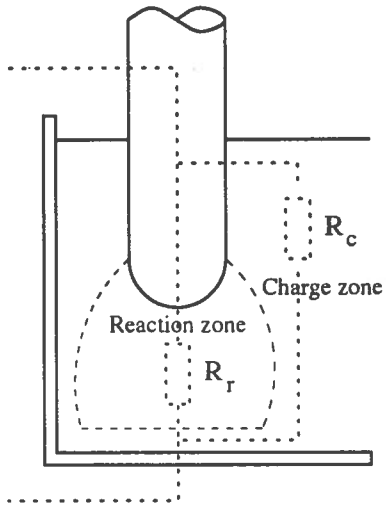

Figure 5.18: Simplified illustration of electrical power distribution in submerged-arc furnace.

final chemical reactions in the heath of the furnace, must be covered by the electrical power generation P_r, near the electrode tips in the reaction zone. If too much of the electric energy is dissipated in the charge zone to heat and melt the raw materials, a deficiency of energy dissipation in the reaction zone may cause incomplete chemical reaction patterns. Thus, the distribution of electric power generation within the furnace is a critical operation parameter.

The furnace operating resistance R is given as:

$$\frac{1}{R} = \frac{1}{R_r} + \frac{1}{R_c} \tag{5.23}$$

and the total power dissipation is given as:

$$P = \frac{{V_e}^2}{R} \tag{5.24}$$

where the electrode-to-hearth voltage is denoted V_e. The power generation in the charge zone R_c is given as:

$$P_c = \frac{{V_e}^2}{R_c} \tag{5.25}$$

The power distribution factor of the furnace C_q, can be defined as the fraction between the charge power and the total power dissipation in the

furnace (Westly, 1974; 1975):

$$C_q = \frac{P_c}{P} = \frac{R}{R_c} \tag{5.26}$$

The factor C_q, which varies between 0 and 1, indicates the power distribution, and the higher the value, the larger portion of the total power generation is consumed in the heating and melting of raw materials, and less is available for the chemical reactions in the inner furnace.

The power distribution factor can to some extent be controlled by the choice of the furnace operating resistance at a given set of raw materials, but this is complicated since the power distribution factor cannot be measured.

According to Westly (1974, 1975) there is an optimal power distribution C_Q, with respect to furnace operations for each process, for a given set of raw materials. The furnace operating resistance should be given by:

$$R = C_Q \, R_c \tag{5.27}$$

If too large an operating resistance is used, this will cause too much electrical power generation in the charge zone, and a furnace condition characterized by slag formation and tapping problems, abnormal electrode wear and current insensitivity to electrode movements, may occur (Westly, 1974; 1975).

5.3.2 Electrical operation characteristics

The furnace production is closely related to the electrical environment in the furnace, and therefore the choices regarding the electrical operation characteristics are critical. The electrical operation objectives can be expressed as (De Waal et al., 1992):

1. Choose operation conditions that maximize the furnace electrical efficiency.
2. Maximize the power input to the furnace by each electrode within the operational constraints of the furnace.

The operational constraints should be known in order to ensure safe operation as close to these limits as possible. The operational constraints in a submerged-arc furnace are among others:

1. The electrode current limit, which is usually given by the electrode conditions.

2. The maximum appearing power delivered to the furnace ("the MVA limit"), which is limited by the power supply or by the furnace transformers.

3. Any primary current limit or total delivered furnace power.

4. Any power demand constraints.

Characteristic curves are frequently used to describe the electrical behavior of a submerged-arc furnace, and the electrical operational constraints can easily be included in the diagram of these characteristic curves. The electrical operating point of the furnace can be found in this curve diagram, which also indicate the possible steps to be taken in order to maximize the furnace power within the operational constraints.

The electrical characteristic diagram and possible applications are further treated by among others Barker (1980, 1981), Rennie (1984) and De Waal et al. (1992).

Figure 5.19 shows the electrical operation characteristics for a furnace similar to the ferrosilicon furnace at Elkem Thamshavn. The furnace operational constraints are assumed to be a MVA limit of 65 MVA and an electrode current limit of 145 kA. Furthermore, the furnace circuit is assumed to be a symmetrical star-circuit with equal resistances and reactances in the three phases. In addition, symmetrical transformer conditions are assumed. The phase reactances are assumed to be $X = 0.60\,\mathrm{m}\Omega$, and the occurrence of arcing is described by the use of the arc power factor description in Eq. 5.1, with $k_{arc} = 0.95$. Figure 5.20 shows a expanded diagram of the characteristic curves in the operation region of current interest.

Three different sets of curves are illustrated in Fig. 5.20 corresponding to the three different operation strategies:

1. **Constant transformer voltages.**

   These curves (the "dash-dotted" lines) describe cases when the applied transformer voltages are held constant, and the phase resistances are varied. These operation curves correspond to furnace conditions with fixed transformer tap positions and thereby constant electrode-to-hearth voltages, and moving the electrodes.

   Such an operation curve can be described by (Barker, 1980):

$$P = 3 \cdot k_{arc} \cdot I_e \cdot \sqrt{V_e^2 - X^2 I_e^2} \tag{5.28}$$

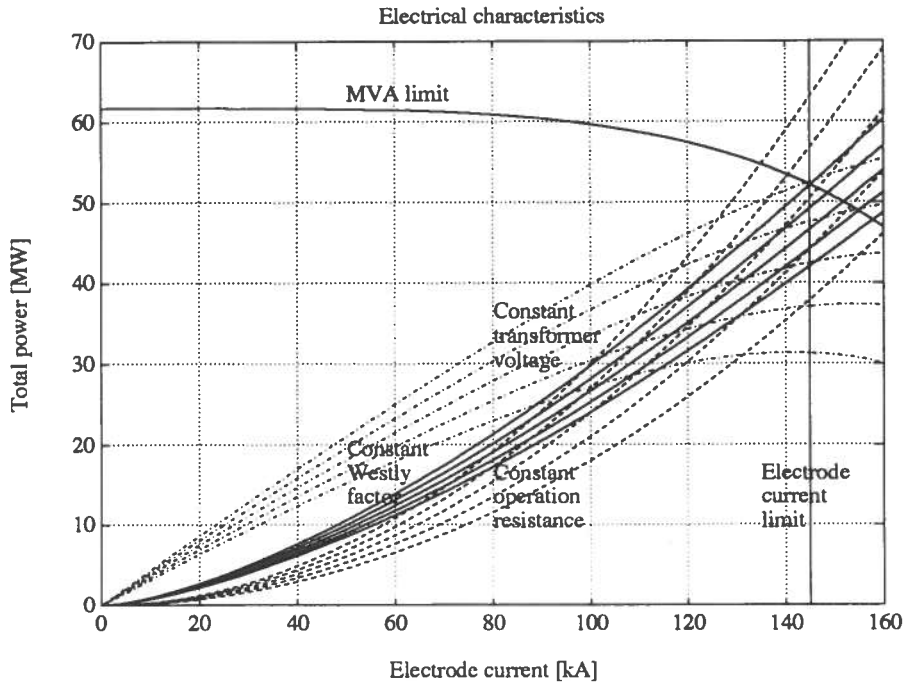

Figure 5.19: Electrical operation characteristics for a ferrosilicon furnace.

where V_e are the electrode-to-hearth voltages, and I_e are the electrode currents. As the electrode-to-hearth voltages are varied in steps by means of changing the transformer tap positions, a family of constant-voltage curves are obtained. The curves are shown for electrode-to-hearth voltages in the range from 110 V to 150 V in steps of 10 V.

2. **Constant operation resistance.**

   These curves ("dashed" lines) describe situations with constant phase resistances, and where the power supply is varied. These operation curves correspond to conditions with constant electrode holder positions and changing the transformer tap positions.

   Such a curve can be described by (De Waal et al., 1992):

$$P = 3 \cdot {I_\epsilon}^2 \cdot R \tag{5.29}$$

   where R are the phase resistances. As the resistances are varied in steps a set of curves is obtained. The operating curves are shown for operation resistances in the the range from 0.60 mΩ to 1.00 mΩ in steps of 0.10 mΩ.

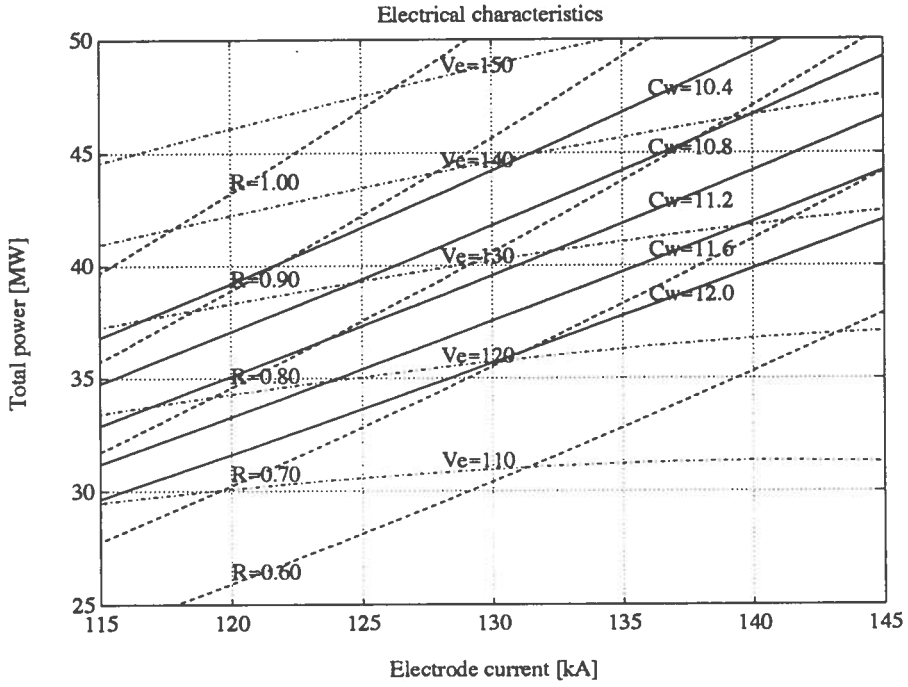

Figure 5.20: The electrical characteristic curves for the operation region.

3. **Constant Westly's factor.**

   These curves ("solid" lines) describe situations where the Westly's factor is held constant, and where the both the phase resistances and the power supply are varied. Westly's factor is defined in Eq. 4.16 and further described in Section 4.2.1.

   Such an operating curve can be described by:

$$P = \left(\frac{I_e}{C_w}\right)^{\frac{3}{2}} \tag{5.30}$$

   where C_w is the Westly's factor. As the Westly's factor is changed in steps, a set of curves is obtained. The operating curves are shown for Westly's factors in the range from 10.4 to 12.0 in steps of 0.4.

The operational constraints are described as follows. The electrode current limit curve is given by:

$$I_e = I_{eMax} = 145 \text{ kA} \tag{5.31}$$

where I_{eMax} denotes the current limit. The MVA limit curve is described by (De Waal et al., 1992):

$$P = 3 \cdot k_{arc} \cdot \sqrt{\left(\frac{MVA_{Max}}{3}\right)^2 - \left(X\, I_e{}^2\right)^2} \tag{5.32}$$

where $MVA_{Max} = 65$ MVA denotes the operational limit regarding the electrical supply.

Optimizing the electrical environment

Strategies for optimizing the electrical environment in the furnace with respect to furnace production, can be derived and illustrated based on the characteristic curve diagrams in Fig 5.19 and 5.20. Barker (1980, 1981) and De Waal et al. (1992) describe furnace operation strategies based on the characteristic diagrams and argue for the following two-stage operation strategy:

1. First, control the furnace resistance by moving the electrodes.
2. Then, slowly adjust the transformer tap positions to maximize the furnace power input within the electrical constraints.

The curves of constant Westly's factor illustrate an alternative furnace operation strategy which has been discussed by Westly (1974, 1975) and Holmelid, Kvassheim and Westly (1984). Then, the furnace is operated corresponding to a curve of constant Westly's factor as illustrated in Fig 5.19 and 5.20. The operation strategy then becomes:

1. Control the furnace Westly's factor by controlling the electrode currents in accordance with equal reference values for the three electrode currents given by Westly's formula in Eq. 4.16:

   $$I_{ref\,e} = C_w\, P^{\frac{2}{3}} \tag{5.33}$$

   where $I_{ref\,e}$ denotes the current reference value, C_w denotes the Westly's factor, and P denotes the total furnace power.

2. Then, slowly adjust the transformer tap positions to maximize the furnace power input within the electrical constraints.

The characteristic diagrams show that these two operational strategies give somewhat different results in the choice of electrical parameters. Electrical control strategies of submerged-arc furnaces are further discussed in Chapter 6

5.3.3 The behavior of the electrical conditions

The electrical variables in a submerged-arc furnace are influenced by a large number of external circumstances, in addition to internal effects like the interaction between the electrical phases. The electrical power supply and the electrode tip position in the furnace are used as control inputs to the furnace, and therefore the electrical furnace conditions are affected by the electrical control system. The electrical environment is also strongly influenced by the furnace operations, during the stoking of the furnace and tapping of the metal product. Finally, the electrical system is heavily disturbed by occasional variations in the electrical conductivity in the charge burden and in the arcing conditions in the cavities.

In this section the typical behavior of the electrical variables is illustrated by means of measurement data from the furnace at Elkem Thamshavn. These measurement data show both the effects of furnace operations as well as the effects of disturbances and control activities.

The effect of furnace operations on the electrical variables

Figure 5.21 shows the effects of the furnace stoking/charging and tapping operations on the furnace power level. The furnace power level is a controlled variable within prescribed dead-zone bounds. A significant high-frequency variation within the dead-zone bounds is present, and some larger power drops occur in connection with some of the stoking operations. These power drops are probably forced by the furnace safety system to reduce electrode currents, increasing beyond the furnace current limit.

Figure 5.22 shows the responses of the electrode currents. The electrode currents which are controlled variables within prescribed dead-zone bounds, are heavily disturbed and show high-frequent behavior around low-frequent trends. The electrode currents are effected by the stoking operations which may result in sudden changes in electrical conductivity in the charge and the arcing conditions in the cavities.

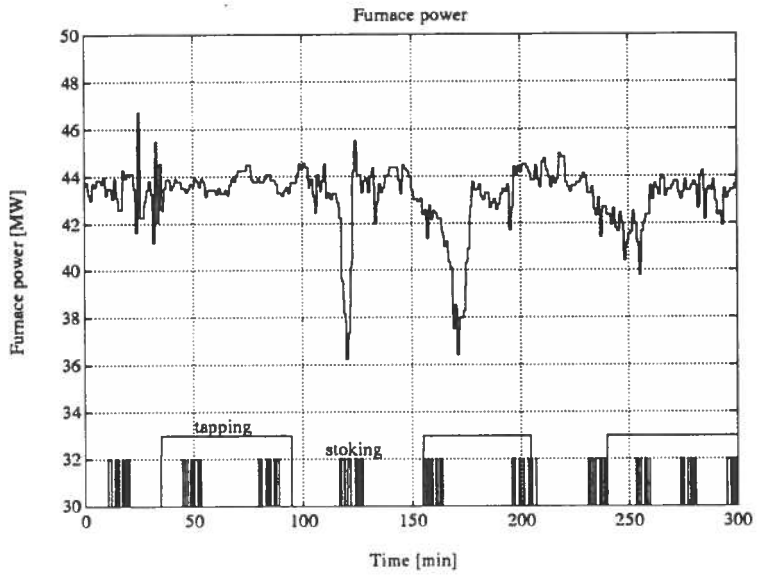

Figure 5.21: The furnace power level and the furnace operations.

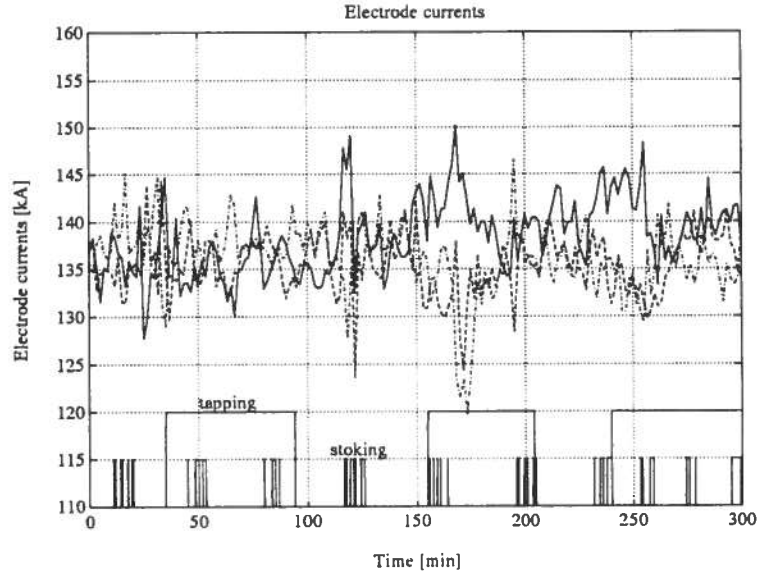

Figure 5.22: The electrode currents and the furnace operations.

The effect of the operations on the electrical conductivity is further illustrated in Fig. 5.23, which shows the responses of the measured phase resistances. The resistance responses show considerable high-frequent variations around more low-frequent trends, which may differ between the phases. The conductivity changes due to the stoking operations are clear. Rapid changes in the resistances in both directions, may occur during a stoking operation:

- A sudden decrease in a phase resistance can be explained by a breakdown of the cavity walls and that the cavity becomes more or less filled with charge materials. This may result in reduced arcing or even a short-circuited arc, and increased ohmic conduction in that electrical phase, and thereby a reduction in the phase resistance.

- An increased phase resistance may be explained by the current paths in the charge burden being destroyed during the stoking operation.

Figure 5.23 also shows that the resistances are effected by the tapping operation. A sudden decrease in a phase resistance is observed in the beginning of a tapping operation. The resistances also show a rising trend when no tapping of metal occurs and the amount of liquid metal in the cavities is increasing, and an opposite trend when tapping occurs and the amount of liquid metal is decreasing.

Figure 5.24 shows the response of the electrode holder positions. The displacements of the electrodes are applied as control inputs in the current control of the furnace, and Fig. 5.24 illustrates the control activities in the current control. The responses show frequent control activities, and indicate that the control parameters could be better adjusted to reduce the amount of "needless" electrode movements. A varying effect of the electrode displacements can be observed by the sudden increase in the amount of electrode displacements. This should be especially considered when adjusting the control parameters.

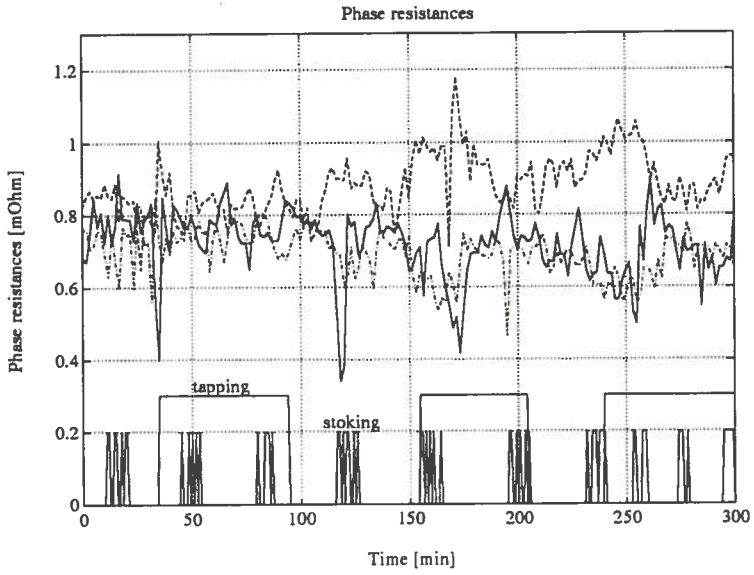

Figure 5.23: The phase resistances and the furnace operations.

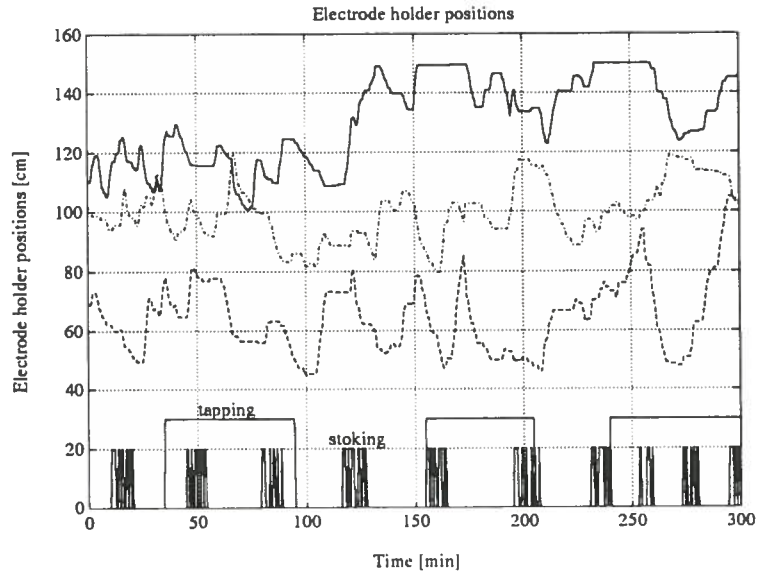

Figure 5.24: The electrode holder positions and the furnace operations.

Figure 5.25 shows the response of the electrode voltages. The electrode voltages undergo high-frequent variations similar to the electrode currents and the phase resistances. The electrode voltages are also influenced by the reduced power level of the furnace.

The harmonics content in the electrode voltages are shown in Fig. 5.26. The harmonics content are influenced by the general trend of the electrode voltages, as well as the occurrence of arcing in the electrical phases.

The situation of "short-circuited" arcs with extreme high electrode currents and reduced transformer tap positions can be observed by a reduced harmonics content in that specific electrode voltage. Furthermore, the harmonics content fluctuate within the stoking cycles with a maximum just before the stoking operation and a subsequent decrease when stoking occurs. Furthermore, a rising trend of the harmonics content can be observed during tapping of metal and an opposite trend when no tapping occurs.

5.4 Concluding remarks

In this chapter the electrical environment in a ferrosilicon furnace has been analyzed and investigated with respect to:

- The effects of arcing.
- The electrical interaction effect.
- The effects of furnace operations.
- Variations in measurements.

Furthermore, electrical aspects of the operation of the furnace have been discussed, forming a basis for discussing electrical control strategies.

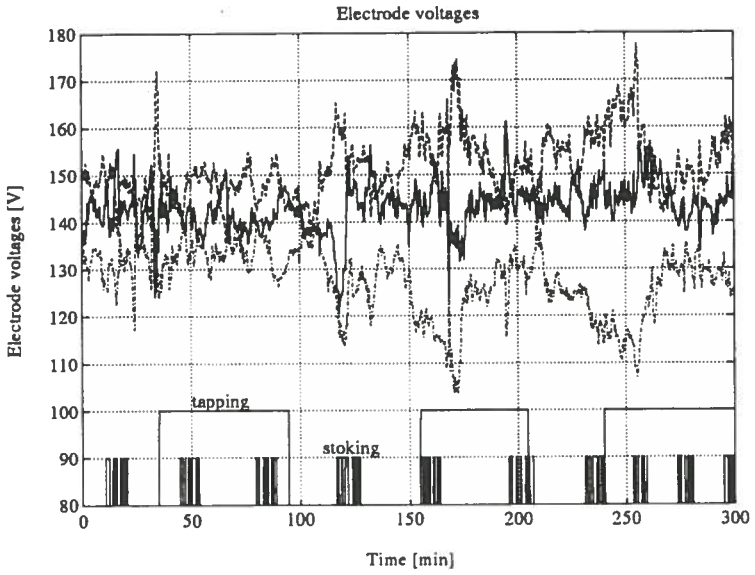

Figure 5.25: The electrode voltages and the furnace operations.

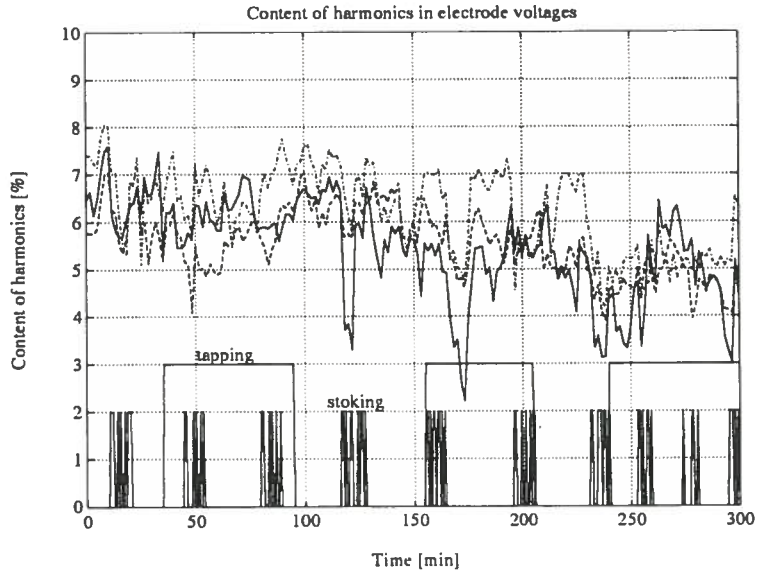

Figure 5.26: The harmonics content in electrode voltages and the furnace operations.

Chapter 6

Electrical control strategies

The electrical environment plays a fundamental role in the operation of a submerged-arc furnace which is the source of the required energy consumed in the chemical reactions in the furnace. Therefore, satisfactory electric control is essential. This chapter discusses electrical strategies for a ferrosilicon furnace. A conventional electrical control system is described and analyzed. Next, a decoupling electrode current controller is proposed and compared to a conventional current controller by simulation examples. Finally, an optimization guideline regarding the control parameters in a conventional current controller is proposed based on simulation studies.

6.1 A conventional electrical control system

A electrical control system frequently used on ferrosilicon furnaces has previously been briefly described in Section 2.5. The objects of the electrical control system can be summarized as:

1. Control the total electrical power delivered to the furnace.
2. Control the distribution of electrical power dissipation in the furnace:
   (a) Between the three electrodes
   (b) Between the different regions in the furnace

Different electrical control strategies have previously been discussed in Section 5.3.2.

6.1.1 Elkem's electrical control system

The electrical control system which is used at Elkem's ferrosilicon and silicon plants and is applied at the furnace at Elkem Thamshavn, has a hierarchic structure with "high-level" power controllers and "low-level" electrode

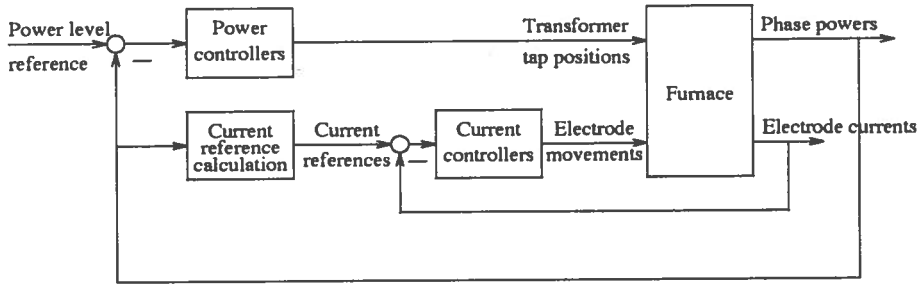

Figure 6.1: The Elkem electrical control system

controllers (Holmelid, Kvassheim and Westly, 1984). Figure 6.1 shows the principle of this control structure.

The high-level power controllers control the delivered power to the electrodes, while low-level current controllers control the electrode currents. The power distribution in the furnace is controlled by the choosing the reference values for the electrode currents based on the total power level. In Elkem's electrical control system this is carried out by the use of Westly's formula in Eq. 5.33, and the current references are found as:

$$I_{ref\,e} = C_w\, P^{\frac{2}{3}} \tag{6.1}$$

where $I_{ref\,e}$ denotes the current reference value, C_w denotes the Westly's factor, and P denotes the total furnace power. In this control strategy all electrode current are generally controlled towards a common reference value, which is found from Eq. 6.1. However, it could be argued against the use of a common reference value, since the electrical conditions in the furnace can differ significantly between the three phases.

6.1.2 Electrical control problems

Considerable problems are connected with electrical control, and in particular electrode control, of large three-phase submerged-arc furnaces. The major problems can be outlined as:

1. The interaction effects between the electrical phases, which was previously discussed in Section 5.2.

2. Problems due to large reactances and asymmetry in the three-phase electrical circuit. This is thoroughly discussed by Barker and Stewart (1980), Barker (1980, 1981), Barker et al. (1992) and De Waal et al. (1992). Important problems are:

(a) "Live and dead phases".

This is a situation where the power dissipation in one of the electrical phases increases ("live phase"), while it decreases in another phase ("dead phase"), and remains unchanged in the third. This can be explained as follows. Assuming a furnace with the electrical phase sequence 1, 2, 3, and that the reactance in phase 1 is larger than the reactances in phase 2 and 3, and that the electrode currents are controlled towards equal references, and thus:

$$I_{e1} = I_{e2} = I_{e3}$$

Then, the power dissipation in phase 3 will be large, the power in phase 1 normal, and the power in phase 2, low:

$$P_3 > P_1 > P_2$$

This problem may be caused by for instance by asymmetry in the electrical connection to the furnace, or the tapping of metal from the furnace.

(b) Insensitivity to electrode movements.

If the reactance in an electrical phase increases, the changes in the phase resistance must be increased to obtain an equal current response as with lower reactance. This means increased electrode movements with increasing reactance in the case of current control.

3. Unreliable measurements of the electrical variables, as discussed in Section 2.4.2.

4. Major disturbances to the electrical conductivity and arching conditions.

5. Control input uncertainties due to changing effects of electrode movements to the electrical conditions.

6. Difficulties in deciding the electrical working-point.

6.1.3 The power control system

The delivered power level is controlled by using the transformer tap positions as control inputs by adjusting the applied transformer voltages. In principle the power controller could be a multivariable controller since the furnace is usually connected to three independent transformers. However,

symmetric furnace transformers are usually desirable due to symmetry requirements on the primary side of the transformers. Therefore, transformers are controlled simultaneously and symmetrically, and thus the power controller is a monovariable control system.

Asymmetric transformer control operations have successfully been applied in furnaces with large transformer steps in order to reduce the size of the "effective" steps in the power supply to the three electrodes.

The low-level electrode controllers in the control strategy are treated in the following section.

6.2 The electrode control system

The electrode control system can be utilized by different control strategies that differ in the choice of the controlled variables:

- Electrode current controllers.
- Phase resistance controllers, or shortly just resistance controllers.

These control structures both use electrode displacements as control input variables. These controllers have almost similar effects on the furnace operation, but some differences in their properties may become important when considering specific furnaces. Electrode control systems are discussed among others by Barker (1980, 1981), Holmelid, Kvassheim and Westly (1984) and Barker et al. (1992).

6.2.1 The current controller

A conventional current control system consists of three monovariable controllers. Each of them tries to control the current in its related electrode by lifting and lowering the electrode, but without taking any account of the interaction effect between the control loops. A schematic diagram of a conventional current control system is shown in Fig. 6.2, where I_{ei} are the electrode currents, h_i are the electrode positions, and $I_{ref\,ei}$ are the current reference values.

The electrical interaction effect will cause problems for current control, because a displacement of one electrode will affect the currents in the other electrodes, too. This interaction effect between the electrical phases is illustrated by the dotted lines in the "furnace" box in Fig. 6.2. In fact,

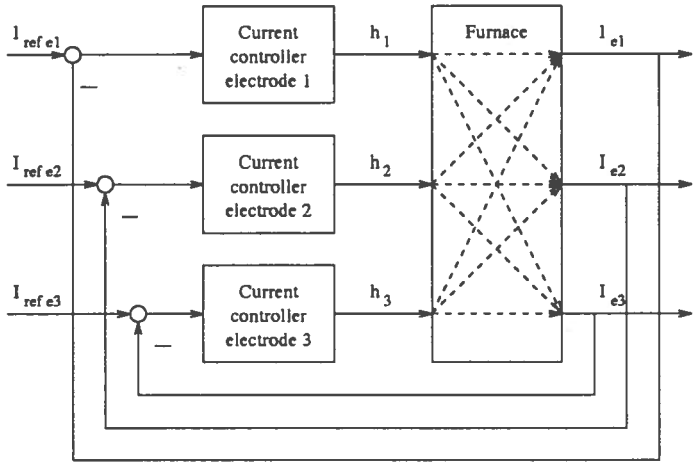

Figure 6.2: A conventional current control system.

advice has been given against current control owing to this interaction effect (Barker, 1980; 1981; Barker et al., 1992).

However, in control engineering interaction effects between the control loops are commonly experienced when monovariable controllers are applied for a multivariable process. This is discussed for instance by Balchen and Mummé (1988). It is shown in Section6.3that the interaction problem is eliminated by extending the current controller with a decoupling element that cancels the couplings between the electrical phases.

6.2.2 The control algorithm

The control algorithm used in the current controller at the furnace at Elkem Thamshavn is a so-called **dead-zone controller**. This is also the control algorithm applied in the power controllers. According to Sochacky and Gaillot (1984), dead-zone control algorithms have reached a wide range of application regarding furnace control.

The current controllers are utilized as dead-zone control algorithms with fixed electrode displacement. The principle of control algorithm is illustrated in Fig. 6.3. The currents have to exceed the dead-zone bounds around the reference values for a specified time period, "the time-before-action", before the controller acts and moves the belonging electrode the fixed displacement.

This dead-zone controller has three control parameters with specific related properties:

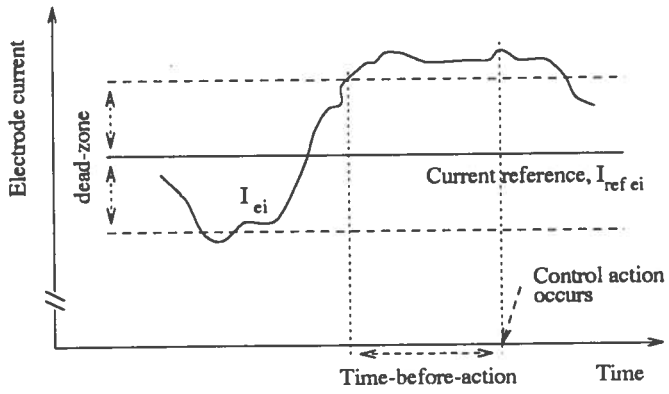

Figure 6.3: The dead-zone control algorithm.

1. The size of the fixed electrode displacement.
2. The extension of the dead-zone bound.
3. The length of the time-before-action period.

and the controller will attain different control properties as a result of the choice of these parameters. Considering the current controllers, the dead-zone control algorithm is chosen mainly because of the presence of large disturbances in the electrical conditions in the furnace, and the control parameters are tuned to obtain a disturbance rejection which is as good as possible.

Section 6.4.2 shows how the dead-zone control algorithm may obtain the properties of reducing the interaction effects between the electrical phases. Furthermore, a guideline for parameter adjustment for the control parameters in the current control application is given.

6.2.3 The phase resistance controller

An alternative electrode control strategy is obtained by controlling each of the phase resistances by rising and lowering the electrode that belongs. The structure of the resistance controllers can in principle be similar to the current controllers discussed above. Resistance controllers are discussed among others by Barker (1980, 1981) and Barker et al. (1992).

6.2.4 Comparison between current and resistance control strategies

The current and resistance control strategies have somewhat different properties. A comparison between the two electrode control strategies applied

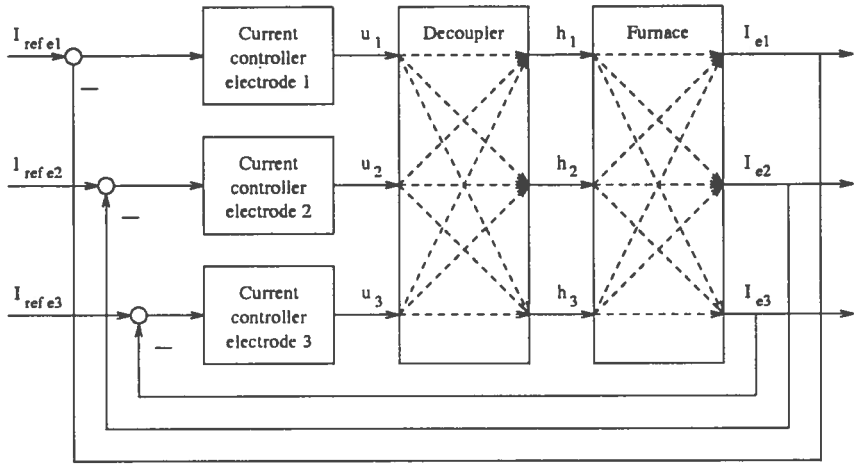

Figure 6.4: A non-interacting current control system.

on a ferrosilicon furnace is summarized in Table 6.1.

The main disadvantage connected to the current control strategy is the interaction effect between the control loops, while the strategy is strengthened by the accurate current measurements and the fact that the currents are controlled to be within the operational constraints.

The opposite properties are connected with the resistance control strategy. The resistance controller has a negligible interaction effect between the control loops, but the strategy is based on somewhat unreliable measurements of the electrode voltages. The currents are not controlled and could go beyond the operational limits and cause actions from the furnace safety system. Furthermore, the resistances are partly dependent variables given by the charge composition, and hence the use as controlled variables yields limited degree of freedom. Finally, the resistances may not be suitable to describe the electrical conditions in the presence of arcing

6.3 A non-interacting current controller

A non-interacting current controller is achieved by extending the controller with a decoupling element as shown in Fig. 6.4 (Valderhaug and Sletfjerding, 1992). The decoupler cancels interaction effects between the electrical phases in the furnace, and the current controller will now only affect the current in the electrical phase that belongs. This canceling effect is illustrated by the dotted lines in the "decoupler" box in Fig. 6.4.

Table 6.1: A comparison between current and resistance control of ferrosilicon furnaces.

Current control	Resistance control
Advantages	
• Accurate current measurements. • The electrode currents are controlled to be within operational constraints.	• A negligible interaction effect between the control loops.
Disadvantages	
• Significant interaction effect between the control loops.	• The resistance calculations are based on unreliable voltage measurements. • The electrode currents are not controlled variables and can go beyond the operational current constraints. • The phase resistances are to some extent dependent variables given by the charge composition. • Resistances may be a unsatisfactorily description in the presence of arcing.

Alterations in the electrode positions Δh_i, which are assumed to correspond to changes in the arc lengths Δh_{ai}, in the decoupling control structure can be expressed as:

$$\underline{\Delta h} = D \cdot \underline{\Delta u} \tag{6.2}$$

where vector $\underline{\Delta u}$ contains the changes in the controller outputs. A change in the controller output Δu_1 will now result in changes in the electrode positions by Δh_1, Δh_2 and Δh_3, in a way that only affects the current I_{e1}.

A simplified linearized model of the complete control system including the decoupler will be:

$$\underline{\Delta i_e} = (H \cdot D) \cdot \underline{\Delta u} = H_D \cdot \underline{\Delta u} \tag{6.3}$$

where matrix H is the model of the current-controlled furnace given in Eq. 5.11, matrix D is the decoupler, and matrix H_D is the resulting system model.

The resulting system between the controller outputs deviations $\underline{\Delta u}$ and the current deviations $\underline{\Delta i_e}$, will now be diagonal, and hence matrix H_D only contains diagonal elements.

The decoupler matrix D can be found by inverting Eq. 6.3:

$$D = [H]^{-1} \cdot H_D \tag{6.4}$$

where matrix H_D can be looked upon as the desired system matrix of the resulting system. A simple choice of H_D will be the diagonal elements in matrix H. Thus, the decoupler matrix can be found from:

$$D = [H]^{-1} \cdot \mathrm{diag}(H) \tag{6.5}$$

6.4 Simulation analyses of current control strategies

This section first analyzes the conventional and the non-interacting current controllers by simulation studies and their control properties are compared. The steady-state simulation model is described in Section 4.3.2, and extended with the conventional electric control system and with the decoupling current controller. In both control strategies the dead-zone control algorithm are used to control the furnace power as well as the electrode

currents. During the simulation the model parameters were similar to the simulation studies in Section 5.2.4 and outlined in Tables 5.5 and 5.6.

At the end of the section the focus is turned to the adjustment of the control parameters in the conventional current control algorithm, and the effects of proper parameter adjustment are shown by simulations.

6.4.1 Conventional versus decoupling control strategies

In this section the properties of the conventional and the decoupling current control structures are analyzed by simulation studies.

The dead-zone control algorithms discussed in Section 6.2.2 are equal in all three phases and are implemented with the following control parameters:

Dead-zone	2.0 kA
Time-before-action	3.0 s
Electrode displacement	1.0 cm

The decoupler is realized as discussed in the previous section. Thus, the electrode displacements in the decoupling control strategy are given by Eq. 6.2. The "desired" system matrix $\boldsymbol{H}_D$, is chosen to consist of the diagonal elements of the current-electrode displacement model $\boldsymbol{H}$, given in Eqs. 5.11 and 5.21. The decoupler matrix elements as well as the electrode displacements, are normalized, in order to obtain maximum electrode displacements comparable to the conventional current controller.

The ability of the current controllers to handle the interaction effect are investigated by simulation cases involving step-like alterations in the phase resistances and phase reactances.

Step response to charge resistance alterations

First, an example is simulated with a step-like change in the charge resistance in phase 3:

$$R_{c3} \ : \ 0.4 \rightarrow 2.4 \, \mathrm{m}\Omega \, , \ \text{at} \, t = 5 \, \mathrm{s}$$

This has the conventional and the non-interacting current controller. Figure 6.5 shows the response of the conventional controller, while the response of the decoupling controller is shown in Fig. 6.6.

The response of the conventional controller in Fig. 6.5 shows its inability to handle the interaction effect. The effect of the change in the electrical

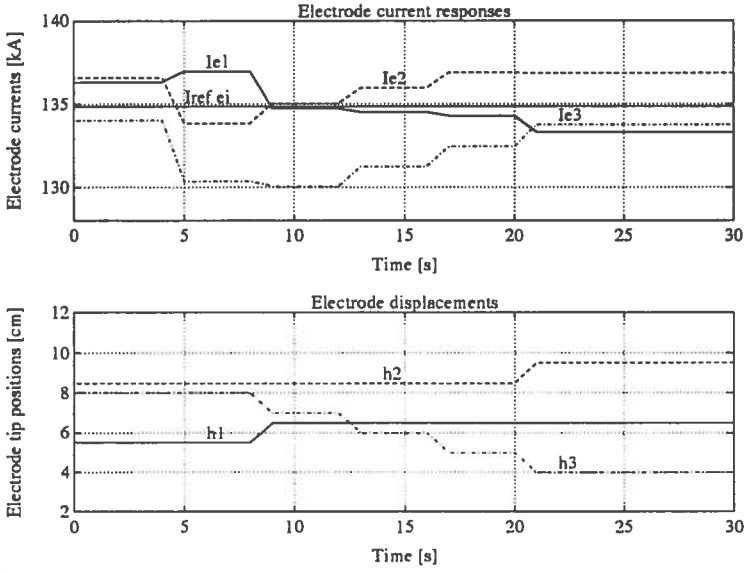

Figure 6.5: Response of the conventional current controller. The charge resistance in phase 3, R_{c3}, is altered from 0.4 to 2.4 mΩ at $t = 5$ s.

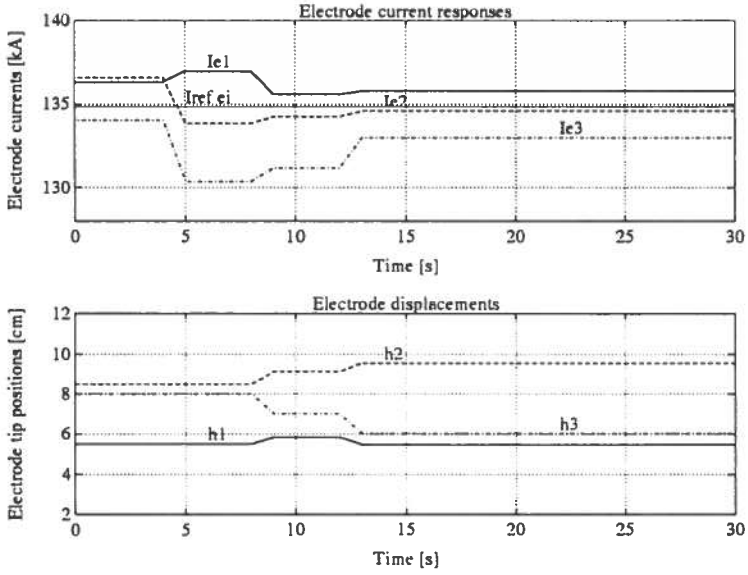

Figure 6.6: Response of the decoupling current controller. The charge resistance in phase 3, R_{c3}, is altered from 0.4 to 2.4 mΩ at $t = 5$ s.

conditions in phase 3, due to the charge resistance alternation, is moved to the other phases because of the control action occurring in phase 3, and the interaction effect is clearly illustrated.

Figure 6.6 shows the decoupler response to the similar case. The non-interacting controller takes into account the interaction effect, and all three electrodes are moved when the control action occurs in phase 3. This results in less electrode movements and a shorter transient period.

Step response to phase reactance alterations

Next, the effects of a step-like change in the reactance in phase 1:

$$X_1 \; : \; 0.71 \rightarrow 0.65\,\mathrm{m}\Omega\,, \;\; \text{at } t = 5\,\mathrm{s}$$

is investigated through simulations with the conventional and the non-interacting current controller. Figure 6.7 shows the response of the conventional controller, while Fig. 6.8 shows the response of the decoupling controller.

The response of the conventional controller clearly illustrates the interaction effects between the control loops, while the response of the decoupler shows that the interaction effects are canceled, resulting in an improved response.

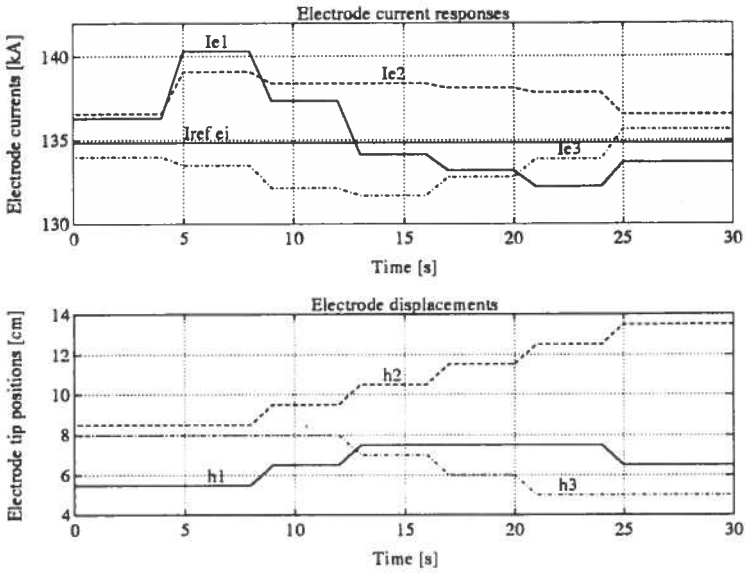

Figure 6.7: Response of the conventional current controller. The reactance in phase 1, X_1, is altered from 0.71 to 0.65 mΩ at $t = 5$ s.

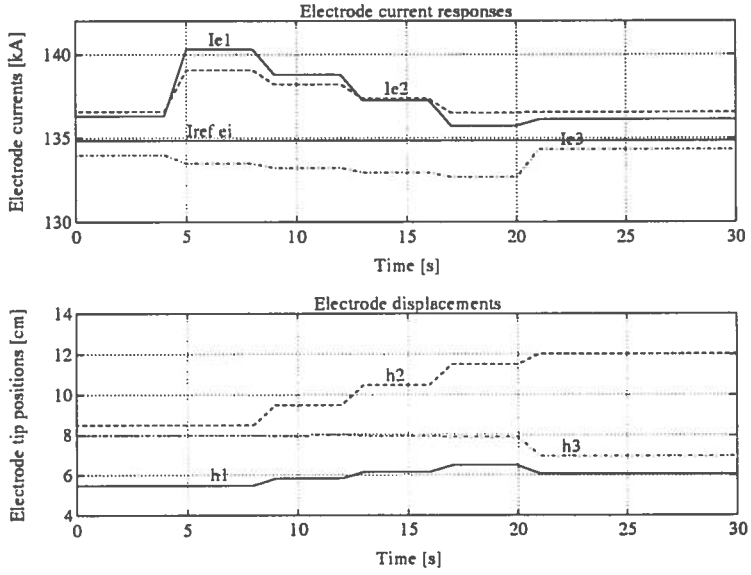

Figure 6.8: Response of the decoupling current controller. The reactance in phase 1, X_1, is altered from 0.71 to 0.65 mΩ at $t = 5$ s.

Step response to electrode-to-electrode resistance alterations

The final simulations illustrate the responses to changes in the current paths in the furnace. In the original model description the electrode-to-electrode conductance is neglected and hence the electrode-to-electrode resistances are set to infinity. This is the model that is applied when the decoupler is calculated. Figures 6.9 and 6.10 show the responses of the conventional and the decoupling controllers when the electrode-to-electrode resistances are set to:

$$R_{12} = R_{23} = R_{31} \ : \ \infty \rightarrow 10.0\,\mathrm{m}\Omega\,, \ \text{at}\ t = 5\,\mathrm{s}$$

The responses show that the decoupler handles the altered conditions better than the conventional controller, in spite the fact that the decoupler is designed based on a model with a different structure. The conventional controller suffers from the interaction effects between the electrical phases, which results in additional electrode movements and an increased transient period.

Further simulation studies verify that the decoupler strategy has superior properties compared to a conventional controller. However, the conventional controller's property of rejecting interactions can be improved by a proper adjustment of the control parameters, but this can only be obtained at the expense of the other control properties. This is further discussed in the last part of this section.

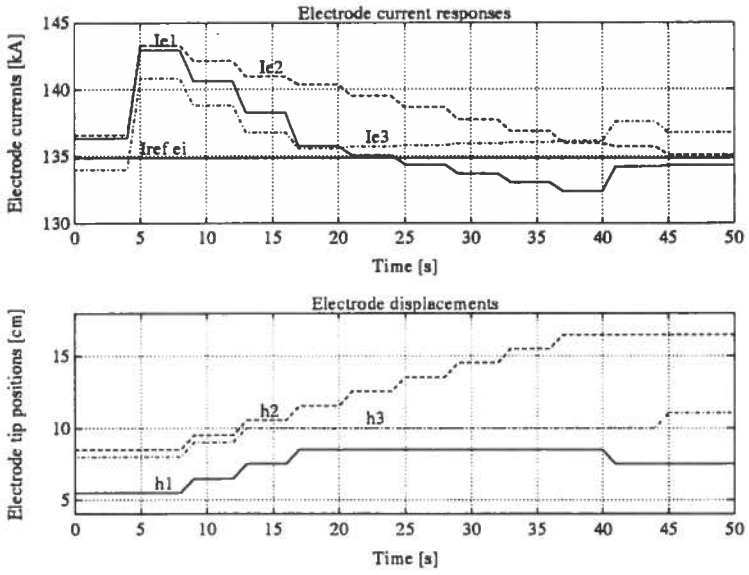

Figure 6.9: Response of the conventional current controller. The electrode-to-electrode resistances in all phases, $R_{dir\,i}$, are set to 10.0 mΩ at $t = 5$ s.

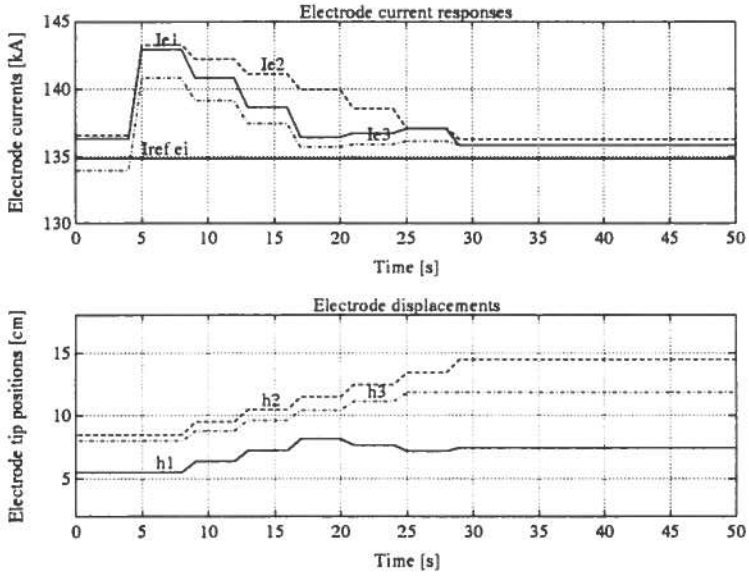

Figure 6.10: Response of the decoupling controller. The electrode-to-electrode resistances in all phases, $R_{dir\,i}$, are set to 10.0 mΩ at $t = 5$ s.

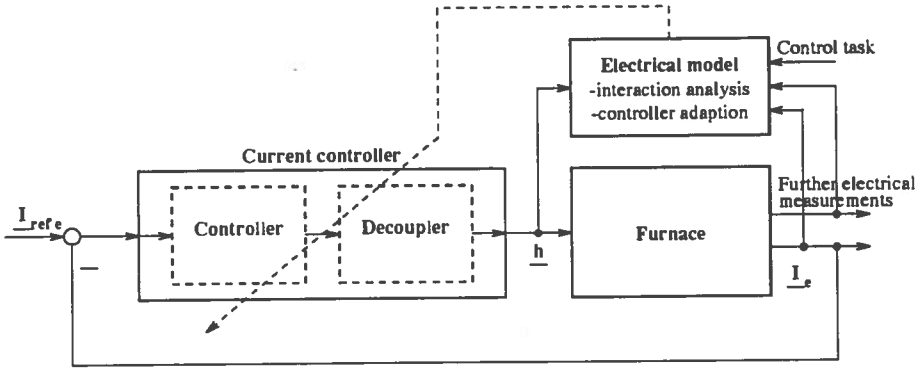

Figure 6.11: A non-interacting model-based current control system.

Implementation of the decoupling control strategy.

Figure 6.11 shows how the decoupling control structure could be implemented on a furnace. Due to the continuously varying electrical conditions in the furnace, an electrical model description is supposed to be applied on-line in parallel to the furnace. This system surveys the electrical conditions, the interaction effect and the control sensitivity in order to adapt the decoupler and the control parameters.

Comparison between the conventional and the decoupling control strategies

The interaction analysis shows that the electrical interaction effects are significant in ferrosilicon furnaces. The conventional current controller has poor properties in rejecting this effect if the control parameters are not properly adjusted. The proposed non-interacting current controller cancels the interaction between the electrical phases. This will remove current variations due to the interaction, and may also reduce undesirable electrode movements. The novel control strategy will enable the use of current control in large submerged-arc furnaces with its benefits, but without the usual disadvantages connected to the method.

However, the drawback with the decoupling control strategy is the uncertainty connected with the current-displacement model, in Eqs. 5.11 and 5.21, which is used in the synthesis of the decoupler matrix. This is further discussed in Section 5.2.4.

Table 6.2 summarizes the advantages and disadvantages connected with the conventional current controller and the decoupling control structure.

Table 6.2: A comparison between the use of conventional and decoupling current control structures on ferrosilicon furnaces.

Conventional controller	Decoupler
Advantages	
• Robust control structure. • Simple and easy to understand. • Good control properties are obtainable if the control parameters are proper adjusted.	• Cancells the interaction effect between the control loops. • Improved control properties with less electrode movements and shorter transient periods.
Disadvantages	
• Interaction between the control loops. • Needless electrode movements and transient periods due to the interaction.	• The decoupler based on a model of the electrical conditions in the furnace, which is connected with large uncertainties. • A somewhat complex structure.

The uncertainties connected to the conduction in the burden of a ferrosilicon furnace and the difficulties in establishing a reliable current-displacement model based on furnace measurements, do not favor the use of the decoupling structure on such furnaces. However, the concept should be

considered for use in furnaces with more well-defined electrical conduction paths, such as pure ohmic smelting furnaces and open-arc furnaces.

The difficulties connected with any implementation of the decoupler on ferrosilicon furnaces, have increased the importance of proper parameter adjustment in the conventional current controller.

6.4.2 Optimizing the control parameters in the dead-zone algorithm

The properties of the conventional current controller on ferrosilicon furnaces can be significantly improved by a proper adjustment of the control parameters based on their mutual properties and influence on the final control properties. The current control objectives are to keep the electrode currents close to their reference values without any unnecessary movements of the electrodes.

The following guidelines for adjusting the control parameters are proposed:

- **The electrode displacement.**

  The size of the fixed electrode displacements should be as small as possible, but with sufficient effects on the electrode currents. This depends on the furnace equipment, but common displacements are about 1 cm.

  The fixed electrode displacement parameter is usually utilized as the time-period when the electrode is moved. Generally, the time-periods corresponding to a specific electrode displacement will be different whether the electrode is raised or lowered. Therefore, these time-periods should be chosen separately corresponding to the desired displacement in both directions.

  Furthermore, the electrode current sensitivities to electrode displacements are different regarding upward or downward movements. Generally, upward movements have less effect on the electrode current compared to downwards. Therefore, the fixed electrode displacements in upward and downward directions should be chosen to have similar effects on the electrode current.

- **The dead zone.**

  The extension of the dead-zone bound should be chosen to reject the interaction effect between the electrical phases. Therefore, the sizes of the dead-zone bounds should be larger than the electrode current

deviations as results of electrode displacements due to control actions occurring at the other electrodes.

If the fixed electrode displacement is denoted Δh^*, the current dead-zone bound is denoted $\Delta I_e{}^*$, and the current-displacement model is denoted $\boldsymbol{H}$, the requirement regarding the dead-zone extension can be expressed as:

$$\Delta I_e{}^* > \max\left(\left|\{\boldsymbol{H}\}_{ij}\right|\right) \cdot \Delta h^* \tag{6.6}$$

where $\{\boldsymbol{H}\}_{ij}$ denote the off-diagonal elements in matrix $\boldsymbol{H}$.

Simulation experience supports the following guideline:

$$\Delta I_e{}^* \approx 2 \cdot \max\left(\left|\{\boldsymbol{H}\}_{ij}\right|\right) \cdot \Delta h^* \tag{6.7}$$

Furthermore, the dead-zone extensions should be different in upward and downward directions due to the difference in the current sensitivities to electrode displacements.

- **The time-before-action.**

  The length of the time-before-action period should be chosen with regard to the disturbance rejection properties of the controller. The choice of the time-before-action period regarding disturbance rejection, meets comparable considerations such as the choice of the integral-time in a conventional PI controller.

  It can be stated that the time-before-action period Δt^*, should be in the range of the half-periods of the dominant high-frequent disturbances, affecting the electrical environment:

$$\Delta t^* \approx \frac{1}{2} \cdot T_{HF} \tag{6.8}$$

  where T_{HF} represents the periods of the high-frequent disturbances at the "limit-frequency", corresponding to the band-width of the controller.

Optimization procedure

The following optimization procedure regarding the the dead-zone control parameters can therefore be stated:

1. Decide the upward and downward electrode displacements.
2. Decide the upward and downward dead-zone based on the calculation of the interaction effects and the controller's ability to reject these effects.

3. Decide the time-before-action period based on an evaluation of the disturbance frequencies and the controller's disturbance rejection properties.

Simulation examples

The steady-state model with the conventional current controller and with model parameters as outlined in Tables 5.5 and 5.6, is used to simulate various sets of control parameters in order to illustrate the effects of proper parameter adjustment.

- **The dead-zone bounds**

  The effect of the size of the dead-zone bound on the interaction between the electrical phases is illustrated in Figs. 6.12 and 6.13.

  Figure 6.12 shows how the controllers respond to a change in the reactance in phase 1:

$$X_1 \ : \ 0.71 \rightarrow 0.80\,\mathrm{m}\Omega\,, \ \text{at}\ t = 5\,\mathrm{s}$$

  when a dead-zone bound of 2.0 kA is applied. The interaction effect between the control loops is clearly illustrated. The movement of one electrode due a control action, leads to subsequent control actions applied on the other electrodes, because the interaction forces the other currents outside the dead-zone bound.

  The current-electrode displacement model $\boldsymbol{H}$ at the start of the simulations, previously given in Eq. 5.21, is:

$$\boldsymbol{H} = \begin{pmatrix} -2.33 & -1.33 & 0.38 \\ 0.46 & -1.84 & -1.28 \\ -1.63 & 0.42 & -1.80 \end{pmatrix} \tag{6.9}$$

  According to the proposed dead-zone guideline in Eq. 6.7, the dead-zone bound should be:

$$\begin{aligned} \Delta I_\epsilon^{\star} &\approx 2 \cdot \max\left(\left|\{\boldsymbol{H}\}_{ij}\right|\right) \cdot \Delta h^{\star} \\ &= 2 \cdot 1.63[\mathrm{kA/cm}] \cdot 1.0[\mathrm{cm}] \approx 3.0\mathrm{kA} \end{aligned} \tag{6.10}$$

  Figure 6.13 shows the response for a dead-zone bound of 3.0 kA. The improvements from Fig. 6.12 are remarkable, and the interaction effects between the controllers are considerably rejected.

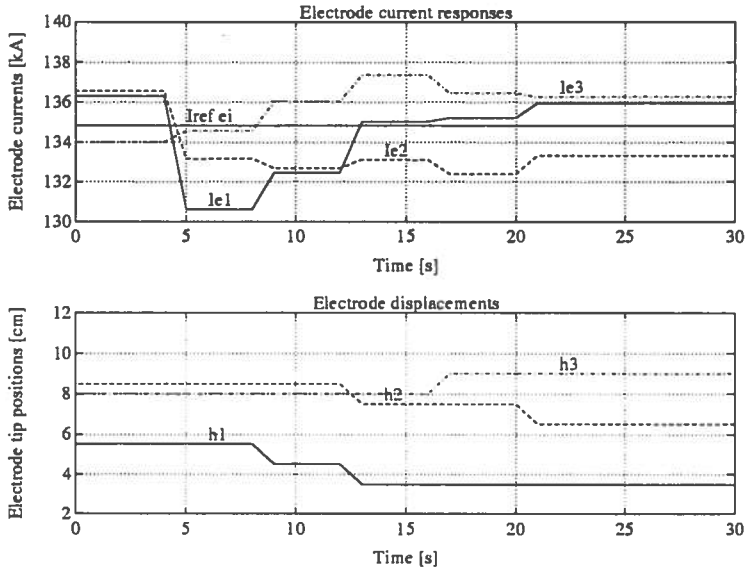

Figure 6.12: Response of the conventional current controller, dead-zone bound = 2 kA. Reactance in phase 1, X_1, is altered from 0.71 to 0.80 mΩ at $t = 5$ s.

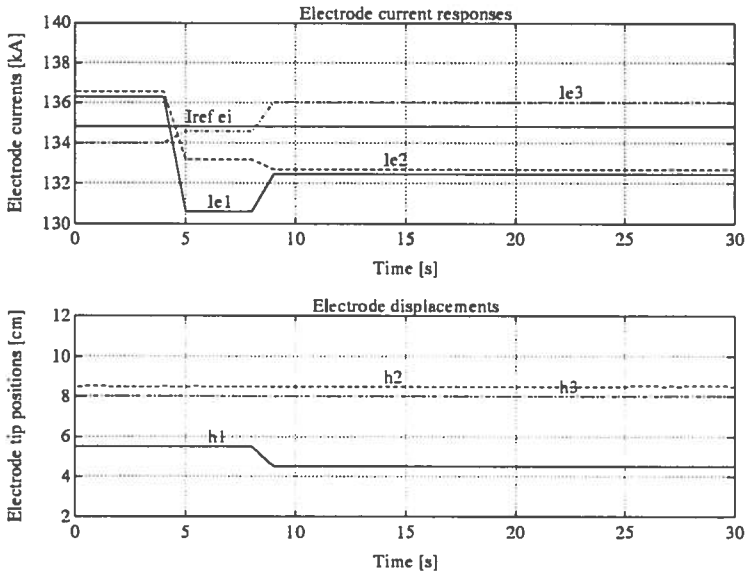

Figure 6.13: Response of the conventional current controller, dead-zone bound = 3 kA. Reactance in phase 1, X_1, is altered from 0.71 to 0.80 mΩ at $t = 5$ s.

- **The time-before-action period**

  The effect of the time-before-action period is illustrated in Figs. 6.14 and 6.15. During this simulation the charge resistances R_{ci} and the metal bath resistances R_m, are exposed to high-frequent disturbances:

$$R_{ci} = [1 + 0.5 \cdot \sin(\pi/5\, t + \phi_{ci}) + w_{ci}] \cdot R_{ci0} \tag{6.11}$$

$$R_{mi} = [1 + 0.2 \cdot \sin(\pi/6\, t + \phi_{mi}) + w_{mi}] \cdot R_{mi0} \tag{6.12}$$

  where ϕ_{ci} and ϕ_{mi} denote different phase angles, w_{ci} and w_{mi} denote random effects, and R_{ci0} and R_{ci0} denote the original values.

  Figure 6.14 shows the response when a time-before-action period of 3.0 s is applied. It illustrates how the controllers try to reject the high-frequent disturbances, which result in considerable unnecessary electrode movements.

  The guideline regarding the time-before-action period in Eq. 6.8 yields the following time period:

$$\Delta t^{\star} \approx \frac{1}{2} \cdot T_{HF} = \frac{1}{2} \cdot 12.0\ [\mathrm{s}] = 6.0\ [\mathrm{s}] \tag{6.13}$$

  Figure 6.15 shows the effect of the controllers with a time-before-action period of 5.0 s, and it illustrates the effect of a proper time period adjustment. The high-frequent disturbances are "let through" by the controller without attempting of rejecting the high-frequent deviations.

6.5 Concluding remarks

The topic of this chapter has been the electric control system of a ferrosilicon furnace. A conventional electric control strategy is discussed, and the focus has especially been on the current control strategy. A decoupling current controller is proposed and compared to conventional current control by simulation studies. However, the decoupler turned out to be unfavorable due to model uncertainty. Therefore, the conventional current controller is further studied and improved by optimizing the control parameters, and finally, guidelines for optimizing the control parameters in the conventional current controller are proposed based on simulation studies.

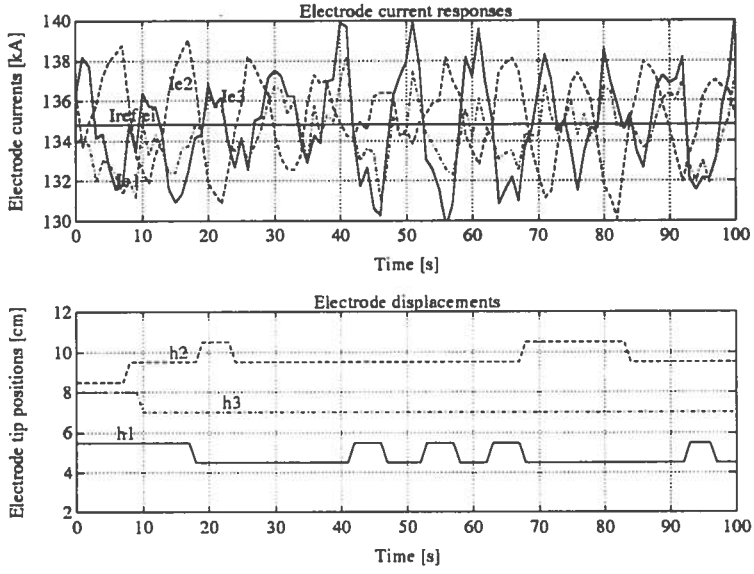

Figure 6.14: Response of the conventional current controller, time-before-action = 3 s.

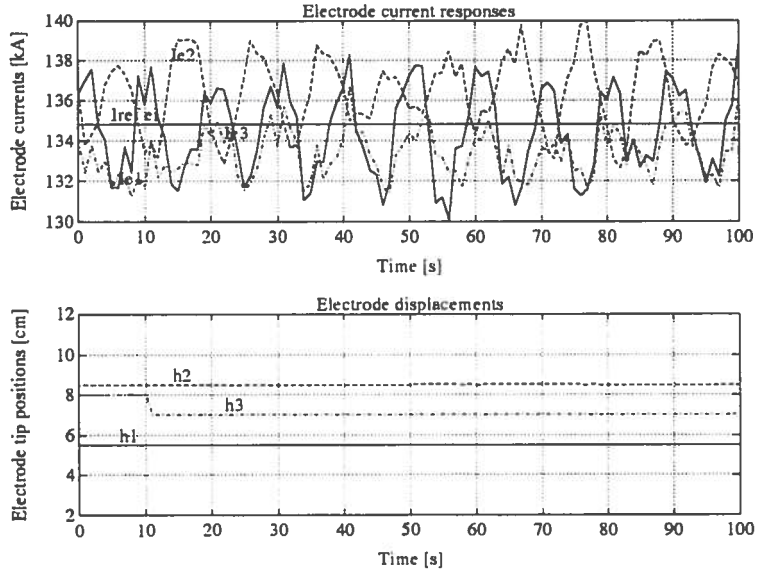

Figure 6.15: Response of the conventional current controller, time-before-action = 5 s.

Chapter 7

The ferrosilicon process

The topic of this chapter is the ferrosilicon process. The chapter starts by discussing the chemical reactions in the ferrosilicon process and a stoichiometric model of the silicon process, which can represent the ferrosilicon process as well, is described. Next, important terms related to the process are defined, and models of possible reaction patterns are discussed. The next topic is the metallurgical control of the process. The metallurgical control tasks and how they can be achieved by control are discussed, and the importance of different process inputs and outputs are treated. Finally, a dynamic model of the silicon process, which is used in further analyses o the process, is described.

7.1 Introduction to the ferrosilicon process

A brief introduction to the ferrosilicon process and the operation and control of submerged-arc furnaces is previously given in Sections 2.2 and 2.3.

Ferrosilicon alloys are produced by reducing quartz with carbon in electric furnaces. Iron dioxide is added to give the alloy the desired grade, which indicates the percentage weight fraction of silicon. Ferrosilicon alloys are produced with different iron contents. The most common alloy qualities are FeSi 45%, FeSi 75% and FeSi 90%. Pure silicon (98-99%) is produced by the same technique. but without the addition of iron, and with slightly different carbon materials.

The overall reaction for FeSi 75%, assuming that the silicon content in the added quartz is completely transformed to silicon, can be described by:

$$12\,SiO_2 + Fe_2O_3 + a\,C \rightarrow 2\,\text{“}FeSi_6\text{”} + b\,CO + c\,CO_2 \qquad (7.1)$$

where a, b and c depend on the reduction of the iron oxide, and where the quotation marks indicate that the ferrosilicon is an alloy not a chemical compound. The iron oxide will mainly be reduced in the upper part of the furnace, for instance by the upstreaming CO gas in accordance with the reaction:

$$Fe_2O_3 + 3\,CO \rightarrow 2\,Fe + 3\,CO_2 \tag{7.2}$$

Assuming that the iron oxide is reduced completely by this reaction, the overall reaction for FeSi 75% with a silicon yield of $x \cdot 100\%$, becomes:

$$\frac{1}{1-x}\,12\,SiO_2 + Fe_2O_2 + a\,C \rightarrow \frac{x}{1-x}\,2\,\text{“}FeSi_6\text{”} + 12\,SiO + b\;CO + c\,CO_2 \tag{7.3}$$

The ferrosilicon process is closely related to the pure **silicon process**. If the produced alloy has more than 60% silicon content, the reduction of iron oxide consumes the “excess” of carbon monoxide from the reduction of quartz, in accordance with Eq. 7.2. Therefore, in theory, the carbon demand of the ferrosilicon process will not depend on the presence of iron, or it will just be slightly increased in accordance with industrial practice from production of FeSi 75%, and the process behaves similarly to the silicon process.

The reduction of quartz is the limiting factor in the ferrosilicon process, and qualitatively speaking the process will be easier to carry out the higher the iron content of the alloy (Schei and Larsen, 1982; Schei and Halvorsen 1991). Thus, the ferrosilicon process can be described by models of the pure silicon process, provided that the model parameters are properly adjusted, and the pure silicon process is treated in the further discussion.

7.2 A stoichiometric model of the (ferro)silicon process

The stoichiometric model described in this section, is based on the work of Schei and Larsen (1982) and Schei and Halvorsen (1991). In the following the term the “silicon process” is used to describe the ferrosilicon process as well as the pure silicon process. In the model any impurities in the raw materials are neglected and the process is regarded as a chemical reaction between pure materials. The term “stoichiometric model” is related to the aim of the model, which has been a description of the process by means

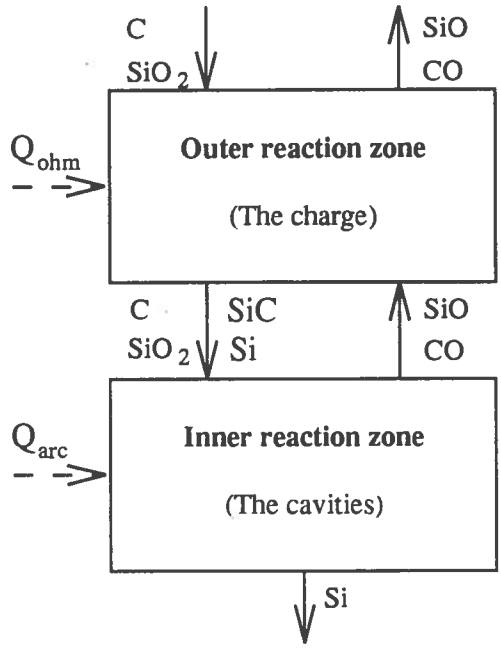

Figure 7.1: A schematic illustration of the two-stage model of the silicon process.

of the chemical equations with the main elements present in the process (Schei and Halvorsen, 1991).

The silicon process can be regarded as a two-stage process, and thus, from a modelling point of view the process can be divided into two reaction zones:

- **An inner zone:** consisting of the cavities and the surrounding charge.
- **An outer zone:** consisting of the charge above the cavities.

Figure 7.1 illustrates the model with the two reaction zones, indicating the assumed material flow in connection with the zones and the heat inputs, Q_{arc} and Q_{ohm}, which denote heat generation due to arcing and ohmic conduction, respectively.

7.2.1 The inner reaction zone

The cavities in the hearth of the furnace can be regarded as constantly stirred tank reactors. Most of the heat is generated in this region of the furnace by the electric arcs (Q_{arc}), which also create strong stirring in the cavities. The inner zone is supplied from the outer reaction zone with:

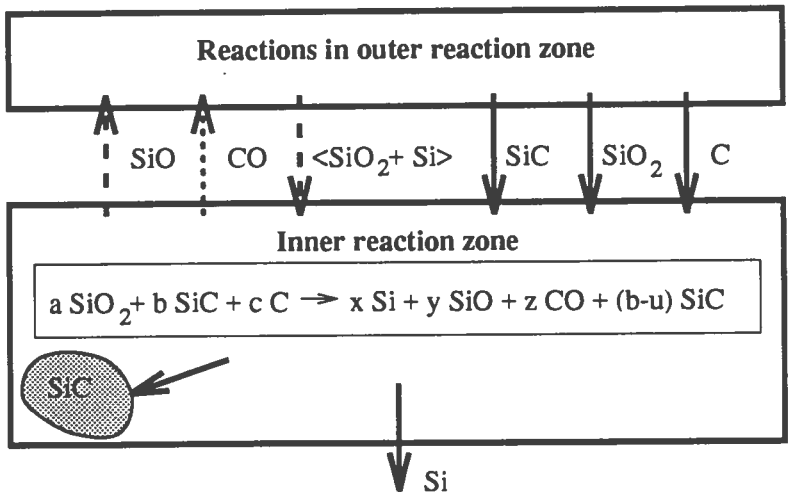

Figure 7.2: Model of inner reaction zone.

- SiO_2, SiC, "condensate" $< SiO_2 + Si >$, and possible C.

SiO and CO gases leave the inner zone and flow towards the outer zone, while Si is drained from the inner zone. The temperature in the inner zone is about 2300 K.

In the cavities there is a complicated reaction pattern between the present reactants and large amount of energy is consumed. It is observed that SiO_2, SiC and C disappear, while a mixture of SiO and CO gases and liquid Si are formed, and occasionally solid SiC is deposited. Figure 7.2 shows the material flow and the overall chemical reaction in the inner reaction zone.

According to be Schei and Halvorsen (1991), the overall chemical reactions in the inner zone can be expressed as :

$$a\,SiO_2 + b\,SiC + c\,C \rightarrow x\,Si + y\,SiO + z\,CO + (b-u)\,SiC \qquad (7.4)$$

where a, b and c are the coefficients for the materials added from the outer reaction zone, u is the coefficient for the consumption of SiC, and x, y and z are the coefficients for the Si, SiO and CO products.

The equilibrium condition for the free formation of free formation of Si is given by the reaction (Schei and Halvorsen, 1991):

$$SiO(g) + SiC(s) \rightarrow 2\,Si(l) + CO(g) \qquad (7.5)$$

where g, l and s denote gas, liquid and solid phases, respectively. This equilibrium is illustrated in Fig. 7.3, where a point below the curve corre-

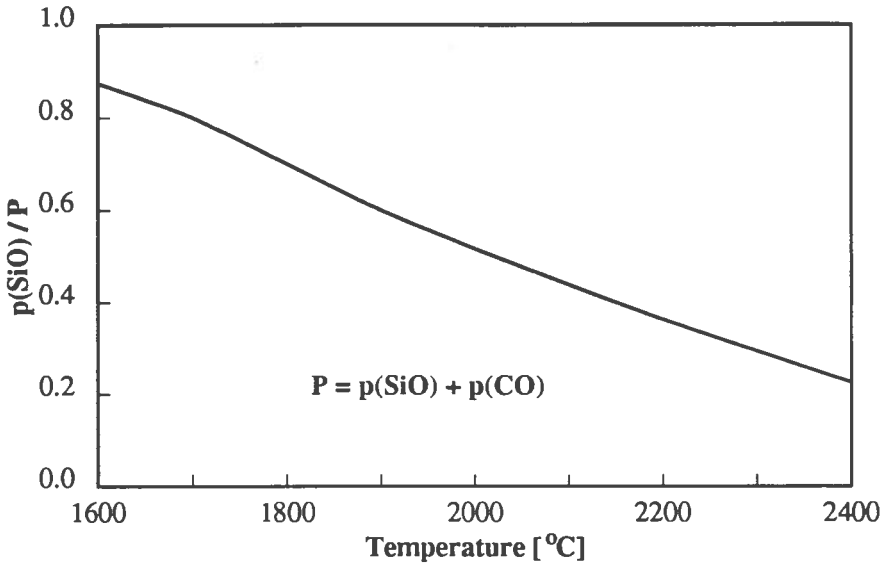

Figure 7.3: The equilibrium $SiO(g) + SiC(s) = 2\,Si(l) + CO(g)$, based on Schei and Halvorsen (1991).

sponds to a situation where free Si is unstable. For a given temperature this defines a minimum content of SiO in the gas mix that must be satisfied before free Si is to be formed. The gas leaving the inner reaction zone can be characterized by a property s, defined as (Schei and Halvorsen, 1991):

$$s = \frac{p_{SiO}}{p_{SiO} + p_{CO}} \tag{7.6}$$

The property s is assumed to be a constant for a given charge and furnace operation mode. The temperatures in the cavities of silicon furnaces are measured to be around 2000 °C (Schei and Larsen, 1982), and hence the equilibrium for the reaction between SiO and SiC in these cavities will correspond to approximately $s = 0.5$.

If Si is present in the inner zone, the reaction in Eq. 7.4 will run as long there is SiO_2 present. When SiC is present, the gas composition will be given by the s-property in Eq. 7.6. If the SiC is consumed, SiO_2 can react with Si, and the s-property is no longer a restriction, and the SiO content is determined by the availability of SiO_2 (Schei and Halvorsen, 1991). Therefore, the reaction in the inner zone can occur in two ways:

1. The reaction is governed by the s-property in Eq. 7.6.

2. The reaction is governed by the stoichiometry of the reactants.

This is further discussed in Schei and Halvorsen (1991).

The overall reaction in Eq. 7.4 can formally be described by a combination of the following reactions:

1. The SiO producing reactions:

$$2\,SiO_2 + SiC \rightarrow 3\,SiO + CO \tag{7.7}$$

$$SiO_2 + Si \rightarrow 2\,SiO \tag{7.8}$$

2. The Si producing reaction:

$$SiO + SiC \rightarrow 2\,Si + CO \tag{7.9}$$

3. And in the presence of C, the SiC producing reaction:

$$SiO + 2\,C \rightarrow SiC + CO \tag{7.10}$$

It should be noticed that supply of SiC from the outer reaction zone is highly important for the reaction pattern in the inner zone, and hence the production of SiC in the outer reaction zone is a necessary intermediate stage in the process.

The inner zone reaction is strongly endothermic and receives the necessary energy from the electric arcs in the cavities, together with ohmic conduction in the cavity walls. A considerable part of this energy is transported to the outer zone by the production and subsequent condensation of SiO. This "recycling" of SiO between the reaction zones has the effect of some kind of a heat pump, supplying energy for heating and melting the solids in the upper reaction zone.

The presence of C in the inner zone can result in an increasing content of SiC in the cavities, and as time goes by this will damage the production. An optimal reaction pattern means that all the C should react to SiC in the outer zone and enter the inner reaction zone as SiC and not as C. However, there will always be some C present in the inner zone due to the carbon electrodes in the cavities.

The objectives of the inner reaction zone can be summarized as:

- Production of Si.
- Production of SiO.
- Taking up energy and transferring it to the outer zone by the production and release of SiO gas, which partly condensate in the outer zone.

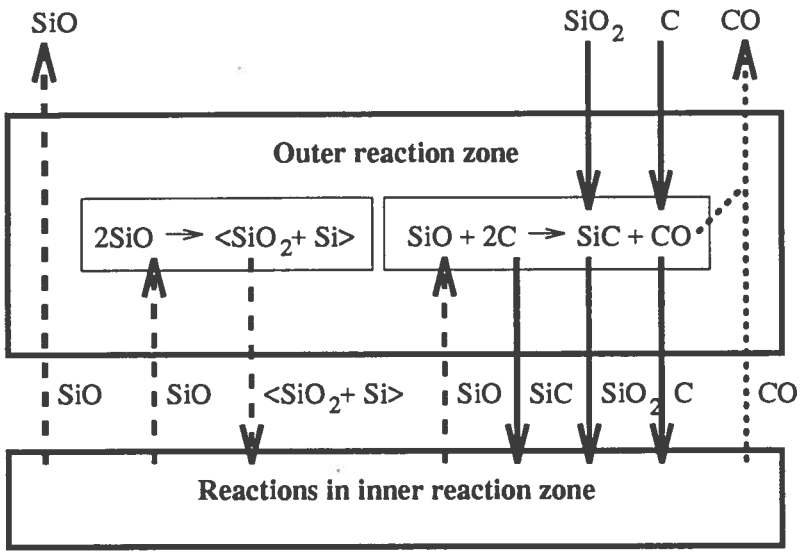

Figure 7.4: Model of outer reaction zone.

7.2.2 The outer reaction zone

This part of the furnace behaves like a packed bed reactor. At the top the solid raw materials, quartz (SiO_2) and various carbon material (C), are added through the charging of the furnace, and the upper zone is supplied with SiO and CO gases flowing up from the inner reaction zone.

The solid materials are heated mainly by released chemical reaction energy and heat conduction from the hearth of the furnace, but also partly by electric conduction in the charge, Q_{ohm}. The temperature in the outer reaction zone is in the range 1000-2000 K.

Quartz partly melts and a countercurrent reaction occurs between the carbon materials and the upstreaming SiO gas, producing SiC. Furthermore, some of the SiO gas condenses, while the remaining SiO leaves the zone together with the CO gas. At the top of the furnace these gases further react with oxygen to silica fume (SiO_2) and CO_2, but this is not considered in the model. The outer zone supplies the inner reaction zone with SiO_2, which is softened or partly melted, SiC, "condensate" $< SiO_2 + Si >$, as a result of the condensation of SiO, and any unreacted C.

The chemical reactions occurring in the upper reaction zone as well as the material flows, are illustrated in more detail in Fig. 7.4. The main reactions in the upper reaction zone are:

1. The reaction between the carbon materials and the upstreaming SiO gas:

$$SiO + 2\,C \rightarrow SiC + CO \tag{7.11}$$

producing SiC and CO.

2. The condensation of SiO:

$$SiO \rightarrow \frac{1}{2} < SiO_2 + Si > \tag{7.12}$$

The SiO condensation produces a lot of heat and acts like the main heat source for the upper reaction zone.

This condensation will if possible, continue until the furnace top is heated sufficiently to let the SiO gas escape from the furnace, or until gas channel is formed in the charge and releases the SiO gas.

The outer reaction zone has three main tasks:

1. Recovery of SiO gas streaming up from the inner zone.
2. Production of SiC.
3. Heating and melting of raw materials.

7.3 Definitions of process related terms

This section defines some important terms related to the operation and analyses of ferrosilicon and silicon furnaces.

7.3.1 Silicon yield and silicon loss

The silicon yield of the furnace can be defined as the amount of silicon produced as alloy in proportion to the total silicon content in the added charge (Schei and Halvorsen, 1991). Compared with the overall chemical reaction of the silicon process:

$$a\,SiO_2 + c\,C \rightarrow x\,Si + y\,SiO + z\,CO + u\,SiC \tag{7.13}$$

the silicon yield can be expressed as:

$$\text{Silicon yield} = \frac{x}{a} \tag{7.14}$$

The silicon loss, which is the amount of silicon leaving the furnace as silicon monoxide in proportion to the total silicon content in the added charge, can be expressed as:

$$\text{Silicon loss} = \frac{y}{a} \tag{7.15}$$

7.3.2 Specific energy consumption

The specific energy consumption of the process is commonly used as a key description of how successfully the furnace is operated. The **specific energy consumption** can be defined as the amount of electric energy added to the furnace per tonne of produced silicon alloy (Schei and Halvorsen, 1991). The overall chemical reaction is:

$$a\,\mathrm{SiO_2}(298K) + c\,\mathrm{C}(298K) \rightarrow \\ x\,\mathrm{Si}(T_{Si}) + y\,\mathrm{SiO}(T_{CO}) + z\,\mathrm{CO}(T_{CO}) + u\,\mathrm{SiC}(T_{SiC}) \qquad (7.16)$$

If the coefficients and temperatures in this reaction are known, the energy consumption can be calculated:

$$\text{Energy consumption} = p \cdot \Delta H\,(\text{Reaction Eq. 7.16}) \qquad (7.17)$$

where p is the thermal efficiency factor of the furnace, which has a value of about 1.2 for large furnaces.

The furnace silicon yield and specific energy consumption are among the most important key figures that describe the furnace operation conditions.

7.3.3 Carbon turnover

The carbon materials will normally not react completely with SiO in the outer reaction zone. During the reaction in Eq. 7.11 the carbon materials are transformed to SiC. The SiC formation starts at the surface of the carbon particles and makes a layer of porous SiC. Therefore, the SiO has to diffuse through this layer to react with carbon, and as the layer thickness increases, the reaction slows down (Schei and Halvorsen, 1991).

Referring to the two-zone model of the silicon process, the **carbon turnover** is defined as the portion of carbon that reacts in the outer zone.

The carbon turnover will be dependent on the conditions in the charge burden (the outer zone), and the composition of the carbon materials plays an important role. Important factors that have a significant influence on the carbon turnover are:

Reactivity : The reactivity of the carbon materials depends on the material properties, such as porosity, and strongly influences the chemical reaction rates. High reactivities of the carbon materials yield a high turnover.

Particle sizing: The sizes of the carbon particles will affect the carbon turnover directly since the reaction rates depend on the volume of the particles. Larger carbon particles lead to a lower carbon turnover.

Residence time: The carbon turnover also depends on the residence time of the carbon materials in the outer zone. A short residence time yields a low turnover. The residence time depends in turn on the height of the charge burden above the cavities, the sizes of the charge particles and the general consistency of the charge.

Temperature: The charge temperature affects the reaction rates in the charge, as well as the residence times of the charge materials, and thereby also the carbon turnover.

Countercurrent contact: The reaction rates are heavily affected by the countercurrent contact conditions between the solid materials and the upstreaming gas. Any uneven distribution of upstreaming gas in the charge will decrease the carbon turnover. Any segregation of charge particles, which denotes separation due to size differences, will have a similar effect.

7.3.4 The charge carbon content

The carbon content in the charge is an important factor in the operation of ferrosilicon furnaces. In industrial operation the carbon content is chosen based on raw material analyses and experience, and the content is corrected according to the furnace behavior. The carbon content of the charge can be defined by the parameter x in $SiO_2 + x\ C$ (Schei and Halvorsen, 1991).

Figure 7.5 shows the principle relationship between the silicon yield of the furnace and the carbon content of the charge (Schei and Halvorsen, 1991). The figure shows that there is a maximum in the silicon yield as a function of the charge carbon content. and hence the corresponding carbon content is denoted " optimal".

According to Schei and Halvorsen (1991), a carbon content that is lower than the optimal value, gives the following overall reaction in the inner zone:

$$a\ SiO_2 + c\ C \rightarrow x\ Si + y\ SiO + z\ CO \tag{7.18}$$

while a higher carbon content than optimum, gives the overall reaction:

$$a\ SiO_2 + c\ C \rightarrow x\ Si + y\ SiO + z\ CO - u\ SiC \tag{7.19}$$

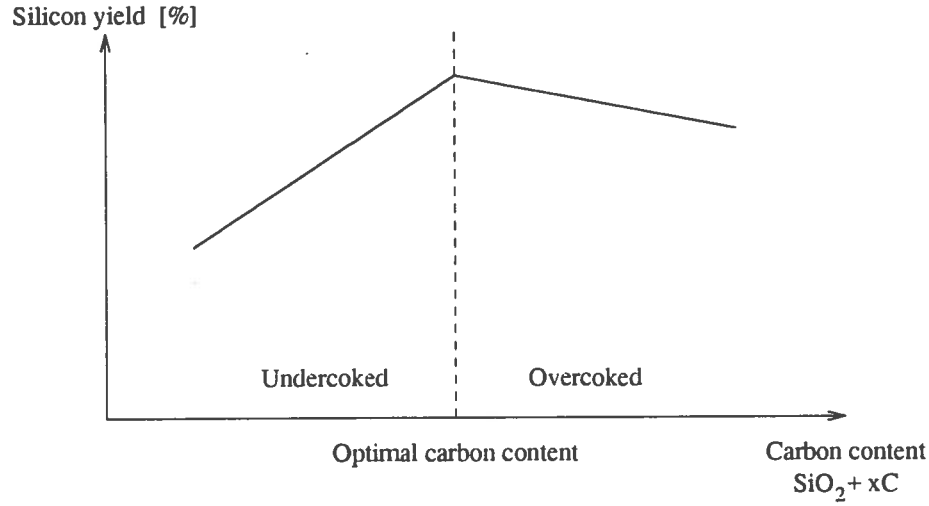

Figure 7.5: Silicon yield as function of the charge carbon content.

The terms overcoked charge (carbon surplus) and undercoked charge (carbon deficit) are defined by referring to the optimal carbon content, as illustrated in Fig. 7.5.

- **Overcoked charge**

  The furnace has an **overcoked** charge if the silicon yield is **reduced** by an **increase** in the carbon content.

  This could alternatively be expressed as the furnace having an overcoked charge if the silicon yield is increased by an decrease in the carbon content.

- **Undercoked charge**

  The furnace has an **undercoked** charge if the silicon yield is **increased** by an **increase** in the carbon content.

  Or alternatively, the furnace has an overcoked charge if the silicon yield is reduced by a decrease in the carbon content.

The properties of the carbon materials strongly influence dependency of the silicon yield on the charge carbon content. A change in the carbon material properties will result in a change in the optimal carbon content. Figure 7.6 shows the silicon yield as a function of the carbon content for situations with low and high carbon turnovers (Schei and Halvorsen, 1991; Halvorsen, Schei and Downing, 1992). Figure 7.6 indicates that a lower carbon turnover implies a lower optimal value for the carbon content. The

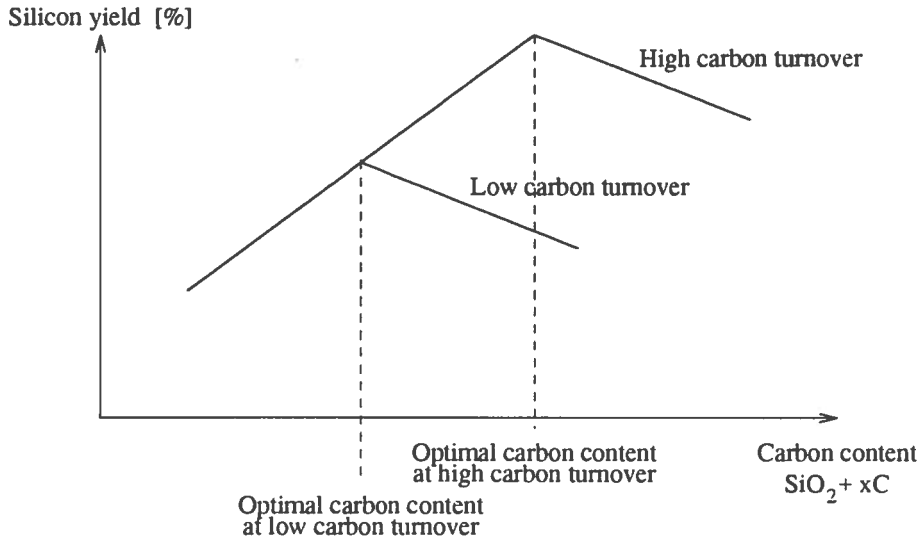

Figure 7.6: The influence of variations of the carbon turnover on the silicon yield.

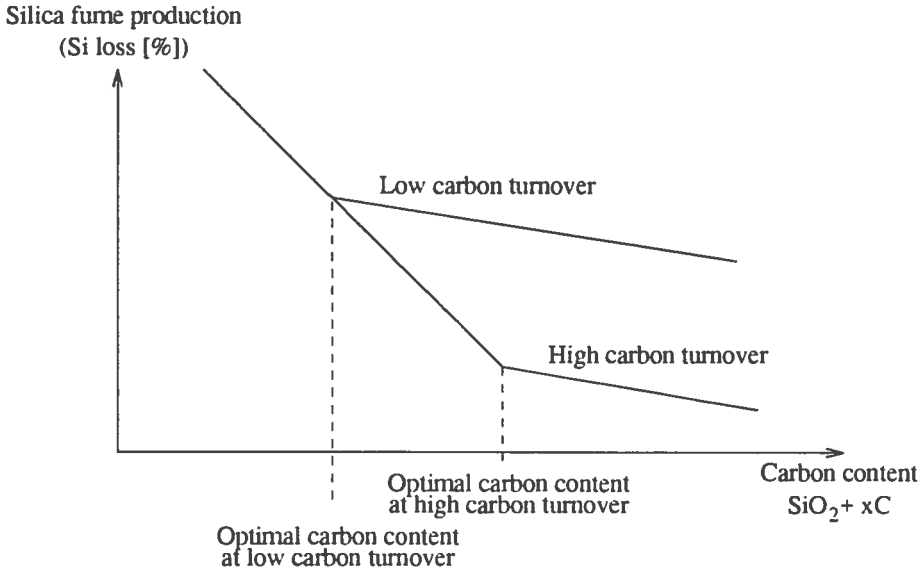

Figure 7.7: Silicon loss as a function of charge carbon content at different carbon turovers.

relation between the carbon content and the silicon yield could alternatively be expressed in terms of the furnace silicon loss as shown in Fig. 7.7.

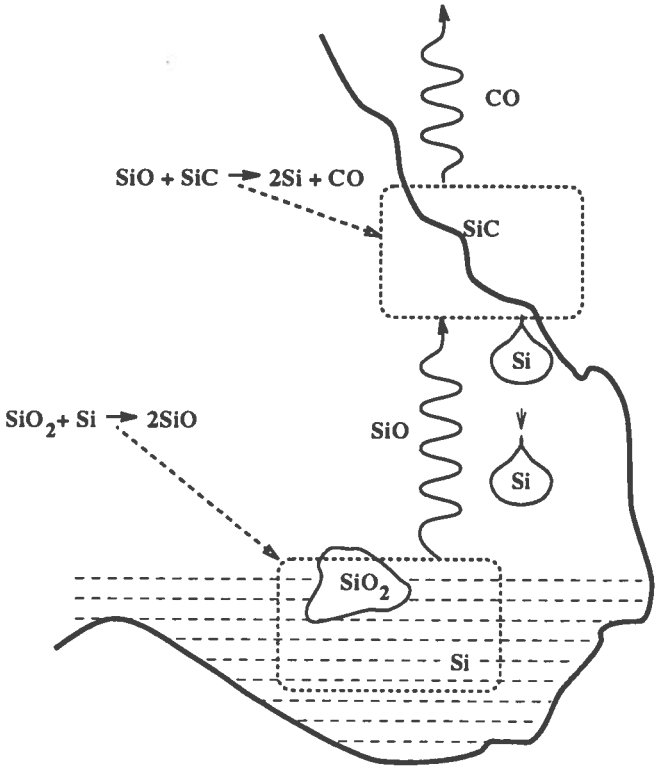

Figure 7.8: A possible reaction pattern in the cavity

7.4 Qualitative models of the reaction patterns

When analyzing the silicon process and how it is affected by conditions like the reactivity of the carbon materials, it can be useful to apply qualitative models of the reaction patters occurring in the different zones in the process. The following discussion is based on the work of Schei and Larsen (1982) and Schei and Halvorsen (1991).

7.4.1 Cavity reaction patterns

A possible reaction pattern that can occur in the cavities is discussed in the following. Figure 7.8 schematically shows a cavity in a silicon furnace and the occurrence of the chemical reactions:

$$SiO_2 + Si \rightarrow 2\,SiO \tag{7.20}$$

$$SiO + SiC \rightarrow 2\,Si + CO \tag{7.21}$$

At the bottom of the cavity there is a bath of liquid Si. In the Si bath lumps of SiO_2 are present and help the possibility of the reaction between

SiO_2 and Si in Eq. 7.20. This reaction forms SiO gas, which in turn rises up until it meets the cavity wall, containing SiC. Then a reaction in Eq. 7.21 between the upstreaming SiO and the SiC in the cavity wall occurs, and liquid Si and CO gas are produced. Then the Si flows back to the bath and the CO gas flow up through the charge. It is also possible that the reaction between SiO_2 and Si in Eq. 7.20 can occur in the cavity walls, as liquid Si flows over SiO_2 present in the walls.

This reaction pattern can be expressed by the overall reaction:

$$\mathrm{a\ SiO_2 + b\ SiC \rightarrow x\ Si + y\ SiO + z\ CO} \tag{7.22}$$

where the stoichiometric coefficient a expresses the extent of reaction in Eq. 7.20, and b expresses the extent of the reaction in Eq. 7.21. This reaction pattern depends strongly on whether SiC is produced at a place where it can be reached by the upstreaming SiO gas. Therefore, the amount of produced Si is directly dependent on the availability of SiC.

Another possible cavity reaction is:

$$\mathrm{2\ SiO_2 + SiC \rightarrow 3\ SiO + CO} \tag{7.23}$$

This reaction can be expressed by a combination of the reactions in Eq. 7.20 and 7.21, with $a = 2$ and $b = 1$. This is an SiO producing reaction, and a simple explanation of the reaction is that any "new" Si is not produced because the SiO gas does not meet "enough" SiC at the cavity walls, and SiO gas escapes from the cavities.

This reaction could also be utilized by the gas phase CO-CO_2:

$$\mathrm{2\ SiO_2 + 2\ CO \rightarrow 2\ SiO + 2\ CO_2} \tag{7.24}$$

$$\mathrm{2\ CO_2 + SiC \rightarrow 3\ CO + SiO} \tag{7.25}$$

The reaction occurs as CO gas reacts with SiO_2 lumps in the Si bath or in the cavity walls, producing the gases SiO and CO_2. Then, the CO_2 gas in turn reacts with SiC in the cavity walls, forming CO and SiO gases.

The atmosphere in the cavities will most probably be strongly stirred by the occurrence of electric arcs. Therefore, the cavity gases will be significantly mixed, and the gas consuming reactions will not be dependent to happen straight above the gas producing reactions. In addition, the arcing effect can also result in the spreading of liquid Si because of the impinging of the metal bath.

7.4.2 Charge reaction patterns

The carbon reaction in the charge can be described as follows. A carbon particle is assumed to be moved closer to the inner zone, where it is heated and comes in touch with the upstreaming SiO, and reacts in accordance with:

$$SiO + 2\,C \rightarrow SiC + CO \tag{7.26}$$

The result will be that the remaining carbon particle becomes surrounded by an SiC layer, and the reaction stops up when the SiO does not reach the carbon.

As the particle comes closer to the cavities, the temperature can increase sufficiently high, so that the SiC layer can react with the SiO gas:

$$SiO + SiC \rightarrow 2\,Si + CO \tag{7.27}$$

The result is that the SiC layer is consumed, free Si is produced, and carbon is uncovered. The carbon then in turn reacts with the SiO gas, and the reaction pattern is "iteratively" repeated.

This reaction pattern explains why the sizing of the carbon particles is important for the carbon turnover. If the carbon particles are too large, the carbon may not be consumed completely, and the carbon may enter the inner reaction zone.

7.5 Metallurgical control of a ferrosilicon furnace

The operation and control of a ferrosilicon furnace has previously been described in Section 2.5. The discontinuous furnace operations are summarized as an introduction to the further discussion.

Furnace operations

The furnace operations consist of the following activities:

- **Stoking and charging.**

  In the stoking operation the upper part of the charge burden is stirred in order to mix the charge materials and destroy gas channel formations in the charge, in addition the cavities are partly filled with charge materials.

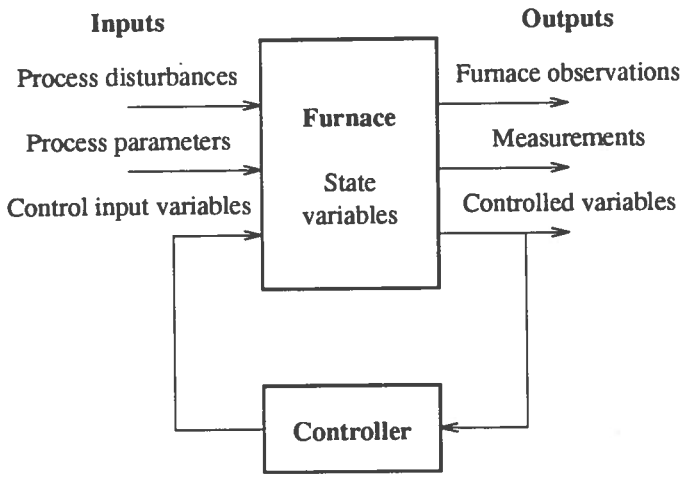

Figure 7.9: Illustration of furnace with its input and output variables and its control system.

Then new materials are charged, and the furnace is further stoked to mix and distribute the added raw materials. Then follows a period of about half an hour with no furnace operations.

- **Tapping.**

  The tapping of ferrosilicon from the furnace bottom is also a discontinuous operation. Thus the content of produced metal in the furnace will fluctuate within the tapping periods, which are between one and two hours.

- **"Quartzing" and "coking".**

  Separate addition of raw materials, usually quartz but also carbon material, directly at the furnace surface is sometimes used as a metallurgical control activity in addition to ordinary charging in order to adjust the local material balance.

7.5.1 A system theoretic description of a ferrosilicon furnace

Figure 7.9 shows a simple illustration of a ferrosilicon furnace, its input and output variables, and its control system, as seen from a system theoretic point of view.

The furnace is affected by three different classes of input variables:

1. **Control input variables:** Controllable variables that are used actively in the control of the furnace.

2. **Process parameters:** These are controllable variables that not are used in the control of the furnace, but are occasionally altered to obtain certain effects.

3. **Disturbances:** Such variables are not controllable and hence beyond our control.

The furnace output variables can be classified in the three categories:

1. **Controlled variables:** Measurement variables that are used actively in the control of the furnace.

2. **Measurements:** Measurement variables that are not used in the control system.

3. **Furnace observations:** Manual observations of process conditions.

In addition the furnace is characterized by its internal **state variables**, which are the variables we actually want to control and identify through the measurements and observations.

7.5.2 Metallurgical control task

The metallurgical control task regarding ferrosilicon furnace operation can be stated as:

> **Controlling the chemical processes and reaction patterns in the furnace in order to attain some kind of "optimal" furnace conditions.**

In order to succeed in this task, the process control system must fulfill the following requirements:

- **Controllability.**

  The applied control input variables must affect the process state variables we want to control in a way that the control task can be achieved.

- **Observability.**

  The applied measurement variables must give sufficient information about the process state variables of current interest.

In addition the "optimal" furnace condition must be specified and it should be expressible in terms of these process state variables.

7.5.3 Process state variables

There are a large number of process state variables in a ferrosilicon furnace. Based on the two-stage model description of the silicon process presented in Section 7.2, the following state variables can be stated:

- **Concentrations:**

  The concentrations in the cavities ("the inner zone") and the charge burden ("the outer zone") should be considered as state variables for the following reactants:

  - SiO_2 (solid and liquid)
  - C (solid)
  - SiC (solid)
  - Si (liquid)
  - SiO (gas)
  - Condensate
  - CO (gas)

- **Material flows:**

  - Downwards flow of liquid materials.
  - The gas flows.

- **Temperature and pressure:**

  - The temperatures in the charge burden.
  - The temperatures in the cavities.
  - The pressure in the cavities.
  - The partial pressures of SiO in the cavities which corresponds to the SiO fractions in the cavity atmospheres.

- **Geometry:**

  - The positions of the interface-zone between the cavities and the charge.
  - The heights of the charge burden above the cavities.
  - The volume or extension of the cavities.

- **Outer variables:**
  - The SiO flow from the furnace top.
  - The CO flow from the furnace top.
  - The temperature of the gas leaving the furnace.
  - The Si flow from the furnace (the tapped metal rate).
  - The temperature of the metal.

The state variables in the inner zone can be regarded as concentrated variables for each of the three cavities, while the state variables in the outer zone in principle are distributed in three dimensions.

Reduced property state variables

However, the furnace can be regarded as three separate sub-processes, containing one cavity and the charge burden above it, with varying degrees of interaction, corresponding to the assumptions in the stoichiometric model in Section 7.2. The relative large number of state variables can be reduced, and the following property state variables characterize each of these sub-processes:

- The cavity temperature.
- The partial pressures of SiO in the cavities.
- The SiC content in the cavity.
- The Si production rate from the cavity.
- The charge height.
- The carbon turnover in the outer zone.
- The furnace's carbon content.
- The SiO flow from the top.

An alternative model view of the furnace is to consider it to be composed of the three cavities constituting the inner zone and one common charge burden constituting the outer zone. In this way the furnace is characterized by the three sets of cavity variables and one common set of charge variables. Table 7.1 summarizes the process state variables that characterize the furnace in such a model view. The dimensions of the variables and an indication of how they can be achieved are also given in Table 7.1.

Table 7.1: Overview of property state variables characterizing the metallurgical conditions in a ferrosilicon furnace.

State variable	Dimension	Achieved by:
Cavity temperature	3	Estimator or indicated by indirect measurements
The partial pressures of SiO in the cavities	3	Estimator or indicated by indirect measurements
SiC content in cavity	3	Estimator
Si production rate	1	Calculated based on measurements
The charge height	1	Estimator or evaluation based on observations
The carbon turnover	1	Estimator or evaluation based on observations
SiO flow from furnace	1	Measured
The carbon content of the furnace	1	Estimator or indicated by indirect measurements

7.5.4 Furnace optimization

The conventional metallurgical control strategy of a ferrosilicon furnace can be regarded as an optimizing controller with a hierarchic structure.

Optimization task

At the top level the furnace condition is optimized by the metallurgists, executing the following optimization tasks:

1. **Minimize the specific energy consumption.**
2. **Maximize the furnace silicon yield:**
   - **Maximize metal production.**
   - **Minimize released silica fume flow.**

by manipulating the furnace's controllable input variables such as the choice of raw materials, the carbon content in the added charge, the operation procedures, the set-points for any carbon controller, and the electrical working point utilized as the set-points for the electrical control system on lower levels.

An optimizing control strategy seems reasonable for the ferrosilicon process because the existence of a certain production optimum with respect to reaction patterns in the furnace. This is illustrated by the stoichiometric model in Section 7.2 and the furnace production dependency of the carbon content as shown in Figs. 7.5, 7.6 and 7.7.

Profit function

The optimization task for a ferrosilicon furnace can in principle be expressed in terms of a profit function:

$$J_{\$} = \{(w_{\mathrm{FeSi}} \cdot Pr_{\mathrm{FeSi}}) + (w_{\mathrm{SiO}} \cdot Pr_{\mathrm{SiO}})\} - \left\{(w_{\mathrm{SiO_2}} \cdot Pr_{\mathrm{SiO_2}}) + (w_{\mathrm{C}} \cdot Pr_{\mathrm{C}}) + (Q_{\mathrm{MWh}} \cdot Pr_{\mathrm{MWh}}) + (Q_{\mathrm{El}} \cdot Pr_{\mathrm{El}})\right\} \tag{7.28}$$

where w represents the material flows of the different materials indicated by the subscript notation, and Pr represents the specific prices or costs for the materials. Q_{MWh} denotes the energy consumption, and Q_{El} denotes the electrode consumption, while Pr_{MWh} denotes the specific energy price, and Pr_{El} denotes the specific electrode paste price.

Constraints

When executing the optimization of the profit function in Eq. 7.28 the operational and physical constraints must be considered. Typical operational constraints are:

- The SiC content in the inner zone of the furnace should be kept below some limit:

$$x_{SiC\ hearth} < x_{SiC\ hearth\,Max}$$

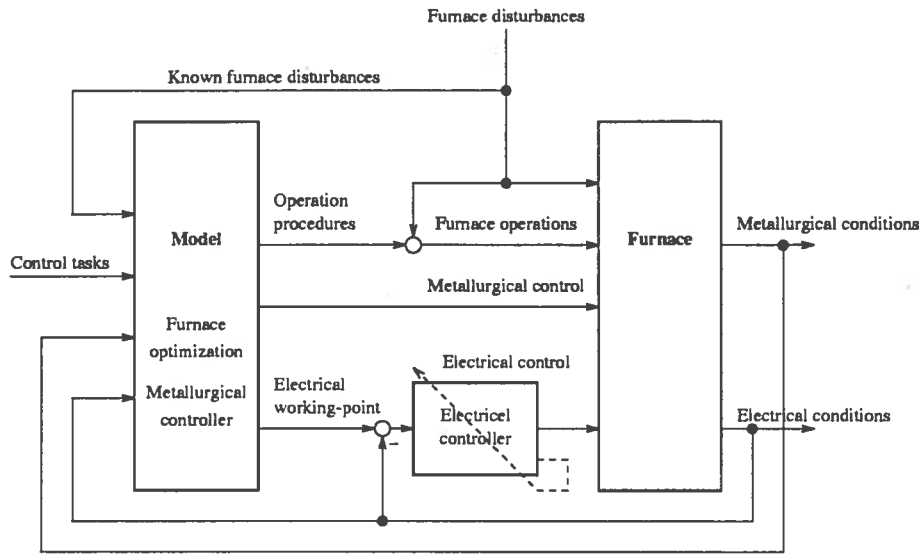

Figure 7.10: An optimizing hierarchic furnace control strategy.

- The furnace power level is restricted:

$$P < P_{Max}$$

- The electrode currents are restricted:

$$I_e < I_{e\,Max}$$

while the physical constraints are given by the furnace dimensions and equipment.

Strategy for optimizing metallurgical conditions

Figure 7.10 shows the principle of an optimizing metallurgical controller with a hierarchic structure. The core of the system, which is represented by the left box, denoted "Model", should be regarded as being composed of:

1. **Furnace models.**

   These furnace models are supposed to include:

   - The metallurgists' knowledge and evaluation experience.
   - Model representations of the furnace or parts of the furnace, which can be on-line implementations as well as off-line.

2. **Furnace optimizer.**

   The furnace optimizing strategy, which based on the furnace models and the furnace measurements and observations, tries to achieve the metallurgical control task by manipulating the process parameters and the set-points for the furnace control system.

3. **Metallurgical controller.**

   The metallurgical controller includes the manual metallurgical control strategies and any automatic controller, such as the carbon controller described in Section 7.5.8.

Presently, this is almost exclusively a manual operation. Regarding the ferrosilicon process, the best way of upgrading this optimizing control strategy is by introducing step-like improvements, instead of making efforts in developing a complete automatic system. Examples of such improvements that successfully could be implemented in the system, are:

1. Models describing parts of the process should be included in the optimizing control strategy. The models could be implemented in parallel on-line to the furnace or alternatively they should be available for the furnace metallurgists.

   Such models already exist, describing for instance:

   - The chemical reactions, as described in Section 7.6.
   - The stoichiometric relationship, as described in Section 7.2.
   - The electrical conditions in the furnace, as described in Sections 4.3.2 and 4.4.

2. The development of improved measurement systems for identifying process state variables that are not directly measurable. This is the topic of Section 8.4, where two novel concepts for estimating inner process variables are presented.

   These estimates of process state variables can be applied in metallurgical controllers as well as in the manual optimization and control of the furnace.

7.5.5 Metallurgical control input variables

In principle several candidates are available for use as control input variables in the metallurgical control of a ferrosilicon furnace:

- The composition of added charge. This is denoted **carbon content**, referring to the stoichiometric relationship between carbon materials and quartz in the added charge. This can be expressed by x in $SiO_2 + x$ C.

- The amount charge added to the furnace during the stoking operation and its distribution across the furnace surface. This is denoted **charge feed control** and is usually determined by the operator.

- The distribution of carbon content across the furnace surface which is denoted **carbon distribution**.

  In principle both the charge feed and its carbon content can be varied separately for each of the furnace charging tubes. At the furnace at Elkem Thamshavn, this means that the charge feed and its composition can be varied separately in each of the ten charging tubes.

  However, the total carbon content of the added charge is specified and further restrictions are set regarding the total charge feed. Thus, the degree of freedom for the carbon control input variables is limited. This results in that the dimensions of both the carbon content and the charge feed input control input variables are one.

- The **electrical working-point**, which partly is utilized as the set-points of the electrical control system. The electrical working-point may contain:

  - The furnace electrical power level.
  - The electrical power distribution within the furnace.
  - Electrical control set points: The electrode currents or phase resistances.
  - Electrical control parameters.

- The procedures for the stoking/charging and tapping operations and the execution of quartzing and coking activities.

- The decisions regarding the raw materials and related properties, such as:

  - Carbon materials:
    * The mutual distribution of carbon materials between coke, coal, charcoal and wood chips.
    * The raw material qualities regarding particle sizing, reactivity, porosity etc.

- Quartz materials:
  - * Raw material qualities regarding particle sizing, reactivity, porosity etc.
- Iron oxide:
  - * Raw material qualities regarding particle sizing, reactivity, porosity etc.
- The distribution of particle sizing between the different kinds of raw materials.

These control input variable candidates have very different properties, and there are for instance considerable differences in how they can be altered and especially regarding their possible alteration frequencies. The response times also vary significantly between these variable, and major uncertainties are connected with some of them. Table 7.2 summarizes some of the properties connected with the input variables to the furnace.

The input variables related to the charge addition, the charge feed, the carbon content and the carbon distribution, have typical alteration frequencies of about 1/1h, while their response times are between 2-6 hours. The uncertainty connected with the charge input variables may be significant. This is because the added charge materials in the sense that important properties such as sizing, porosity and humidity, are continuously varying, and thus the exact properties of these input variables are not known.

The input variables related to the electrical working-point have a higher frequent character with possible alterations below 1 min, but with varying response times in the range of 1 min - 4 hours. Relatively small uncertainties are connected with the electrical working-point variables compared to the other metallurgical input variables.

The operation procedures are in fact changed every time they are executed as a result of changing operators. and thus major uncertainties are connected with them. However, controlled alterations in the execution of these procedures take a very long time.

The choices regarding the raw materials are typical low-frequency input variables. Relatively high-frequent changes in the fractions between the different raw materials can be executed from day to day, while the purchases of raw materials have time-horizons of months and years. As with the

Table 7.2: Properties of metallurgical input variables.

Input variable	Dimension	Alteration	Response time	Uncertainty
Charge feed	10 (1)	1 hour	2-6 hours	significant
Carbon content	10 (1)	1 hour	2-6 hours	significant
Carbon distribution	10 (1)	1 hour	2-6 hours	significant
Electrical working point	5 – 10	< 1 min	1 min-4 hours	small
Operation procedures	–	–	1-4 hours	major
Raw materials	> 10	days-months	1-4 hours	major

charge input variables the choices regarded the raw materials used as input variables to the furnace, are connected with major uncertainties.

Some of the furnace input variables can easily be applied as automatic control control input variables with a possibility of relatively high-frequent alterations, while the decisions regarding the raw materials and the operation procedures and the executions of them, have the character of long-term variables and can be regarded as "ordinary" control input variables.

Classification of metallurgical control variables

The different natures of the available controllable input variables and their properties would support a hierarchic classification of the variables:

- **Control input variables:**

  Variables used in the continuous metallurgical control of the furnace.

- Charge feed.
- Carbon content.
- Carbon distribution.
- The electrical working point.

- **Process optimization variables:**

  Variables used in long-term process optimization.

  - Raw materials decisions.
  - Operation procedures.
  - Set-points of metallurgical controllers.

A ferrosilicon furnace is usually operated at a specified electrical power level corresponding to a "constant" furnace reaction volume, which is the case at the furnace at Elkem Thamshavn. The furnace volume is controlled manually by the operators, attaining a constant charge level in the furnace, and hence the charge feed will be given by the furnace production rate. As a result of this the charge feed and the furnace power level hardly can be used as control input variables in the metallurgical control of the furnace. Therefore, these variables are applied in the long-term process optimization.

Thus the available control input variables at the furnace become:

- The added carbon content.
- The carbon distribution.
- The electrical working point, utilized at the furnace at Elkem Thamshavn as the choice of the Westly's factor in the calculation of the electrode current references.

7.5.6 Metallurgical output variables

The output variables from a ferrosilicon furnace can be divided into measurements of process variables and furnace observations and product analyses.

Measurements

A ferrosilicon furnace has few or no direct measurements of the inner process state variables, and generally only process variables that are available from the outer furnace are measured. The furnace measurements can be outlined as:

- **Waste gas measurements:**
  - The content of silica fume in the waste gas.
  - The temperature of the waste gas.
  - The waste gas flow.
- **Measurements at the tapping of ferrosilicon metal:**
  - The amount of tapped metal.
  - The temperature of tapped metal
- **Electrical measurements:**
  - Three electrode currents.
  - Three electrode voltages.
  - The total power dissipation.
  - The power dissipation in each phase.
  - Resistances and reactances in each of the phases.
- **Adapted electrical measurements:**
  - The content of harmonics in the three electrode voltages.
  - Lissajous figures
- **Electrode holder positions** for the three electrodes.

In addition some measurements which are part of the furnace safety system may be available.

The amount of tapped metal will to some extent indicate the production rate of ferrosilicon. Furthermore, the furnace material balance can in principle be found from the amount of charge feed, tapped metal and the content of silica fume in the waste gas. However, this is complicated by the discontinuous charging and tapping and the significant residence time in the furnace.

The present conventional metallurgical control strategies make use of the content of harmonics in the electrode voltages and the electrode holder positions as controlled variables in the control loop. The silica fume measurement, the temperature of the waste gas, and the amount and temperature of tapped metal, are applied in the evaluation of the metallurgical control and the furnace conditions. The silica fume measurement is also used as an indication tool for the stoking and procedure operations. The silica fume

Table 7.3: Overview of available measurements on a ferrosilicon furnace.

Measurement	Dimension	Usage
Silica fume	1	Metallurgical control and evaluation. Furnace operations.
Waste gas temperature	1	Furnace evaluation
Waste gas flow	1	Furnace evaluation
Tapped metal	1	Metallurgical control and evaluation.
Metal temperature	1	Furnace evaluation.
Electrical variables	> 16	Electrical control. Furnace evaluation.
Harmonics contents	3	Metallurgical control and evaluation.
Electrode holder positions	3	Metallurgical control and evaluation.

measurement system and its relation to the actually amount of silica fume is discussed by Gudmundsson and Hannesson (1992).

Table 7.3 outlines some of the available measurements on a ferrosilicon furnace.

Observations and product analyses

The observations of the furnace surface are important in the metallurgists' evaluation of the furnace conditions. Important furnace observations and analyses are:

- **Observations at tapping of metal:**
  - The tapping conditions in general.
  - The tapping rate.
  - The content of slag.
- **Observations at the furnace surface:**
  - The color of flames.
  - The blow of silica fume.
  - Electrode consumptions.
- **Analyses of metal products:**
  - Metal analyses regarding contents of impurities.
  - Slag analyses.

The color of the flames and the behavior of the silica fume blows at the furnace top reflect the chemical reactions in the furnace, while the electrode consumption indicates the arcing conditions and the current paths in the furnace.

The furnace conditions and the connected chemical reaction patterns will influence the tapping of metal from a furnace, and the product qualities and the slag content strongly depend on these conditions. Therefore, analyses of the metal product and slag can yield considerable information about the reaction patterns in the furnace.

Upon tapping of a ferrosilicon furnace various kinds of slag are observed. The tapping operators usually characterize the different slag materials by their properties and appearance, examples of this are "green-slag" and "ball-slag". Analyses of the different slag materials can be important tools in evaluation of the reaction patterns in the furnace. This is further treated in Section 8.2.3.

7.5.7 Difficulties related to metallurgical control

The difficulties related to metallurgical control of a ferrosilicon furnace are mainly the result of the following:

1. The limited knowledge about the process and its interior interaction effects.

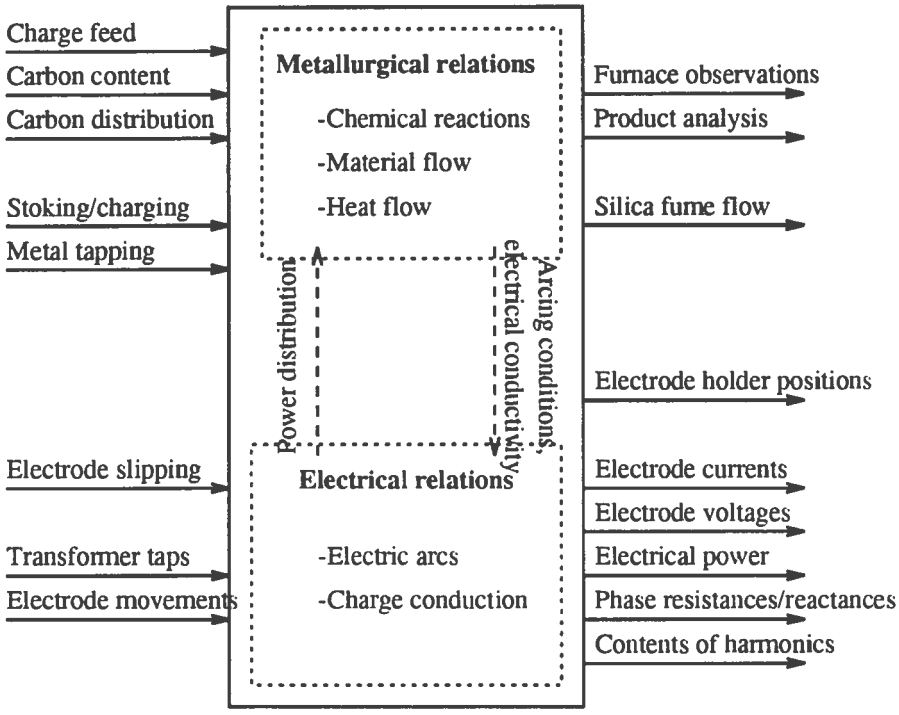

Figure 7.11: A model of a ferrosilicon furnace.

2. The lack of direct measurements of the process conditions, as discussed in Section 7.5.6.

3. Considerable process disturbances.

4. Major control input uncertainties, as discussed in Section 7.5.5.

Interactions between the furnace conditions

A ferrosilicon furnace contains different sub-processes which interact closely. Figure 7.11 illustrates of a qualitative model of such a furnace. The furnace is modeled in two separate sub-processes covering the metallurgical and the electrical relations, respectively. The various input and output variables are indicated where they are supposed to affect the process, and the mutual interactions between the sub-processes are illustrated.

The electrical sub-process acts like the power generation source to the metallurgical relations, and the electrical power distribution directly affects the chemical reactions and the material and heat flow in the furnace. The metallurgical variables in turn, affect the electrical conductivity in the charge

and the arcing conditions.

The input variables to each of the sub-processes also affect the others because of this interaction. In the same way the output variables will reflect both sub-processes and this creates difficulties in deciding the causes of observed responses.

Disturbances

The main disturbances in the process affecting the metallurgical conditions are improper mixing of the charge materials and the formation of gas channels in the charge, leading to a situation where the desired countercurrent conditions between the reactants and upstreaming gas become unattainable. Furthermore, variations in the residence times of the charge materials, as well as in the charge height, will affect the process reactions significantly. Some of the most important process disturbances can be outlined as:

1. Improper mixing of the charge materials ("segregation").

2. The formation of gas channels in the charge.

3. The changing executions of the stoking, charging and tapping operations.

4. Variation in the residence time of the charge materials.

5. Variation in the charge height above the cavities.

7.5.8 A conventional carbon control strategy

The control of the furnace carbon content is one of the most important metallurgical control activities. The furnace dependency of the carbon content, which is previously discussed in Section 7.3.4, is significant. The major problem regarding carbon controls the lack of reliable measures of the actual carbon content in the furnace, while the furnace carbon content can easily be adjusted by corrections in the carbon content of the added charge mix. Manual carbon control strategies are based mainly on furnace observations and on judgment of the furnace conditions by metallurgists based on their process knowledge. Presently, the use of manual carbon control strategies are predominant compared to the applications of automatic carbon controllers.

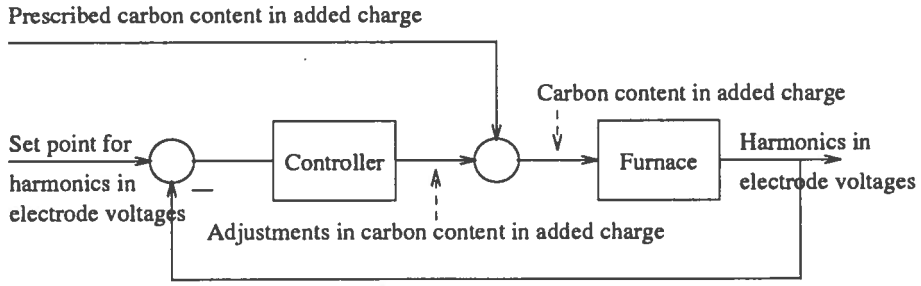

Figure 7.12: Principle of carbon control strategy based on the content of harmonics in the electrode voltages.

A carbon controller based on the content of harmonics in the electrode voltages

A carbon control strategy based on using the measurement of the content of harmonics in the electrode voltages, has been proposed by Skreien (1975). The strategy is based on an assumption that the measurement of the content of harmonics in the electrode voltages indicates the carbon content in the furnace.

The principle of the harmonics-based carbon controller is illustrated in Fig. 7.12. The mean content of harmonics in the electrode voltages is used as the controlled variable, and the carbon content in the added charge is adjusted by the controller operating on deviations in the measured mean content of harmonics from a given reference value. The controller usually operates within a specified bound around a prescribed carbon content and gives corrections to this value, as shown in Fig. 7.12.

The carbon control strategy is based on the following assumptions (Skreien, 1975):

1. Variations in the furnace carbon content result in certain changes in the measured content of harmonics in the electrode voltages:

$$\text{Increased carbon content} \Rightarrow \text{Decreased content of harmonics}$$
$$\text{Decreased carbon content} \Rightarrow \text{Increased content of harmonics}$$

2. The relation can be explained as follows:

   (a) An increased carbon content will result in higher temperatures in the cavities.

(b) The increased cavity temperatures lead to higher electrical conductivity in the cavity atmospheres and therefore in less distortion of the electrical signal as a result of the presence of arcing in the cavities.

(c) The increased temperatures in the cavities also lead to increased temperatures in the charge in the vicinity of the cavities. This will reduce the charge resistance and hence increase the charge conduction in by-pass to the arcing conduction in the cavities. The measured electrode voltages will therefore be even less distorted, and the content of harmonics will decrease.

This carbon control strategy has been used for several years at the furnace at Elkem Thamshavn. An evaluation of the control strategy based on this experience, shows that the control strategy gives good results if the furnace is close to its optimal carbon content.

However, the control strategy is not reliable. The control strategy is based on assumptions that can only be applied in some furnace conditions and that generally do not hold. The measured content of harmonics in the electrode voltages are strongly sensitive to changes in the electrical conductivity and the current paths in the charge. Thus, it is observed that the control strategy fails if the furnace deviates significantly from its optimal carbon content, which is actually when the carbon controller is needed most.

Another problem with the control strategy is the difficulties in choosing the "correct" set point for the mean content of harmonics. This set point value varies significantly and has little physical meaning, and it can hardly be correlated to furnace conditions. In addition, the measures of the contents of harmonics are exposed to significant disturbances, which most probably are due to unpredictable variations in charge conductivity and arcing conditions, creating difficulties for the control utilization.

An extended harmonics-based carbon controller

The harmonics-based carbon controller is often extended with a parallel controller operating on the mean value of the electrode holder position, as illustrated in Fig. 7.13. This extended carbon control is implemented at the furnace at Elkem Thamshavn. The extended control loop operates in parallel to the harmonics controller, and the extension is done in order to reduce the uncertainty connected to the harmonic-based controller.

A qualitative model of the relations between the furnace carbon content and the mean electrode holder position can be stated similarly to the harmonics

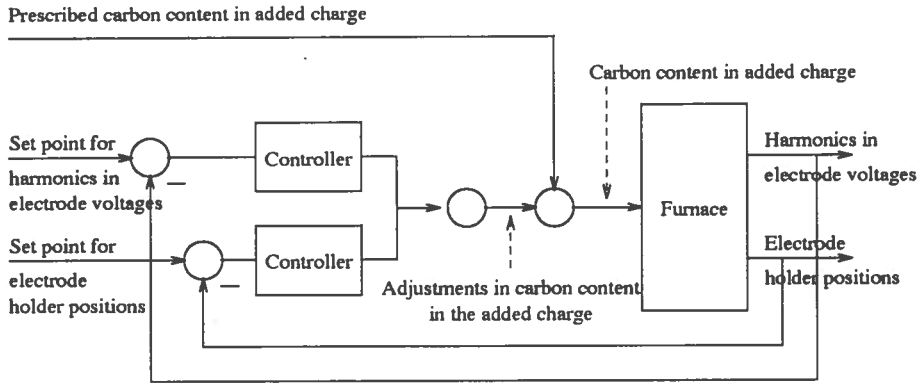

Figure 7.13: Principle of carbon control strategy based on the content of harmonics in the electrode voltages.

model above. This model yields:

Increased carbon content ⇒ Reduced mean electrode holder position
Decreased carbon content ⇒ Increased mean electrode holder position

This model assumption is further treated in Section 8.2.

This control structure is further discussed in Section 8.1.3, describing furnace experiments which are carried out in order to obtain quantitative models for the relations between the added carbon content and the responses in measured harmonics content and electrode holder positions.

7.6 A dynamic model of the silicon process

A dynamic model of the silicon process has been developed by Elkem Research, Norway. The model is thoroughly described by Halvorsen (1988), Halvorsen, Downing and Schei (1989), and Halvorsen, Schei and Downing (1992). It gives a fair description of the chemical reactions in a silicon furnace, and has been made available for the use in this work. The model is applied in simulation studies of various furnace conditions and in the development of novel control strategies for the metallurgical control of ferrosilicon furnaces. The parameters used in the model are adjusted to describe the reactions in a 65 MVA ferrosilicon furnace.

The model of the upper reaction zone is based on a unidimensional distributed description of concentrations of solid and liquid reactants x in the

form:

$$\frac{\partial x_i}{\partial t} + \frac{\partial v_s x_i}{\partial z} = \sum_j \alpha_{ij} R_j - S_i \tag{7.29}$$

where subscripts i and j indicate component i and reaction j respectively, x denotes the concentration, v_s the downward velocity of reactants, α_{ij} the stoichiometric coefficient of component i in reaction j, R the reaction rate, and S denotes the melting rate. This is further described in Halvorsen, Schei and Downing (1992)

The reaction rates for the gas-solid and gas-liquid reactions are described by (Halvorsen, 1988; Halvorsen, Schei and Downing, 1992):

$$R_j = k_j \cdot x_i \cdot \Delta p_j \cdot e^{-E_j/RT} \tag{7.30}$$

where subscript j indicates reaction j, k denotes the reaction rate constant, Δp the reaction pressure (driving force), E the activation energy, R the molar gas constant, and T denotes the temperature. The gas concentrations, gas and solid velocities, and enthalpies are described in a corresponding way. The distributed description of the upper reaction zone is coupled to a similar point description of the inner reaction zone (the hearth).

In the numerical solution the distributed model is approximated by a segment model, and further simplifications regarding gas dynamics and reactant movements are assumed. The simulation model consists in each segment of five differential equations, describing enthalpy and reactant concentrations, while the hearth is described by four differential equations. Nonlinear algebraic equations describe gas fluxes and reactant velocities in the hearth and the charge segments. In addition, there are differential equations describing derived variables such as production amounts and enthalpy losses.

The model corresponds to the following state-space description:

$$\begin{aligned} \dot{\underline{x}} &= \underline{f}(\underline{x}, \underline{u}, \underline{w}) \\ 0 &= \underline{g}(\underline{x}, \underline{u}, \underline{w}) \\ \dot{\underline{q}} &= \underline{h}(\underline{x}, \underline{u}, \underline{w}) \end{aligned} \tag{7.31}$$

where:

$$\underline{x} = \begin{bmatrix} \underline{x}_h \\ \underline{x}_{c_i} \end{bmatrix}$$

and $\underline{x}_h$ and $\underline{x}_{c_i}$, $i = 1 \ldots n$ are vectors containing the states in the hearth and the charge segments respectively. $\underline{u}$ is the control input vector, and vector:

$$\underline{w} = \begin{bmatrix} \underline{w}_h \\ \underline{w}_i \end{bmatrix}$$

contains the gas fluxes and reactant velocities. Vector $\underline{q}$ contains the derived variables, and n is the number of segments. The simulation model contains $(4 + 5n + 6)$ states. The hearth state vector $\underline{x}_h$, is:

$$\underline{x}_h = \begin{cases} \text{concentr. of C} \\ \text{concentr. of SiC} \\ \text{concentr. of "condensate"} \\ \text{enthalpy} \end{cases} \tag{7.32}$$

where "condensate" is given as $1/2 < SiO_2 + Si >$, corresponding to the reaction in Eq. 7.12. The charge segment state vectors $\underline{x}_{c_i}$, are:

$$\underline{x}_{c_i} = \begin{cases} \text{concentr. of } SiO_2 \\ \text{concentr. of C} \\ \text{concentr. of SiC} \\ \text{concentr. of condensate} \\ \text{enthalpy} \end{cases} \tag{7.33}$$

The derived state vector $\underline{q}$, is:

$$\underline{q} = \begin{cases} \text{amount of released SiO} \\ \text{amount of released CO} \\ \text{amount of produced Si} \\ \text{accum. heat losses by radiation} \\ \text{accum. enthalpy in released gas} \\ \text{accum. enthalpy in produced Si} \end{cases} \tag{7.34}$$

The model is based on an assumption of fixed electrical conditions, and it is adapted so that the carbon content in the added charge can be used as a control variable. It is further assumed that the furnace is continuously tapped, and that the furnace reactive volume is constant. The control input vector $\underline{u}$, will then be:

$$\underline{u} = \begin{cases} \text{carbon content in added charge} \end{cases} \tag{7.35}$$

The carbon content is chosen to be a time-discrete control input, corresponding to the furnace operation cycles. The dimension of this control

vector is considerable lower than what is the case in a real furnace, as discussed in Section 7.5.5. However, the carbon content is one of the most critical control input variables, and therefore this control variable is applied in the simulation model. In Section 9.1 this model is used in the simulation of model-based control strategies.

The model can simulate the furnace in two ways:

1. The furnace is assumed to be continuously charged, corresponding to mean operation conditions.

2. The furnace is operated with the discontinuous stoking-charging cycle.

The continuous version seems preferable for use in long-term process analysis since the concerned dynamics is much slower then the operating cycles. The continuous model version is therefore applied in simulation studies of different furnace operation strategies, which is further described in Section 8.3.

7.7 A survey of related model developments

A large number of models describing different phenomena in the charge of submerged-arc furnaces have been developed. Some models describe the chemical reactions in such furnaces, while others focus on heat transfer and the material flows in the furnace burdens. A survey of some of these models are given below:

- **Chemical reaction models.**

  The heat and mass transfer in ferrosilicon and silicon furnaces has been treated by Müller, Olsen and Tuset (1972), discussing stoichiometric models of these processes. In addition this is also treated by Schei and Larsen (1982) and Schei and Halvorsen (1991), as indicated above. The stoichiometric model of the silicon process is further treated by Schäfer (1984) and Mühlbauer and Schäfer (1985). Furthermore, a model of the chemical reactions in the silicon process based on equilibrium calculations, is developed by Johansson and Erikson (1980).

- **Material flow models.**

  The movement of the burden in submerged-arc furnaces has been analyzed and model descriptions of the material flow have been developed by Dyason and See (1978, 1981). The model development

has resulted in increased understanding about the flow patterns and the residence-time distribution in the furnace burden.

- **Heat transfer models.**

  Models describing the heat transfer in submerged-arc furnaces have been developed among others by Kaiser and Downing (1978), Curr (1984), and Waalmann (1988). The models compute the temperature distribution in the furnace burden, and are of especial interest in connection with design and analyses of furnace linings.

7.8 Concluding remarks

The chemical reactions in a ferrosilicon furnace have been discussed in this chapter. The ferrosilicon process can be described by models of the silicon process, and hence the chapter presents a stoichiometric model of the silicon process. The chapter has also described different process related terms that are defined, and gives qualitative models of different reaction patterns.

The ferrosilicon furnace has been analyzed from a system theory point of view, and the metallurgical control of ferrosilicon furnace has been discussed. Important topics in this were:

- Process state variables.
- The metallurgical control task.
- Furnace optimization.
- A systematic discussion and classification of the input variables, the inner state variables, and the output variables of the process.
- Difficulties related to metallurgical control.

This discussion concludes with a recommendation about how the process variables should be used in the metallurgical control of the furnace.

The chapter has also presented conventional carbon control strategies based on the harmonics content in the electrode voltages and electrode holder positions.

The last sections have described a dynamic model of the silicon process, which is used in the further analyses of the process. A survey of related model developments has also been given.

Chapter 8

Analysis of metallurgical process conditions

This chapter further analyzes the metallurgical process conditions in the furnace. The effects of furnace operations on the process conditions are discussed, and their long-term variations are treated. Step-response experiments at the furnace at Elkem Thamshavn are described. These experiments alter the carbon content in the added charge, and the models are described that are used in the synthesis of the conventional carbon controller and which are derived based on these experiments. Different furnace operation conditions such as over- and undercoked conditions, are discussed. Qualitative models of the altered reaction patterns are proposed and compared to furnace experience. In addition, the chapter considers the situation in a furnace with reduced carbon turnover. Over- and undercoked operation cycles are simulated by using the dynamic silicon model, and the results are discussed and related to furnace operation. Finally, two model-based measurement systems for estimating inner process variables in a ferrosilicon furnace, are discussed.

8.1 Analysis of variations in the furnace measurements

The dynamic variations in the furnace measurements are analyzed based on measurement data from the furnace at Elkem Thamshavn. The effects of the furnace operations on the process conditions variations are discussed. Then, the long-term variations of important furnace measurements are treated, and finally, experiments of step response in the added carbon content are described.

8.1.1 The effect of furnace operations

The furnace operations during the stoking and charging cycles and the discontinuous metal tapping cycle, have significant effects on the process conditions. This can be observed for instance by the measurement of the silica fume content in the waste gas flow and the temperature of the waste gas.

Figure 8.1 shows how the stoking/charging and tapping operations affect the silica fume flow, and Fig. 8.2 shows principal trends of the silica fume flow, which can be drawn based on Fig 8.1.

A stoking operation reduces the silica fume flow significantly by mixing the upper part of the charge and destroying the gas channels in the charge. After the stoking, the silica fume flow increases due to the gas channel formation in the charge, until a new stoking becomes necessary and the operation occurs.

A somewhat different dependency is observed versus the tapping cycle. The silica fume flow has a decreasing trend when the furnace is being tapped and a increasing trend when no tapping occurs. This can be explained by the fact that the silica fume flow depends on the amount of liquid Si in the cavities, which is expressed by the reaction in Eq. 7.8. The level of liquid silicon fluctuates within the tapping periods and the silica fume flow varies correspondingly.

The temperature of the waste gas also varies within the stoking/charging cycles, as shown in Fig. 8.3. The waste gas temperature increases during the stoking/tapping operations. The increase in the temperature can be explained by increased combustion of volatile carbon constituents and small carbon particles after the charging of new materials on the furnace.

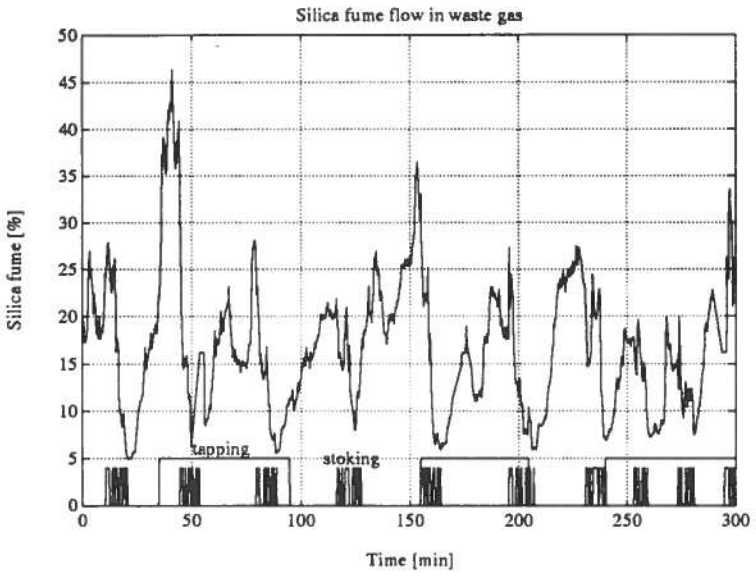

Figure 8.1: The silica fume flow under the influence of the furnace operations.

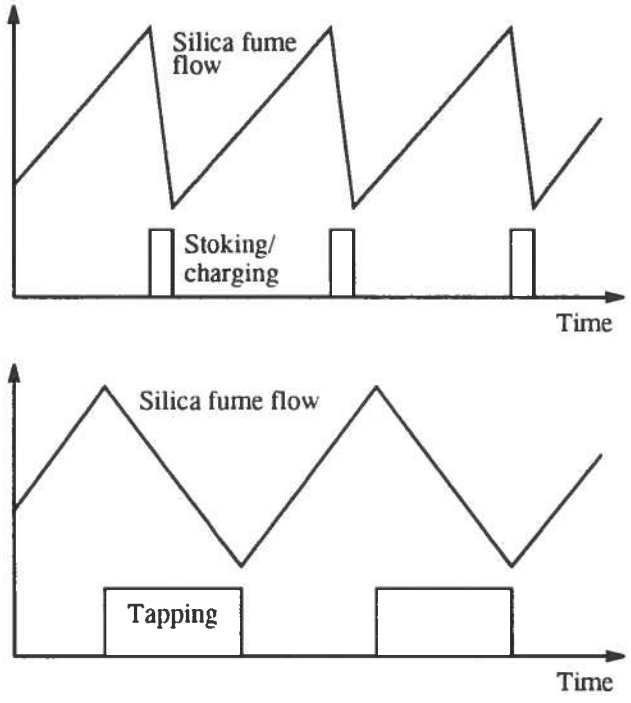

Figure 8.2: The principal trend of the silica fume flow versus the stoking and charging cycles and the tapping cycles.

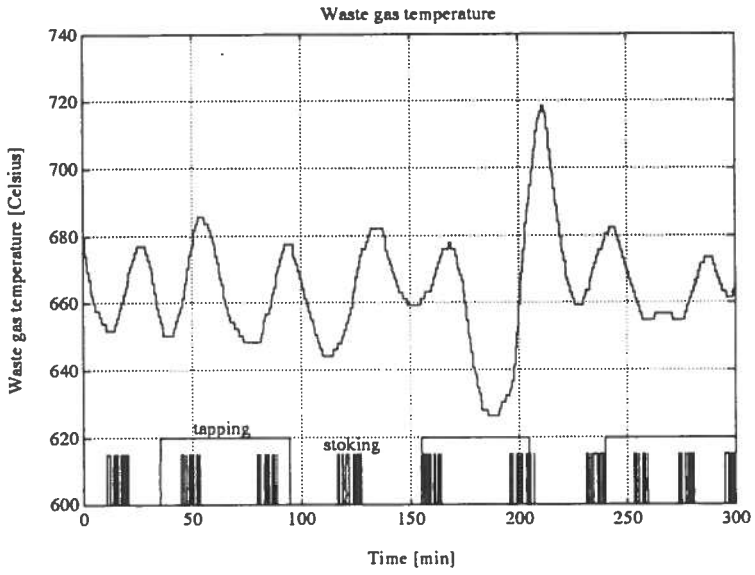

Figure 8.3: The waste gas temperature under the influence of the furnace operations.

8.1.2 Long-term variations in furnace measurements

The silica fume flow

Figure 8.4 shows the variation in the measured silica fume flow from the furnace during a period of 15 days. The measured silica fume flow signal is shown together with a filtered signal with a time constant of 24 hours. The filtered silica fume flow values give a more realistic reflection of the SiO production from the furnace than the the "raw" signal, which depends significantly on the furnace operations. Hence, the filtered signal can be used as indication of the carbon content and other metallurgical conditions in the furnace.

The added carbon content

Figure 8.5 shows the variation in the **fixed carbon** content in the added charge during a period of 15 days. The fixed carbon content corresponds to the actual reactive carbon content in the charge, and it is calculated based on each charge constituent's content of reactive carbon. The fixed carbon content is expressed in %, where 100% corresponds to the stoichiometric relationship between quartz and carbon in the optimal overall reaction:

$$SiO_2 + 2\,C \rightarrow Si + 2\,CO \tag{8.1}$$

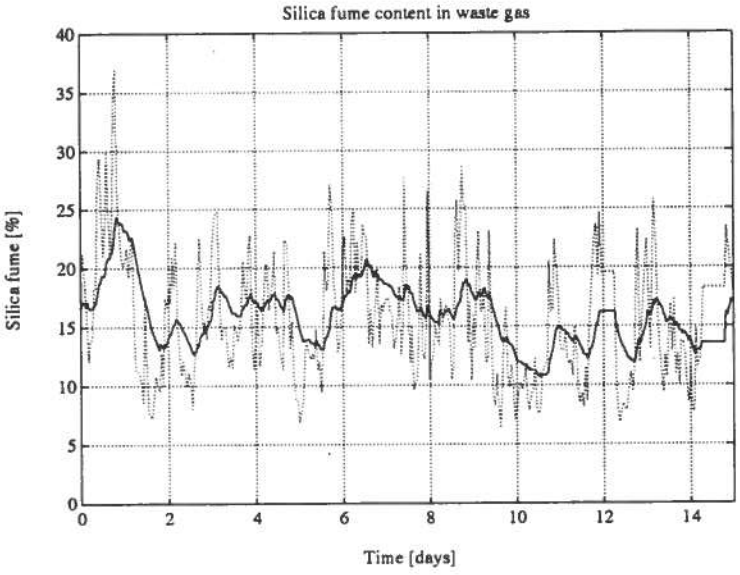

Figure 8.4: Long-term variations of the silica fume flow.

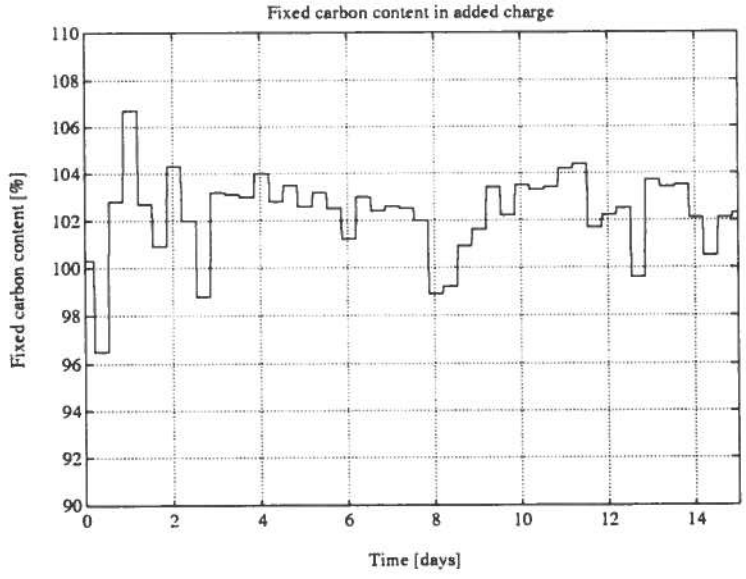

Figure 8.5: Long-term variations of fix carbon content in added charge.

Figure 8.5 shows that there is a clear long-term variation in the fixed carbon content added to the furnace. This reflects the metallurgical control strategies of the furnace.

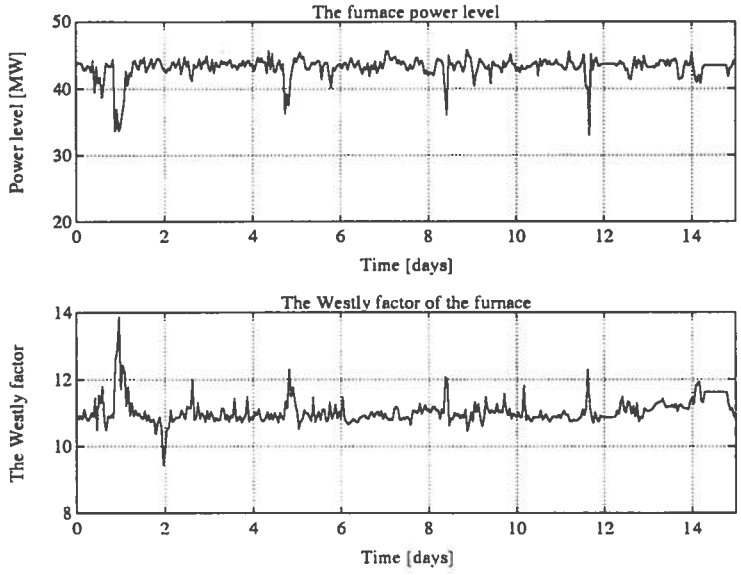

Figure 8.6: Long-term variations of furnace power level and Westly's power factor.

The furnace power level

Figure 8.6 shows the furnace power level and the calculated Westly's power factor of the furnace during a period of 15 days. The furnace power level is a controlled variable and the curve shows that it is satisfactorily controlled, except for some short periods of reduced power level. These periods are most probably the result of reduced transformer tap positions forced by the furnace safety system, or by furnace maintenance activities.

The Westly's power factor is a partly controlled variable which is used in the decision of the electrical working point of the furnace. Figure 8.6 shows that the variable is almost constant except for the periods of reduced power level, which influences the calculation of the Westly's power factor directly.

The contents of harmonics in the electrode voltages

Figure 8.7 shows the long-term variation in the measured contents of harmonics in the electrode voltages. The harmonics content in each of the electrode voltages varies considerably within the period. This variation can be explained by the different changes in the electrical resistance in the three phases. The mean content of harmonics, which is filtered with a time constant of 1 hour, shows less variation and is used as an indication of

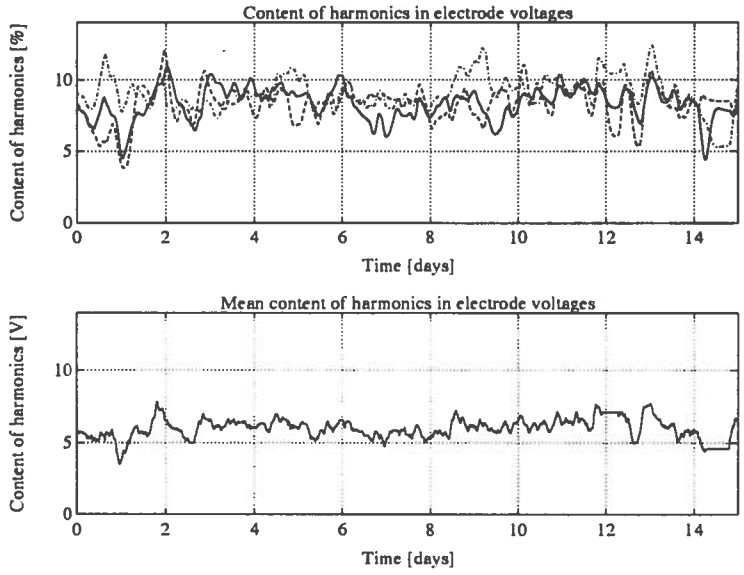

Figure 8.7: Long-term variations of harmonics content in electrode voltages.

carbon content in the furnace, and therefore it is used in the conventional carbon control strategy at the furnace.

The electrode holder positions

Figure 8.8 shows how the electrode holder positions varies during the period of 15 days. The electrode holder positions illustrate the use of the electrode displacements as control inputs in the electrical control of the furnace. Considerable and perhaps superfluous electrode movements have occurred in the period, something that may suggest a different electrical control strategy. Furthermore, it can be observed that two of the three electrodes in turns follow each other with almost similar position, while the third electrode has a position that differs significantly. This is another indignation of weakness in the electrical control system.

The mean electrode holder position, that is filtered with a time constant of 1 hour, illustrates the electrical conductance of the furnace, and it is commonly used as an indication of the carbon content of the furnace, and is thus applied in the conventional carbon controller at the furnace.

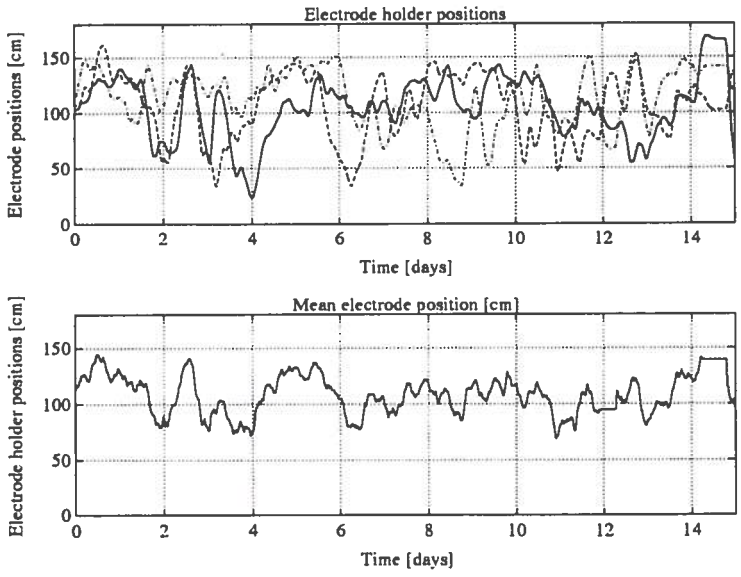

Figure 8.8: Long-term variations of electrode holder positions.

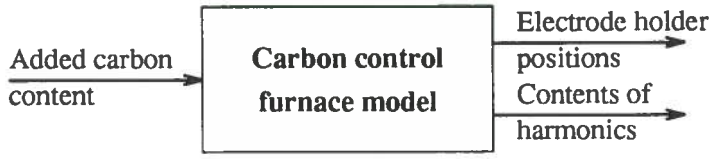

Figure 8.9: Model view applied in conventional carbon control strategy.

8.1.3 Carbon content step response experiments

Two step-response experiments that alter the added carbon content have been carried out at the furnace at Elkem Thamshavn in order to investigate the dynamic effect on the process conditions and the furnace measurements. The conventional carbon control, which previously is discussed in Section 7.5.8 and illustrated in Fig. 7.13, is based on a very simplified furnace model assumption as illustrated in Fig. 8.9. In this carbon control strategy the carbon content in the added charge is controlled based on the mean contents of harmonics in the electrode voltages and the mean electrode holder positions.

A proper adjustments of the carbon controller is difficult due to lack of quantitative knowledge about the input-output relations of the model structure in Fig. 8.9. Therefore, step-response experiments in the added carbon content have been carried out in order to increase the process knowledge

and thus improve the existing carbon control strategy.

Simple input-output model expressions on the linearized frequency-domain form:

$$y_i(s) = \frac{k_i}{1 + T_i s} e^{-\tau_i s} \cdot u(s) \tag{8.2}$$

have been derived based upon the step-response experiments and then used in control synthesis. In the model in Eq. 8.2 u denotes the carbon content input variable, while y_i denote the output variables, respectively the mean harmonic content and the mean electrode holder position. The models are assumed to be of first-order with the time constant T_i and the process gain k_i, and with a time delay of τ_i.

Due to the high-frequent disturbances to the output variables mainly caused by the stoking/charging operations, the output signals are filtered with a time constant of 1 hour in order to reject these effect, and these filtered variables are used in the controller. Therefore, the models describe the relations between the input variable and the filtered output variables.

Experiment 1

Figure 8.10 shows the responses of the mean content of harmonics in the electrode voltages and the mean electrode holder position to an increase of 3% in the added fix carbon content. This corresponds to the range which the conventional carbon controller operates within.

The alteration in the carbon content was prescribed at $t = 1$ h. Due to time delays in the raw material transportation and in the furnace raw material bins, the charge containing the new carbon content was first added to the furnace just after $t = 2$ h. Therefore, the time delay from when a carbon content prescription occurs to when the new charge composition is added to the furnace is estimated to be 2.0 h.

The first experiment failed because it was stopped too early. Figure 8.10 shows a response starting at $t \approx 2$ h, but this is could not be an effect of the altered carbon content in the charge, because at that time the new charge composition had hardly been added to the furnace. However, at $t = 5$ h the carbon content step response starts, but the experiment was ended at $t = 7$ h, and therefore the complete responses could not be observed.

Nevertheless, the experiment indicated a time delay of:

$$\tau_i \approx 4 \text{ h}$$

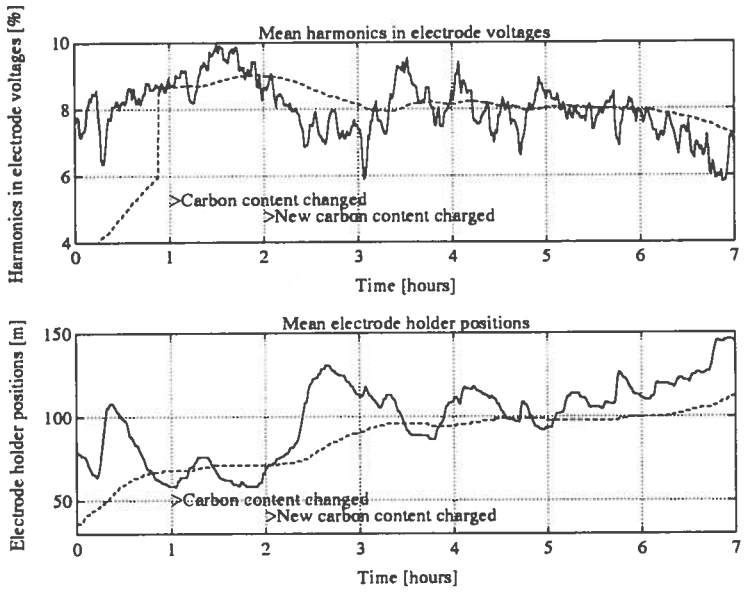

Figure 8.10: Experiment 1: Responses of mean content of harmonics in the electrode voltages and mean electrode holder position to an increase of 3% in the added charge carbon content.

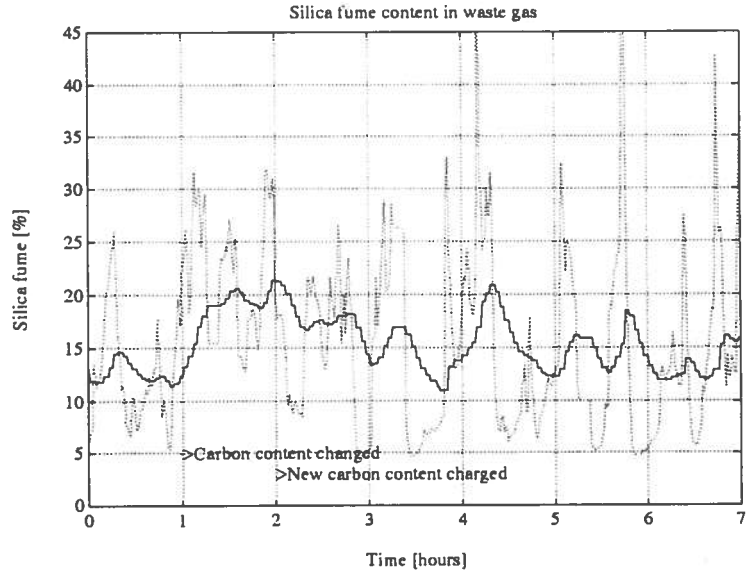

Figure 8.11: Experiment 2: Response of silica fume flow to an increase of 3% in the added charge carbon content.

which means that there is a time delay of 2 h prior to the furnace, and a delay of 2 h in the furnace charge.

The silica fume response to the alteration in the added carbon content is shown in Fig. 8.11. The response of the filtered silica fume flow is more difficult to read, but a falling trend and a time delay of about 2 h can be observed.

The responses of the harmonics, the electrode holders and the silica fume flow correspond to the qualitative model assumptions:

$$\text{Increased carbon content} \Rightarrow \begin{cases} \text{Decreased content of harmonics} \\ \text{Increased electrode holder positions} \\ \text{Reduced silica fume flow} \end{cases}$$

Experiment 2

A new experiment was carried out to establish and complete the model. At this time the fix carbon content in the charge was reduced by 3% . The responses of the harmonics and the electrode holders are shown in Fig. 8.12, while the response of the silica fume flow is shown in Fig. 8.13. The new charge composition was prescribed at $t = 1$ h and was added to the furnace at first $t = 2$ h, and at this time the experiment continued for a sufficient time period.

The responses of the harmonics, electrode holders and the filtered silica fume flow correspond to the qualitative model assumptions:

$$\text{Reduced carbon content} \Rightarrow \begin{cases} \text{Increased content of harmonics} \\ \text{Decreased electrode holder positions} \\ \text{Increased silica fume flow} \end{cases}$$

The responses of the harmonics and the electrode holders indicate a time delay similar to the first experiment. Therefore estimates of time delays of:

$$\tau_i \approx 4 \text{ h}$$

for both responses seem reasonable. The responses indicate equal time constants of:

$$T_i \approx 2 \text{ h}$$

for the responses. The following process gains can be calculated. The harmonics response indicates a gain of:

$$k_1 \approx 1.5 \text{ [\%]}/3.0 \text{ [FixC \%]} = 0.5$$

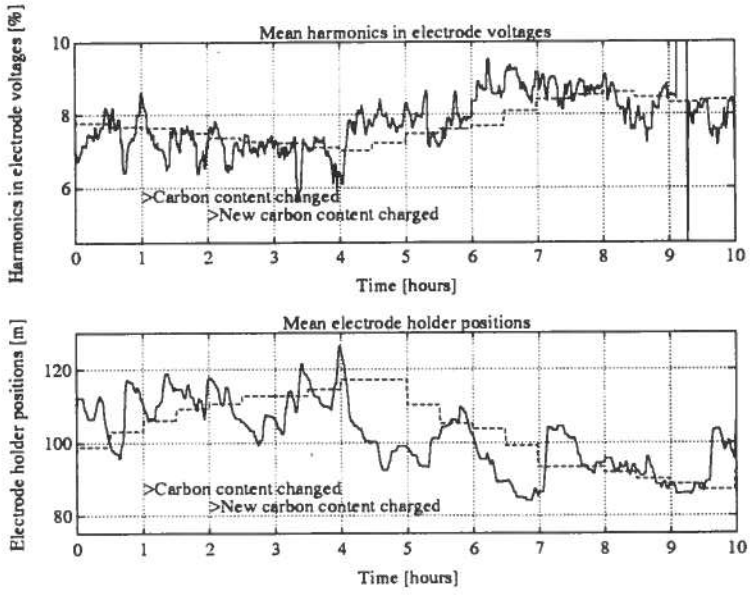

Figure 8.12: Experiment 2: Responses of mean content of harmonics in the electrode voltages and mean electrode holder position to a reduction of 3% in the added charge carbon content.

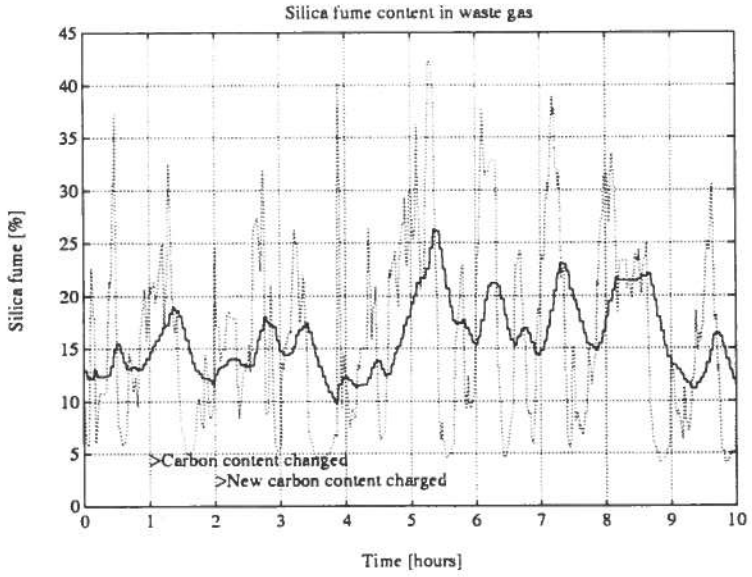

Figure 8.13: Experiment 2: Response of silica fume flow to a reduction of 3% in the added charge carbon content.

while the electrode holders indicate a gain of:

$$k_2 \approx 24.0\ [\text{cm}]/3.0\ [\text{FixC }\%] = 8.0$$

The response of the filtered silica fume flow indicates a time delay of 2 h and a time constant of 1 h. The reduced time delay and time constant compared to the other output variables, can be explained by the fact that the silica fume flow to some extent depends on conditions in the upper part of the furnace, while the others depend on conditions in the hearth of the furnace.

Derived model expressions

The following frequency-domain input-output models can be derived based on these experiment:

1. **The harmonic contents model, $h_1(s)$:**

$$h_1(s) = 0.5\,\frac{1}{1+2.0\,s}\,e^{-4.0\,s} \tag{8.3}$$

2. **The electrode holder positions model, $h_2(s)$:**

$$h_2(s) = 8.0\,\frac{1}{1+2.0\,s}\,e^{-4.0\,s} \tag{8.4}$$

where the frequency variable s correspond to 1/hour.

The simple models of the harmonic contents and the electrode holder positions were applied in the synthesis of the conventional carbon controller by adjusting the control parameters, and significant improvements were realized.

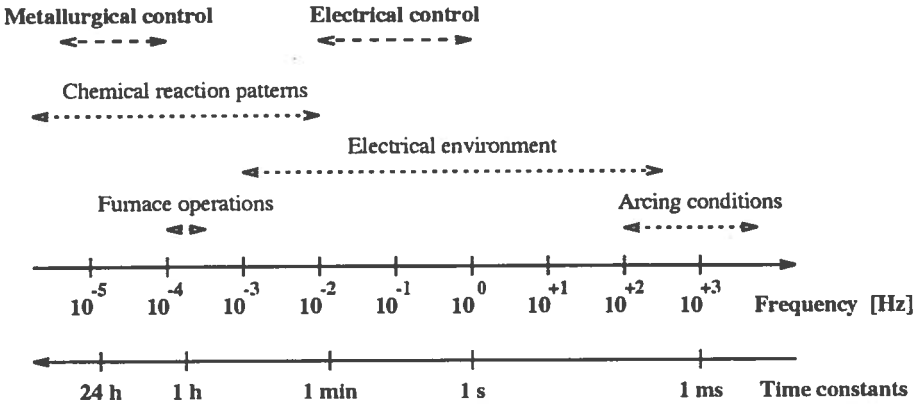

Figure 8.14: Illustration of the dominant frequency regions in a ferrosilicon furnace.

8.1.4 Dominant frequency regions of a ferrosilicon furnace

The process conditions in a ferrosilicon furnace operate within quite different frequency regions. Figure 8.14 illustrates the frequency regions where the various kinds of process conditions are active, as well as the frequency regions of the furnace operations and control activities.

The active furnace frequencies include on one hand very high frequency arcing conditions with time constants below 1 ms, and on the other hand dynamics in the chemical reaction patterns in the furnace with time constant of several days.

8.2 Overcoked and undercoked furnace conditions

The balancing of the carbon content of the charge of a ferrosilicon furnace is a critical task. Due to the lack of direct measurements of the inner furnace conditions, the decision regarding the furnace carbon content must be based on indirect measurements and furnace observations. In this section the over- and undercoked furnace conditions and connected reaction patterns are further discussed and related to available furnace measurements and observations.

8.2.1 Overcoked furnace condition

The following situation is considered: The furnace is assumed to have an optimal carbon content. Then, the carbon content in the added charge

is increased, and the furnace in turn, is changed into a overcoked furnace condition. The remaining furnace properties are kept unchanged.

Reaction patterns for overcoked furnace conditions

The transition from a balanced carbon content to an overcoked situation can be explained by the following reaction pattern:

1. The amount of the carbon reaction:

$$SiO + 2\ C \rightarrow SiC + CO \tag{8.5}$$

   in the outer reaction zone increases due to the increased amount of carbon surface available for reactions with the SiO gas. This results in an increased production of SiC, which in turn enters the inner zone. Since this is an exothermic reaction, the local charge burden temperature may increase.

2. The amount of unreacted carbon entering the inner reaction zone, will increase due to the increased carbon content in the charge. This will result in an increased amount of the carbon reaction in Eq. 8.5 in the cavities as well, and the amount of SiC in the cavities increases.

   A part of this SiC will not react any further, and the process of build-up of SiC in the cavities starts.

3. An overall view of the furnace states that the amount of carbon reaction in Eq. 8.5, increases. This results in increased SiO consumption in the charge, and the SiO flow from the furnace decreases.

4. The Si production by the reaction:

$$SiO + SiC \rightarrow 2\,Si + CO \tag{8.6}$$

   decreases due to the changed cavity conditions.

5. The cavity temperature increases due to the carbon reactions.

6. The amount of SiO production in the cavity decreases.

Furnace observations

In situations where the furnace is assumed to be in an overcoked condition, the following are commonly observed:

- The electrode holder positions are high.

- The amount of harmonics in the electrode voltages are low.
- A (temporary) period with reduced silica fume flow from the furnace.

These observations can be explained based on the models discussed in Sections 7.2 and 7.3.

- **High electrode holder positions**

  A transition to an overcoked furnace situation leads to increased electrical conductivity in the charge burden by partly the increased carbon content and by partly the increased temperatures in the charge.

  The increased conductivity results in increased electrode currents, and the current control system compensates for this by rising the electrodes, and high electrode holder positions are observed.

- **Low content of harmonics**

  Higher temperatures in the cavities may result in less distortion in the electrical states due to arcing. The arcs ignite easier at higher temperatures and the electrical conductivity in the cavity atmosphere increases with temperature. This will be reflected by a lower content of harmonics in the electrode voltages.

  However, the reductions in the harmonic content in the electrode voltages are usually too large (up to 50%), to be explained as the result of changes in arcing conditions. The increased charge conductivity will cause a change in the current distribution between the arcs and the bypass currents in the charge. This results in a situation where a larger fraction of the electrical energy is dissipated in the charge, and the content of harmonics in the electrode voltages decreases.

- **Silica fume production**

  According to the models an overcoked situation corresponds to a decrease in the amount of released SiO gas from the furnace, as shown in Fig. 7.7. This is also observed in industrial furnaces, as least as a temporary effect.

  However, the period with decreased silicon loss is limited. In an overcoked situation the carbon turnover decreases subsequently. This is due to a decrease in the height of the outer reaction zone in the charge. The build-up of SiC in the cavities forces the inner reaction zone upwards in the furnace, and a similar effect has higher electrode tip positions. Thus, the long-term effect of an overcoked situation is increased SiO flow from the furnace. This is illustrated in Fig. 7.7, which shows that a lower carbon turnover for instance as a result of decreased charge height, increases the silica fume curve.

8.2.2 Undercoked furnace condition

Similarly to the analysis of overcoked conditions, the furnace is assumed to have an optimal carbon content at first. Then, the carbon content in the added charge is decreased, and the furnace in turn, is changed into a undercoked furnace condition, while the remaining furnace properties are kept unchanged.

Model of the reaction patterns in an undercoked situation

The transition from a balanced carbon content to an undercoked situation can be explained by the following reaction pattern:

1. The reduction of the carbon content in the charge results in a reduced amount of the carbon reaction:

$$SiO + 2\,C \rightarrow SiC + CO \tag{8.7}$$

   Since this is an exothermic reaction this could result in a locally cooler charge burden. This will also result in a decreased amount of SiC entering the inner reaction zone.

2. The reduced amount of SiC in the inner zone will lead to less of the reaction between SiO and SiC:

$$SiO + SiC \rightarrow 2\,Si + CO \tag{8.8}$$

   in the inner zone, and the production of Si is reduced.

3. A larger amount of SiO gas will leave the inner reaction zone. The reaction between SiO_2 and Si:

$$SiO_2 + SiO \rightarrow 2\,SiO \tag{8.9}$$

   occurs as earlier, but the SiO will not be "recovered" in the cavity wall in the same degree as before.

4. The charge will in turn be saturated with SiO condensate, and the SiO gas will escape the furnace.

5. The changed reaction pattern in the cavities requires an increased energy supply. This results in a decrease in the cavity temperatures.

Furnace observations

At undercoked furnace conditions the following observations are usually made:

- The electrode holder positions are low.
- The amount of harmonics in the electrode voltages are high.
- The silica fume release from the furnace is considerable.

The furnace observations in an undercoked furnace operation mode can be explained as follows:

- **Low electrode holder positions**

  Less amount of exothermic carbon reactions in the charge together with the reduced charge carbon content will result in a reduced charge conduction. This will lead to a decrease in the total electrode current as well. The electrical control system will respond by lowering the electrode to attain the current references, and thereby low electrode holder positions are observed.

- **High content of harmonics**

  The reaction model in Section 7.2, yields a lower temperature in the inner reaction zone. A lower temperature in the cavities results in more distortion of the electrical states because of changed arcing conditions, since the arcs ignite with more difficulty in "cold" surroundings, and the electrical conductivity of the cavity gases decreases with decreasing temperature.

  The effect of undercoked conditions on the harmonics content in the electrode voltages is larger than could be expected from the temperature changes in the cavities. However, the change in the current distribution with a decreased charge current. will yield an increased fraction of power dissipation in the cavities. This will be reflected as an increased content of harmonics in the electrode voltages.

- **Considerable silica fume flow**

  The observed increase in the SiO flow leaving the furnace corresponds to the reaction models. Figure 7.7 illustrates the effect of undercoked furnace conditions on the SiO production from the furnace.

8.2.3 The effects of reduced carbon turnover

In the following it is assumed that the furnace carbon materials are changed in a way that reduces the carbon turnover. The furnace is assumed to have an optimal carbon content when the carbon materials are changed, for instance by increased carbon particle sizes or reduced reactivity, and the further furnace conditions are kept unchanged.

The effects of reduced carbon turnover to the chemical reaction patterns in the furnace are described, and the most probable furnace observations at a reduced carbon turnover situation are discussed. The following reaction patterns should be compared with the stoichiometric model described in Section 7.2

Model of the reaction patterns at reduced carbon turnover

The following model described the reactions patterns in a situation of reduced carbon turnover:

1. The reduced carbon turnover leads to less content of the carbon reaction:

$$SiO + 2\,C \rightarrow SiC + CO \tag{8.10}$$

   in the outer reaction zone.

2. An increased amount of C enters the inner reaction zone due to the reduced carbon turnover. Therefore, the content of the carbon reaction in Eq. 8.10, in the inner zone increases.

   Thus, the carbon reaction has relatively been moved from the outer to the inner reaction zone. This results in an increased production and subsequent build-up of SiC in the cavities. The problem is not necessarily that the furnace produces too much SiC, but more that the SiC is produced at places where it cannot be further consumed.

3. The reduced content of carbon reactions in the outer zone yields an increased content of condensation of SiO:

$$2\,SiO \rightarrow < SiO_2 + Si > \tag{8.11}$$

   in the outer zone.

4. The increased SiO condensation results in an increased supply of "high-reactive" SiO_2 to the inner reaction zone. This will mainly be in the form of "condensate":

$$< SiO_2 + Si > \tag{8.12}$$

However, the SiO condensation can also heat the charge sufficiently to increase the melting of SiO_2, flowing downwards to the cavities.

5. The increased supply of high-reactive SiO_2 to the inner zone will increase the content of the reactions:

$$2\,SiO_2 + SiC \rightarrow 3\,SiO + CO \tag{8.13}$$

$$SiO_2 + Si \rightarrow 2\,SiO \tag{8.14}$$

The amount of produced SiO gas leaving the inner zone will thereby increase.

6. The content of the reaction between SiO and SiC:

$$SiO + SiC \rightarrow 2\,Si + CO \tag{8.15}$$

in the inner zone will be reduced because less SiC is produced in the outer zone.

This reaction is dependent on the SiO gas being able to react countercurrent with the SiC, and the content of the reaction is reduced because less SiC is available for reaction with the upstreaming SiO. The result is less Si production in the inner zone.

7. At a given energy supply the inner reaction zone has a specific SiO production. If the SiO production is increased at an unchanged energy supply, the temperature in the inner zone will decrease.

The inner zone has received an increased amount of high-reactive SiO_2. Usually, the limiting factor of the SiO producing reactions in Eqs. 8.13 and 8.14, is the access of reactive SiO_2. Therefore, the content of the SiO producing reactions will increase, and the temperature in the inner zone will decrease.

8. The increased exothermic SiO condensation in the charge yields an increased temperature in the charge. The charge is subsequently saturated with SiO condensate, and the SiO gas escapes from the furnace.

The increased content of condensate in the charge may "tighten" the charge in a way that creates a more uneven gas distribution. This will result in poorer countercurrent conditions for the carbon reactions and the carbon turnover will further decrease.

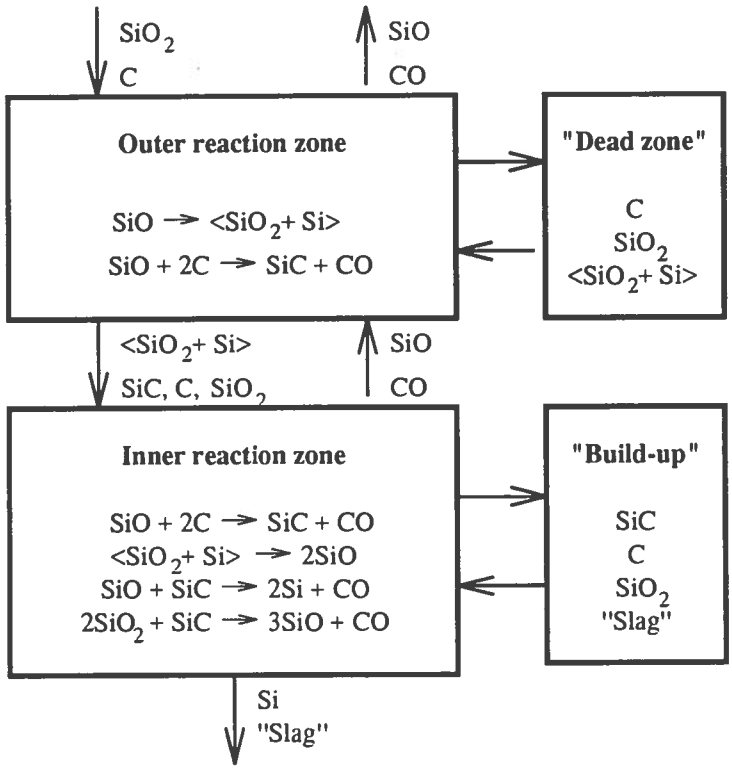

Figure 8.15: Model of reaction pattern at low carbon turnover.

Figure 8.15 schematically shows the reaction patterns in a furnace with reduced carbon turnover. The outer reaction zone has similar reaction patterns as earlier. A "dead-zone" has been added to the model of the charge to describe the build-up of unreacted materials and materials that do not take part in the reactions. The reaction pattern in the inner zone has been extended with the carbon reaction. The build-up of materials in the inner zone is described by a dead-zone containing unreacted SiC, SiO_2, C and slag.

Furnace observations

In a situation with reduced carbon turnover, the following observations can be made for the furnace:

- High electrode holder positions.
- Low content of harmonics in the electrode voltages.
- Considerable increase in released silica fume flow.

- Difficult metal tapping conditions.

These observations, and mainly the first and the second ones, are similar to an overcoked situation which is previously discussed in Section 8.2.1. Therefore, a change of the carbon materials in a way that reduces the carbon turnover without changing the carbon content in the added charge, corresponds to a transition to an overcoked furnace condition. This confirms the relations between the optimal carbon content and the carbon turnover which is discussed in Section 7.3.4 and illustrated in Fig. 7.6.

The relation between the silica fume flow and the carbon turnover is illustrated in Fig. 7.7 and corresponds to the observations. In fact, a furnace which is continuously running in an overcoked condition will be moved into a reduced carbon turnover situation.

The furnace observations at reduced carbon turnover can be explained as follows:

- **High electrode holder positions**

  The increased charge temperature leads to an increased charge conduction and thereby an increased electrode current. In order to compensate for this the electrode controller rises the electrodes, and therefore the high electrode holder positions are observed.

- **Low content of harmonics**

  Due to the changed reaction patterns the temperatures in the cavities has decreased. This may result in more distortion of the electrical states due to less conductive arcing conditions. This would be expected to be reflected by an increased content of harmonics in the electrode voltages.

  However, the increased charge current has resulted in a transition in the electrical power distribution from the electric arcs to charge conduction. Therefore, the fraction of arcing power is decreased and the observed content of harmonics has decreased.

- **Increased silica fume production**

  The reaction pattern model explains the increased silica fume flow from the furnace.

  A furnace condition with reduced carbon turnover will always lead to increased silica fume production. If poorer carbon materials are used, this must be paid for by increased SiO flow. Referring to Fig. 7.6,

showing the silicon yield at different carbon turnover, a reduced carbon turnover will result in reduced silicon yield. The increased silicon loss will come as increased silica fume production. If this fume production is suppressed, the furnace will respond by increasing the build-up of SiC in the cavities, and the production becomes damaged.

- **Observations at the tapping of metal at reduced carbon turnover**

  At a situation with reduced carbon turnover the furnace condition influences the tapping of metal from the furnace. This is usually observed by:

  - **Reduced metal production**
    The reduced silicon metal production is a result of the changed reaction pattern in the furnace. The content of the required SiC producing reaction in the outer reaction is reduced, and the SiC production is relatively moved to the inner zone. Hence, the SiC is present at the "wrong" place in the furnace, and the Si production is thereby reduced.
  - **Increased slag production**
    "Slag" in the (ferro)silicon process is SiO_2, SiC , C and other impurities in the metal product. At reduced carbon turnover there is an increased content of SiO_2, SiC and C in the inner zone, which will build-up in the cavities. These materials may melt or soften in a way that they may follow the liquid Si during tapping.
  - **Reduced temperature of tapped metal**
    The temperature of the tapped metal is usually lower when there is reduced carbon turnover. This is most probably a result of more difficult tapping conditions. The metal flows slower and thereby its temperature is reduced due to the increased heat transfer to the surroundings.

Slag analysis at reduced carbon turnover

Analysis of green-slag samples was carried out at Elkem Thamshavn at a situation when the furnace had low carbon turnover and operational difficulties with significant slag production.

The analysis showed that the green-slag mainly consisted of:

$$< 2\,SiO_2 + SiC >$$

This material is usually characterized as "tight green material" (Schei and Larsen, 1982). This could be the result of the reaction:

$$3\,SiO + CO \rightarrow < 2\,SiO_2 + SiC > \tag{8.16}$$

This reaction can described by the following reaction pattern:

1. First, condensation of SiO gas in the charge:

$$4\,SiO \rightarrow 2\ <\ Si + SiO_2\ > \tag{8.17}$$

   Condensate is commonly characterized as "a tight brown material" (Schei and Larsen, 1982).

2. Then, the Si in the condensate reacts with the upstreaming CO:

$$2\,Si + CO \rightarrow SiC + SiO \tag{8.18}$$

The content of the slag producing reaction in Eq. 8.16 can give information about the total reaction pattern and the furnace condition as well.

A significant amount of green-slag indicates a large SiO production in the inner reaction zone and a low carbon turnover in the furnace.

Furnace operation strategy

A situation with reduced carbon turnover results in the following operational problems:

- The electrical power distribution is undesirable in the way that a too large fraction of the electrical power is dissipated in the charge.
- The current distribution in the furnace is changed by increased charge conduction. This may result in significant electrode-to-electrode conduction, and hence the electrical control system fails as the electrode-to-electrode currents are less sensitive to electrode movements.
- Increased silica fume production.
- Reduced Si metal production and problems with the tapping operation.

The following operation strategy should be used to respond the reduced carbon turnover situation:

- **Carbon content**

  The furnace has turned to an overcoked conditions as a result of the reduced carbon turnover, and hence the carbon content must be reduced.

- **Electrical conditions**

  The current set-point should be increased in order to force the electrodes deeper into the furnace. This will lead to increased arc currents in the cavities.

- **Reaction patterns**

  The reaction patterns can be controlled by increasing the carbon turnover, for instance by using more reactive carbon materials. In this way the reaction patterns in the furnace can be "turned" to more carbon reactions in the outer zone.

8.3 Analysis by simulation studies

The simulation model of the silicon process previously described in Section 7.6, is applied in studies of various furnace operation strategies. The continuous version of the model is used, and the model parameters have been adjusted to describe the conditions in a ferrosilicon furnace similar to furnace at Elkem Thamshavn. Similar simulations are discussed by Halvorsen, Schei and Downing (1992).

Two different furnace operation cycles are described below. Both cases start with a situation where the furnace has an optimal carbon content and describes the responses of changes in the added carbon content.

1. The first case describes the response of an increase in the added carbon content followed by a significant reduction.

2. The other case describes the opposite situation with a decrease in the added carbon content followed by a significant increase.

8.3.1 An overcoked-undercoked operation cycle

This simulation describes the following situation: The furnace is in a situation where it has a carbon content of 1.8, which is near to the optimal value for the set of parameters used in the model. Then, the carbon content

in the added charge is increased to 1.9 for a period of 7 days, and this is followed by a reduction in the added carbon content to 1.7 for 7 days.

Figure 8.16 shows the responses of the Si production rate and the released SiO flux, while Fig. 8.17 shows the responses of the SiC content in the hearth and the furnace silicon yield.

When the added carbon content is increased to 1.9, the furnace is transferred into an overcoked condition. The Si production rate is slightly increased and the SiO flux is reduced, compared to the optimal starting-point. The furnace silicon yield has a response similar to the Si production rate, while the content of SiC in the hearth is continuously increasing during the period of overcoked charge addition.

At $t = 7$ days the added carbon content is reduced to 1.7. The furnace corresponds to this by a rapid increase in both the Si production rate and the released SiO flux, because the reaction pattern has been changed and the SiC in the hearth is being consumed. The furnace is transferred into an undercoked situation as the amount of SiC in the hearth is reduced, and when the SiC has been consumed the Si production rate drops and the SiO flux increases significantly.

The response of the Si production rate when the furnace conditions is changed from an overcoked to an undercoked condition prevails inverse dynamics and corresponds to an inverse response as result of a system zero in the RHP for a linear system. Further simulations have indicated that the length of this inverse response depends on the step size in the carbon content, and if the carbon content step is reduced, the length of the inverse response is increased.

This inverse response implies an absolute bandwidth limitation if the Si production rate is to be used in the metallurgical control of the furnace. This bandwidth limitation will be given by the position of RHP zero, which corresponds to the length of the length of the inverse response.

The inverse response connected with the Si production rate also explains the weakness with decisions of furnace operation strategies based upon manual observations of limited time length. This is further discussed by Halvorsen, Schei and Downing (1992).

The response of the SiO flux also shows the effect of a system zero, but this response can be regarded as similar to a response given by a system zero in the LHP for a linear system. However, this zero will not give any bandwidth limitations if the SiO flux is used in any carbon control strategy.

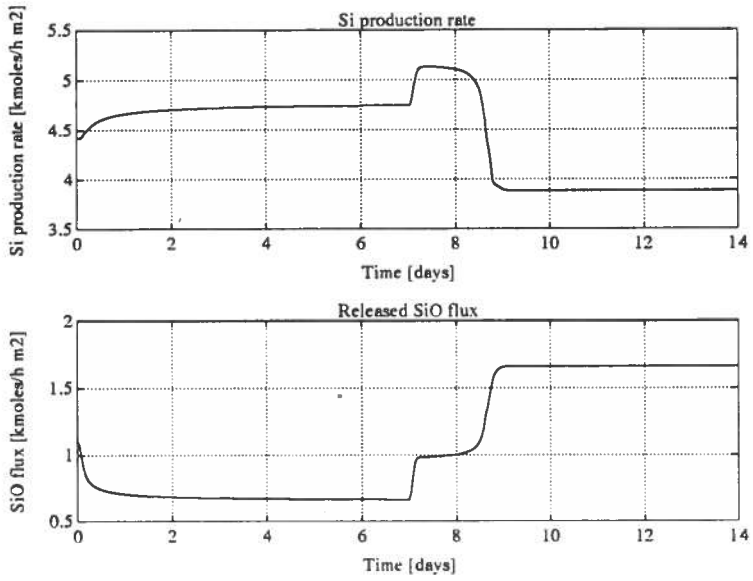

Figure 8.16: Si production rate and released SiO flux in the overcoked-undercoked operation cycle.

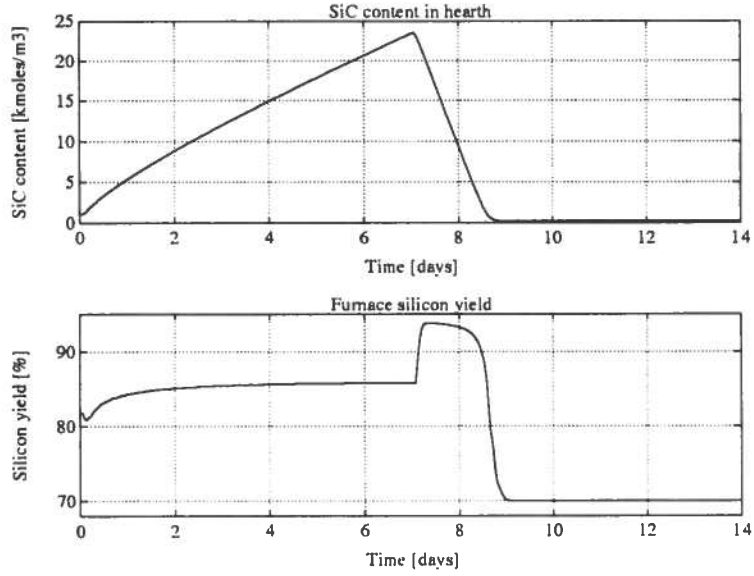

Figure 8.17: SiC content in hearth and furnace silicon yield in the overcoked-undercoked operation cycle.

8.3.2 An undercoked-overcoked operation cycle

This simulation describes the opposite situation compared to the simulation case above. At the beginning the furnace has the near-optimal carbon content of 1.8. Then, the carbon content in the added charge is reduced to 1.7 for a period of 5 days, and this is subsequently followed by an increase in the added carbon content to 1.9 for 4 days.

Figure 8.16 shows the responses of the Si production rate and the released SiO flux, and Fig. 8.17 shows the responses of the SiC content in the hearth and the furnace silicon yield.

The reduction of the added carbon content from the optimal value of 1.8 to 1.7, transfers the furnace into an undercoked condition. The Si production rate decreases and the SiO flux increases. The furnace silicon yield has a similar response as the Si production rate, and the content of SiC in the hearth is slightly reduced and is almost negligible.

At $t = 5$ days the added carbon content is increased to 1.9. The furnace corresponds to this by first-orders responses in both the Si production rate and the released SiO flux, and the Si production rate increases, while the SiO flux decreases. The SiC content in the hearth acts like an integrator and increases continuously, and thus the furnace has been transferred into an overcoked condition.

It should be noted that the responses from an undercoked to an overcoked condition do not show any inverse responses or zero responses that were present in the overcoked-undercoked cycle, and the furnace product outputs show responses similar to pure first-order responses.

8.3.3 Consequences for metallurgical control strategies

The following consequences for metallurgical control strategies can be stated based on the simulation studies:

- **Si production rate.** The simulations have established the presence of inverse dynamics in the response of the Si production rate to alterations in the added carbon content. If the Si production rate is to be used in any carbon control strategies, the bandwidth limitations due to the inverse response must be considered. However, a slow carbon control strategy based on the Si production rate may be useful in addition to other control strategies.

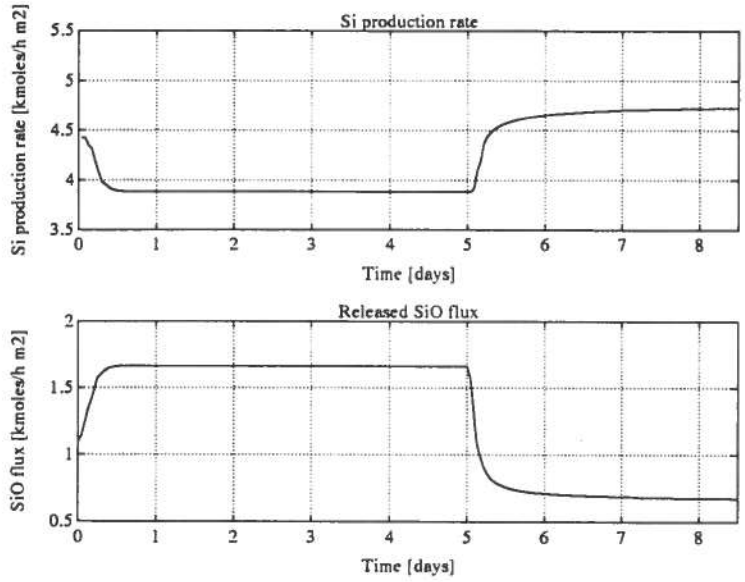

Figure 8.18: Si production rate and released SiO flux in the undercoked-overcoked operation cycle.

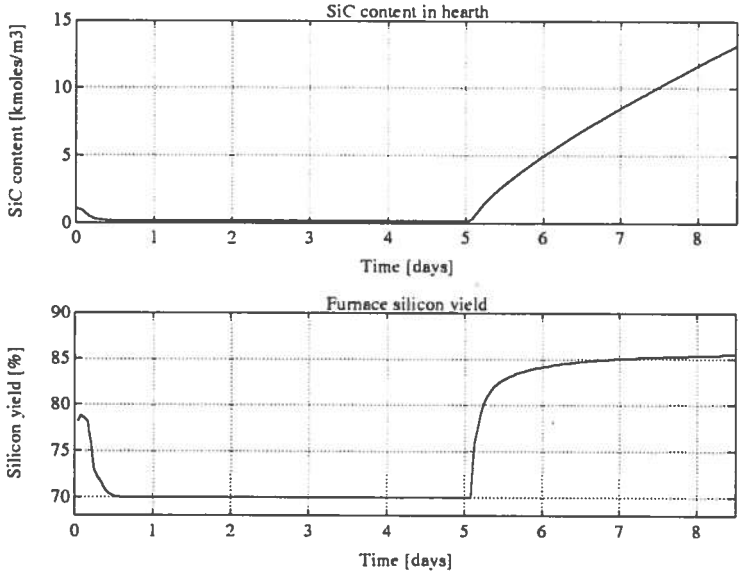

Figure 8.19: SiC content in hearth and furnace silicon yield in the undercoked-overcoked operation cycle.

- **SiO flux.** The simulations indicate a system zero in the SiO flux' response to altered carbon content added to the furnace. This zero dynamic implies no direct band-width limitation if the SiO-flux is used in carbon control.

  However, the sudden changes in the gain between the carbon content alterations and the SiO flux response, may create difficulties, and hence the bandwidth of any control loop should be given by the system zero.

- **SiC content in hearth.** The simulations have verified the importance of the SiC content in the hearth, and that the control of this SiC content is of great importance if successful furnace operations should be obtained.

  The SiC content in the hearth is not directly measurable, and hence the development of methods for estimating this SiC content should receive significant attention.

8.4 Model-based measurement systems

The lack of direct measurements of the inner process variables in a ferrosilicon furnace indicates the need for model-based measurement techniques in the operation and control of such furnaces. The principle of a model-based measurement system is illustrated in Fig. 8.20. The system consists of a model of the process which is implemented online in parallel to the process, and a model adaptation strategy operating on the deviations between the process output and the estimated outputs from the model. When the model outputs are in accordance with the process outputs, the process variables of current interest can be found from the corresponding model variables. The concept of model-based measurements is further treated among others by Balchen and Mummé (1988).

Two different applications of model-based measurement systems on ferrosilicon furnaces are further discussed below.

8.4.1 An electrical model estimator scheme

A model-based measurement system of the inner process variables in submerged-arc furnaces is developed. The estimator scheme is based on a dynamic model of the transient electrical conditions in a ferrosilicon furnace combined with a parameter estimator. The electrical model estimator scheme is illustrated in Fig. 8.21.

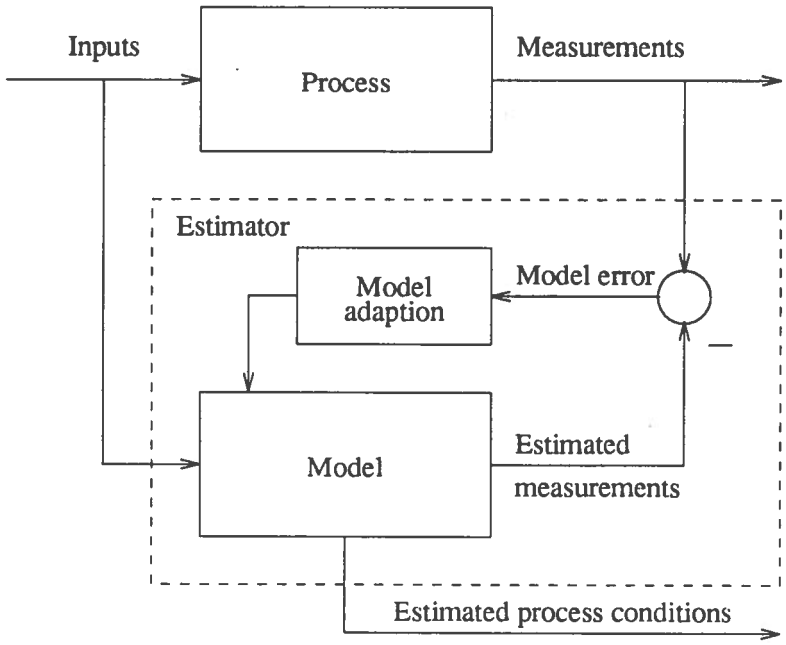

Figure 8.20: The principle of a model-based measurement system.

The model consists of a transient electrical model based on an equivalence circuit of the three-phase electrical system with resistances and inductances equivalent to the current paths in the furnace, and with the arcs in the cavities represented as circuit elements with time-varying resistances found by separate dynamic models of the AC electric arcs. The arc models describe the arcing effects as electric conduction in conductive gas channels and compute the time-varying resistances based on the physical variables in the cavities. The electrical estimator scheme is further discussed in Valderhaug and Balchen (1993).

The electrical model estimator is implemented with the dynamic transient electrical model derived in given Section 4.4.2 and given by Eqs. 4.94 to 4.96. The transient electrical model is implemented with both the proposed AC arc model in Section 3.7.3, which is a modified version of Pfeifer's model (Pfeifer, Fett and Bebber, 1989), as well as Sakulin's simplified arc model (Sakulin, 1980), described in Section 3.7.2, and with the proposed model of the AC anode and cathode voltages in Section 3.7.4. The implementation with the arc model in Section 3.7.3, is described below.

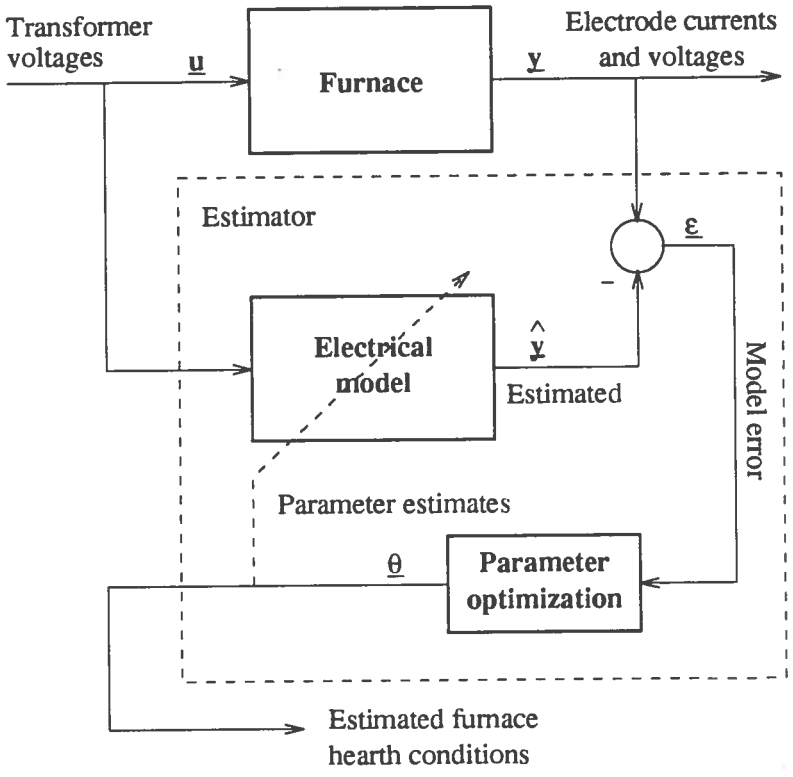

Figure 8.21: The electrical model estimator scheme.

The electrical model

The complete model consisting of the transient electrical model, including channel models for the electric arcs in the three cavities, is implemented in a simulation model. The complete model can be stated as:

$$\begin{aligned} \dot{\underline{x}}_{el} &= \underline{f}_{el}(\underline{x}_{el}, \underline{x}_a, \underline{\theta}_{el}, \underline{u}) \\ \dot{\underline{x}}_a &= \underline{f}_a(\underline{x}_{el}, \underline{x}_a, \underline{\theta}_a) \\ \underline{y} &= \underline{g}(\underline{x}_{el}, \underline{x}_a, \underline{\theta}_{el}) \end{aligned} \tag{8.19}$$

where $\underline{x}_{el}$ is the electrical state vector, $\underline{x}_a$ is the arc state vector, $\underline{u}$ is the model input vector, and $\underline{y}$ is the model output vector:

$$\underline{x}_{el} = \begin{bmatrix} i_{e1} \\ i_{e2} \end{bmatrix} \quad \underline{x}_a = \begin{bmatrix} T_{a1} \\ T_{a2} \\ T_{a3} \end{bmatrix} \quad \underline{u} = \begin{bmatrix} v_{T1} \\ v_{T2} \end{bmatrix}$$

$$\underline{y} = \begin{bmatrix} i_{e1} & i_{e2} & v_{e1} & v_{e2} & v_{e3} \end{bmatrix}^T$$

where i_{e1} and i_{e2} represent the time-varying electrode currents, T_{a1}, T_{a2} and T_{a3} represent the arc channel temperatures, v_{T1} and v_{T2} represent the time-varying transformer voltages, and v_{e1}, v_{e2} and v_{e3} represent the measured time-varying electrode voltages. Furthermore, $\underline{\boldsymbol{\theta}}_{el}$ and $\underline{\boldsymbol{\theta}}_{a}$ represent parameters in the electrical model and the arc models, respectively. The arc state vector contents will depend on which arc model description that is used. In the case of Sakulin's simplified model (Sakulin, 1980), described in Section 3.7.2, the state vector will contain the arc radii r_{ai} instead of the arc temperatures.

The model state variables, the input voltages, the measurements and the model parameters are normalized by scaling in the simulation model. The model parameters, especially the arc model parameters $\underline{\boldsymbol{\theta}}_{a}$, correspond to inner process variables that are important in the operation and control of a ferrosilicon furnace. These variables are generally not measurable on an industrial ferrosilicon furnace, but estimates are achievable by developing a parameter estimator in connection with the model in Eq. 8.19, as previously shown in Fig. 8.21.

The parameter estimator

The parameter estimator that has been developed, is based on an iterative parameter optimization scheme operating on off-line batches of the measurement data and the transformer voltages. The parameter estimation scheme can be described as follows:

1. Fetch the measurement data and the transformer voltage sets from the furnace.

2. Utilization of an iterative parameter optimization:

   (a) Simulate the model the time period T by using the model parameters $\underline{\boldsymbol{\theta}}$, and calculate the model error vector $\underline{\boldsymbol{\epsilon}}$:

   $$\underline{\boldsymbol{\epsilon}}(k) = \underline{\boldsymbol{y}}(k) - \underline{\hat{\boldsymbol{y}}}(k), \quad k = 1 \ldots N \tag{8.20}$$

   where k represents the discrete time variable.

   (b) Calculate the model error index $J(\underline{\boldsymbol{\theta}})$:

   $$J(\underline{\boldsymbol{\theta}}) = \sum_{k=1}^{N} \underline{\boldsymbol{\epsilon}}(k)^T \boldsymbol{Q}\, \underline{\boldsymbol{\epsilon}}(k) \tag{8.21}$$

   where the model error elements can be weighted by the diagonal matrix $\boldsymbol{Q}$.

(c) Minimize the model error index $J(\underline{\boldsymbol{\theta}})$ iteratively with respect to the parameter vector $\underline{\boldsymbol{\theta}}$:

$$\min_{\theta} J(\theta) \tag{8.22}$$

3. Fetch new measurement data sets and so on.

The optimization task is evaluated by the Levenberg-Marquardt least-square minimization method from the Matlab Optimization Toolbox.

The data batches used in the parameter estimation contain:

- The measurement data:
  - The electrode currents: i_{e1} and i_{e2}.
  - The electrode voltages: v_{e1}, v_{e2} and v_{e3}.
- The transformer voltages: v_{T1} and v_{T2}.

The length of the data batches used correspond to 2 electrical periods (20 ms) with sampling intervals of 0.08 ms.

Evaluation of the estimator system

Preliminary analyses of the parameter estimator scheme, that were carried out by mainly simulation studies, have been successful. The model parameters of current interest for estimation are composed of some of the electrical model parameters, such as:

$$\underline{\hat{\boldsymbol{\theta}}}_{el} = \begin{cases} R_{ci} \text{ charge by-pass resistances} \\ R_{mi} \text{ metal bath resistances} \\ R_{bi} \text{ charge bottom resistances} \end{cases} \tag{8.23}$$

and some of the arc model parameters:

$$\underline{\hat{\boldsymbol{\theta}}}_{a} = \begin{cases} h_{ai} \text{ arc lengths} \\ r_{ai} \text{ arc radii} \\ \rho_{ai} \text{ arc conductivity} \\ T_{gi} \text{ cavity temperatures} \end{cases} \tag{8.24}$$

The size of the estimated parameter vector has been 15-20 parameters. An optimization task of this size requires typically 500 iterations to obtain a maximum normalized model error index of 0.0001.

Further studies regarding the parameter identifiability remain, together with implementation of the system on an industrial furnace. This will be further described in Valderhaug and Balchen (1993).

The methodology seems promising and shows good results so far. A satisfactory system implemented on submerged-arc ferrosilicon furnaces will

lead to considerable achievements in the operation and control of such furnaces.

8.4.2 A carbon content estimator

A novel carbon content estimator based on the use of the measurement of the silica fume flow from the furnace has been developed at Elkem Thamshavn. The development of the carbon content estimator is based on a proposal in diploma work by Wasbø (1991) at The Norwegian Institute of Technology, who carried out a comprehensive analysis of furnace measurement data and the mutual correlations. This work has been carried out in close cooperation with the writer of this thesis. The carbon content estimator scheme is qualitatively described below.

The silica fume flow model

The carbon content estimator is based on a black-box model of the silica fume flow from the furnace. Figure 8.22 shows the long-term variation of the measured silica fume flow, filtered with a time-constant of 24 hours, and the fixed carbon content in the added charge. The similarity between the variations in the silica fume flow and the added fixed carbon content is remarkable.

The silica fume model is an input-output ARMAX description of the silica fume flow expressed in terms of the fixed carbon content of the added charge and the mean electrode holder position, as illustrated in Fig. 8.23. The silica fume flow model can in principle be given in the form:

$$y_{\mathrm{SiO}}(t) = c_1 \cdot u_{\mathrm{FixC}}(t - t_1) + c_2 \cdot u_{\mathrm{El}}(t - t_2) \tag{8.25}$$

where $y_{\mathrm{SiO}}(t)$ represents the estimated silica fume flow at the time t, $u_{\mathrm{FixC}}(t - t_1)$ represents the fixed carbon content in the added charge at the time $(t - t_1)$, and $u_{\mathrm{El}}(t - t_2)$ represents the mean electrode holder position at the time $(t - t_2)$. In fact, the applied model contains more terms on the right-hand side of Eq. 8.25, describing previous terms of u_{C} and u_{El}.

The carbon content estimator scheme

The silica fume flow model in Eq. 8.25 is utilized as a recursive ARMAX model and implemented in a recursive parameter estimator scheme, as illustrated in Fig. 8.24.

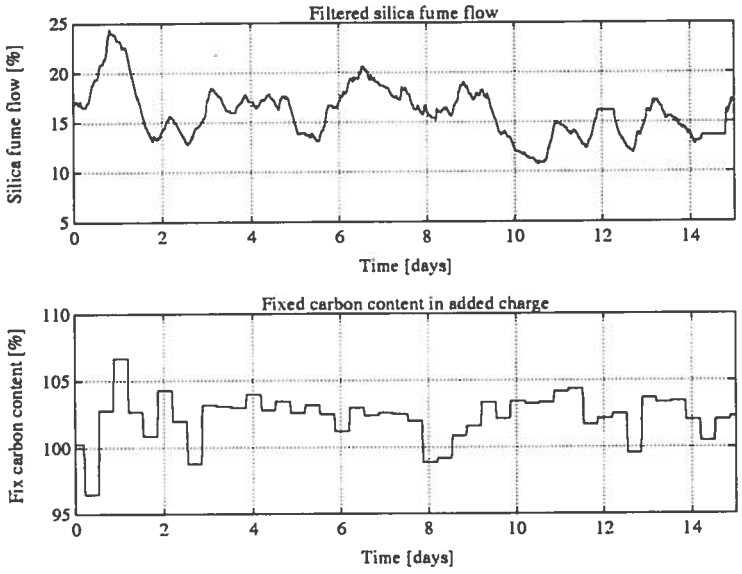

Figure 8.22: Long-term variation in filtered silica fume flow and fixed carbon content in added charge.

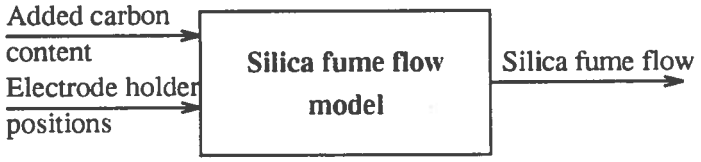

Figure 8.23: The silicon fume flow model.

The estimated model parameter connected to the added carbon content c_1, can be used to determine whether the furnace carbon condition can be described as overcoked or undercoked.

Figure 8.25 shows the principle relation between furnace carbon content and the silica fume flow from the furnace. The slope of the silica fume flow curve is fundamentally different in undercoked and overcoked conditions. The estimated model parameter c_1, can be looked upon as analogous to the slope of the curve in Fig. 8.25, provided the model structure in Eq. 8.25 describes the silica fume flow satisfactorily. And hence, the estimated model parameter can indicate the furnace carbon condition.

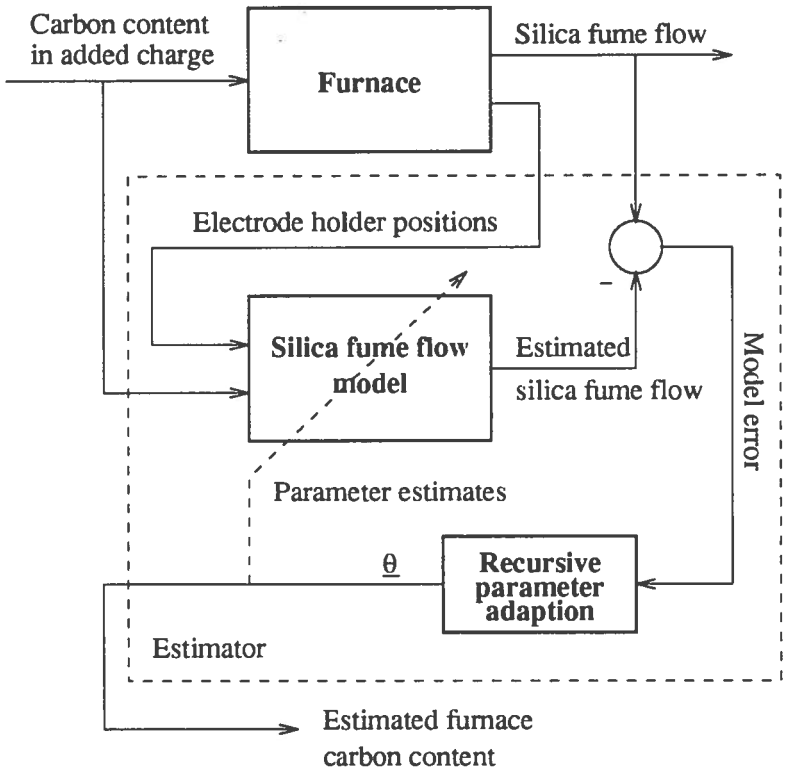

Figure 8.24: The furnace carbon content estimator scheme.

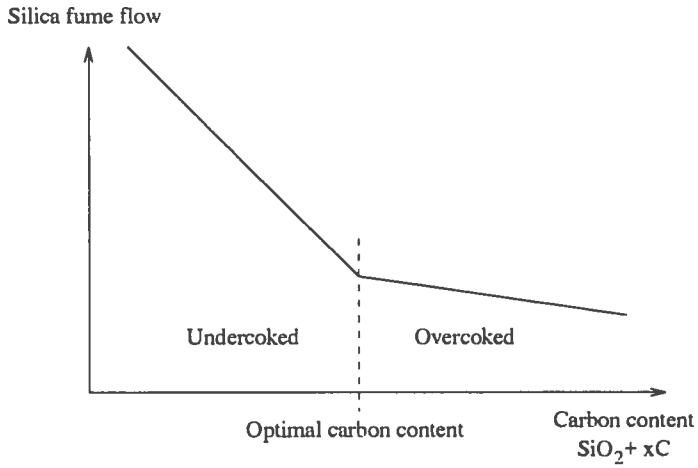

Figure 8.25: The relation between the silica fume flow from the furnace and its carbon content.

The carbon content estimator is presently being tested out at the furnace at Elkem Thamshavn, and the experience so far yields promising results.

8.5 Concluding remarks

In this chapter the metallurgical circumstances in the furnace have been studied further. The effects of furnace operation and long-term process variation have been discussed. Step-response experiments in the added carbon content at the furnace at Elkem Thamshavn, have been described and models used in the synthesis of the conventional carbon controller, are developed.

The over- and undercoked and reduced carbon turnover operation conditions are discussed and qualitative models are proposed and compared to furnace experience. This is also investigated by simulation studies, that also established the presence of inverse dynamics in the system between the added carbon content and the furnace metal production, and illustrated the importance of controlling the SiC in the hearth of the furnace.

Finally, two methods for estimating inner process variables in the furnace are presented:

- An electrical model estimator.

  The model is based on a transient model of the electrical conditions in the furnace, included dynamic arc models, and implemented in an iterative parameter optimization scheme.

  The estimated parameters comprise electrical parameters such as resistances in the furnace burden, and arc model parameters such as arc dimensions and the temperature of the arc and the cavities.

- A carbon content estimator.

  The carbon content estimator is based on an input-output model description of the silica fume flow from the furnace. The model is implemented in a recursive parameter estimator scheme, and a parameter is estimated that is closely related to the furnace carbon content.

These model-based measurement systems yield promising results with respect to applications in metallurgical control strategies.

Chapter 9

Metallurgical control strategies

This chapter expands on the metallurgical control of a ferrosilicon furnace. This was previously discussed in Section 7.5. The main conclusions regarding important process variables are given in Section 7.5.3 and summarized in Table 7.1, the input variable are treated in Section 7.5.5 and summarized in Table 7.2, and the output variables from the furnace are discussed in Section 7.5.6 and the available measurements are summarized in Table 7.3.

Two different metallurgical control strategies are discussed in the following. A model-based control strategy based on the dynamic silicon model in Section 7.6, is described. Finally, a strategy using the available measurements in addition to local estimators of inner process variables, as presented in Section 8.4, is proposed.

9.1 A model-based control strategy

The silicon model previously described in Section 7.6, was originally thought to be the core in a model-based control strategy for the metallurgical control of a ferrosilicon furnace. Therefore, the model has been applied in investigations of possible model-based metallurgical control strategies. This is further treated by Valderhaug, Balchen and Halvorsen (1992), and is briefly discussed in the following.

In this section it is assumed that a ferrosilicon furnace can be described by the model given by Eq. 7.31:

$$\begin{aligned} \dot{\underline{x}} &= \underline{f}(\underline{x}, \underline{u}, \underline{w}) \\ 0 &= \underline{g}(\underline{x}, \underline{u}, \underline{w}) \\ \dot{\underline{q}} &= \underline{h}(\underline{x}, \underline{u}, \underline{w}) \end{aligned} \tag{9.1}$$

The hearth and charge state vectors $\underline{x}_h$ and $\underline{x}_c$, are given by Eqs. 7.32 and 7.33, the derived state vector $\underline{q}$ is given by Eq. 7.34, and the control input vector $\underline{u}$ is given by Eq. 7.35. The model vectors have the following dimensions:

$$\begin{aligned} \dim(\underline{x}_h) &= 4 \\ \dim(\underline{x}_c) &= 5\,n \\ \dim(\underline{q}) &= 6 \\ \dim(\underline{u}) &= 1 \end{aligned}$$

where n is the number of segments describing the outer reaction zone.

In the investigations the control strategies are applied to the simulation model. Thus, in a real furnace application an estimator will be necessary to update the model towards the furnace. However, this is not treated in this work.

9.1.1 A model-based set-point control structure

The ferrosilicon process is characterized by a large number of state variables and a relatively low number of control inputs. The metallurgical goal of attaining optimal furnace conditions by controlling the chemical reaction patterns in the furnace, may be difficult to express in terms of the complete process state vector. Hence, the control task should rather be expressed in terms of a property state vector, describing the states we in fact want to control, and in addition this property state vector should have a dimension similar to the control input vector.

A candidate for such a property vector $\underline{z}$, is:

$$\underline{z} = \begin{cases} \underline{y} = \begin{cases} \dot{q}_1 : \text{released SiO flux} \\ \dot{q}_3 : \text{production rate of Si} \end{cases} \\ x_{h2} : \text{concentration of SiC in the hearth} \end{cases} \tag{9.2}$$

The property vector $\underline{z}$ characterizes the circumstances we want to control in a ferrosilicon furnace. Vector $\underline{z}$ also contains the available measurement from the furnace $\underline{y}$, the Si production rate and released SiO flux in the waste gas.

A set point control strategy is chosen. The set point control structure is chosen to be expressed in terms of the property vector $\underline{z}$. The control input $\underline{u}$ is then given by:

$$\underline{u} = \underline{u}_0 + \Delta\underline{u} \tag{9.3}$$

where $\underline{u}_0$ is the control input corresponding to a given set point $\underline{z}_0$. The other control input term $\Delta\underline{u}$, is calculated by a controller operating on deviations in the property vector $\underline{\Delta z}$ around its set-point $\underline{z}_0$.

The controller is chosen to be based on a state-space description of the model in Eq. 9.1, linearized around the working point $(\underline{x}_0, \underline{q}_0, \underline{u}_0)$:

$$\begin{aligned} \Delta\underline{\dot{x}} &= \boldsymbol{A}\,\Delta\underline{x} + \boldsymbol{B}\,\Delta\underline{u} \\ \Delta\underline{\dot{q}} &= \boldsymbol{H}\,\Delta\underline{x} \end{aligned} \tag{9.4}$$

where the vector deviations are given by:

$$\begin{aligned} \Delta\underline{x} &= \underline{x} - \underline{x}_0 \\ \Delta\underline{u} &= \underline{u} - \underline{u}_0 \\ \Delta\underline{q} &= \underline{q} - \underline{q}_0 \end{aligned}$$

The measurements of the process conditions $\underline{y}$ are given as a sub-vector of $\underline{\dot{q}}$. This yields:

$$\Delta\underline{y} = \boldsymbol{D}_1\,\Delta\underline{\dot{q}} = \boldsymbol{D}_1\boldsymbol{H}\,\Delta\underline{x} \tag{9.5}$$

where:

$$\Delta\underline{y} = \underline{y} - \underline{y}_0$$

The property vector $\underline{z}$, defined in Eq. 9.2, can thereby be expressed as:

$$\Delta\underline{z} = \begin{pmatrix} \boldsymbol{D}_1\,\Delta\underline{\dot{q}} \\ \boldsymbol{D}_2\,\Delta\underline{x} \end{pmatrix} = \boldsymbol{D}\,\Delta\underline{x} \tag{9.6}$$

where:

$$\Delta\underline{z} = \underline{z} - \underline{z}_0$$

The control structure is chosen to be based on state feedback control. The state space controller is chosen to be an LQ controller of the form:

$$\Delta \underline{u} = \boldsymbol{G}\, \Delta \underline{x} \tag{9.7}$$

where the control matrix $\boldsymbol{G}$ is found by optimization of the performance index:

$$J = \int_0^\infty \left(\Delta \underline{z}^T \boldsymbol{Q} \Delta \underline{z} + \Delta \underline{u}^T \boldsymbol{P} \Delta \underline{u} \right) dt \tag{9.8}$$

with respect to $\Delta \underline{u}$. This optimization task is equivalent with the optimization of:

$$J = \int_0^\infty \left(\Delta \underline{x}^T \tilde{\boldsymbol{Q}} \Delta \underline{x} + \Delta \underline{u}^T \boldsymbol{P} \Delta \underline{u} \right) dt \tag{9.9}$$

where the new state weight matrix $\tilde{\boldsymbol{Q}}$ is given by:

$$\tilde{\boldsymbol{Q}} = \boldsymbol{D}^T \boldsymbol{Q} \boldsymbol{D}$$

and where the Eq. 9.9 is optimized subject to the system in Eq. 9.4.

The optimal deviation control input is given by:

$$\Delta \underline{u} = \boldsymbol{G}\, \Delta \underline{x} \tag{9.10}$$

and the control input is given as:

$$\underline{u} = \underline{u}_0 - \boldsymbol{G} \left(\underline{x}_0 - \underline{x} \right) \tag{9.11}$$

This model-based control strategy is illustrated in Fig. 9.1. The strategy is based on a state estimator, because the states cannot be measured directly on a furnace. The property set point vector $\underline{z}_0$ and other operation parameters $\underline{p}$ are assumed to be found from long-term process optimization. The working point ($\underline{x}_0$, $\underline{q}_0$, $\underline{u}_0$) can be found from $\underline{z}_0$ assuming stationary conditions ($\dot{\underline{x}}_0 = 0$). However, in this section we only focus on the state controller which will be the first step in the development of a complete control strategy, and the dashed box in Fig. 9.1 shows the part of the scheme covered by this work.

An alternative optimizing model-based control strategy is the **quasi-dynamic optimal control**-method (Balchen and Mummé, 1988), where the control input is given as

$$\underline{u} = \underline{u}_0 + \Delta \underline{u} \tag{9.12}$$

and where $\underline{u}_0$ is found from optimization of a performance index at steady-state (or slowly varying) conditions. A minimum variation controller (LQ), which operates on deviations around these conditions, calculates $\Delta \underline{u}$.

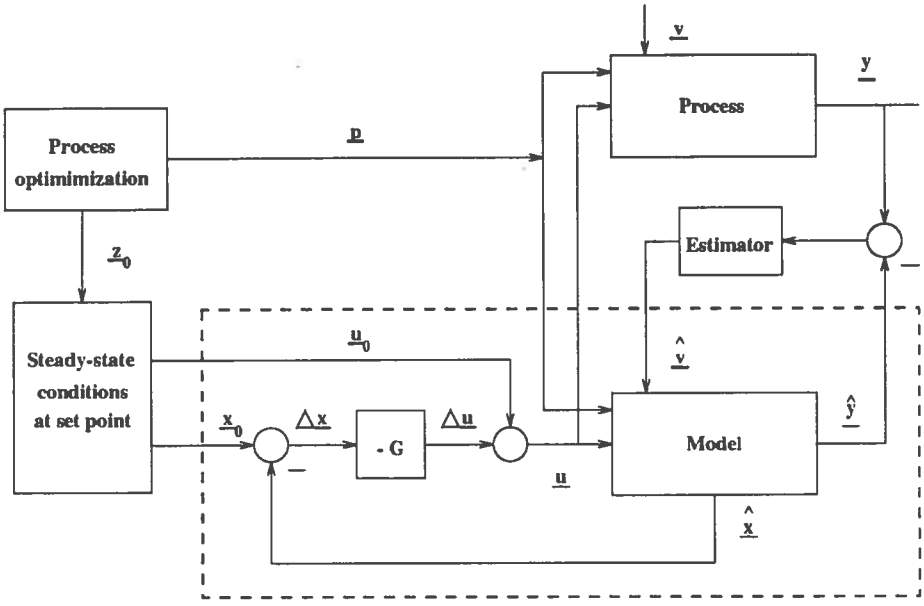

Figure 9.1: A model-based control strategy.

Control synthesis

The simulation model in Eq. 9.1 is implemented with $n = 5$, with a given set of parameters. The linearized model in Eq. 9.4 is found numerically at steady-state conditions ($\underline{x}_0$, $\underline{q}_0$, $\underline{u}_0$), corresponding to the property vector set point $\underline{z}_0$.

The system matrices $\boldsymbol{A}$ and $\boldsymbol{B}$ are found to be highly structured:

$$\boldsymbol{A} = \begin{bmatrix} a_{hh} & a_{h1} & 0 & 0 & 0 & 0 \\ a_{1h} & a_{11} & a_{12} & 0 & 0 & 0 \\ a_{2h} & a_{21} & a_{22} & a_{23} & 0 & 0 \\ a_{3h} & a_{31} & a_{32} & a_{33} & a_{34} & 0 \\ a_{4h} & a_{41} & a_{42} & a_{43} & a_{44} & a_{45} \\ a_{5h} & a_{51} & a_{52} & a_{53} & a_{54} & a_{55} \end{bmatrix} \boldsymbol{B} = \begin{bmatrix} 0 \\ 0 \\ 0 \\ 0 \\ 0 \\ b_5 \end{bmatrix} \tag{9.13}$$

$$\boldsymbol{H} = \begin{bmatrix} h_h & h_1 & h_2 & h_3 & h_4 & h_5 \end{bmatrix} \tag{9.14}$$

where a_{ij}, $i,j = h, 1 \ldots 5$, are sub-matrices concerning the states in the hearth and the charge segments, b_5 is the sub-vector concerning the top segment, and h_i are sub-matrices concerning the derived states and the states in hearth and the charge segments.

The system $(\boldsymbol{A}, \boldsymbol{B})$ is stable and controllable, even though the examination

of the controllability turned out to be numerically ill-conditioned. Furthermore, the system $(\boldsymbol{A}, \boldsymbol{D}_1\boldsymbol{H})$ is observable, and the model state variables can theoretically be estimated by a state estimator using the process measurements.

The state weight matrix $\boldsymbol{Q}$ in Eq. 9.8 is chosen to be diagonal with matrix element magnitudes corresponding to acceptable property state variations, and the control weight matrix $\boldsymbol{P}$ is chosen to avoid large variation in the control input variable.

The optimal controller is implemented in the simulation model as a discrete controller and analyzed by simulation examples, which is discussed in Valderhaug, Balchen and Halvorsen (1992). The simulations indicate promising properties of the control structure, in spite of the fact that only the added carbon content is is applied as control variable. However, this study has focused on applying the control strategy at the simulation model, and the validity of this model is critical regarding any success of the implementation of the model-based control strategy in Fig. 9.1 on a real furnace.

Model evaluation and suggestions for model improvements

The stated model in Eq. 9.1 gives a fair description of the chemical reactions in the silicon process. However, it will still have limited validity as a model of a real furnace. The main objections to the model can be summarized:

1. The simplified point description of the inner reaction zone gives an unsatisfactory reflection of the furnace conditions, especially the interface-zone between the inner zone and the charge segments.

2. The model only describes the metallurgical conditions and the interaction with the electrical environment is not taken into account. If the model should be applied on-line to a furnace, this leads to problems because the available measurements mainly describe electrical conditions.

3. The model is unidimensional, describing only vertical variations in the furnace, and homogeneous conditions are assumed across the horizontal cross section. This may be a too simplified approach.

4. There is large uncertainty in the choice of several important model parameters, such as the reaction rates of the different chemical reactions in the process.

5. The model has not been developed for on-line application purposes. Major adaptation are therefore necessary to extend the model with

descriptions of disturbance effects, and utilization of control inputs and measurement variables.

Furthermore, the present simulation model has an interface that is not usable in on-line application, which must be proper adopted.

Thus, an on-line implementation of the present model and the development of a state estimator based on this model seems to be impracticable, and presently, the implementation of the complete model-based control strategy is an unrealistic goal. However, if the model is proper adapted, it can become the core in a future model-based control strategy for ferrosilicon furnaces.

9.2 An alternative metallurgical control strategy

An alternative and more feasible metallurgical control strategy is to use the available measurements at the furnace, reflecting the metallurgical conditions, and in addition apply local estimators of inner process variables, as presented in Sections 8.4.1 and 8.4.2. Figure 9.2 shows the principle of this metallurgical control structure.

The controller operates on the available furnace measurements that reflect the metallurgical condition:

- The metal production rate.

  This variable can be calculated based on the amount of tapped metal per day. Regarding the use of the metal production, the presence of the inverse response, which was established in Section 8.3, yields limitations in the bandwidth of a controller operating on the metal production rate. Hence, a calculation of this variable based upon the daily production amount will most probable be sufficient, since the bandwidth limitations are in this range of frequencies.

- The silica fume flow leaving the furnace

- The electrode holder positions.

- The content of harmonics in the electrode voltages.

In addition the controller makes use of the following estimated process variables:

- Cavity variables such as the arc dimensions and temperatures, the cavity temperatures, and the resistances in various sections of the charge burden, found by the electrical model estimator.

- The furnace's carbon content found by the silica fume model estimator.

The controller uses the following metallurgical control input variables:

- The added carbon content.
- The electrical working point utilized as the choice of the Westly's power factor in the calculation of the set-point for the electrical control system.

The metallurgical controller interacts with a higher-level furnace optimizer, which may be the process metallurgists, manipulating the furnace parameters and the metallurgical set points, as previously discussed in Section 7.5.4.

This control strategy can be regarded as an extension of the conventional carbon controller, operating on the harmonics contents in the electrode voltages and the electrode holder positions, as described in Section 7.5.8.

9.3 Concluding remarks

In this chapter possible metallurgical control strategies have been discussed. A model-based control strategy based upon the dynamic model of the silicon process, is discussed. However, the present status of available model descriptions of a complete ferrosilicon furnace is unsatisfactory, and this is something that is negative to such a control strategy.

Therefore, an alternative control strategy is proposed based on the use of the available measurements and local estimators of inner process variables. This strategy is actually an extension of the present carbon controller, applied at several furnaces.

The conclusion is to recommend this strategy for metallurgical control. However, if the dynamic model of the silicon process is properly adapted, this model should be included in the control strategy.

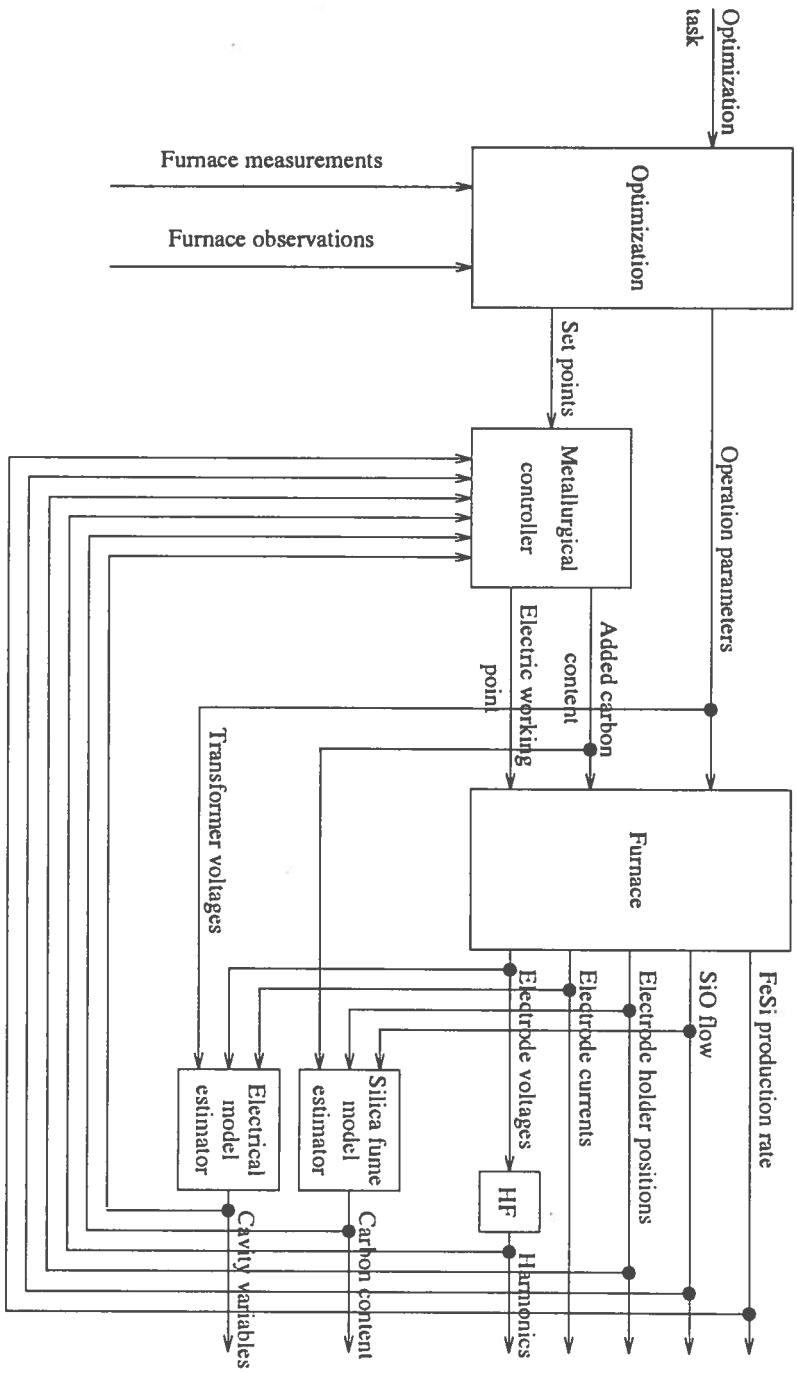

Figure 9.2: A proposed metallurgical control structure using furnace measurements and estimates of inner process variables.

References

Ahlers, H. and K. Timm (1987). Untersuchungen von frei brennenden Gleichstromlichtbögen bis 12 MW an Elektrostahlöfen. Teil 1: Experimentelle Ergebnisse. *Elektrowärme International, Vol 45, B5, October 1987*, B224-B235.

Ahlers, H. and K. Timm (1987). Untersuchungen von frei brennenden Gleichstromlichtbögen bis 12 MW an Elektrostahlöfen. Teil 2: Modellbildung. *Elektrowärme International, Vol 45, B6, December 1987*, B291-B302.

Ahlers, H. (1988). *Experimentelle und theoretische Untersuchungen von frei brennenden Gleichstromlichtbogen bis 12 MW an Elektrostahlöfen.* Dissertation, Fachbereich Maschinenbau der Universität der Bundeswehr Hamburg, Germany.

Balchen, J. G., and K. I. Mummé (1988). *Process Control: Structures and applications.* Van Nostrand Reinhold Company Inc., New York. Chap. 2.16, pp. 83-89. Groeneveld (1992).

Barker, I. J. (1980a). An Electrode Controller for Submerged Arc Furnaces. *3rd IFAC Symposium on Automation in Mining, Mineral and Metal Processing, Montreal.*

Barker, I. J. (1980b). Arching in the electrical circuit of a submerged-arc furnace. *Elektrowärme International, Vol 38, B1, February 1980*, B28-B32.

Barker, I. J., and A. B. Stewart (1980). Inductive reactance and the operation of large submerged-arc furnaces. *Journal of the South African Institute of Mining and Metallurgy, Vol. 80, No. 3, March 1980*, 123-128.

Barker, I. J. (1981). An Electrode Controller for Submerged Arc Furnaces. *National Institute for Metallurgy, Randsburg, South Africa, Report No. 2129.*

Barker, I. J., A. de Waal, M. S. Rennie and J. Klopper (1992). The interaction effect in submerged-arc furnaces. *Proc. 49th Electric Furnace Conference, Toronto, 1991, Iron and Steel Society, AIME, 1992.* pp. 305-310.

Bean, D. P. A. and M. S. Rennie (1985). The development and installation of a microcomputer-based data logger, and the analysis and evaluation of data. *Mintek, Measurement and Control Division, Randsburg, South Africa, Report No. M105D.*

Billings, S. A. (1975). *Modelling, Identification and Control of an Electric Arc Furnace.* PhD thesis, Sheffield University.

Billings, S. A., F. M. Boland and H. Nicholson (1979). Electric Arc Furnace Modelling and Control. *Automatica, Vol. 15, 1979*, 137-148.

Billings, S. A. (1981). Modelling and Identification of a Three-Phase Electric-Arc Furnace. *H. Nicholson (Ed.): Modelling of Dynamical Systems, Volume 2.* Institution of Electrical Engineers, London, pp. 63-80.

Bowman, B., G. R. Jordan and F. Fitzgerald (1969). The physics of high-current arcs. *Journal of the Iron and Steel Insitute, June 1969*, 798-805.

Bowman B. ang G. R. Jordan (1970). The magnetic stability of furnace arcs. *Preprints I.E.E. Conference-Gas Discharge, London, 1970*, 231-235.

Bowman, B. (1972). Convective heat transfer and power balance in high-current free-burning arcs. *Elektrowärme International, Vol 30, B2, April 1972*, B87-B93.

Bowman, B. (1976). Electrical characteristics of arc furnaces allowing for current swings. *6th Congress on Electroheat (UIE), Liege*, Section 1a, Paper no. 10.

Bowman, B. (1979). Distribution of current and self-induced stirring force in the bath of an arc furnace. *Elektrowärme International, Vol. 37, B6, December 1979*, B310-B315.

Bowman, B. (1982). Solution of arc-furnace electrical circuit in terms of arc voltage. *Iron and Steelmaking, Vol. 9, No. 4, 1979.*

Breton, E. (1980). The maze of ferrosilicon production. *37th Electric Furnace Conference Proceedings, 1979, Detroit*, Vol. 37, Iron and Steel Society, AIME, 1980.

Bretthauer, K., and K. Timm (1971). Über die Messung elektrischer Größen auf der Hochstromseite von Drehstromöfen. *Elektrowärme International, Vol 29, 7, 1971*, 381-387.

Bretthauer, K., A. A. Farschschi and K. Timm (1975). Die Messung elektrischer Größen von Lichtbögen in Elektrostahlöfen. *Elektrowärme International, Vol 33, B5, October 1975*, B221-B225.

Bretthauer, K., and A. A. Farschschi (1980). Ersatzschaltbild der Knapsackschaltung und Messung der Badspennung. *Elektrowärme International, Vol 38, B3, June 1980*, B132-B135.

Browne, T. E. (1950). The Electric Arc as a Circuit Element. *Journal of The Electrochemical Society, Vol. 102, No. 1, 1955*, 27-37.

Budde, A. Strauß and B. Schmidt (1976). Mathematische Modellierung elektrotermischer Prozesse (dargestellt am Calciumcarbidprozeß). Teil I: Modellierung von physikalisch-chemischen Teilprozessen in der Hauptreaktionszone. *Chem. Techn., Vol. 28, No. 10, October 1976*, 585-587.

Budde, A. Strauß and B. Schmidt (1978a). Mathematische Modellierung elektrotermischer Prozesse (dargestellt am Calciumcarbidprozeß). Teil II: Modellierung des elektriscen Strömungsfeldes in der Hauptreaktionszone. *Chem. Techn., Vol. 30, No. 6, June 1978*, 287-289.

Budde, A. Strauß and B. Schmidt (1978b). Mathematische Modellierung elektrotermischer Prozesse (dargestellt am Calciumcarbidprozeß). Teil III: Modellierung des Stoffänderungsvorgänge in der Hauptreaktionszone. *Chem. Techn., Vol. 30, No. 12, December 1978*, 617-620.

Budde, A. Strauß, M. Schreier and B. Schmidt (1979). Mathematische Modellierung elektrotermischer Prozesse (dargestellt am Calciumcarbidprozeß). Teil IV: Modellierung der elektrischen und physikalischen Teilprozesse in der Neutral- und Vorwärmzone. *Chem. Techn., Vol. 31, No. 10, October 1979*, 510-514.

Budde, A. Strauß, B. Schmidt and M. Schreier (1980). Mathematische Modellierung elektrotermischer Prozesse (dargestellt am

Calciumcarbidprozeß). Teil V: Modellierung eines Carbidreaktors in Rechteckbauweise (Reaktormodell). *Chem. Techn., Vol. 32, No. 4, April 1980*, 181-183.

Budde, K., M. Schreier, F. Schröter and W. Wintzer (1988). Modellierung von elektrotermischen Prozessen. *Chem. Techn., Vol. 40, No. 11, November, 1988*, 482-485.

Budde, K., M. Schreier and F. Schröter (1989a). Mathematisches Modell eines Siliciumreaktors. *Elektrowärme International, Vol 47, B6, December 1989*, B320-B325.

Budde, K., M. Schreier and F. Schröter (1989b). Mathematisches Modell eines Siliciumreduktionsofens. *34. Intern. Wiss. Koll., TH Ilmenau 1989.*

Bøckman, O. C. (1960). Crater Resistance of Submerged Arc Smelting Furnaces Simulated by a Simple Model. *Journal of the Electrochemical Society, Vol. 107, No. 8, August 1960.*

Bøckman, O. C. (1971) Arrangement for measuring the crater voltages in a three phase electric furnace with electrodes arranged in delta. *Norwegian patent no. 3919/71, October 22, 1971.*

Chang, C. W. and J. Szekely (1982). Plasma applications in metals processing. *Journal of Metals, February 1982*, 57-63.

Channon, W. P., R. C. Urquhart and D. D. Howat (1974) The mode of current transfer between electrode and slag in the submerged-arc furnace. *Journal of the South African Institute of Mining and Metallurgy*, Vol. 75, No. 1, August 1974, 4-7.

Curr, T. R. (1984). Energy transfer in the hearths of submerged-arc furnaces. *Mintek, Pyrometallurgy Division, Report No. M150.*

De Waal, A., I. J. Barker, M. S. Rennie, J. Klopper and B. S. Groeneveld (1992). Electrical factors affecting the economic optimization of submerged-arc furnaces. *INFACON 6. Proceedings of the 6th International Ferroalloys Congress, Cape Town*, Volume 1, SAIMM, Johannesburg, 1992, 247-252.

Dmochowski, Z. (1981). Hochstrommessungen bei Lichtbogenöfen. *Elektrowärme International, Vol 39, B5, October 1981*, B254-B261.

Downing, J. H., and L. Urban (1966). Electrical Conduction in Submerged Arc Furnaces. *Journal of Metals, Vol. 18, March 1966*, 337-344.

Downing, J. H. (1977). Mathematical model of an electric furnace producing ferroalloys. *World Electrotechnical Congress, Moscow*, Section 4a, Paper no. 16.

Downing, J. H., and F. W. Leavitt (1979). Mathematical model of an electric smelting furnace. *36th Electric Furnace Conference Proceedings, December 5-8 1978, Toronto*, Vol. 36, Iron and Steel Society, AIME, 209-217.

Downing, J. H., and F. W. Leavitt (1980). The mathematical model of a resistive electric smelting furnace. *INFACON '80*, Lausanne.

Dyason, G. J. and J. B. See (1978). *The movement of the burden in submerged-arc furnaces for the production of high-carbon ferromanganese.* Report No. 1967, National Institute for Metallurgy, Randsburg, South Africa.

Dyason, G. J. and J. B. See (1981). Burden movement in submerged-arc ferromanganese furnaces. *Metallurgical Transactions B, Vol. 12B, March 1981*, 149-160.

Edels, H. (1973). Properties of high pressure ultra high current arcs. *Proc. 11th Int. Conf. Phenomena in Ionized Gases, Vol. 2, 1973, Prague: Czeck. Acad. Sci.*, 9-59.

Ekrann, S. and T. Sira (1982). A model for solving the Maxwell quasi-stationary equations in a three phase electric reduction furnace. *Modeling, identification and control, Vol. 3, No. 4, 1982*, 231-242.

Grigat, R. R., and K. Timm (1990). Echtzeitmessung der Induktivitäten des Hochstromsystems und der LIchtbogenspannungen in Drehstrom-Lichtbogenöfen. *Elektrowärme International, Vol 48, B3, August 1990*, B115-BB124.

Gudmundsson, E. B. and T. Hanneson (1992). On-line measurements of silica dust. *INFACON 6. Proceedings of the 6th International Ferroalloys Congress, Cape Town*, Volume 1, SAIMM, Johannesburg, 1992, 201-204.

Halvorsen, S. A. (1988). Dynamic model of a metallurgical shaft reactor with irreversible kinetics and moving lower boundary. *Proc. 2nd European Symposium on Mathematics in Industry, March 1-7, 1987, Oberwolfach.* Teubner, Stuttgart, 211-223.

Halvorsen, S. A., J. H. Downing, and A. Schei (1989). Developing a unidimensional simulation model for producing silicon in an electric furnace. *4th European Conference on Mathematics in Industry, Strobl, Austria.*

Halvorsen, S. A., A. Schei and J. H. Downing, (1992). A unidimensional dynamic model for the (ferro)silicon process. *50th Electric Furnace Conference Proceedings, November 10-13 1992, Atlanta.*

Heiss, W. D. (1978). Mathematical model of an electric smelting furnace (I). *Elektrowärme International, Vol 36, B2, April 1978*, B111-B117.

Heiss, W. D. (1979). Mathematical model of an electric smelting furnace (II). *Elektrowärme International, Vol 37, B6, December 1979*, B304-B309.

Heiss, W. D. (1981). Fields, power density and effective resistance in the electrode and furnace of an electric smelter. *Elektrowärme International, Vol 39, B5, October 1981*, B243-B249.

Heiss, W. D. (1982). Modelling and simulation of electric smelting furnaces. *Ironmaking and Steelmaking, Vol. 9, No. 5, 1982.*

Holmelid, A., J. Westly and L. T. Kvassheim (1984). Electric Control of Ferrosilicon Submerged-Arc Furnaces. *Control '84, Mineral/Metallurgical Processing.* AIME.

Horoszko, E. (1982). Some critical remarks on the Knapsack connection system. *Elektrowärme International, Vol 40, B5, October 1982*, B252-B256.

Hoyaux M. F. (1968). *Arc physics.* Volume 8: Applied physics and engineering, Springer-Verlag, New York, 1968.

Höke W. and Kh. Bretthauer (1981). Die Schwankungen des Spannungsbedarfs des Hochstromlichtbogens in einem Lichtbogenofen infolge der Bogenbewegung. *Elektrowärme International, Vol 39, B5, October 1981*, B274-B282.

Hsu K. C., K. Etemadi and E. Pfender (1983). Study of the free-burning high-intensy argon arc. *Journal of Applied Physics, Vol. 54, No. 3, March 1983*, 1293-1301.

Innvær, R (1992). A status for the Soderberg smelting electrode. *Proceedings 12th International Congress on Electroheat (UIE), Electrotech92, Montreal*

Jie-min, Z., Z. Tian-cong and M. Chi (1990). Mathematical model and computer simulation of Soderberg electrodes in electric smelting furnace. *Elektrowärme International, Vol 48, B4, October 1990*, B210-B215.

Johansson, T. and G. Eriksson (1980). Technical Aspects on the Silicon Arc Furnace Process Based on Chemical and Thermal Equilibrium Computations. *Scandinavian Journal of Metallurgy, Vol. 9*, 283-291

Jones G. R. and M. T. C. Fang (1980). The physics of high-power arcs. *Rep. Prog. Phys., Vol. 43, 1980*, pp. 1415-1465.

Jordan G. R, B. Bowman and D. Wakelam (1970). Electrical and photographic measurements of high-power arcs. *J. Phys. D: Appl. Phys., Vol. 3, 1970*, 1089-1099.

Juuso, E. (1980). A computer analysis of temperature distribution and energy consumption in a submerged arc furnace used in the production of high-carbon ferrochromium. *Acta Universitas Ouluensis, Series C Technica No. 17, Technica Processionum., No. 3.*

Juuso, E. K. (1989a). Multilayer simulation of heat flow in a submerged-arc furnace used in the production of feroalloys. *Preprints of the 5th Symposium on Control of Distributed Parameter Systems, Perpignan, France, June 26-29 1989.*

Juuso, E. K. and P. Uronen (1989b). Hierarchical simulation of ferroalloy processes. *Preprints of the 6th Symposium on Automation in Mining, Mineral and Metal Processing, Buenos Aires, September 4-8 1989.*

Juuso, E. K. (1990). Multilayer simulation and expert systems in multilevel process control. *Preprints 11th IFAC World Congess, Tallinn, Estonia, August 13-17, 1990.*

Kaiser R. H. and J. H. Downing (1978). Heat Transfer Through the Hearth of an Electric Smelting Furnace and Its Impact on Operations. *35th Electric Furnace Conference Proceedings, December 6-9 1977. Chicago*, Vol. 35, Iron and Steel Society, AIME, 119-126.

Kalic, Dj., S. Bogdanovic and R Bulajic (1980). Measurements of electric quantities relevant to optimization the steel melting arc furnace operation. *9th International Congress on Electroheat (UIE), Cannes*

Kalic, Dj., S. Bogdanovic and R Bulajic (1982). Analysis of the three-phase non-linear electric circuit of the arc furnace for steel production. *Elektrowärme International, Vol 40, B1, February 1982*, B24-B29.

Kegel, K. (1979). Kraftwirkungen auf den Lichtbogen in einem Lichtbogenofen zum Stahlschmelzen. *Elektrowärme International, Vol 37, B6, December 1979*, B300-B304.

Keyser N. H. (1988). Heat Transfer Through the Hearth of an Electric Smelting Furnace and Its Impact on Operations. *45th Electric Furnace Conference Proceedings, December 8-11 1987, Chicago*, Vol. 45, Iron and Steel Society, AIME, 203-207.

Köhle, S. (1985). Lineares Ersatzschaltbild des Hochstromsystems von Drehstrom Lichtbogenöfen. *Elektrowärme International, Vol 43, B1, February 1985*, B16-B25.

Köhle, S. (1988). Linearisierte Modelle für die Kopplung der elektrischen Größen von Drehstrom-Lichtbogenöfen. *Elektrowärme International, Vol 46, B5, October 1988*, B264-B273.

Köhle, S. (1989). Adding to the equivalent circuit diagram of threephase a.c. arc furnaces with coupled ohmic load. *Elektrowärme International, Vol 47, B2, April 1989*, B88-B94.

Kurbiel, A. (1982). Matematisches Modell einer Lichtbogenanlage. *Elektrowärme International, Vol 40, B5, October 1982*, B240-B247.

Kurbiel, A. (1986). Einfluß verschiedener Eigenschaften der Elektrodenregelung auf den Betrief von Lichtbogenöfen. *Elektrowärme International, Vol 44, B6, December 1986*, B267-B271.

Latham D. J. (1980). A channel model for long arcs in air. *Phys. Fluids, Vol. 23, No. 8, August 1980*, 1710-1715.

Lowke, J. J. (1970). Characteristics of Radiation-Dominated Electric Arcs. *Journal of applied physics, Vol. 41, No. 6, May 1970*, 2588-2600.

Lowke, J. J. and H. C. Ludwig (1975). A simple model for high-current arc stabilized by forced convection. *Journal of Applied Physics, Vol. 46, No. 8, August 1975*, 3352-3360.

Maske K. U. (1984). The reduction of chromite in a transferred-arc plasma furnace. *Mintek, Pyrometallurgy Division, Report no. M178.*

McKelliget J. W. and J. Szekely (1983). A mathematical model of the cathode region of a high intensity carbon arc. *J. Phys. D: Appl. Phys., Vol. 16, 1983*, 1007-1022.

Mentel J. (1977). The influence of vaporization upon the roots of a high current arc. I. Different forms of vaporization in the arc roots. *Appl. Phys. 14 1977*, 269-276.

Mühlbauer, A. and J. Schäfer (1985). Modelluntersuchungen zum Leistungsumsetzung in Silizium-Reduktionsöfen. *4th Arc Furnace Meeting, Budapest, September 24-27, 1985.*

Müller, H. (1969). Überblick über elektrotermische Verfahren. *Chemie-Ing.-Techn., Vol. 41, No. 4, 1969*, 190-196..

Müller, M. B., S. E. Olsen and J. K. Tuset (1972). Heat and mass transfer in the ferrosilicon process. *Scandinavian Journal of Metallurgy, Vol. 1, 1972*, 145-155.

Nicholson, H., and R. Roebuck (1972). Simulation and Control of Electrode Position Controllers for Electric Arc Furnaces. *Automatica, Vol. 8, 1972*, 683-693.

Norden K. (1980). *Beitrag zur Modellbildung für den dynamischen Wechselstromlichtbogen im Elektrostahlöfen.* Dissertation, Fachbereich Maschinenbau der Hochschule der Bundeswehr Hamburg, Germany.

Ochs, T. L., A. D. Hartman and S. L. Witkowski (1986). Waveform Analysis of Electric Furnace Arcs as a Diagnostic Tool. *US Bureau of Mines, Report of Investigations No. 9029.*

Okamura, M., M. Watanabe, K. Usui and J. Kon (1972). UHP Arc Furnaces Electrodes-Effects of Arc and Esitimation of quality by Use of a Model Arc Furnace. *7th International Congress on Electroheat (UIE), 1972.*

Otani, Y., M. Saito, K. Usui and N. Chino (1968). The inner structure of the submerged arc furnace. *6th International Congress on Electroheat (UIE), Brighton*, paper no. 112.

Persson, J. A. (1979). Conduction characteristics of electric furnaces. *36th Electric Furnace Conference Proceedings, December 5-8 1978, Toronto*, Vol. 36, Iron and Steel Society, AIME, 111-117.

Persson, J. (1986). Silicon production - Looking back and ahead. *43th Electric Furnace Conference Proceedings, December 10-13 1985, Atlanta*, Vol. 43, Iron and Steel Society, AIME, 251-254.

Persson, J. A. (1990). Analyzing the electrical characteristics of arc furnaces. *47th Electric Furnace Conference Proceedings, October 29-November 1 1989, Orlando*, Vol. 47, Iron and Steel Society, AIME, 31-36.

Pfeifer, H., F. N. Fett and H. J. Bebber (1989). Model development for free burning A.C. plasma jets. *Elektrowärme International, Vol 47, B3, June 1989*, B124-B130.

Pfender E. (1978). Electric arcs and arc gas heaters. In *M. E. Hirsh and H. J. Oskam (Ed.): Gaseous electronics, Volume I: Electrical discharges*, Academic Press, New York, 1978. pp. 291-398.

Rennie, M. S. (1975a). The electrical-resistance characteristics of the charge in the electric reduction furnace. *National Institute for Metallurgy, Randsburg, South Africa, Report No. 1606.*

Rennie, M. S. (1975b). The electrical conductivity of the charge in a ferrosilicon furnace. *National Institute for Metallurgy, Randsburg, South Africa, Report No. 1622.*

Rennie, M. S. (1983). Arc monitoring on a 100 kVA experimental furnace. *Mintek, Measurement and Control Division, Report No. M83.*

Rennie, M. S. (1984). The operation, control, and design of submerged-arc ferro-alloy furnaces. *Proceedings of Mintek 50, International conference on mineral science and technology, March 26-30 1984, Sandton, South Africa*, Vol. 2, The Council for Mineral Technology, Randburg, South Africa.

Sakulin, M. (1980). Das Betriebverhalten des Lichtbogenöfens am Netz: Studien mit Hilfe eines digitalen Simulationmodelles. *9th International Congress on Electroheat (UIE). Cannes.*

Sakulin, M. (1981a). Zur Berechnung von Gleichstromlichtbogen. *Elektrowärme International, Vol 39, B2, April 1981*, B93-B98.

Sakulin, M. (1981b). A model for computer-aided simulation of electric arcs. *AMS 81 Conference, Lyon, Vol. 2*, 32-35.

Sakulin, M. (1982a). Rechnerische Bestimmung der Kennlinien von Gleichstromlichtbögen mit Hilfe von Kanalmodellen. *Elektrowärme International, Vol 40, B1, February 1982*, B18-B24.

Sakulin, M. (1982b). Ein Modell für den dynamischen Wechselstromlichtbogen und seine Anwendung zur Simulation von Lichtbogenöfen. *Fachberichte Hüttenpraxis Metallweiterverarbeitung, Vol. 20, No. 3, 1982.*

Sakulin, M. (1982c). Simulation of electric arcs in melting furnaces. *Electroheat for Metals, Cambridge, September 21-23 1983*, British National Committee for Electroheat, 1.4.1-1.4.22.

Sakulin, M. (1985). Betriefsverhalten von Drehstromlichtbogenöfen - Studie über den Einfluß stochastischer Bogenlängenänderungen. *4th Arc Furnace Meeting, Budapest, September 24-27 1985.*

Sanders, N., K. Etemadi, K. C. Hsu and E. Pfender (1982). Studies of the anode region of a high-intensity argon arc. *Journal of Applied Physics, Vol. 53, No. 6, June 1982*, 4136-4145.

Schäfer, J. (1985). *Über die Leistungsumsetzung im Reduktionsofen bei der Herstellung von Silicium.* Dr. Ing. Dissertation, Fakultät Maschinenwesen der Universität Hannover.

Schäfer, J. and A. Mühlbauer (1985). Energieumsetzung in Siliciumreduktionöfen. *Elektrowärme International, Vol 43, B5, October 1985*, B220-B224.

Schei, A., and K. Larsen (1979). *Inside the ferrosilicon furnace.* 16 mm film, produced by Elkem-Spigerverket a/s, 1979.

Schei, A., and K. Larsen (1982). A stoichiometric model of the ferrosilicon process. *39th Electric Furnace Conference Proceedings, December 8-11 1981, Houston*, Vol. 39, Iron and Steel Society, AIME, 301-309.

Schei, A., and S. A. Halvorsen (1991). A stoichiometric model of the silicon process. *Proc. Ketil Motzfeldt Symposium, The Norwegian Institute of Technology, May 24, 1991, Trondheim, Norway.*

Schwartz, B. (1988). *Regelung elektrischer Größen an Drehstrom-Licht bogenöfen.* Dr. Ing. Dissertion, Fachbereich Maschinenbau, Universität der Bundeswehr, Hamburg.

Schwartz, B., and K. Timm (1989). Regelung elektrischer Größen an Drehstrom-Lichtbogenöfen. *Elektrowärme International, Vol 47, B1, February 1989*, B12-B22.

Skreien, N. (1975). Method for determining operating conditions in electrical furnaces. *U.S. patent no. 3,909,242, September 30, 1975.*

Sochacky, M. R. and R. Gaillot (1984). The microprocessor arc regulator - The regulator of the '80's. *41st Electric Furnace Conference Proceedings, December 6-9 1983, Detroit*, Vol. 41, Iron and Steel Society, AIME, 215-220.

Sommer, G. (1979). The cancer project: A summary of the computer-aided operation of a 48 MVA ferrochromium furnace. *National Institute for Metallurgy, Randsburg, South Africa, Report No. 2032, November 28th 1979.*

Stanek, J. (1977) *Electric melting of glass.* Elsevier Scientific Publishing Company, Amsterdam.

Stewart, A. B. (1980). *An Analysis of the Electrical Circuit of Submerged-Arc Furnaces.* PhD thesis, University of Cape Town, South Africa.

Stewart, A. B., I. J. Barker (1981). A solution to measurement problems and interaction effects in the control of submerged-arc furnaces. *2nd INFACON Congress, Lausanne, 1980.*

Stewart, A. B., G. Sommer (1981). The measurements of electrical variables in a submerged-arc furnace. *National Institute for Metallurgy, Randsburg, South Africa, Report No. 2093, April 15th 1981.*

Szekely, J. and J. McKelliget (1981). A mathematical model of heat and fluid flow phenomena in the electric arc furnace. *3rd Arc Furnace Meeting, September 2-4 1981, Miskolc, Hungary.*

Szekely, J. and N. J. Themelis (1970) *Rate phenomena in process metallurgy.* John Wiley & Sons. Inc., New York.

Szekely, J. and J. McKelliget (1984). A mathematical model of electric furnace operations and its use for control and process optimization. *Control '84, Mineral/Metallurgical Processing.* AIME.

Urquhart, R. C., P. R. Jochens and D. D. Howat (1974). The dissipation of electrical power in the burden of a submerged arc furnace. *31st Electric Furnace Conference Proceedings, December 5-7 1973, Cincinatti*, Iron and Steel Society, AIME, 73-78.

Urquhart, R. C. (1978). The role of the coke bed in electric furnace production of ferroalloys. *35th Electric Furnace Conference Proceedings, December 6-9 1977, Chicago*, Vol. 35, Iron and Steel Society, AIME, 19-20.

Ushio, M., J. Szekely and C. W. Chang (1981). Mathematical modelling of flow field and heat transfer in high-current arc discharge. *Ironmaking and Steelmaking, No. 6 1981*, 279-286.

Valderhaug, Aa., and P. Sletfjerding (1992). A non-interacting electrode current controller for submerged-arc furnaces. *Proc. 49th Electric Furnace Conference, Toronto, 1991, Iron and Steel Society, AIME, 1992.* pp. 311-320.

Valderhaug, Aa., J. G. Balchen and S. A. Halvorsen (1992). Modelbased control of the ferrosilicon process. *3rd IFAC Symposium on Dynamics and Control of Chemical Reactors, Distillation Columns and Batch Processes (DYCORD +'92), April 26-29 1992, College Park, Maryland.*

Valderhaug, Aa., and J. G. Balchen (1993). Estimation of inner process conditions in submerged-arc furnaces by electric arc modelling. *Submitted to Measurement and Control Applied to Mining, Minerals and Metal Processing, 12th IFAC World Congress, July 19-23 1993, Sydney.*

Veillette P. and D. Simard (1985). Electric arc characteristics using high speed cinematography and spectroscopy. *42nd Electric Furnace Conference Proceedings, December 9-12 1975, Houston*, Vol. 42, Iron and Steel Society, AIME, 173-182.

Waalmann, J. G. (1988). Estimating the condition of the heat resistant lining in an electric reduction furnace. *Modeling, identification and control, Vol. 9, No. 1, January 1988*, 47-56.

Wasbø, S. O. (1991). Modelling of silica fume production in ferrosilicon furnaces. Siv. ing. thesis (in Norwegian). Department of Engineering Cybernetics, The Norwegian Institute of Technology, Trondheim, Norway, 1991.

Westly, J. (1974). Resistance and heat distribution in a submerged-arc furnace. *INFACON '74, Johannesburg.*

Westly, J. (1976). Critical Parameters in Design and Operation of Submerged Arc Furnaces. *33rd Electric Furnace Conference Proceedings, December 9-12 1975, Houston*, Vol. 33, Iron and Steel Society, AIME, 47-53.

Wintzer, W. (1988). *Experimentelle Untersuchung und Mathematische Modellierung des Calciumcarbid-Prozesses.* Doktor Ingenieur Disser-

tation, Technischen Hochschule "Carl Schmorlemmer" Leuna-Merseburg.

Zherdev, I., I. Ploykov, D. Moscovtsev and E. Yaskov (1968). Methods and results of investigation into the operation of submerged arc ferrosilicon furnaces. *6th International Congress on Electroheat (UIE), Brighton*, paper no. 113.

Appendix A

Electric arc modelling

Electric arc model derivations are treated in this appendix. At first, a model of the flow phenomena in the cathode region of an electric arc, is described. Then, an analytic model of a DC arc is described.

A.1 Modelling of induced cathode flow phenomena

The induced flow phenomena in the cathode region can be described by the momentum and continuity equations for a high-intensity arc column (Pfender, 1978; Sanders and colleagues, 1982; Ahlers, 1988). The derivation of the flow description will be significantly simplified if homogeneous conditions are assumed in the arc regions. In the following the derivation of Ahlers (1988) is described.

Figure A.1 shows schematically the induced flow phenomena in the cathode region of a free-burning arc, described by the three arc root regions:

1. The pumping region.
2. The inflow region.
3. The contraction region.

in addition to the arc column. The derivation is based upon a power balance of the gas flow in the different arc regions as illustrated in Fig. A.1. It is further based on the following assumptions:

1. A homogeneous constant current density j_C is assumed at the cathode spot. Thus, the cathode spot radius can be expressed by:

$$r_C = \sqrt{\frac{I_a}{\pi\, j_C}} \tag{A.1}$$

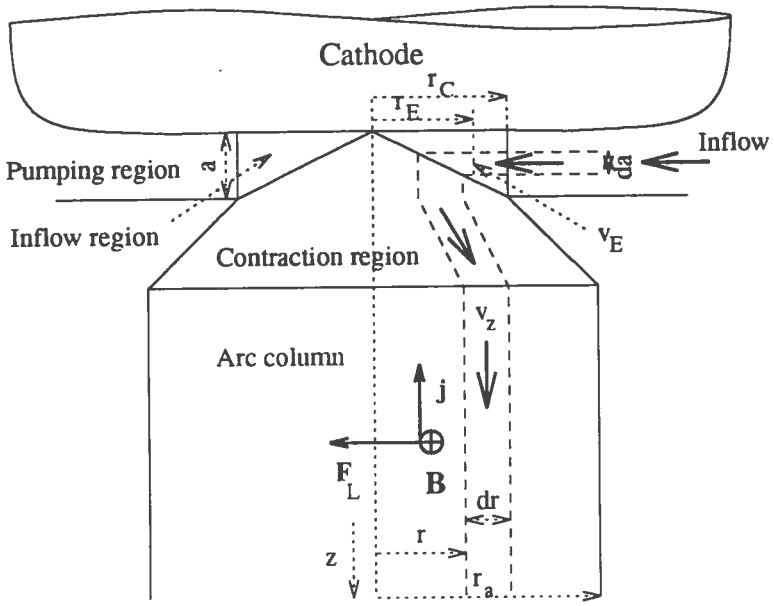

Figure A.1: Schematic illustration of induced plasma flow in the cathode region.

2. A constant mass density ρ_a is assumed in the different arc regions.

3. The plasma flow is assumed to be radial in the inflow region v_E, while it is assumed to be parallel to the current density vector in the contraction region and the arc column v_z.

4. The current density is assumed to be constant in the arc column:

$$j_z = \frac{I_a}{\pi r_a^2} \tag{A.2}$$

Mechanical power input

The mechanical power input to the gas flow is given as:

$$P_{in,m} = \int_V \boldsymbol{F}_L \, \boldsymbol{v} \, dV \tag{A.3}$$

where $\boldsymbol{F}_L$ is the Lorentz force, dV represents a volume-element, V the total volume, and $\boldsymbol{v}$ the plasma flow. This power input will only be effective in the inflow region.

The equation of continuity applied on the regions:

$$dA \, v_z(r) = dA_E \, v_E(r_E) \tag{A.4}$$

where:

$$dA = 2\pi\, r\, dr \tag{A.5}$$

$$dA_E = 2\pi\, r_E\, da \tag{A.6}$$

yields:

$$v_E(r_E = v_z(r)\, r\, dA\, v_z(r)\, \frac{1}{da}\, \frac{1}{r_E} \tag{A.7}$$

And the volume element of interest can be expressed by:

$$dV_E = 2\pi\, r_E\, dr_E\, da \tag{A.8}$$

The azimuthal magnetic field density in the inflow region is given by:

$$B_\theta(r_E) = \frac{\mu_0}{r_E} \int_0^{r_E} j_C(\xi)\, \xi\, d\xi = \frac{\mu_0}{2}\, j_C\, r_E \tag{A.9}$$

where B_θ is the azimuthal magnetic field and μ_0 is the magnetic permeability of vacuum. The mechanical power input then becomes:

$$\begin{aligned} dP_{m,in} &= \int_{r_E = r\frac{r_C}{r_a}}^{r_a} j_C \left(\frac{\mu_0}{2} j_C r_E\right) (2\pi\, r_E\, dr_E\, da)\, 2\pi\, r_E\, dr_E \\ &= \frac{\mu_0}{2}\, \pi\, {j_c}^2\, v_z(r)\, r\, dr\, {r_C}^2 \left(1 - \left(\frac{r}{r_a}\right)^2\right) \end{aligned} \tag{A.10}$$

The power input in the inflow region is used to increase the kinetic energy and the arc pressure:

$$dP_{m,in} = dP_{kin} + dP_p \tag{A.11}$$

Increase in kinetic energy

The increase in kinetic energy can be expressed as:

$$dP_{kin} = \frac{1}{2}\, v_z(r)^2\, d\dot{m} \tag{A.12}$$

where $\dot{m}$ represents the arc mass flow:

$$d\dot{m} = \rho_a\, 2\pi\, r\, dr\, v_z(r) \tag{A.13}$$

This yields:

$$dP_{kin} = \pi \rho_a\, r\, dr\, v_z(r)^3 \tag{A.14}$$

Pressure work

The power dissipation due to pressure work is:

$$dP_p = \Delta p(r)\, 2\pi\, r\, dr\, v_z(r) \tag{A.15}$$

The pressure increase $\Delta p(r)$ can be derived from:

$$\Delta p(r) = \int_r^{r_a} j_z\, B_\theta(\xi)\, d\xi \tag{A.16}$$

where the azimuthal magnetic field density is:

$$B_\theta(r) = \frac{\mu_0}{2}\, j_z\, r \tag{A.17}$$

The pressure increase then becomes:

$$\Delta p(r) = \frac{\mu_0}{4}\, {j_z}^2\, {r_a}^2 \left(1 - \left(\frac{r}{r_a}\right)^2\right) \tag{A.18}$$

and the power dissipation due to pressure work can be derived as:

$$dP_p = \frac{\mu_0}{2}\, \pi\, {j_c}^2 \left(\frac{r_C}{r_a}\right)^2 \left(1 - \left(\frac{r}{r_a}\right)^2\right) {r_C}^2\, r\, dr\, v_z(r) \tag{A.19}$$

where the current density in the arc column is expressed in terms of the cathode spot current density:

$$j_z = \left(\frac{r_C}{r_a}\right)^2 j_C \tag{A.20}$$

Plasma flow description

An expression of the radial distribution of the axial plasma flow can be found be inserting Eqs. A.10, A.14 and A.19, into Eq. A.11:

$$v_z(r) = \sqrt{\frac{\mu_0}{2\,\rho_a}}\, r_C\, j_C \sqrt{1 - \left(\frac{r_C}{r_a}\right)^2} \sqrt{1 - \left(\frac{r}{r_a}\right)^2} \tag{A.21}$$

The velocity has its maximum v_{max} at the arc axis:

$$v_{max} = v_z(r = 0) = \sqrt{\frac{\mu_0}{2\,\rho_a}}\, r_C\, j_C \sqrt{1 - \left(\frac{r_C}{r_a}\right)^2} \tag{A.22}$$

and the velocity distribution can be expressed as:

$$v_z(r) = v_{max} \sqrt{1 - \left(\frac{r}{r_a}\right)^2} \tag{A.23}$$

A.2 Analytic model of DC arc columns

A large number of analytic models of free-burning DC arc columns have been presented in the recent years, among others by Edels (1973), Pfender (1978), Jones and Fang (1980), Szekely and McKelliget (1981), Ushio, Szekely and Chang (1982), Sanders and colleagues (1982), McKelliget and Szekely (1983), Hsu, Etemadi and Pfender (1983) and Ahlers (1988). The model descriptions generally consist of the following equations:

1. Equations describing equilibrium thermodynamics.
2. Conservation equations for mass, motion and energy of the plasma fluid, modified to include effects of the Lorentz force, radiation transport and Joule power input.
3. Maxwell's equations.
4. The generalized Ohm's law for partly ionized gases.
5. The radiation energy transport equations.

The various models are based on slightly different assumptions. The model described below is based mainly on the work of Ushio, Szekely and Chang (1982), Sanders and colleagues (1982), McKelliget and Szekely (1983) and Hsu, Etemadi and Pfender (1983), and with the following assumptions:

1. The plasma is in LTE. As discussed earlier, high-power arcs have high electron density ensuring that all particle species attain a common temperature, and LTE is a valid assumption. According to Jones and Fang (1980) the plasma can therefore be treated as a single fluid and its thermodynamics and transport properties can uniquely be described by two thermodynamic properties, like temperature and pressure.
2. The arc plasma is electrically neutral.
3. The arc plasma is optically thin. The assumption of an optically thin arc plasma is reasonable since the re-absorption of radiation compared to the total radiative loss over all wavelengths is insignificant (Hsu, Etemadi and Pfender, 1983; Sanders and colleagues, 1982). The radiation transfer is neglected within the arc plasma, and only radiative losses from the arc plasma to the surroundings are taken into account.
4. The arc column is steady and rationally symmetric and the resulting equations are two-dimensional.

5. The flow is driven from only electromagnetic forces.
6. Gravity effects are neglected.
7. Assumption of the nature of the flow, laminar or turbulent flow. In the model described below, laminar flow is assumed.
8. Heat dissipation due to viscosity effects and thermal diffusion are negligible.
9. Assumption of the specific heat, density and viscosity of the plasma.
10. The spatial distribution of the current is known and thus the electromagnetic forces can be calculated from the Maxwell equations.

The steady-state model equations for a free-burning DC arc column expressed in cylindrical coordinates (r, z, θ) and based on the stated assumptions, are:

Mass conservation

$$\nabla \cdot (\rho \boldsymbol{v}) = 0 \tag{A.24}$$

$$\Downarrow$$

$$\frac{\partial}{\partial z}(\rho v_z) + \frac{1}{r}\frac{\partial}{\partial r}(\rho r v_r) = 0 \tag{A.25}$$

where ρ is the mass density, and v_z and v_r are the axial (z) and radial (r) velocity components, respectively.

The equations of motion (Navier-Stoke equations)

$$\rho(\boldsymbol{v} \cdot \nabla)\boldsymbol{v} = \nabla p - \nabla \boldsymbol{\tau} + \boldsymbol{F}_L \tag{A.26}$$

where p is the pressure, $\boldsymbol{\tau}$ is the stress tensor including laminar and turbulent stresses, and $\boldsymbol{F}_L$ is the body force vector representing the electromagnetic force field:

$$\boldsymbol{F}_L = \boldsymbol{j} \times \boldsymbol{B} \tag{A.27}$$

Assuming laminar flow (Sanders and colleagues, 1982; Hsu, Etemadi and Pfender, 1983; Ahlers, 1988), the flow velocity components can be described by:

$$\begin{aligned}\frac{\partial}{\partial z}\left(\rho v_z^2\right) + \frac{1}{r}\frac{\partial}{\partial r}(\rho r v_z v_r) &= -\frac{\partial p}{\partial z} + 2\frac{\partial}{\partial z}\left(\mu \frac{\partial v_z}{\partial z}\right) \\ &+ \frac{1}{r}\frac{\partial}{\partial r}\left(\mu r \frac{\partial v_z}{\partial r}\right) + \frac{1}{r}\frac{\partial}{\partial r}\left(\mu r \frac{\partial v_r}{\partial z}\right) + j_r B_\theta\end{aligned} \tag{A.28}$$

$$\frac{\partial}{\partial z}(\rho\, v_z\, v_r) + \frac{1}{r}\frac{\partial}{\partial r}\left(\rho\, r\, v_r^2\right) = -\frac{\partial p}{\partial r} + \frac{\partial}{\partial z}\left(\mu\,\frac{\partial v_r}{\partial z}\right) + \frac{\partial}{\partial z}\left(\mu\,\frac{\partial v_z}{\partial r}\right) + \frac{2}{r}\frac{\partial}{\partial r}\left(\mu\, r\,\frac{\partial v_r}{\partial r}\right) - \frac{2\,\mu\, v_r}{r^2} - j_z B_\theta \quad \text{(A.29)}$$

where p is the pressure, μ is the viscosity, j_r and j_z are the radial and axial current density, and B_θ is the self-induced magnetic field.

The case of turbulent flow is treated among others by Ushio, Szekely and Chang (1981), Szekely and McKelliget (1981) and McKelliget and Szekely (1983). The turbulent nature of the flow can be described by using an effective viscosity μ_{eff} in the Navier-Stoke equations:

$$\mu_{eff} = \mu + \mu_T \quad \text{(A.30)}$$

where μ_T is the turbulent viscosity calculated from a model describing the turbulent kinetic energy and the turbulent dissipation.

Energy conservation

$$\rho(\boldsymbol{v}\cdot\nabla H) = \nabla\cdot\lambda\,\nabla T + \frac{j^2}{\sigma} + \frac{5}{2}\frac{k_B}{e}\,\boldsymbol{j}\cdot\nabla T - P_R \quad \text{(A.31)}$$

where H is enthalpy, λ thermal conductivity, T temperature, j current density, σ electrical conductivity, k_B Boltzmann constant, e elementary electron charge, and P_R radiative losses per unit volume. Laminar flow is assumed, and thus the effect of turbulent kinetic energy and dissipation of turbulent energy are neglected. It is further assumed that the plasma can be treated as a perfect gas:

$$H(T) = c_p\, T + H_0(T_0) \quad \text{(A.32)}$$

and

$$p = \sum_l N_l\, k_B\, T \quad \text{(A.33)}$$

where c_p is the specific heat at constant pressure, k_B is the Boltzmann constant, N_l is the particle densities of electrons, ions and neutrals, and l is the number of particle species. The energy balance of the arc column and thus the temperature, can be described by:

$$\frac{\partial}{\partial z}(\rho\, v_z\, c_p\, T) + \frac{1}{r}\frac{\partial}{\partial r}(\rho\, r\, v_r\, c_p\, T) = \frac{\partial}{\partial z}\left(\lambda\,\frac{\partial T}{\partial z}\right) + \frac{1}{r}\frac{\partial}{\partial r}\left(\lambda\, r\,\frac{\partial T}{\partial r}\right) + \left(\frac{j_z^2 + j_r^2}{\sigma}\right) + \left(\frac{5}{2}\frac{k_B}{e}\right)\cdot\left(j_z\,\frac{\partial T}{\partial z} + j_r\,\frac{\partial T}{\partial r}\right) - P_R \quad \text{(A.34)}$$

The energy conservation equation contains:

1. On the left-hand side: Two convection terms.
2. From left to right on the right-hand side:
   (a) Two conduction terms.
   (b) A Joule heating term.
   (c) A term representing the transport of electron enthalpy due to the drift of the electrons.
   (d) A radiation term.

Current conservation

$$\nabla \cdot \boldsymbol{j} = 0 \tag{A.35}$$

$$\Downarrow$$

$$\frac{\partial j_x}{\partial z} + \frac{1}{r}\frac{\partial}{\partial r}(r j_r) = 0 \tag{A.36}$$

or equivalently:

$$\boldsymbol{j} = -\sigma \nabla \Phi = \sigma \boldsymbol{E} \tag{A.37}$$

$$\nabla \cdot (\sigma \nabla \Phi) = 0 \tag{A.38}$$

$$\Downarrow$$

$$\frac{\partial}{\partial z}\left(\sigma \frac{\partial \Phi}{\partial z}\right) + \frac{1}{r}\frac{\partial}{\partial r}\left(\sigma r \frac{\partial \Phi}{\partial r}\right) = 0 \tag{A.39}$$

or expressed in terms of the electric field strength:

$$\frac{\partial}{\partial z}(\sigma E_z) + \frac{1}{r}\frac{\partial}{\partial r}(\sigma\, r\, E_r) = 0 \tag{A.40}$$

where σ is the electrical conductivity, Φ is the electrical potential, and E_z and E_r are the axial and radial electric field strength components.

Magnetic field

$$\boldsymbol{j} = \frac{1}{\mu_0} \nabla \times \boldsymbol{B} \tag{A.41}$$

$$\Downarrow$$

$$B_\theta(r) = \frac{\mu_0}{r} \int_0^r \xi\, j_z(\xi) d\xi \tag{A.42}$$

where B_θ is the azimuthal magnetic field and μ_0 is the magnetic permeability of vacuum. This expression can be evaluated from the Maxwell equations.

The solution of the model equations for the entire free-burning arc, excluding only the cathode and anode fall region, is in principle possible. This set of equations represents a highly nonlinear system of coupled differential equations which must be solved simultaneously, in order to obtain the field variables v_r, v_z, T, j_r and j_z as functions of r and z, and an iterative solution procedure is usually applied.

To solve the conservations equations the temperature dependence of thermodynamic and transport properties must be known, including density, constant-pressure specific heat, viscosity, electrical and thermal conductivity and optically thin radiation losses. These properties are strongly temperature dependent and can be difficult to obtain from literature for the atmospheres present in electric furnaces. In addition, proper boundary conditions must be stated. The boundary conditions for a model the arc column are based on symmetry considerations and will stipulate (Ushio, Szekely and Chang, 1983):

1. The velocity field near the cathode.
2. Current density distribution at the end of the cathode region.
3. Temperature distribution at the end of the cathode region.
4. The temperature at the anode.
5. The distribution of velocity, temperature and current along the arc axis.

According to Hsu, Etemadi and Pfender (1983), the current density distribution around the cathode is the most critical boundary condition for the model.

Appendix B

Interaction analysis derivations

B.1 A current-resistance model

An expression showing the relation between electrode currents and resistance variations can be developed from the current model in Eq. 4.66. Inserting the expressions of the phase impedances Z_i in Eq. 4.62, into Eq. 4.66, evaluating the square value of the electrode current magnitudes, and rearranging, yields:

$$
\begin{aligned}
|I_{e1}|^2 &= \frac{|V_T|^2}{Z_{sum}} \Big\{ {R_2}^2 + R_2 R_3 + {R_3}^2 + {X_2}^2 \\
&\quad + X_2 X_3 + {X_3}^2 - \sqrt{3} R_2 X_3 + \sqrt{3} R_3 X_2 \Big\} \\
|I_{e2}|^2 &= \frac{|V_T|^2}{Z_{sum}} \Big\{ {R_1}^2 + R_1 R_3 + {R_3}^2 + {X_1}^2 \\
&\quad + X_1 X_3 + {X_3}^2 + \sqrt{3} R_1 X_3 - \sqrt{3} R_3 X_1 \Big\} \\
|I_{e3}|^2 &= \frac{|V_T|^2}{Z_{sum}} \Big\{ {R_1}^2 + R_1 R_2 + {R_2}^2 + {X_1}^2 \\
&\quad + X_1 X_2 + {X_2}^2 - \sqrt{3} R_1 X_2 + \sqrt{3} R_2 X_1 \Big\}
\end{aligned}
\tag{B.1}
$$

where:

$$
\begin{aligned}
Z_{sum} &= \left(\sum_{k,l=1}^{3} R_k R_l - X_k X_l \right)^2 + \left(\sum_{k,l=1}^{3} R_k X_l \right)^2 \quad k \neq l \\
&= (R_1 R_2 + R_2 R_3 + R_3 R_1 - X_1 X_2 - X_2 X_3 - X_3 X_1)^2 \\
&\quad + (R_1 X_2 + R_1 X_3 + R_2 X_1 + R_2 X_3 + R_3 X_1 + R_3 X_2)^2
\end{aligned}
\tag{B.2}
$$

Linearizing the model in Eq. B.1 using a first order Taylor series expansion around the electrical working-point, denoted by the superscript ^{0}:

$$|I_{ei}| = \left|I_{ei}^0\right| + \Delta i_{ei} \tag{B.3}$$

$$R_i = R_i^0 + \Delta r_i \tag{B.4}$$

and assuming constant reactances and no interaction between the arc resistances. This gives the following model of electrode current deviations Δi_{ei} in terms of resistance variations Δr_i:

$$\begin{aligned}
\Delta i_{e1} &= \frac{|V_T|^2}{{Z_{sum}^0}^2}\left\{\frac{\alpha_{11}}{|I_{e1}^0|}\Delta r_1 + \frac{\alpha_{12}}{|I_{e1}^0|}\Delta r_2 + \frac{\alpha_{13}}{|I_{e1}^0|}\Delta r_3\right\} \\
\Delta i_{e2} &= \frac{|V_T|^2}{{Z_{sum}^0}^2}\left\{\frac{\alpha_{21}}{|I_{e2}^0|}\Delta r_1 + \frac{\alpha_{22}}{|I_{e2}^0|}\Delta r_2 + \frac{\alpha_{23}}{|I_{e2}^0|}\Delta r_3\right\} \\
\Delta i_{e3} &= \frac{|V_T|^2}{{Z_{sum}^0}^2}\left\{\frac{\alpha_{31}}{|I_{e3}^0|}\Delta r_1 + \frac{\alpha_{32}}{|I_{e3}^0|}\Delta r_2 + \frac{\alpha_{33}}{|I_{e3}^0|}\Delta r_3\right\}
\end{aligned} \tag{B.5}$$

The matrix elements α_{ij} are:

$$\begin{aligned}
\alpha_{11} &= -\Big(R_2^{0\,2} + R_2^0 R_3^0 + R_3^{0\,2} + X_2^{0\,2} + X_2^0 X_3^0 + X_3^{0\,2} \\
&\quad - \sqrt{3}R_2^0 X_3^0 + \sqrt{3}R_3^0 X_2^0\Big) Z_{\Pi 1}^0 \\
\alpha_{12} &= \frac{1}{2}\left(2R_2^0 + R_3^0 - \sqrt{3}X_3^0\right) Z_{sum}^0 - \Big(R_2^{0\,2} + R_2^0 R_3^0 + R_3^{0\,2} \\
&\quad + X_2^{0\,2} + X_2^0 X_3^0 + X_3^{0\,2} - \sqrt{3}R_2^0 X_3^0 + \sqrt{3}R_3^0 X_2^0\Big) Z_{\Pi 2}^0 \\
\alpha_{13} &= \frac{1}{2}\left(2R_3^0 + R_2^0 + \sqrt{3}X_2^0\right) Z_{sum}^0 - \Big(R_2^{0\,2} + R_2^0 R_3^0 + R_3^{0\,2} \\
&\quad + X_2^{0\,2} + X_2^0 X_3^0 + X_3^{0\,2} - \sqrt{3}R_2^0 X_3^0 + \sqrt{3}R_3^0 X_2^0\Big) Z_{\Pi 3}^0 \\
\alpha_{21} &= \frac{1}{2}\left(2R_1^0 + R_3^0 + \sqrt{3}X_3^0\right) Z_{sum}^0 - \Big(R_1^{0\,2} + R_1^0 R_3^0 + R_3^{0\,2} \\
&\quad + X_1^{0\,2} + X_1^0 X_3^0 + X_3^{0\,2} + \sqrt{3}R_1^0 X_3^0 - \sqrt{3}R_3^0 X_1^0\Big) Z_{\Pi 2}^0 \\
\alpha_{22} &= -\Big(R_1^{0\,2} + R_1^0 R_3^0 + R_3^{0\,2} + X_1^{0\,2} + X_1^0 X_3^0 + X_3^{0\,2} \\
&\quad + \sqrt{3}R_1^0 X_3^0 - \sqrt{3}R_3^0 X_1^0\Big) Z_{\Pi 2}^0 \\
\alpha_{23} &= \frac{1}{2}\left(2R_3^0 + R_1^0 - \sqrt{3}X_1^0\right) Z_{sum}^0 - \Big(R_1^{0\,2} + R_1^0 R_3^0 + R_3^{0\,2} \\
&\quad + X_1^{0\,2} + X_1^0 X_3^0 + X_3^{0\,2} + \sqrt{3}R_1^0 X_3^0 - \sqrt{3}R_3^0 X_1^0\Big) Z_{\Pi 2}^0
\end{aligned} \tag{B.6}$$

$$\alpha_{31} = \frac{1}{2}\left(2R_1^0 + R_2^0 - \sqrt{3}X_2^0\right) Z_{sum}^0 - \left(R_1^{0\,2} + R_1^0 R_2^0 + R_2^{0\,2} + X_1^{0\,2} + X_1^0 X_2^0 + X_2^{0\,2} - \sqrt{3}R_1^0 X_2^0 + \sqrt{3}R_2^0 X_1^0\right) Z_{\Pi 1}^0$$

$$\alpha_{32} = \frac{1}{2}\left(2R_2^0 + R_1^0 + \sqrt{3}X_1^0\right) Z_{sum}^0 - \left(R_1^{0\,2} + R_1^0 R_2^0 + R_2^{0\,2} + X_1^{0\,2} + X_1^0 X_2^0 + X_2^{0\,2} - \sqrt{3}R_1^0 X_2^0 + \sqrt{3}R_2^0 X_1^0\right) Z_{\Pi 2}^0$$

$$\alpha_{33} = -\left(R_1^{0\,2} + R_1^0 R_2^0 + R_2^{0\,2} + X_1^{0\,2} + X_1^0 X_2^0 + X_2^{0\,2} - \sqrt{3}R_1^0 X_2^0 + \sqrt{3}R_2^0 X_1^0\right) Z_{\Pi 3}^0$$

where:

$$Z_{\Pi 1}^0 = (R_2^0 + R_3^0) \sum_{k,l=1}^{3} (R_k^0 R_l^0 - X_k^0 X_l^0) + (X_2^0 + X_3^0) \sum_{k,l=1}^{3} (R_k^0 X_l^0) \ , \quad k \neq l$$

$$Z_{\Pi 2}^0 = (R_1^0 + R_3^0) \sum_{k,l=1}^{3} (R_k^0 R_l^0 - X_k^0 X_l^0) + (X_1^0 + X_3^0) \sum_{k,l=1}^{3} (R_k^0 X_l^0) \ , \quad k \neq l$$

$$Z_{\Pi 3}^0 = (R_1^0 + R_2^0) \sum_{k,l=1}^{3} (R_k^0 R_l^0 - X_k^0 X_l^0) + (X_1^0 + X_2^0) \sum_{k,l=1}^{3} (R_k^0 X_l^0) \ , \quad k \neq l$$

B.2 A resistance-electrode displacement model

A model of the effect of electrode movements on the resistances is evaluated below. The evaluation is based on Billings (1981) and adapted to the current paths in submerged-arc furnaces.

Arc voltages and measured phase resistances

The arc voltages V_{ai}, can be related to the arc lengths h_{ai}, by using the steady-state Nottingham model:

$$V_{ai} = V_{ACi} + E_{ai}h_{ai} = V_{ACi} + k_{ai}h_{ai} \tag{B.7}$$

where $E_{ai} = k_{ai}$ is the electric field strength (the voltage coefficient) of the arc, and V_{ACi} is the sum of the anode and cathode voltage drops.

In a submerged-arc furnace the electrode resistances will be affected by electrode movements. In the following the electrode resistances are computationally divided in two:

1. The resistances of the electrode portions inside the cavities: R_{ec}.
2. The resistances of the electrode portions in and above the charge: R_{eu}.

These resistances can be expressed in terms of the electrode resistivity ρ_e, the electrode cross-section A_e, the electrode lengths h_{ei}, the cavity heights $h_{cav\,i}$, and the arc lengths h_{ai}:

$$R_{eui} = (h_{ei} - h_{cav\,i} + h_{ai}) \frac{\rho_e}{A_e} \tag{B.8}$$

$$R_{eci} = (h_{cav\,i} - h_{ai}) \frac{\rho_e}{A_e} \tag{B.9}$$

The following relations between the arc voltages and the electrode resistances, and electrode displacements Δh_{ai} can be derived:

$$\Delta v_{ai} = k_{ai}\, \Delta h_{ai} \tag{B.10}$$

$$\Delta r_{eui} = \frac{\rho_e}{A_e} \Delta h_{ai} \tag{B.11}$$

$$\Delta r_{eci} = -\frac{\rho_e}{A_e} \Delta h_{ai} \tag{B.12}$$

Measured electrode voltages

An expression of the changes in the resistances due to electrode movements can be developed based on the measured electrode voltages. Depending on whether the arc voltages are described by the arc "resistance" expression in Eq. 4.59 or by the Nottingham equation in Eq. B.7, two different expressions of the measured electrode voltages V_{ei} are achieved:

$$V_{ei} = [Z_{ei} + R_{bi} + R_{ki}]\, I_{ei} \tag{B.13}$$

$$\begin{aligned} V_{ei} &= [Z_{ei} + R_{bi}]\, I_{ei} + [R_{eci} + R_{mi}]\, I_{ai} + V_{ai} \\ &= [Z_{ei} + R_{bi} + R_{li}]\, I_{ei} + R_q V_{ai} \end{aligned} \tag{B.14}$$

where R_{qci} are the ratios between the charge resistance and the sum of cavity and charge resistances for each phase:

$$R_{qci} = \frac{R_{ci}}{R_{eci} + R_{mi} + R_{ci}} \tag{B.15}$$

and R_{li} are the resulting cavity resistances with the arcs short-circuited:

$$R_{li} = \frac{(R_{eci} + R_{mi})\, R_{ci}}{R_{eci} + R_{mi} + R_{ci}} \tag{B.16}$$

The magnitudes of the electrode voltages $|V_{ei}|$ in Eqs B.13 and B.14, can be evaluated as:

$$\begin{aligned} |V_{ei}| &= \left\{(R_{eui} + R_{bi} + R_{ki})^2 + X_{ei}^2\right\}^{1/2} |I_{ei}| \\ &= |Z_{mi}|\ |I_{ei}| \end{aligned} \tag{B.17}$$

or equivalently as:

$$|V_{ei}| = \left\{(R_q V_{ai} + [R_{eci} + R_{bi} + R_{li}]\, I_{ei})^2 + (X_{ei} I_{ei})^2\right\}^{1/2} \tag{B.18}$$

where Z_{mi} denote the "measured" phase impedances. The magnitudes of these "measured" phase impedances $|Z_{mi}|$, are defined as:

$$\begin{aligned} |Z_{mi}| &= \left\{(R_{eui} + R_{bi} + R_{ki})^2 + X_{ei}^2\right\}^{1/2} \\ &= \left\{R_{mi}^2 + X_{ei}^2\right\}^{1/2} \end{aligned} \tag{B.19}$$

Linearizing Eq. B.17 by using a first order Taylor series expansion of the electrode currents I_{ei} and the phase resistances R_i around the electrical working-point:

$$|I_{ei}| = \left|I_{ei}^0\right| + \Delta i_{ei} \tag{B.20}$$

$$R_i = R_i^0 + \Delta r_i \tag{B.21}$$

gives a linearized model of the voltage deviations Δv_{ei}, expressed in terms of the current and resistance deviations Δi_{ei} and Δr_i:

$$\Delta v_{ei} = \left|Z_{mi}^0\right| \Delta i_{ei} + \frac{|I_{ei}^0|}{|Z_{mi}^0|} R_{mi}^0\, \Delta r_i \tag{B.22}$$

Linearizing Eq. B.18 in the same way by using a first order Taylor series expansion of the electrode currents I_{ei}, the arc voltages V_{ai}, and the electrode resistances R_{eui} and R_{eci} around the electrical working-point:

$$|I_{ei}| = \left|I_{ei}^0\right| + \Delta i_{ei} \tag{B.23}$$

$$V_{ai} = V_{ai}^0 + \Delta v_{ai} \tag{B.24}$$

$$R_{eui} = R_{eui}^0 + \Delta r_{eui} \tag{B.25}$$

$$R_{eci} = R_{eci}^0 + \Delta r_{eci} \tag{B.26}$$

yields:

$$\Delta v_{ei} = \frac{1}{|Z_{mi}^0|} \left\{\left(R_{mi}^0 R_{sci}^0 + X_{ei}^2\right) \Delta i_{ei} + R_{mi}^0 \tilde{k}_{ai}^0\, \Delta h_{ai}\right\} \tag{B.27}$$

where R_{sci} are the resulting phase resistances with the arcs short-circuited:

$$R^0_{sci} = R^0_{ei} + R_{bi} + R^0_{li} \tag{B.28}$$

R_{qai} are the ratios between the arc resistance and the sum of cavity and charge resistances for each phase:

$$R^0_{qai} = \frac{R^0_{ai}}{R^0_{ai} + R^0_{eci} + R_{mi} + R_{ci}} \tag{B.29}$$

and $\tilde{k}_{ai}$ are the "effective" arc voltage characteristics:

$$\tilde{k}^0_{ai} = R^0_{qci} k^0_{ai} + \left|I^0_{ei}\right| \frac{\rho_e}{A_e} - {R^0_{qci}}^2 \left|I^0_{ei}\right| \left[1 - R^0_{qai}\right] \frac{\rho_e}{A_e} \tag{B.30}$$

The resistance-electrode displacement model

A relationship between the resistance deviations Δr_i, and electrode displacements Δh_{ai}, can be found by combining Eqs. B.22 and B.27:

$$\begin{aligned} &\left|Z^0_{mi}\right| \Delta i_{ei} + \frac{|I^0_{ei}|}{|Z_{mi}|} R^0_{mi} \, \Delta r_i \\ &= \frac{1}{|Z^0_{mi}|} \left\{ \left(R^0_{mi} R^0_{sci} + X^2_{ei} \right) \Delta i_{ei} + \left(R^0_{mi} \tilde{k}^0_{ai} \right) \Delta h_{ai} \right\} \end{aligned} \tag{B.31}$$

Eliminating the current deviations in equation B.31 by inserting the relationship between the current and resistance deviations from Eq. 5.7:

$$\frac{\Delta i_{ei}}{\Delta r_i} = \tilde{\alpha}_{ii} = \frac{|V_T|^2}{{Z^0_{sum}}^2 |I_{ei}|} \alpha_{ii} \tag{B.32}$$

and rearranging, yields a model of how electrode displacements affect the phase resistances:

$$\Delta r_i = \beta_i \, \Delta h_{ai} \tag{B.33}$$

where the model parameter β_i is given by:

$$\beta_i = \frac{\tilde{k}^0_{ai}}{(R^0_{mi} - R^0_{sci}) \, \tilde{\alpha}_{ii} + |I^0_{ei}|} \tag{B.34}$$

B.3 Derivation of Barker's interaction factors

The Barker's interaction factors (Barker, 1981) described by Eqs. 5.13 and 5.14, are closely related to the current-resistance model given in Eq. 5.7

and B.5, and Barker's interaction model is actually a special case of this model.

Barker's interaction factors can be derived from the current-resistance model in Eq. B.5. This will be only shown for the f_{11}-interaction factor, thus the other interaction factor can be derived in a similar way.

The following relation between resistance variation in phase 1 and the corresponding electrode current deviations in phase 1, is obtained from Eq. 5.7:

$$\Delta i_{e1} = \frac{|V_T|^2}{{Z^0_{sum}}^2} \cdot \frac{\alpha_{11}}{|I_{e1}|} \cdot \Delta r_1 \tag{B.35}$$

By inserting the assumptions of Barker (1981) stated in Eq. 5.12 which define the electrical working point, into the current-resistance model and the expression of α_{11} in Eq. B.6 and Z^0_{sum} in Eq. B.2: get:

$$\alpha_{11} = -18R\left(R^2 + X^2\right)^2 , \quad Z_{sum} = 9\left(R^2 + X^2\right)^2 \tag{B.36}$$

the following relation is obtained:

$$\begin{aligned} \Delta i_{e1} &= -\frac{|V_T|^2}{|I_{e1}|} \cdot \frac{2R}{9} \cdot \frac{1}{(R^2 + X^2)^2} \cdot \Delta r_1 \\ &= -\frac{|V_T|^2}{|I_{e1}|} \cdot \frac{2R}{9} \cdot \frac{1}{|Z_m|^4} \cdot \Delta r_1 \end{aligned} \tag{B.37}$$

By inserting the relationship between line and phase voltages:

$$|V_T| = \sqrt{3} \cdot |V_m| = \sqrt{3} \cdot |Z_m|\,|I_{e1}| \tag{B.38}$$

we get:

$$\Delta i_{e1} = -\frac{2}{3} \cdot \frac{|I_{e1}|}{|Z_m|^2} \cdot R \cdot \Delta r_1 \tag{B.39}$$

which is equivalent to Barker's interaction factor f_{11}:

$$\frac{\Delta i_{e1}}{|I_{e1}|} = \left\{-\frac{2}{3} \cdot \frac{R}{|Z_m|}\right\} \cdot \frac{\Delta r_1}{|Z_m|} \tag{B.40}$$

Appendix C

Included papers

This appendix contain the papers that have been written in connection with the work on "Modelling and control of submerged-arc ferrosilicon furnaces":

- **Appendix C.1**

  Valderhaug, Aa., and P. Sletfjerding (1992). A non-interacting electrode current controller for submerged-arc furnaces. *Proc. 49th Electric Furnace Conference, Toronto, 1991, Iron and Steel Society, AIME, 1992.* pp. 311-320.

- **Appendix C.2**

  Valderhaug, Aa., J. G. Balchen and S. A. Halvorsen (1992). Modelbased control of the ferrosilicon process. *3rd IFAC Symposium on Dynamics and Control of Chemical Reactors, Distillation Columns and Batch Processes (DYCORD +'92), April 26-29 1992, College Park, Maryland.*

C.1 Paper by Valderhaug and Sletfjerding (1992)

A NON-INTERACTING ELECTRODE CURRENT CONTROLLER FOR SUBMERGED-ARC FURNACES

Aasgeir Valderhaug

Division of Engineering Cybernetics
The Norwegian Institute of Technology
N-7034 Trondheim, Norway

Peder Sletfjerding

Elkem a/s Research, Information Technology
PO.Box 40 Vaagsbygd, N-4602 Kristiansand, Norway

ABSTRACT

A linearized steady-state model describing the electrical conditions in a current-controlled submerged-arc furnace is developed. The interaction effect between the electrical phases is analyzed by furnace experiments and model simulations. The properties of a conventional current control system is examined, and a novel current control structure is proposed. The novel controller cancels the electrical interaction effect by the use of a decoupler, which can be derived from the current model. The controller will thereby remove current variations due to the interaction effect. This may also reduce undesirable electrode movements with belonging disadvantageous disturbances to the metallurgical reactions in the furnace.

INTRODUCTION

The production of ferrosilicon and other alloys in three-phase submerged-arc furnaces consumes large amounts of electric energy, and the economic potential of optimal furnace operations is considerable. As a result of this, strong efforts have been made in studying and analyzing the operation of electric furnaces in order to develop optimal operation and control strategies [1, 2, 3]. However, a three-phase submerged-arc ferrosilicon furnace is a complex process consisting of various closely interacting sub-processes, such as metallurgical (chemical), thermal, electrical and mechanical processes, and the control of such a furnace has turned out to be quite complicated. The main problems are the lack of direct measurements of the process variables in the heart of the furnace, and furthermore, the complex interactions between the electrical, thermal and metallurgical conditions in the furnace.

The electrical sub-process is a fundamental basis for the metallurgical reaction processes in the furnace, and a satisfactory electrical control is essential. The object of electrical control is to obtain a favorable electrical power distribution in the furnace. A conventional electrical control system for a submerged-arc furnace consists usually of a high-level power controller and low-level electrode controllers. Generally, two different kinds of electrode controllers are used, depending on the choice of control variables: electrode currents, or furnace resistances or impedances. In this paper we will focus on electrode current controllers. Considerable problems are connected with electrical control, and in particular electrode control, of large three-phase submerged-arc furnaces. The major problems are unreliable measurements of the electrical variables, unpredictable changes in electrical conductivity and arching conditions, and the interaction effect between the electrical phases. The interaction effect will especially cause problems for current control, because a displacement of one electrode will affect the currents in the other electrodes, too. In fact, advice has been given against current control owing to this interaction effect [4, 5]. However, we will show that this problem can be eliminated by extending the current controller with a decoupling element that cancels the couplings between the electrical phases.

The paper is organized as follows: In the first section of the paper submerged-arc ferrosilicon furnaces with conventional electrical control systems are briefly described, and an electrical equivalence circuit is stated. Next, a steady-state electrical model is developed, and based on it a model of a current-controlled submerged-arc furnace is derived. This model describes the electrical interaction effect, which is analyzed and illustrated by simulation examples and experiments on a submerged-arc furnace. Finally, a non-interacting electrode current controller is proposed, and both controllers are analyzed and illustrated by simulation examples.

THE SUBMERGED-ARC FURNACE

A schematic diagram of a three-phase submerged-arc ferrosilicon furnace is shown in Figure 1. The electrodes, which are symmetrically arranged in the circular furnace, are submerged into the charge and conduct the electrical energy into the heart of the furnace. Cavities, in which the currents form electric arcs, appear by heavy heat generation in the charge around the electrode tips. The main part of the chemical processes occur at high temperatures in and near these cavities. The solid reactants of the process: quartz, coke, carbon and iron, are added through feeding tubes at the top of the furnace, and waste gas: carbon monoxide and silica gas, are released. The product: ferrosilicon, forms pools below the cavities and is drained from tapholes at the bottom of the furnace.

The Electrical Circuit

An equivalent circuit description of a three-phase submerged-arc furnace is shown in Figure 2. The electrical energy is supplied from the three-phase a.c. mains

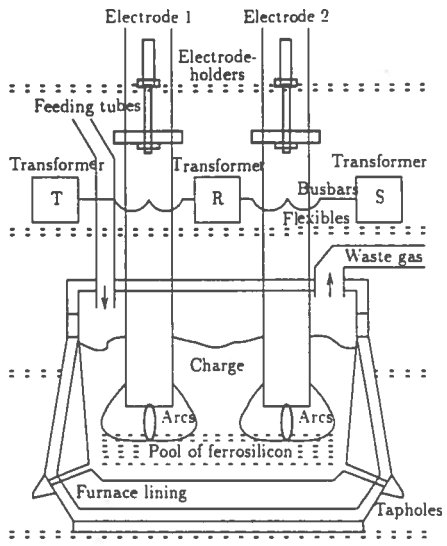

Figure 1: A three-phase submerged-arc ferrosilicon furnace, showing two out of three electrodes.

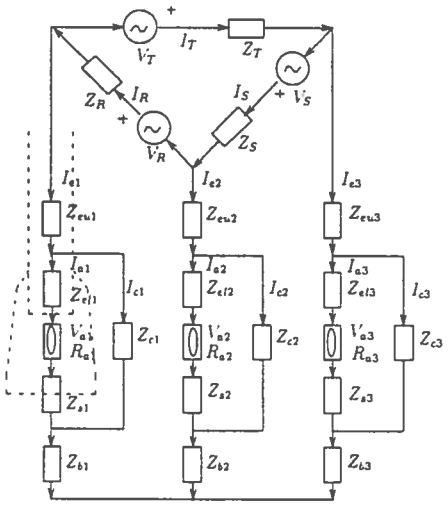

Figure 2: Equivalence circuit of a three-phase submerged-arc furnace. (The electrode and arc cavity are indicated for one of the electrical phases.)

by three transformers, symmetrically connected by busbars and flexibles to the electrodes in a delta-connection. The electrical energy is transformed from a line voltage of 22kV to typically 250V. The furnace resistivity are low, typically 1mΩ, and the secondary currents are very high, typically phase currents of 150 kA for a 60 MVA furnace. At such high currents the magnetic induction is considerable, and the symmetric transformer connection is necessary to obtain symmetric reactances in the furnace and avoid large reactive losses. The currents are conducted through the electrodes to the heart of the furnace. The main current paths in the furnace are between the electrode tips and the metal pools in and beneath the cavities. Compared with these currents the conduction in the charge directly between the electrodes is small and is neglected throughout this paper. The electrical circuit in the furnace is than assumed to be a delta-star circuit, as shown in Figure 2. The main part of the electric energy in the furnace is dissipated in the cavities by electric arcs between the electrodes and the molten pool, or near the cavity walls by ohmic conductance in parallel with the arcs.

The electrode currents cannot be measured directly on the secondary side of the transformer because of the high currents, and corresponding values are therefore obtained by measurements on the primary phase currents. The phase voltages between the electrodes and the electrical star-point in the furnace bottom, are measured in a way that almost removes measurements error due to induced inductive voltages.

Electrical Control Of Submerged-Arc Furnaces

The object of electrical control is to obtain an optimal electrical power distribution in the furnace. This involves controlling the delivered power and the electrode currents. The power controllers use the transformer taps as control variables to attain a predetermined power consumption. The current controllers control the electrode currents by moving the electrodes, and the current reference values are chosen in a way that ensures a desirable power distribution in the furnace [1, 4, 5, 6].

A conventional current control system consists of three monovariable controllers. Each of them tries to control the current in the belonging electrode by lifting and lowering it, but without taking any account of the interaction effect between the currents. A schematic diagram of a conventional current control system is shown in Figure 3, where I_{ei} are the electrode currents, h_i are the electrode positions, and I_{refei} are the current reference values. The interaction effect between the electrical phases is illustrated by the dotted lines in the "furnace-box" in the Figure 3.

The current control algorithm is usually a dead-zone controller with fixed electrode displacement. The current

have to exceed the dead-zone bounds around the reference values for a specified time period before the controller act, as shown in Figure 4. This particular control algorithm

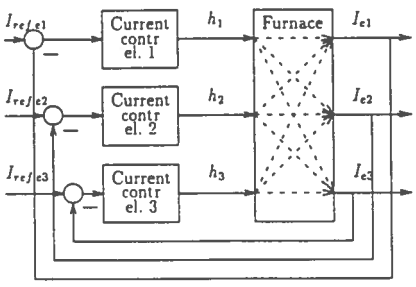

Figure 3: A conventional current control system.

is chosen mainly because of the large disturbances to the electrical conditions in the furnace. The three control parameters: the fixed electrode displacement, the dead-zone bound, and the time-before-action period, are tuned to reject the disturbances as good as possible.

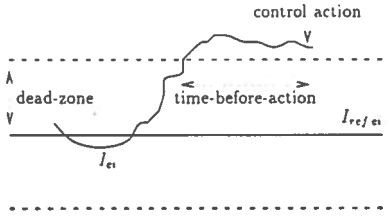

Figure 4: The dead-zone control algorithm.

MODELLING

A steady-state description of the electrode currents and a model of a current-controlled submerged-arc furnace will be developed based on the following assumptions:

1. The notation symbols are defined when first used. The main principles are: Uppercase letters: voltages V, currents I and impedances Z, are *phasors* (complex quantities). Lowercase letters denote time-varying variables, superscript 0 is used to denote stationary quantities, and the Δ-values are used to describe deviations from stationary values. The following subscripts notation is used:

R, S, T,	Tr	transformers, electrical phases
1, 2, 3,	i	electrode/phase no. ($i = 1, 2, 3$)
e		electrode (total length)
eu		electrode, *upper* part (in and above the charge)
el		electrode, *lower* part (in the arc cavities)
a		arc
c		charge
s		smelted (ferrosilicon) pool in the cavity bottoms
b		furnace bottom

2. The transformer voltages V_R, V_S and V_T are symmetrical in the phase sequence R-S-T:

$$\begin{aligned} V_R &= |V_{Tr}|\,[1 + j \cdot 0] \\ V_S &= |V_{Tr}|\left[-1/2 - j \cdot \sqrt{3}/2\right] = V_R a^2 \\ V_T &= |V_{Tr}|\left[-1/2 + j \cdot \sqrt{3}/2\right] = V_R a \end{aligned} \quad (1)$$

where $|V_{Tr}|$ is the common voltage magnitude and a is the complex three-phase operator.

3. The impedances in the transformers, busbars and flexibles Z_R, Z_S and Z_T are identical in all three phases:

$$Z_R = Z_S = Z_T = Z_{Tr}$$

where Z_{Tr} is the common impedance.

4. The electrical reactances in each phase can be lumped into variable electrode reactances X_{eui}.

5. A movement of one electrode Δh_i, will lead to a corresponding change in the arc length Δh_{ai}:

$$\Delta h_i = \Delta h_{ai}$$

Steady-state current models have been derived from equivalence circuit descriptions of steel furnaces [7, 8, 9, 10]. The current paths in submerged-arc furnaces are different from those in steel furnaces, and some modifications are necessary in these models to describe submerged-arc furnaces, but the derivation of the model mainly follows the derivation of these models [7, 8, 9].

A Steady-State Electrical Model

A steady-state description of the electrode currents in the furnace can be developed based on the equivalent circuit in Figure 2 and the stated assumptions. A voltage balance of the transformer delta-circuit give:

$$V_R + V_S + V_T = Z_{Tr}\,(I_R + I_S + I_T) = 0 \quad (2)$$

where I_R, I_S and I_T are the currents in the transformer delta-circuit. Combining Eq. 2 with current balances at

the nodes between the transformer circuit and the electrodes and assuming equal impedances in the transformer circuit, we will get the following relation between the transformer and electrode currents I_{ei}:

$$I_R = \frac{1}{3}[I_{e1} - I_{e2}] \ , \quad I_S = \frac{1}{3}[I_{e2} - I_{e3}] \qquad (3)$$

Voltages balances of the circuits between electrodes 1-2, and 2-3, give:

$$\begin{aligned} V_R &= Z_{Tr}I_R + [Z_{eu1} + R_{b1}]I_{e1} + [R_{el1} + R_{s1}]I_{a1} + V_{a1} \\ &\quad - ([Z_{eu2} + R_{b2}]I_2 + [R_{el2} + R_{s2}]I_{a2} + V_{a2}) \qquad (4) \\ V_S &= Z_{Tr}I_S + [Z_{eu2} + R_{b2}]I_{e2} + [R_{el2} + R_{s2}]I_{a2} + V_{a2} \\ &\quad - ([Z_{eu3} + R_{b3}]I_{e3} + [R_{el3} + R_{s3}]I_{a3} + V_{a3}) \qquad (5) \end{aligned}$$

where $Z_{eui} = R_{eui} + X_{eui}$ are the impedances of the electrode sections in and above the charge, R_{eli} are the resistances of the electrode sections in the cavities, R_{si} are the resistances in the smelted metal pool in the cavity bottoms, R_{bi} are the resistances in the furnace bottom, I_{ai} are the arc currents, and V_{ai} are the arc voltages.

It is not possible to get an analytic expression of the electrode currents in terms of the arc voltages V_{ai} [11]. However, this will be possible if the arc voltages is described by nonlinear arc resistances R_{ai} [9]:

$$V_{ai} = R_{ai}I_{ai} \qquad (6)$$

Inserting the expression of the arc voltages in Eq. 6 and the current balances at the circuit nodes into the voltage balances in Eqs. 4 and 5, eliminating the transformer currents by Eq. 3, and rearranging the equations, give:

$$\begin{aligned} V_R &= Z_1I_{e1} - Z_2I_{e2} \\ V_S &= Z_2I_{e2} - Z_3I_{e3} \end{aligned} \qquad (7)$$

where the phase impedances Z_i are:

$$\begin{aligned} Z_i &= R_i + j \cdot X_i \\ R_i &= 1/3\, R_{Tr} + R_{eui} + R_{bi} + R_{ki} \\ X_i &= 1/3\, X_{Tr} + X_{eui} \\ R_{ki} &= \frac{R_{ci}(R_{eli} + R_{ai} + R_{si})}{R_{ci} + R_{eli} + R_{ai} + R_{si}} \end{aligned}$$

and R_{ki} are the resulting resistances for the cavities with arching effects present. Combining Eq. 7 with the current balance in the circuit star-point:

$$I_{e1} + I_{e2} + I_{e3} = 0 \qquad (8)$$

gives the following expressions of the electrode currents I_{ei}, in terms of the phase impedances Z_i, the transformer voltage magnitude V_R, and the three-phase operator a:

$$\begin{aligned} I_{e1} &= \frac{[-aZ_2 + Z_3]}{Z_1Z_2 + Z_2Z_3 + Z_3Z_1}V_R \\ I_{e2} &= \frac{[a^2Z_1 - Z_3]}{Z_1Z_2 + Z_2Z_3 + Z_3Z_1}V_R \\ I_{e3} &= \frac{[-a^2Z_1 + aZ_2]}{Z_1Z_2 + Z_2Z_3 + Z_3Z_1}V_R \end{aligned} \qquad (9)$$

Model Of Current-Controlled Submerged-Arc Furnace

A model of how electrode displacements affect the electrode currents can be developed based on the current model in Eq. 9. The model can be stated as:

$$\begin{pmatrix} \Delta i_{e1} \\ \Delta i_{e2} \\ \Delta i_{e3} \end{pmatrix} = H \cdot \begin{pmatrix} \Delta h_{a1} \\ \Delta h_{a2} \\ \Delta h_{a3} \end{pmatrix} \qquad (10)$$

where Δi_{ei} are the current deviations as results from electrode displacements, Δh_{ai} and matrix H is on the form:

$$H = \begin{pmatrix} h_{11} & h_{12} & h_{13} \\ h_{21} & h_{22} & h_{23} \\ h_{31} & h_{32} & h_{33} \end{pmatrix}$$

The matrix elements h_{ij}, describe the effect of electrode movements on the electrode currents. Matrix H depends on the resistances, the reactances and the arc characteristics in the furnace. The model is derived by developing a current-resistance model, describing how resistance variations affect the electrode currents, and combining it with a resistance-electrode displacement model. Matrix H can be looked upon as a linearized, steady-state transfer matrix between the input and the output of the current-controlled electrical system in a submerged-arc furnace.

The current-resistance model

A linearized model of how changes in resistance Δr_i, affect the electrode currents is developed in Appendix A. The model is found to be:

$$\begin{aligned} \Delta i_{e1} &= \frac{|V_R|^2}{Z_{sum}^{02}}\left\{\frac{\alpha_{11}}{|I_{e1}^0|}\Delta r_1 + \frac{\alpha_{12}}{|I_{e1}^0|}\Delta r_2 + \frac{\alpha_{13}}{|I_{e1}^0|}\Delta r_3\right\} \\ \Delta i_{e2} &= \frac{|V_R|^2}{Z_{sum}^{2}}\left\{\frac{\alpha_{21}}{|I_{e2}^0|}\Delta r_1 + \frac{\alpha_{22}}{|I_{e2}^0|}\Delta r_2 + \frac{\alpha_{23}}{|I_{e2}^0|}\Delta r_3\right\} \qquad (11) \\ \Delta i_{e3} &= \frac{|V_R|^2}{Z_{sum}^{2}}\left\{\frac{\alpha_{31}}{|I_{e3}^0|}\Delta r_1 + \frac{\alpha_{32}}{|I_{e3}^0|}\Delta r_2 + \frac{\alpha_{33}}{|I_{e3}^0|}\Delta r_3\right\} \end{aligned}$$

where the matrix elements α_{ij} are defined in Eq. 26 and Z_{sum} is defined in Eq. 24 in Appendix A. These model parameters are all expressions in terms of the phase impedances, which are measurable, and a numerical expression of the current-resistance model can easily be computed.

The relationship between the model in Eq. 11 and the *interaction factors* for electric furnaces developed by I. J. Barker in [5], is shown in Appendix B.

The resistance-electrode displacement model

A linearized model of how changes in resistances Δr_i, are related to electrode displacements Δh_{ai}, is developed in Appendix C. The model is assumed to be diagonal, which means that electrode movements in one phase affect only the resistance in that phase. The model expression

can be found in Eq. 36 and can be written as:

$$\begin{pmatrix} \Delta r_1 \\ \Delta r_2 \\ \Delta r_3 \end{pmatrix} = \begin{pmatrix} \beta_1 & 0 & 0 \\ 0 & \beta_2 & 0 \\ 0 & 0 & \beta_3 \end{pmatrix} \begin{pmatrix} \Delta h_{a1} \\ \Delta h_{a2} \\ \Delta h_{a3} \end{pmatrix} \qquad (12)$$

This model will depend on the partly unknown current paths in the furnace. The model parameters β_i, are expressions in terms of the arc characteristics and the various resistances in the heart of the furnace. These quantities can hardly be measured, and numerical values will more or less be based on assumptions. As a result of this, only an approximate model can be computed from Eq. 12. However, this model is useful in simulation studies of the electrical conditions in the furnace, and a more accurate numerical model can be achieved from furnace experiments.

The current-electrode displacement model

A complete model describing the changes in electrode currents ΔI_{ei}, as a result of electrode displacements Δh_{ai}, is obtained by inserting the resistance model in Eq. 12 into the current-resistance model in Eq. 11. The model is found to be:

$$\begin{pmatrix} \Delta i_{e1} \\ \Delta i_{e2} \\ \Delta i_{e3} \end{pmatrix} = \frac{|V_R|^2}{Z^{02}_{sum}} \begin{pmatrix} \frac{o_{11}\beta_1}{|I^o_{e1}|} & \frac{o_{12}\beta_2}{|I^o_{e1}|} & \frac{o_{13}\beta_3}{|I^o_{e1}|} \\ \frac{o_{21}\beta_1}{|I^o_{e2}|} & \frac{o_{22}\beta_2}{|I^o_{e2}|} & \frac{o_{23}\beta_3}{|I^o_{e2}|} \\ \frac{o_{31}\beta_1}{|I^o_{e3}|} & \frac{o_{32}\beta_2}{|I^o_{e3}|} & \frac{o_{33}\beta_3}{|I^o_{e3}|} \end{pmatrix} \begin{pmatrix} \Delta h_{a1} \\ \Delta h_{a2} \\ \Delta h_{a3} \end{pmatrix} \qquad (13)$$

or written in vector form:

$$\underline{\Delta I_e} = H \cdot \underline{\Delta h_a} \qquad (14)$$

where vector $\underline{\Delta I_e}$ contains the changes in the electrode currents and $\underline{\Delta h_a}$ contains the electrode displacements. The model in Eq. 13 and Eq. 14 is a linearized input-output description at steady-state electrical condition of a current-controlled submerged-arc furnace.

INTERACTION ANALYSIS

The electrical interaction effect in a submerged-arc ferrosilicon furnace is analyzed both by furnace experiments and simulation studies.

Furnace Experiments

The interaction effect is analyzed by experiments on the furnace by moving one electrode at a time while the others are fixed, and examining the corresponding changes in electrode currents and resistances. Figure 5 shows a typical step-response experiment. Several experiments have been carried out for all electrodes and in both directions, and the models in Eq. 12 and Eq. 13 can be found numerically.

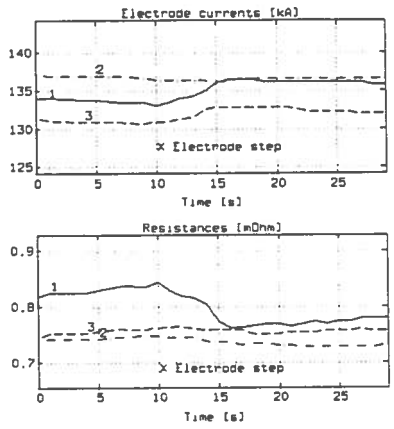

Figure 5: Step-response experiment on a submerged-arc furnace. Electrode 1 is lowered by 1.15 cm at $t = 10$ s.

Figure 5 shows that there is a considerable variation in the electrical states due to disturbance effects, but the effects by an electrode displacement on the electrode currents and resistances are still significant. However, the presence of disturbances makes it necessary to use some kind of filtering technique on the measured signals before the numerical models can be computed. Lowering electrode 1 by 1.15 cm results in the following deviations in the electrode currents [kA], and resistances [mΩ]:

$$\Delta i_{e1} = 3.57 \quad \Delta i_{e2} = 0.13 \quad \Delta i_{e3} = 1.91$$
$$\Delta r_1 = -0.080 \quad \Delta r_2 = -0.017 \quad \Delta r_3 = -0.003$$

The effects of electrode movements varied to some extent from one experiment to another, but displacements in the same direction yield corresponding results. Generally, the electrical conditions seemed to be more sensitive to downwards displacements then upwards, something that is a contradiction to the model assumption of accordance between electrode movements and changes in arc lengths. In the model calculations only downwards experiments are used, and based on this the following resistance-electrode displacement model [mΩ/cm] is found:

$$\begin{pmatrix} \Delta r_1 \\ \Delta r_2 \\ \Delta r_3 \end{pmatrix} = \begin{pmatrix} 0.070 & -0.002 & -0.019 \\ 0.014 & 0.047 & 0.004 \\ 0.003 & -0.006 & 0.049 \end{pmatrix} \begin{pmatrix} \Delta h_{a1} \\ \Delta h_{a2} \\ \Delta h_{a3} \end{pmatrix} \qquad (15)$$

Likewise, the input-output model of the current-controlled

system [kA/cm] is found to be:

$$\begin{pmatrix} \Delta I_{e1} \\ \Delta I_{e2} \\ \Delta I_{e3} \end{pmatrix} = \begin{pmatrix} -3.11 & -1.30 & 0.65 \\ -0.12 & -1.55 & -1.46 \\ -1.66 & 0.94 & -1.45 \end{pmatrix} \begin{pmatrix} \Delta h_{a1} \\ \Delta h_{a2} \\ \Delta h_{a3} \end{pmatrix} \quad (16)$$

Some electrical asymmetry were present while the experiments were carried out, something that can explain the asymmetric current model.

Simulation studies

The electrical conditions in a submerged-arc furnace as shown in the equivalence circuit in Figure 2, together with a conventional electrical control system, are implemented in a simulation model. The interaction effects are analyzed in simulation studies with model parameters comparable to the furnace experiments. The resistance-electrode displacement model [mΩ/cm] is computed as:

$$\begin{pmatrix} \Delta r_1 \\ \Delta r_2 \\ \Delta r_3 \end{pmatrix} = \begin{pmatrix} 0.041 & 0 & 0 \\ 0 & 0.033 & 0 \\ 0 & 0 & 0.033 \end{pmatrix} \begin{pmatrix} \Delta h_{a1} \\ \Delta h_{a2} \\ \Delta h_{a3} \end{pmatrix} \quad (17)$$

This model is based on assumptions on the resistances in the heart of the furnace, but it is fairly acceptable compared to the experiment model in Eq. 15. The computation of the current-electrode displacement model [kA/cm] gives the following result:

$$\begin{pmatrix} \Delta I_{e1} \\ \Delta I_{e2} \\ \Delta I_{e3} \end{pmatrix} = \begin{pmatrix} -2.30 & -1.33 & 0.38 \\ 0.48 & -1.81 & -1.28 \\ -1.62 & 0.43 & -1.80 \end{pmatrix} \begin{pmatrix} \Delta h_{a1} \\ \Delta h_{a2} \\ \Delta h_{a3} \end{pmatrix} \quad (18)$$

The simulation model computes a model that is comparable to the experiment model in Eq. 16. However, a better accordance between the simulation and experiment models is achievable if the model parameters is more properly adjusted.

Barker's interaction factors [5] give a dimensionless description of the interaction effect. This is further discussed in Appendix C. The following interaction factor matrix is computed:

$$F = \begin{pmatrix} -0.45 & -0.33 & 0.09 \\ 0.09 & -0.44 & -0.31 \\ -0.32 & 0.10 & -0.44 \end{pmatrix} \quad (19)$$

This confirms that the interaction effect is considerable in a submerged-arc ferrosilicon furnace.

A NON-INTERACTING CURRENT CONTROLLER

A non-interacting current controller is achieved by extending the controller with a decoupling element as shown in Figure 6. The decoupler cancels interaction effects between the electrical phases in the furnace, and a current controller will now only affect the currents in the belonging electrical phase. This canceling effect is illustrated by the dotted lines in the "decoupler" box in the figure. Changes in the electrode positions Δh_i, which correspond to changes in arc lengths Δh_{ai}, will now be given as:

$$\underline{\Delta h} = D \cdot \underline{\Delta u} \quad (20)$$

where vector $\underline{\Delta u}$ contains changes in the controller outputs. A change in the controller output Δu_1 will now result in changes in the electrode positions by Δh_1, Δh_2 and Δh_3, in a way that only affect the current I_{e1}.

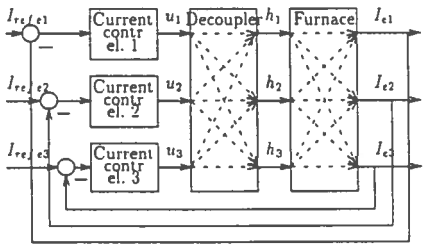

Figure 6: A non-interacting current control system.

A simplified linearized model of the control system including the decoupler will be:

$$\underline{\Delta I_e} = (H \cdot D) \cdot \underline{\Delta u} = H_D \cdot \underline{\Delta u} \quad (21)$$

where H is the furnace model, D is the decoupler and H_D is the resulting system model. The system between the controller outputs deviations $\underline{\Delta u}$ and the current deviations $\underline{\Delta I_e}$ will now be diagonal, and H_D contains only diagonal elements. The decoupler can be found from

$$D = [H]^{-1} \cdot H_D \quad (22)$$

where H_D is the desired system matrix.

SIMULATION OF THE CONTROL STRATEGIES

The conventional and the non-interacting controller's abilities of handling the interaction effect is analyzed by simulations. Cases involving step-like alternations in resistances and reactances and time-varying resistances and reactances are examined. An example with a step-like change in reactance is discussed below. Figure 7 shows the response of the conventional controller, and the decoupling controller's response is shown in Figure 8.

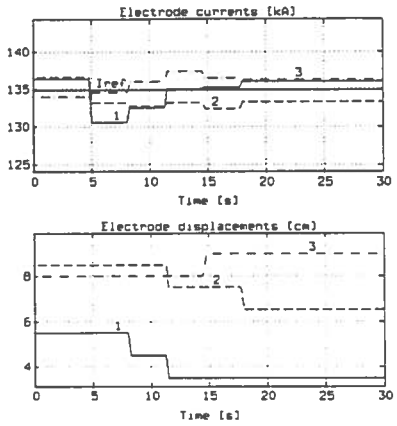

Figure 7: Response of the conventional controller. The reactance in phase 1 is increased by 10 % at $t = 5$.

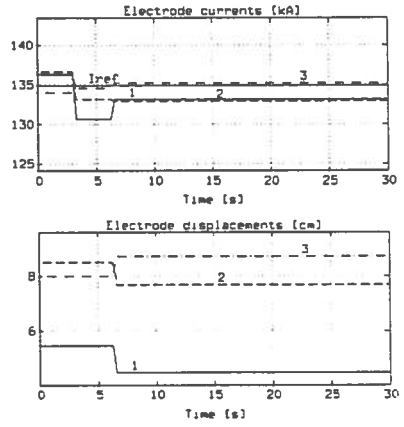

Figure 8: Response of the non-interacting controller. The reactance in phase 1 is increased by 10 % at $t = 5$.

The dead-zone control algorithm, as discussed in a previous section, with the following parameters:

dead-zone	:	2.0 kA
time-before-action	:	3.0 s
electrode displacement	:	1.0 cm

is used in both controllers. The decoupler is realized as discussed in the previous section. The electrode displacements is given by Eq. 20, and the "desired" system matrix H_D, is chosen to consist of the diagonal elements of the current-electrode displacement model H.

The response of the conventional controller in Figure 7 shows its inability of handling the interaction effect. The changes in the electrical conditions in phase 1 as a result of the reactance alternation, is moved to the other phases because of the control action in phase 1. Figure 8 shows the decoupler response to the similar case. The non-interacting controller takes into account the interaction effect, and all three electrodes are moved when the control action occur in phase 1. This results in less electrode movements and a shorter transient period. Further simulation studies verify that the decoupler strategy has superior properties compared to a conventional controller. However, the conventional controller property of rejecting interactions can be improved by a proper adjustment of the control parameters, but this can only be obtained at the expense of the other control properties.

CONCLUSION

The interaction analysis shows that the electrical interaction effects are significant in submerged-arc furnaces. The conventional current controller has poor properties in rejecting this effect if not the control parameters are properly adjusted. The proposed non-interacting current controller cancels the interaction between the electrical phases. This will remove current variations due to the interaction, and may also reduce undesirable electrode movements. The novel control strategy will enable the use of current control in large submerged-arc furnaces with its benefits, but without the usual disadvantages connected to the method. The controller will in the near future be tested out on a submerged-arc ferrosilicon furnace.

ACKNOWLEDGMENTS

The work is a part of a research program on model-based control of ferrosilicon furnaces between Elkem a/s, Norway and The Division of Engineering Cybernetics at The Norwegian Institute of Technology, and has been financially supported by Elkem a/s, Norway and The Royal Norwegian Council for Scientific and Industrial Research (NTNF). We would like to thank the people at Elkem Thamshavn a/s, Norway and Elkem a/s Research, Norway for their cooperation and support.

REFERENCES

1. J. Westly, *"Resistance and Heat Distribution in a Submerged-Arc Furnace"*, INFACON, Johannesburg, South Africa, 1974.
2. E. Breton, *"The Maze of Ferrosilicon Production"*, 37th Electric Furnace Conference, Detroit, USA, 1979.
3. A. B. Stewart, *"An Analysis of the Electrical Circuit of Submerged-Arc Furnaces"*, PhD thesis, University of Cape Town, South Africa, 1980.
4. I. J. Barker, *"An Electrode Controller for Submerged Arc Furnaces"*, Report No. 2129, National Institute for Metallurgy, Randsburg, South Africa, 1981.
5. I. J. Barker, *"An Electrode Controller for Submerged Arc Furnaces"*, 3rd IFAC Symposium on Automation in Mining, Mineral and Metal Processing, Montreal, Canada, 1980.
6. A. Holmelid, J. Westly and L. T. Kvassheim, *"Electric Control of Ferrosilicon Submerged-Arc Furnaces"* Control '84 Mineral/Metallurgical Processing, AIME, 1984.
7. H. Nicholson and R. Roebuck, *"Simulation and Control of Electrode Position Controllers for Electric Arc Furnaces"*, Automatica, Vol. 8, 1972, pp. 683-693.
8. S. A. Billings, *"Modelling, Identification and Control of an Electric Arc Furnace"*, PhD thesis, Sheffield University, UK, 1975.
9. S. A. Billings, *"Modelling and Identification of a Three-Phase Electric-Arc Furnace"*, H. Nicholson (Ed.): Modelling of Dynamical Systems, Volume 2, Institution of Electrical Engineers, London, 1981, pp 63-80.
10. B. Schwartz, *"Regelung elektrischer Größen an Drehstrom-Lichtbogenöfen"*, Dr.-Ing.-Dissertion, Fachbereich Maschinenbau, Universität der Bundeswehr Hamburg, Germany, 1988.
11. B. Schwartz and K. Timm, *"Regelung elektrischer Größen an Drehstrom-Lichtbogenöfen"*, Elektrowärme International, Vol 47, B1, February 1989, pp B12-B22.

APPENDIX A

DERIVATION OF THE CURRENT-RESISTANCE MODEL

An expression showing the relation between electrode currents and resistance variations can be developed from the current model in Eq. 9. Inserting the expressions of the phase impedances Z_i, into Eq. 9, evaluating the square value of the electrode current magnitudes, and rearranging, yields:

$$\begin{aligned}
|I_{e1}|^2 &= \frac{|V_R|^2}{Z_{sum}}\left\{R_2^2 + R_2R_3 + R_3^2 + X_2^2 + X_2X_3 + X_3^2 - \sqrt{3}R_2X_3 + \sqrt{3}R_3X_2\right\} \\
|I_{e2}|^2 &= \frac{|V_R|^2}{Z_{sum}}\left\{R_1^2 + R_1R_3 + R_3^2 + X_1^2 + X_1X_3 + X_3^2 + \sqrt{3}R_1X_3 - \sqrt{3}R_3X_1\right\} \qquad (23) \\
|I_{e3}|^2 &= \frac{|V_R|^2}{Z_{sum}}\left\{R_1^2 + R_1R_2 + R_2^2 + X_1^2 + X_1X_2 + X_2^2 - \sqrt{3}R_1X_2 + \sqrt{3}R_2X_1\right\}
\end{aligned}$$

where:

$$\begin{aligned}
Z_{sum} &= \left(\sum_{k,l=1}^{3} R_kR_l - X_kX_l\right)^2 + \left(\sum_{k,l=1}^{3} R_kX_l\right)^2 \quad k \neq l \qquad (24) \\
&= (R_1R_2 + R_2R_3 + R_3R_1 - X_1X_2 - X_2X_3 - X_3X_1)^2 \\
&\quad + (R_1X_2 + R_1X_3 + R_2X_1 + R_2X_3 + R_3X_1 + R_3X_2)^2
\end{aligned}$$

Linearizing the model in Eq. 23 using a first order Taylor series expansion with

$$|I_{ei}| = \left|I_{ei}^0\right| + \Delta i_{ei}\,, \quad R_i = R_i^0 + \Delta r_i$$

and assuming constant reactances and no interaction between the arc resistances, give the following model of electrode current deviations Δi_{ei}, in terms of resistance variations Δr_i:

$$\begin{aligned}
\Delta i_{e1} &= \frac{|V_R|^2}{Z_{sum}^{02}}\left\{\frac{a_{11}}{|I_{e1}^0|}\Delta r_1 + \frac{a_{12}}{|I_{e1}^0|}\Delta r_2 + \frac{a_{13}}{|I_{e1}^0|}\Delta r_3\right\} \\
\Delta i_{e2} &= \frac{|V_R|^2}{Z_{sum}^{02}}\left\{\frac{a_{21}}{|I_{e2}^0|}\Delta r_1 + \frac{a_{22}}{|I_{e2}^0|}\Delta r_2 + \frac{a_{23}}{|I_{e2}^0|}\Delta r_3\right\} \qquad (25) \\
\Delta i_{e3} &= \frac{|V_R|^2}{Z_{sum}^{02}}\left\{\frac{a_{31}}{|I_{e3}^0|}\Delta r_1 + \frac{a_{32}}{|I_{e3}^0|}\Delta r_2 + \frac{a_{33}}{|I_{e3}^0|}\Delta r_3\right\}
\end{aligned}$$

The matrix elements a_{ij} are:

$$a_{11} = -\left(R_2^{02} + R_2^0R_3^0 + R_3^{02} + X_2^{02} + X_2^0X_3^0 + X_3^{02}\right.$$

$$- \sqrt{3}R_2^0X_3^0 + \sqrt{3}R_3^0X_2^0\Big) Z_{\Pi 1}^0$$

$$a_{12} = \frac{1}{2}\left(2R_2^0 + R_3^0 - \sqrt{3}X_3^0\right) Z_{sum}^0 - \left(R_2^{02} + R_2^0R_3^0 + R_3^{02} + X_2^{02} + X_2^0X_3^0 + X_3^{02} - \sqrt{3}R_2^0X_3^0 + \sqrt{3}R_3^0X_2^0\right) Z_{\Pi 2}^0$$

$$a_{13} = \frac{1}{2}\left(2R_3^0 + R_2^0 + \sqrt{3}X_2^0\right) Z_{sum}^0 - \left(R_2^{02} + R_2^0R_3^0 + R_3^{02} + X_2^{02} + X_2^0X_3^0 + X_3^{02} - \sqrt{3}R_2^0X_3^0 + \sqrt{3}R_3^0X_2^0\right) Z_{\Pi 3}^0$$

$$a_{21} = \frac{1}{2}\left(2R_1^0 + R_3^0 + \sqrt{3}X_3^0\right) Z_{sum}^0 - \left(R_1^{02} + R_1^0R_3^0 + R_3^{02} + X_1^{02} + X_1^0X_3^0 + X_3^{02} + \sqrt{3}R_1^0X_3^0 - \sqrt{3}R_3^0X_1^0\right) Z_{\Pi 2}^0$$

$$a_{22} = -\left(R_1^{02} + R_1^0R_3^0 + R_3^{02} + X_1^{02} + X_1^0X_3^0 + X_3^{02} + \sqrt{3}R_1^0X_3^0 - \sqrt{3}R_3^0X_1^0\right) Z_{\Pi 2}^0 \quad (26)$$

$$a_{23} = \frac{1}{2}\left(2R_3^0 + R_1^0 - \sqrt{3}X_1^0\right) Z_{sum}^0 - \left(R_1^{02} + R_1^0R_3^0 + R_3^{02} + X_1^{02} + X_1^0X_3^0 + X_3^{02} + \sqrt{3}R_1^0X_3^0 - \sqrt{3}R_3^0X_1^0\right) Z_{\Pi 2}^0$$

$$a_{31} = \frac{1}{2}\left(2R_1^0 + R_2^0 - \sqrt{3}X_2^0\right) Z_{sum}^0 - \left(R_1^{02} + R_1^0R_2^0 + R_2^{02} + X_1^{02} + X_1^0X_2^0 + X_2^{02} - \sqrt{3}R_1^0X_2^0 + \sqrt{3}R_2^0X_1^0\right) Z_{\Pi 1}^0$$

$$a_{32} = \frac{1}{2}\left(2R_2^0 + R_1^0 + \sqrt{3}X_1^0\right) Z_{sum}^0 - \left(R_1^{02} + R_1^0R_2^0 + R_2^{02} + X_1^{02} + X_1^0X_2^0 + X_2^{02} - \sqrt{3}R_1^0X_2^0 + \sqrt{3}R_2^0X_1^0\right) Z_{\Pi 2}^0$$

$$a_{33} = -\left(R_1^{02} + R_1^0R_2^0 + R_2^{02} + X_1^{02} + X_1^0X_2^0 + X_2^{02} - \sqrt{3}R_1^0X_2^0 + \sqrt{3}R_2^0X_1^0\right) Z_{\Pi 3}^0$$

where:

$$Z_{\Pi 1}^0 = \left(R_2^0 + R_3^0\right) \sum_{k,l=1}^{3} \left(R_k^0R_l^0 - X_k^0X_l^0\right) + \left(X_2^0 + X_3^0\right) \sum_{k,l=1}^{3} \left(R_k^0X_l^0\right), \quad k \neq l$$

$$Z_{\Pi 2}^0 = \left(R_1^0 + R_3^0\right) \sum_{k,l=1}^{3} \left(R_k^0R_l^0 - X_k^0X_l^0\right) + \left(X_1^0 + X_3^0\right) \sum_{k,l=1}^{3} \left(R_k^0X_l^0\right), \quad k \neq l$$

$$Z_{\Pi 3}^0 = \left(R_1^0 + R_2^0\right) \sum_{k,l=1}^{3} \left(R_k^0R_l^0 - X_k^0X_l^0\right) + \left(X_1^0 + X_2^0\right) \sum_{k,l=1}^{3} \left(R_k^0X_l^0\right), \quad k \neq l$$

APPENDIX B

DERIVATION OF THE RESISTANCE-ELECTRODE DISPLACEMENT MODEL

A model of the effect of electrode movements on the resistances is evaluated below. The evaluation is based on [9] and adapted to the current paths in submerged-arc furnaces.

Arc Voltages And Electrode Resistances

The arc voltages V_{ai}, can be related to the arc lengths h_{ai}, by using the steady-state solution of Cassie's equation [9]:

$$V_{ai} = V_{a0i} + k_{ai}h_{ai} \quad (27)$$

where k_{ai} is the arc voltage coefficient and V_{a0i} is the arc interface voltage drop. In a submerged-arc furnace the electrode resistances will be affected by electrode movements, too. The electrode resistance is computationally divided in two: The resistance in the lower part of the electrode (inside the cavity) R_{eli}, and the resistance of the upper part of it (in and above the charge) R_{eui}. These resistances can be expressed in terms of the electrode resistivity ρ_e, the electrode cross-section A_e, the electrode lengths h_{ei}, the cavity heights h_{cavi}, and the arc lengths h_{ai}:

$$R_{eui} = (h_{ei} - h_{cavi} + h_{ai})\frac{\rho_e}{A_e}, \quad R_{eli} = (h_{cavi} - h_{ai})\frac{\rho_e}{A_e}$$

The are voltages and the electrode resistances are related to electrode displacements Δh_{ai}, in the following way:

$$\Delta v_{ai} = k_{ai}\Delta h_{ai}, \quad \Delta r_{eui} = \frac{\rho_e}{A_e}\Delta h_{ai}, \quad \Delta r_{eli} = -\frac{\rho_e}{A_e}\Delta h_{ai}$$

Measured Electrode Voltages

An expression of the changes in the resistances due to electrode movements can be developed based on the measured electrode voltages. Depending on if the arc voltages are described by Eq. 6 or Eq. 27, we will get two different expressions of the measured electrode voltages V_{mi}:

$$V_{mi} = [Z_{eui} + R_{bi} + R_{ki}]I_{ei} \quad (28)$$

$$V_{mi} = [Z_{eui} + R_{bi}]I_{ei} + [R_{eli} + R_a]I_{ai} + V_{ai} = [Z_{eui} + R_{bi} + R_{li}]I_{ei} + R_{qi}V_{ai} \quad (29)$$

where R_{qci} are the ratios between the charge resistance and the the sum of cavity and charge resistances for each phase, and R_{li} are the resulting cavity resistances with the arcs short-circuited:

$$R_{qci} = \frac{R_{ci}}{R_{eli} + R_{ai} + R_{ci}}, \quad R_{li} = \frac{(R_{eli} + R_{ai})R_{ci}}{R_{eli} + R_{ai} + R_{ci}}$$

The magnitudes of the electrode voltages $|V_{mi}|$, can be evaluated as:

$$|V_{mi}| = \left\{(R_{eui} + R_{bi} + R_{ki})^2 + X_{eui}^2\right\}^{1/2}|I_{ei}| = |Z_{mi}|\,|I_{ei}| \quad (30)$$

$$|V_{mi}| = \left\{(R_{qi}V_{ai} + [R_{eli} + R_{bi} + R_{li}]I_{ei})^2 + (X_{eui}I_{ei})^2\right\}^{1/2} \quad (31)$$

where the magnitudes of "measured" phase impedances $|Z_{mi}|$, are defined as:

$$|Z_{mi}| = \left\{(R_{eui} + R_{bi} + R_{ki})^2 + X_{eui}^2\right\}^{1/2} = \left\{R_{mi}^2 + X_{eui}^2\right\}^{1/2} \quad (32)$$

Linearizing Eq. 30 by evaluating a first-order Taylor series expansion with:

$$|I_{ei}| = |I_{ei}^0| + \Delta i_{ei}\ , \quad R_{mi} = R_{mi}^0 + \Delta r_i$$

gives a linearized model of the voltage deviations Δv_{mi}, in terms of the current and resistance deviations Δi_{ei} and Δr_i:

$$\Delta v_{mi} = \left|Z_{mi}^0\right| \Delta i_{ei} + \frac{|I_{ei}^0|}{|Z_{mi}^0|} R_{mi}^0\, \Delta r_i \quad (33)$$

Linearizing Eq. 31 in the same way with:

$$|I_{ei}| = |I_{ei}^0| + \Delta i_{ei}\ , \quad V_{ai} = V_{ai}^0 + \Delta v_{ai}$$
$$R_{eui} = R_{eui}^0 + \Delta r_{eui}\ , \quad R_{eli} = R_{eli}^0 + \Delta r_{eli}$$

gives:

$$\Delta v_{mi} = \frac{1}{|Z_{mi}^0|}\left\{\left(R_{mi}^0 R_{sci}^0 + X_{eui}^2\right)\Delta i_{ei} + R_{mi}^0 \hat{k}_{ai}^0\, \Delta h_{ai}\right\} \quad (34)$$

where R_{sci} are the resulting phase resistances with the arcs short-circuited, R_{qai} are the ratios between the arc resistance and the sum of cavity and charge resistances for each phase, and $\hat{k}_{ai}$ are the "effective" arc voltage characteristics:

$$R_{sci}^0 = R_{eui}^0 + R_{bi} + R_{ki}^0$$
$$R_{qai}^0 = \frac{R_{ai}^0}{R_{ai}^0 + R_{eli}^0 + R_{ai} + R_{ci}}$$
$$\hat{k}_{ai}^0 = R_{qci}^0 k_{ai}^0 + \left|I_{ei}^0\right| \frac{\rho_e}{A_e} - R_{qci}^{02} \left|I_{ei}^0\right| \left[1 - R_{qai}^0\right] \frac{\rho_e}{A_e}$$

A Resistance-Electrode Displacement Model

A relationship between the resistance deviations Δr_i, and electrode displacements Δh_{ai}, can be found by combining Eqs. 33 and 34:

$$\left|Z_{mi}^0\right| \Delta i_{ei} + \frac{|I_{ei}^0|}{|Z_{mi}|} R_{mi}^0\, \Delta r_i = \frac{1}{|Z_{mi}^0|}\left\{\left(R_{mi}^0 R_{sci}^0 + X_{eui}^2\right)\Delta i_{ei} + \left(R_{mi}^0 \hat{k}_{ai}^0\right)\Delta h_{ai}\right\} \quad (35)$$

Eliminating the current deviations in equation 35 by inserting the relationship between the current and resistance deviations from Eq. 11:

$$\Delta i_{ei}/\Delta r_i = \alpha_{i1} = \frac{|V_R|^2}{Z_{sum}^{02} |I_{ei}|} a_{i1}$$

and rearranging, yields:

$$\Delta r_i = \frac{\hat{k}_{ai}^0}{\left(R_{mi}^0 - R_{sci}^0\right)\alpha_{i1} + |I_{ei}^0|}\, \Delta h_{ai} = \beta_i\, \Delta h_{ai} \quad (36)$$

APPENDIX C

BARKER'S INTERACTION FACTORS

I. J. Barker analyzed the interaction effect in submerged-arc furnaces and developed the *interaction factors* for electric furnaces in [5]. The model were developed based on the assumption of equal resistances and reactances in each phases and stiff electrode-to-electrode voltages:

$$R_i = R\ , \quad X_i = X\ , \quad Z_{Tr} = 0 \quad (37)$$

The interaction factors describe a dimensionless current-resistance model:

$$\frac{\Delta I_{ei}}{|I_{ei}|} = f_{ij} \cdot \frac{\Delta r_j}{|Z_m|} \quad (38)$$

The model is symmetric and the interaction factors f_{ij}, are given as:

$$f_{11} = f_{22} = f_{33} = -\frac{2}{3} \cdot \frac{R}{|Z_m|}$$
$$f_{21} = f_{32} = f_{13} = \frac{1}{3} \cdot \frac{-0.5R + 0.866X}{|Z_m|} \quad (39)$$
$$f_{31} = f_{23} = f_{12} = \frac{1}{3} \cdot \frac{-0.5R - 0.866X}{|Z_m|}$$

The interaction factors can be derived from the current-resistance model in Eq. 11. However, this will only be shown for the f_{11}-element. From Eq. 11 we have the following relationship:

$$\Delta I_{e1} = \frac{|V_R|^2}{Z_{sum}^{02}} \cdot \frac{a_{11}}{|I_{e1}|} \cdot \Delta r_1$$

By inserting the assumptions stated in Eq. 37 into the expression of a_{11} in Eq. 11 and Z_{sum} in Eq. 24, we get:

$$a_{11} = -18R\left(R^2 + X^2\right)^2\ , \quad Z_{sum} = 9\left(R^2 + X^2\right)^2$$

This yields:

$$\Delta I_{e1} = -\frac{|V_R|^2}{|I_{e1}|} \cdot \frac{2R}{9} \cdot \frac{1}{\left(R^2 + X^2\right)^2} \cdot \Delta r_1 = -\frac{|V_R|^2}{|I_{e1}|} \cdot \frac{2R}{9} \cdot \frac{1}{|Z_m|^4} \cdot \Delta r_1$$

By inserting the relationship between line and phase voltages:

$$|V_R| = \sqrt{3} \cdot |V_m| = \sqrt{3} \cdot |Z_m|\,|I_{e1}|$$

we get:

$$\Delta I_{e1} = -\frac{2}{3} \cdot \frac{|I_{e1}|}{|Z_m|^2} \cdot R \cdot \Delta r_1$$

which is the same as the interaction factor expression:

$$\frac{\Delta I_{e1}}{|I_{e1}|} = \left\{-\frac{2}{3} \cdot \frac{R}{|Z_m|}\right\} \cdot \frac{\Delta r_1}{|Z_m|} \quad (40)$$

C.2 Paper by Valderhaug, Balchen and Halvorsen (1992)

MODELBASED CONTROL OF THE FERROSILICON PROCESS *

Aasgeir Valderhaug and Jens G. Balchen

Division of Engineering Cybernetics
The Norwegian Institute of Technology, N-7034 Trondheim, Norway

Svenn Anton Halvorsen

Elkem a/s Research, Information Technology
P O. Box 40 Vaagsbygd, N-4602 Kristiansand, Norway

Abstract. A novel control strategy is presented for the ferrosilicon process. The strategy focuses on the control of the chemical process patterns in a submerged-arc ferrosilicon furnace, based on a dynamic model developed for the silicon process. The paper describes the first step in the development of such a control strategy and concentrates on synthesis and analyses of a state feedback controller.

Keywords. Process control, process models, modelbased control, metallurgy, metallurgical industries, submerged-arc furnace, reduction furnace.

INTRODUCTION

The production of ferrosilicon alloys in electric submerged-arc furnaces consumes large amounts of electric energy. The financial potential of optimal furnace operation is considerable, and strong efforts have been made in studying and analyzing the operation of this process. However, the process has turned out to be quite difficult to control, and optimal furnace operations seem hard to obtain (Breton, 1979; Westly, 1974). This is because the ferrosilicon process consists of various chemical, thermal, electrical and mechanical sub-processes. The main problems are the lack of direct measurements of the process conditions, the complex interaction between the subprocesses, the still limited knowledge about the chemical reaction patterns, and considerable process disturbances and control input uncertainties. The control tasks concerning the ferrosilicon furnace can be divided in two:

- To control the electrical states to ensure a favorable electrical power distribution, which is a fundamental basis for the rest of the process (Valderhaug and Sletfjerding, 1991).
- To control the chemical processes and reaction patterns in the furnace. This will be denoted as *metallurgical control.*

*Presented at 3rd IFAC Symposium DYCORD+'92, April 27-29 1992, College Park, Maryland, USA.

The purpose of this paper is to present a concept for a modelbased control strategy for the metallurgical control of the ferrosilicon process. At present, this is mainly a manual operation and is the metallurgist's responsibility based on process knowledge and observations, and no reliable automatic control systems are available. This is particularly due to the lack of direct measurements of the process conditions. These circumstances point to the need for a modelbased control strategy of the metallurgical control of ferrosilicon furnaces.

The paper is organized as follows: In the first section a submerged-arc ferrosilicon furnace is briefly described and the chemical reactions in the furnace are treated. Next, a model of the process is presented. Finally, the metallurgical control of the process is discussed, and a modelbased control strategy is proposed and analyzed by simulations.

THE FERROSILICON PROCESS

A schematic diagram of a submerged-arc furnace is shown in Fig. 1. The electric energy is supplied from high-voltage three-phase mains by transformers connected to three electrodes. The electrodes, symmetrically arranged in the circular furnace, are submerged into the furnace burden (*the charge*) to conduct the electric energy

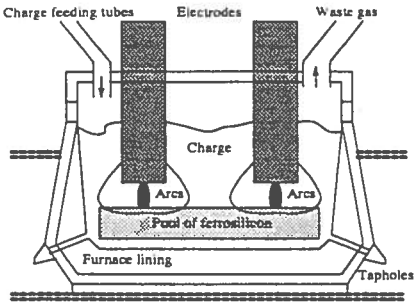

Fig. 1. A submerged-arc ferrosilicon furnace, showing two out of three electrodes.

into the heart of the furnace. Cavities, in which the currents form electric arcs, appear as the result of extensive heat generation in the charge around the electrode tips. The solid reactants of the process; quartz (SiO_2), coke and coal (C), and iron oxide (Fe_2O_2), are added in a specified stoichiometric relationship at the top of the furnace. The reactants are heated, quartz and iron oxide are reduced, and the ferrosilicon product ("FeSi") is drained from tap-holes at the bottom of the furnace. The silicon yield for such a furnace is about 90 %, which means that 10 % of the silicon leaves the furnace as silica gas (SiO). At the top, the gaseous products (SiO and CO) burn with air from the surroundings, and microsilica (SiO_2) and carbon dioxide (CO_2) are formed. The microsilica is recovered from the waste gas leaving the furnace. The production of ferrosilicon in a 65 MVA furnace is more than 120 tonnes/day.

Ferrosilicon alloys are produced with different iron contents. The most common alloys are FeSi 45, FeSi 75 and FeSi 90, where the figures indicate the percentage weight content of silicon. The overall reaction for FeSi 75 with 100% silicon yield, can be described by:

$$12\ SiO_2 + Fe_2O_2 + a\ C \longrightarrow 2\text{"}FeSi_6\text{"} + b\ CO + c\ CO_2 \qquad (1)$$

where a, b and c depend on the reduction of the iron oxide. The ferrosilicon process is closely related to the pure *silicon process*. If the alloy has more than 50% silicon content, the process behaves similarly to the silicon process. The reduction of quartz is the limiting factor in the ferrosilicon process, and qualitatively spoken the process will be easier to carry out the higher the iron content of the alloy (Schei and Larsen, 1982; Schei and Halvorsen 1991). Thus, the ferrosilicon process can be described by models of the pure silicon process, provided that the model parameters are properly adjusted, and in the further discussion the pure silicon process is treated.

Furnace operations. A ferrosilicon furnace is operated in the following discontinuous cycle:

- The furnace is *stoked*: The upper part of the charge is stirred and the charge materials are mixed, gas channels in the charge are destroyed, and the cavities may to some extent be filled.
- Next, raw materials are added (*charged*), and the furnace is filled up to a given charge level.
- Then comes a period with no operations. As time goes the cavities increase, gas channels are formed in the charge, and the charge is heated. The reactivity of the charge decreases due to reduced contact between the gases and the reactants. Finally, the temperature of the gas leaving the furnace increases strongly, the microsilica content in it increases rapidly, and a new stoking is necessary. The length of such an operation cycle is about half an hour.

The tapping of ferrosilicon is also usually discontinuous, and the content of produced metal in the furnace will fluctuate within the tapping periods, which are about an hour.

Metallurgical control. In principle several candidates are available for use as control variable in the metallurgical control of a ferrosilicon furnace:

- The composition of added charge, which will be denoted *carbon coverage*, referring to the stoichiometric relationship between carbon and quartz.
- The choice of electrical working-point: The power consumption in the furnace, the power distribution between the hearth and the charge, and the electrical control parameters.
- The choice of procedures for the stoking/charging and tapping operations.
- The choice of raw materials regarding the qualities of coke, coal, quartz and iron oxide, the choice of particle sizing of the raw materials and the particle sizing distribution between them, and the proportion between coke and carbon in the added carbon mixture.

These candidates have very different properties. Some of them are typically long-term variables with a limited possibility of high-frequent variations. The choice of raw material properties and operation procedures belong to this category and cannot be regarded as ordinary control variables. However, they should be taken into account when

considering long-term process optimization. Furthermore, a ferrosilicon furnace is usually operated at a specified electrical power consumption corresponding to a "constant" reaction volume, and the amount of charge added will be given by the production rate. This leaves us with the following control variables available for use in continuous metallurgical control: The carbon coverage and the choice of electrical working point.

The ferrosilicon process has no direct measurements of the inner process conditions, and only variables available from the outer furnace are measured: The amount of tapped metal, which indicates the production rate of ferrosilicon, and the content of microsilica in the waste gas. In addition, the temperatures of tapped metal and waste gas are measured. The electrical states on the other hand, are well instrumented, but they will at best be indirect measures of the process conditions in the hearth of the furnace.

The main disturbances of the process are improper mixing of the charge reactants and gas channel formations in the charge, leading to a situation where the desired countercurrent conditions between the reactants and upstreaming gas become unattainable. Furthermore, the residence-time of the reactants in the charge or the charge height can be reduced and result in less effective reactions. There will also be some degree of uncertainty concerning the added charge due to variations in composition and material properties.

The chemical reactions

The ferrosilicon process can be regarded as a two-stage process. From a modelling point of view it can be divided into two reaction zones: An inner zone, consisting of the cavities and the surrounding charge, and an upper zone, consisting of the charge above the cavities, as shown in Fig. 2 (Schei and Larsen, 1982: Schei and Halvorsen 1991).

The upper reaction zone. This part of the furnace behaves like a packed bed reactor. The solid materials are heated by partly electric conduction (Q_{cond}) and released chemical reaction energy, and the temperature is in the range 1000-2000 K. Quartz melts and countercurrent reactions occur between carbon materials and upstreaming silica gas from the hearth of the furnace and silicon carbide (SiC) is produced:

$$SiO + 2\,C \rightarrow SiC + CO \qquad (2)$$

Furthermore, the excess of silica gas "condenses" and releases large amounts of energy through the

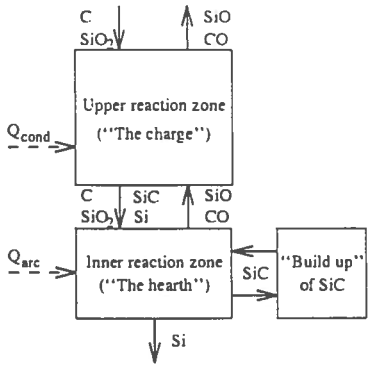

Fig. 2. A schematic model of the silicon process.

reaction:

$$SiO \rightarrow \frac{1}{2}[SiO_2 + Si] \qquad (3)$$

This condensation will if possible, continue until the furnace top is heated sufficiently to let the silica gas escape from the furnace.

The production of SiC is a necessary intermediate stage in the process. An optimal reaction pattern means that all the carbon should leave this zone and enter the inner reaction zone as SiC and not as C.

The inner reaction zone ("The hearth"). The cavities in the hearth of the furnace can be regarded as constantly stirred tank reactors. Most of the heat is generated in this region of the furnace by the electric arcs (Q_{arc}), which create strong stirring in the cavities. The temperature is about 2300 K. In the cavities there is a complicated reaction pattern between the present reactants, consuming large amounts of energy. The main part of the silicon is produced in this zone, and the smelted metal forms pools below the cavities. The reactions can formally be described by a combination the following:

$$SiO_2 + Si \rightarrow 2\,SiO \qquad (4)$$

$$SiO + SiC \rightarrow 2Si + CO \qquad (5)$$

and, if carbon is present, the reaction given in Eq. (2) occurs as well. The presence of carbon in the inner zone can result in an increasing content of SiC in the cavities, and as time goes by this will damage the production.

The gas leaving this zone consists of about 50 % SiO and 50 % CO, according to thermodynamic. The content of SiO will be somewhat lower if FeSi is produced. The "recycling" of SiO between the reaction zones (Eqs. (3) and (4)) has the effect

of some kind of a heat pump, supplying energy for heating and melting the solids in the upper reaction zone.

The overall reaction in the silicon process can be stated as:

$$(1+x)\ SiO_2 + (2+x)\ C \rightarrow Si + x\ SiO + (2+x)\ CO \qquad (6)$$

where x denotes the *silicon loss*, silica gas (SiO) leaving the furnace in proportion to added silica (quartz). The *silicon recovery*, produced silicon in proportion to added silica (quartz), is given as $1/(1+x)$.

MODEL OF THE SILICON PROCESS

A dynamic model of the silicon process has been developed by Elkem a/s Research, Norway (Halvorsen, 1988; Halvorsen, Downing and Schei, 1989). The model gives a fair description of the chemical reactions in a silicon furnace and has been chosen to be used in the development of novel control strategies for the metallurgical control of ferrosilicon furnaces. The model parameters are adjusted to describe the reactions in a 65 MVA ferrosilicon furnace.

The model of the upper reaction zone is based on a unidimensional distributed description of concentrations of solid and liquid reactants in the form:

$$\frac{\partial c_i}{\partial t} + \frac{\partial v_s c_i}{\partial z} = \sum_j \alpha_{ij} R_j - S_i \qquad (7)$$

where subscripts i and j indicate component i and reaction j respectively, c denotes the concentration, v_s the downward velocity of reactants, α_{ij} the stoichiometric coefficient of component i in reaction j, R the reaction rate, and S denotes the melting rate. The reaction rates for the gas-solid and gas-liquid reactions are described by (Halvorsen, 1988):

$$R_j = k_j \cdot c_i \cdot \Delta p_j \cdot e^{-E_j/RT} \qquad (8)$$

where subscript j indicates reaction j, k denote the reaction rate constant, Δp the reaction pressure (driving force), E the activation energy, R the molar gas constant, and T denotes the temperature. The gas concentrations, gas and solid velocities, and enthalpies are described in a corresponding way. The distributed description of the upper reaction zone is coupled to a similar point description of the inner reaction zone (the hearth).

In the numerical solution the distributed model is approximated by a segment model, and further simplifications regarding gas dynamics and reactant movements are assumed. The simulation model consists in each segment of five differential equations describing enthalpy and reactant concentrations, while the hearth is described by four differential equations. Nonlinear algebraic equations describe gas fluxes and reactant velocities in the hearth and the charge segments. In addition, there are differential equations describing derived variables such as the amount of production and enthalpy losses.

The model corresponds to the following state-space description:

$$\begin{aligned} \dot{\underline{x}} &= \underline{f}(\underline{x}, \underline{u}, \underline{w}) \\ 0 &= \underline{g}(\underline{x}, \underline{u}, \underline{w}) \\ \underline{q} &= \underline{h}(\underline{x}, \underline{u}, \underline{w}) \end{aligned} \qquad (9)$$

where $\underline{x} = \left[\underline{x}_h^T, \underline{x}_{c_i}^T\right]^T$, $i = 1 \ldots n$, and $\underline{x}_h$ and $\underline{x}_{c_i}$ are vectors containing the states in the hearth and the charge segments respectively. $\underline{u}$ is the control input vector, and vector $\underline{w} = \left[\underline{w}_h^T, \underline{w}_i^T\right]^T$ contains the gas fluxes and reactant velocities. Vector $\underline{q}$ contains the derived variables, and n is the number of segments. The simulation model contains $(4 + 5n + 6)$ states. The hearth state vector is:

$$\underline{x}_h = \begin{cases} \text{concentr. of C} \\ \text{concentr. of SiC} \\ \text{concentr. of "condensate"} \\ \text{enthalpy} \end{cases} \qquad (10)$$

where "condensate" is given as $1/2\,[SiO_2 + Si]$, corresponding to the reaction in Eq. (3). The charge segment state vectors are:

$$\underline{x}_{c_i} = \begin{cases} \text{concentr. of } SiO_2 \\ \text{concentr. of C} \\ \text{concentr. of SiC} \\ \text{concentr. of condensate} \\ \text{enthalpy} \end{cases} \qquad (11)$$

The derived state vector is:

$$\underline{q} = \begin{cases} \text{amount of released SiO} \\ \text{amount of released CO} \\ \text{amount of produced Si} \\ \text{accum. heat losses by radiation} \\ \text{accum. enthalpy in released gas} \\ \text{accum. enthalpy in produced Si} \end{cases} \qquad (12)$$

The model is based on an assumption of fixed electrical conditions, and it is adapted so that the carbon coverage in the added charge can be used as a control variable. The control input vector will then be:

$$\underline{u} = \{ \text{carbon coverage in added charge} \qquad (13)$$

The carbon coverage is chosen to be a time-discrete control input, corresponding to the furnace operation cycle. The model will later be

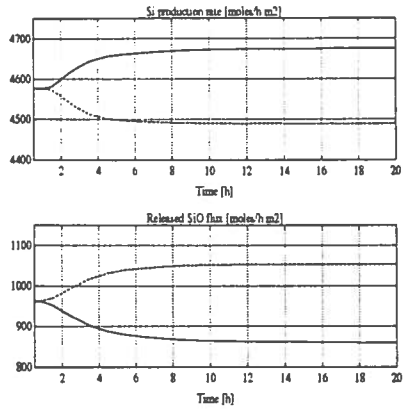

Fig. 3. Step responses of Si production rate and released SiO flux to variations in carbon coverage. (Solid line: 1 % increase, dashed line: 1% decrease.)

further adapted so that the choice of electrical working-point can be included in the control input vector.

The model can simulate the furnace in two ways, either with the discontinuous stoking-charging cycle, or with continuous charging, corresponding to mean operation conditions. The continuous version seems preferable for use in a model-based control strategy, as the concerned dynamics are much slower then the operating cycles. The state sensitivities to changes in the carbon coverage control input is analyzed by step response simulations as shown in Fig. 3.

A MODELBASED CONTROL STRATEGY

The ferrosilicon process is characterized by a large number of state variables and a relatively low number of control inputs. The goal of the metallurgical control is to attain "optimal" furnace conditions by controlling the chemical processes and reaction patterns in the furnace. However, this may be difficult to express in terms of the state vector, and the controllability of the process may be limited due to the low dimension of the control input vector. This problem can be avoided by expressing the control task in terms of a property state vector, describing the states we in fact want to control. The property vector should be in the size of the control input vector and chosen based on process knowledge. A possible candidate is:

$$\underline{z} = \left\{ \begin{array}{l} \underline{y} = \left\{ \begin{array}{l} \dot{q}_1 : \text{released SiO flux} \\ \dot{q}_3 : \text{production rate of Si} \end{array} \right. \\ x_{h2} : \text{concentr. of SiC in the hearth} \end{array} \right. \quad (14)$$

The property vector $\underline{z}$ characterizes the circumstances we want to control in a ferrosilicon furnace. Vector $\underline{z}$ also contains the available measurement from the furnace $\underline{y}$, the Si production rate and released SiO flux in the waste gas.

The metallurgical control is at present mainly a manual operation, and there are several potential control strategies. As a first attempt *a set point control strategy* expressed in terms of the property vector $\underline{z}$, is chosen. The control input is given as $\underline{u} = \underline{u}_0 + \Delta\underline{u}$, where u_0 is the control input corresponding to a given set point $\underline{z}_0$, and Δu is calculated by a controller operating on deviations in the property vector $\Delta\underline{z}$ around $\underline{z}_0$. The controller is based on a state-space description of the model in Eq. (9), linearized around the working point $(\underline{x}_0, \underline{q}_0, \underline{u}_0)$, and uses state feedback control.

$$\begin{aligned} \Delta\dot{\underline{x}} &= A\,\Delta\underline{x} + B\,\Delta\underline{u} \\ \Delta\underline{q} &= H\,\Delta\underline{x} \end{aligned} \quad (15)$$

where $\Delta\underline{x} = \underline{x} - \underline{x}_0$, $\Delta\underline{u} = \underline{u} - \underline{u}_0$ and $\Delta\underline{q} = \underline{q} - \underline{q}_0$. The measurements of the process conditions $\underline{y}$ is given as a sub-vector of $\dot{q}$:

$$\Delta\underline{y} = D_1\,\Delta\underline{\dot{q}} = D_1 H\,\Delta\underline{x} \quad (16)$$

where $\Delta\underline{y} = \underline{y} - \underline{y}_0$. The property vector $\underline{z}$, defined in Eq. (14), is:

$$\Delta\underline{z} = \begin{pmatrix} D_1\,\Delta\underline{\dot{q}} \\ D_2\,\Delta\underline{x} \end{pmatrix} = D\,\Delta\underline{x} \quad (17)$$

where $\Delta\underline{z} = \underline{z} - \underline{z}_0$.

The state space controller is chosen to be an LQ controller found by optimization of the performance index:

$$J = \int_0^\infty (\Delta\underline{z}^T Q \Delta\underline{z} + \Delta\underline{u}^T P \Delta\underline{u})\; dt \quad (18)$$

with respect to $\Delta\underline{u}$. This task is equivalent with the optimization of:

$$J = \int_0^\infty \left(\Delta\underline{x}^T \tilde{Q} \Delta\underline{x} + \Delta\underline{u}^T P \Delta\underline{u}\right)\; dt \quad (19)$$

where $\tilde{Q} = D^T Q D$, subject to the system in Eq. (15). The optimal deviation control input is given by:

$$\Delta\underline{u} = G\Delta\underline{x} \quad (20)$$

and the control input is given as:

$$\underline{u} = \underline{u}_0 - G\,(\underline{x}_0 - \underline{x}) \quad (21)$$

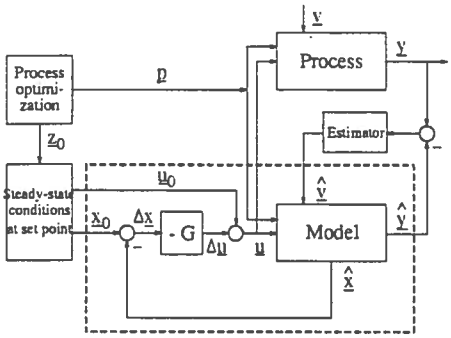

Fig. 4. A modelbased control strategy.

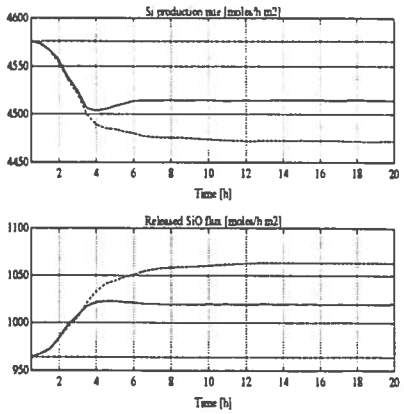

Fig. 5. Step responses of Si production rate and released SiO flux to changes in raw material properties. (Solid line: controlled system, dashed line: uncontrolled system, and dotted line: referances.)

The modelbased control strategy is illustrated in Fig. 4. The strategy is based on a state estimator, because the states cannot be measured directly. The property set point vector $\underline{z}_0$ and other operation parameters $\underline{p}$ are found from long-term process optimization, and the working point $(\underline{x}_0, \underline{q}_0, \underline{u}_0)$ can be found from $\underline{z}_0$ assuming stationary conditions ($\underline{\dot{z}}_0 = 0$). However, in this paper we focus only on the state controller as the first step in the development of a complete control strategy. The dashed box in Fig. 4 shows the part of the scheme covered by this work.

An alternative optimizing modelbased control strategy is the *quasi-dynamic optimal control*-method (Balchen and Mummé, 1988). In this method the control input is given as $\underline{u} = \underline{u}_0 + \Delta\underline{u}$, where u_0 is found from optimization of a performance index at steady-state (or slowly varying) conditions, and a minimum variation controller (LQ) operates on deviations around these conditions, calculates Δu.

Control synthesis and simulations

The model is implemented with $n = 5$, with a given set of parameters. The linearized model in Eq. (15) is found numerically at steady-state conditions $(\underline{x}_0, \underline{q}_0, \underline{u}_0)$, corresponding to the property vector set point $\underline{z}_0$. The system matrices A and B are highly structured:

$$A = \begin{bmatrix} a_{hh} & a_{h1} & 0 & 0 & 0 & 0 \\ a_{1h} & a_{11} & a_{12} & 0 & 0 & 0 \\ a_{2h} & a_{21} & a_{22} & a_{23} & 0 & 0 \\ a_{3h} & a_{31} & a_{32} & a_{33} & a_{34} & 0 \\ a_{4h} & a_{41} & a_{42} & a_{43} & a_{44} & a_{45} \\ a_{5h} & a_{51} & a_{52} & a_{53} & a_{54} & a_{55} \end{bmatrix} \quad B = \begin{bmatrix} 0 \\ 0 \\ 0 \\ 0 \\ 0 \\ b_5 \end{bmatrix}$$

$$H = \begin{bmatrix} h_h & h_1 & h_2 & h_3 & h_4 & h_5 \end{bmatrix}$$

where a_{ij}, $i, j = h, 1 \ldots 5$, are sub-matrices concerning the states in the segments i and j, b_5 is the sub-vector concerning the top segment, and h_i are sub-matrices concerning the derived states and the states in segment i. The system (A, B) is stable and controllable, even though the examination of the controllability turned out to be numerically ill-conditioned. Furthermore, the system $(A, D_1 H)$ is observable, and the model state variables can theoretically be estimated by a state estimator using the process measurements.

The state weight matrix Q in Eq. (18) is chosen to be diagonal with matrix element magnitudes corresponding to acceptable property state variations, and the control weight matrix P is chosen to avoid large variation in the control input variable. The optimal controller is implemented in the simulation model as a discrete controller and is analyzed by simulation examples. Figure 5 shows the step responses of Si production rate and released SiO flux to changes in some raw material properties for the controlled and uncontrolled systems. The property variables are controlled satisfactorily, and the control input varied in an acceptable range during the simulation. The simulations indicate promising properties, even though no optimization on the weight matrices Q and P has been evaluated, and further studies in optimizing the state feedback controller should be evaluated.

Evaluation of the control strategy

The simulation studies have shown that the process can be controlled by the proposed state feedback controller. As the controller uses state variables that are not measurable, the implementation of such a controller must be based on a state estimator. The stated model in Eq. (9) gives a fair

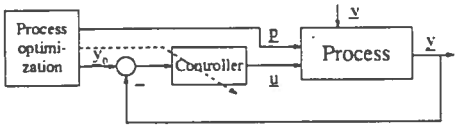

Fig. 6. An output feedback control structure.

description of the chemical reactions in the silicon process, but will still have a limited validity as a model of a real furnace. The main objections to the model are that it only describes vertical variations in the furnace, assuming homogeneous conditions across the horizontal cross section, the simplified point description of the inner reaction zone, and the large uncertainty in the choice of several model parameters. Thus, the implementation of a state estimator based on this model seems to be impracticable, and presently, the implementation of the complete modelbased control strategy is an unrealistic goal.

A possible solution to this problem is to develop a reduced order controller. The proposed set point controller can be further adapted to for instance a reduced order state controller with feedback only from some property states, or to an output feedback controller with feedback from the process measurements, as shown in Fig. 6 (Anderson and Moore, 1989). The reduced order controller could in addition to the available measurements, use estimates of some inner process conditions based on an electrical model estimator.

The synthesis of the reduced order controllers will be based on the proposed modelbased state feedback controller, using the knowledge gained from analyses and simulation studies. The controllers will be implemented in the simulation model and further analyzed prior to an prospective implementation on the furnace. The development of an applicable metallurgical control strategy will be the topic of continuous work.

CONCLUSION

A modelbased control strategy for the ferrosilicon process is proposed, and the first step in the development of of such a strategy, the synthesis of a state feedback controller, is described. At present, a reduced order control structure based on the state feedback controller, seems preferable. Further studies in optimizing the state feedback controller and the development of alternative reduced order control structures, together with process optimization, are topics for continuous work.

ACKNOWLEDGEMENTS

The work is a part of a research program on modelbased control of ferrosilicon furnaces in which The Division of Engineering Cybernetics at The Norwegian Institute of Technology and Elkem a/s, Norway take part. The work has been financially supported by Elkem a/s and The Royal Norwegian Council for Scientific and Industrial Research (NTNF).

REFERENCES

Anderson, B. D. O., and J. B. Moore (1989). Optimal Control: Linear quadratic methods. Prentice-Hall International, Inc., Chap. 10.4, pp. 317-319.

Balchen, J. G., and K. I. Mummé (1988). Process Control: Structures and applications. Van Nostrand Reinhold Company Inc., New York. Chap. 2.16, pp. 83-89.

Breton, E. (1979). *The maze of ferrosilicon production*, 37th Electric Furnace Conference, Detroit.

Halvorsen, S. A. (1988). *Dynamic model of a metallurgical shaft reactor with irreversible kinetics and moving lower boundary.* Proc. 2nd European Symposium on Mathematics in Industry, March 1-7, 1987, Oberwolfach, Teubner, Stuttgart 1988. pp 211-223.

Halvorsen, S. A., J. H. Downing, and A. Schei (1989). *Developing a unidimensional simulation model for producing silicon in an electric furnace.* 4th European Conference on Mathematics in Industry, Strobl, Austria.

Schei, A., and K. Larsen (1982). *A stoichiometric model of the ferrosilicon process.* Proc. 39th Electric Furnace Conference, 1981, Houston. Iron and Steel Society, AIME, 1982. pp 301-309.

Schei, A., and S. A. Halvorsen (1991). *A stoichiometric model of the silicon process.* Proc. Ketil Motzfeldt Symposium, The Norwegian Institute of Technology, May 24th, 1991, Trondheim, Norway.

Valderhaug, Aa., and P. Sletfjerding (1991). *A non-interacting electrode current controller for submerged-arc furnaces.* 49th Electric Furnace Conference, Toronto

Westly, J. (1974). *Resistance and heat distribution in a submerged-arc furnace*, INFACON Johannesburg.